N° d'ordre : 40270

Université Lille 1

École Doctorale des Sciences Pour l'Ingénieur

Thèse

pour obtenir le grade de

Docteur de l'Université des Sciences et Technologies de Lille

Spécialité : Génie Électrique

Présentée et soutenue publiquement par

Keyu CHEN

le 5 mai 2010

COMMON ENERGETIC MACROSCOPIC REPRESENTATION AND UNIFIED CONTROL STRUCTURE FOR DIFFERENT HYBRID ELECTRIC VEHICLES

Membres du jury :

M. Prof. Josep BALCELLS SENDRA, *Examinateur*, Universitat Politècnica de Catalunya

M. Prof. Alain BERTHON, *Codirecteur de la thèse*, Université de Franche-Comté

M. Prof. Alain BOUSCAYROL, *Directeur de la thèse*, Université de Lille 1

M. Prof. Thierry-Marie GUERRA, *Examinateur*, Université de Valenciennes et Haut Cambrésis

M. Prof. Philippe LATAIRE, *Rapporteur*, Vrije Universiteit Brussel

M. Prof. Claude MARCHAND, *Rapporteur*, Université Paris XI

M. Ladimir PRINCE, *Invité*, PSA Peugeot Citroën

M. Dr. Rochdi TRIGUI, *Examinateur*, INRETS Bron

REPRÉSENTATION ÉNERGÉTIQUE MACROSCOPIQUE ET STRUCTURE DE COMMANDE COMMUNES POUR DIFFÉRENTS VÉHICULES ÉLECTRIQUES ET HYBRIDES

Acknowledgement

I would like to express my deep and sincere gratitude to my supervisor, Professor Alain BOUSCAYROL at University of Lille, for his hardworking, perseverance and creativity.

I am deeply grateful to my co-supervisor, Professor Alain BERTHON at University of Franche-Comté, for his continuous support in the Ph.D. program.

My thanks must also go to Dr. Rochdi TRIGUI at LTE-INRETS of Lyon, for his scientific support.

Special thanks also to Professor Claude MARCHAND from University of Paris XI and Prof. Philippe LATAIRE from Vrije Universiteit Brussel, the reviewers of this thesis, for their encouragement, constructive comments and questions.

I would like to thank the rest of my thesis committee: Professor Josep BALCELLS SENDRA from Universitat Politècnica de Catalunya, Professor Thierry-Marie GUERRA from University of Valenciennes and Haut Cambrésis and Mr. Ladimir PRINCE from PSA Peugeot Citroën, for their insightful comments and their inspirations.

I would like to acknowledge Professor Betty LEMAIRE-SEMAIL of University of Lille, head of the control team of L2EP, for her support.

I would like to express my gratitude to those persons who were important to the Ph. D research works; and who spent their time and shared their knowledge. This thesis would not have been possible without their contributions.

Résumé

Le domaine du transport, l'un des plus grands secteurs d'énergie, doit affronter des défis importants tels que la sécurité énergétique, le changement climatique et les problèmes de la pollution. Pour répondre à cela, les Véhicules Électriques et Hybrides (VEHs) deviennent une option intéressante. L'un des problèmes clés liées au développement des VEHs est la conception de la commande de ce type de système complexe, lequel est composé de plusieurs sources et sous-systèmes. En utilisant la Représentation Énergétique Macroscopique (REM) qui est une représentation graphique basée sur l'énergie, une structure de commande peut être déduire directement par inversion du modèle. L'objectif de cette thèse est d'établir une REM commune capable de décrire différentes architectures de VEHs. A partir de cette REM, une structure de commande générale est obtenue. Cette structure de commande peut être utilisée pour l'étude de VEH série, parallèle et mixte, en changent seulement différents valeurs de paramètres. Cette REM permet de mieux comprendre les flux de puissance principaux des différent VEHs. En utilisant une approche descendante, la modélisation et la commande des différent VEHs ont été réalisées de manière générale, même si ces VEHs peuvent être très différents les uns des autres en termes de structure. Le temps requis pour la conception de la commande peut être ainsi considérablement réduit. Qui plus est, avec la même structure de commande, les différents VEHs peuvent être comparés plus facilement. La structure commune a été validée expérimentalement sur un émulateur de véhicule hybride série. Différentes gestions énergétiques plus efficaces de VEHs pourraient être développées et comparées. De ce fait, la consommation de carburant et l'émission de CO2 peuvent être réduites.

Abstract

The transportation domain, one of the largest energy sectors, is currently facing huge challenges, including energy security, climate change and pollution problems. To meet these challenges, Hybrid Electric Vehicles (HEVs) have become an interesting option. One of the key issues related to HEV development is the control design of such complex systems, which are composed of multiple sources and subsystems. Using Energetic Macroscopic Representation (EMR), an energy based graphical description, the inversion-based control structure of the system can be deduced directly. The objective of this thesis is to establish a common EMR which can describe different HEVs. From this common EMR, a unified control scheme is deduced, which can be used for the study of series, parallel, and series-parallel HEVs, by simply setting different parameter values. The common EMR offers a better understanding of the main power flows of different HEVs. Using this top-down approach, the modeling and control design of different HEVs have been achieved in a general way, despite the fact that HEVs can be very different from each other in terms of structure. The time required for control design can be significantly reduced. Furthermore, given the same control structure, different HEVs could be easily compared. Experimental results have been validated the control scheme commune using a Hardware-in-the-loop simulation for a series HEV in a real-time environment. Based on this work, more efficient energy managements of HEVs could be achieved and compared, and thus to reduce HEV fuel consumption and CO2 emissions.

Contents

Introduction

The transportation domain, one of the largest energy sectors, must face huge challenges such as energy security, climate change and pollution problems. Although fossil fuel resources are limited, the demand for oil has increased significantly. This growth has come from new demands for personal-use vehicles powered by conventional Internal Combustion Engines (ICEs). It is estimated that oil supply and demand will be out of balance in 2030 [Eshani 2005]. The transport sector is responsible for a significant and growing share of greenhouse gas emissions and air pollution. Government agencies and organizations have therefore developed more stringent standards for fuel consumption and emissions. The transport sector needs other options to meet these challenges.

Battery-powered Electric Vehicles (BEVs) appear to be an ideal solution to deal with problems related to climate change and pollution, since they have zero local oil consumption and zero local emissions. However, issues such as high costs, short driving ranges and long charging times have highlighted their limitations [Raskin 2006] [Chan 2010]. Alternative fuels, such as natural gas, biofuel and Hydrogen, offer other possibilities. Natural gas vehicles produce fewer harmful emissions than other classic fossil fuels, but they have the same problems as ICE vehicles, such as limited resources and emission of CO_2. Issues related to biofuels involve developing new feedstocks, production processes, and land requirements. Key issues for fuel cell vehicles include hydrogen production, on-board hydrogen storage, the development of refueling infrastructure, and efficiency improvement. Each option has its advantages and drawbacks. Might it be possible to combine different energy sources and drivetrains, as is the case with Hybrid Electric Vehicles (HEVs)? HEVs combine at least two drivetrains, one based on fuels with ICEs, and the other based on batteries with Electric Machines and Power Electronics. Electric drivetrains have high efficiency, and can further optimize the efficiency of the ICE and thus reduce oil consumption. At the same time, HEVs have greater driving range than BEVs. In 1997, the first commercial mass-market hybrid vehicle, the Toyota Prius, was sold in Japan. Subsequently, more than 20 models of HEVs have been introduced to the auto market. Despite these advantages, HEVs do not yet play a major role in the automotive market. The most important reason is the high price of HEVs. Other key issues related to HEV development involve the drivetrain design, batteries, and control design. Promotion of HEV research involves multiple skills. Furthermore, timely exchange and cooperation between academic and industrial partners is essential.

In this context, MEGEVH (Modélisation Energétique et Gestion d'Energie de Véhicules Hybrides / Energy Modeling and Energy Management of Hybrid Vehicles) was established in 2005. It is a thematic group of the inter-regional network "RT3" (Recherche Technologique sur les Transports Terrestres / Technological Research for Land Transport) of the French Ministry of Research. It is made up of academic institutions and industrial partners

that work on HEVs in France. The objective of MEGEVH is to foster collaboration regarding energetic modeling, energy management and energy optimization of HEVs.

Using different modeling approaches [Gao 2007], different vehicle architectures have been discussed [Wipke 1999] [Bogosyan 2007]. In most of the cases, these architectures are modeled using structural approaches. These structural approaches are very useful when the aim is to quickly build a HEV model. These approaches however can not directly yield the control scheme. In order to obtain the control scheme systematically, causal and functional modeling approaches are necessary. Compared to other approaches, Energetic Macroscopic Representation (EMR), as a graphical description, focuses on system functions and offers a macroscopic energetic view. Thanks to these features, EMR and its inversion-based control contribute significantly to the control design and energy management of HEVs.

EMR has been successfully applied to different MEGEVH projects [Lhomme 2007] [Allegre 2009] [Letrouve 2009]. In these studies, each HEV or system was examined separately and independently. Each HEV had its own EMR and its own inversion-based control scheme (bottom-up approach). However, HEVs have some common points in terms of power flows. A common energetic macroscopic modeling for different HEVs is possible (top-bottom approach).

MEGEVH-macro is interested in HEV modeling using energetic descriptions for control purposes. Two parallel Ph. Ds have been undertaken within the framework of MEGEVH-macro. These Ph. Ds involve cooperation between L2EP (Lille), FEMTO-ST (Belfort), LTE (INRETS) and Nexter Systems. One Ph. D focuses on energy sources of HEVs [Boulon 2009-a]. The other - this thesis - focuses on different drivetrains of HEVs.

The objective of this thesis is to establish a common EMR which can describe different HEVs. Based on this common EMR, a unified control scheme which can be used for different HEVs is deduced. Using a common EMR, the main power flows of different HEVs may be better understood. The common points can be revealed, and the differences can be emphasized. Contrary to the other inversion-based control structures deduced individually from each EMR, a unified control scheme can be deduced from the common EMR, which can be used in the study of different HEVs. Like other inversion-based control structures deduced from EMRs, this unified control structure includes two levels: a local level which deals with each subsystem, and a strategy level which is called the energy management or supervision strategy. The use of EMR and the inversion-based control imply that the two levels must operate mutually. The unified control structure therefore highlights the differences both at the local and strategy levels for different HEVs. If modeling and control design of different HEVs can be achieved in a general way, the time required for control design can be significantly reduced. Furthermore, under the same control structure, different HEVs could be easily compared. More efficient energy managements of HEVs could be achieved and compared, to reduce manufacturing costs, fuel consumption and exhausting emissions without sacrificing dynamic performance.

This thesis aims to offer another point view on HEVs using the common EMR, and to propose a new control scheme using the top-down approach. This thesis consists of four chapters.

In chapter I, the background and objective of this thesis are presented. First, the state of the art of HEVs is presented. One of the key issues related to HEV development is the control design of such complex systems. In the second section, different modeling approaches and control design are therefore discussed. In the third section, the objective of this thesis is introduced.

In chapter II, the general approach, using EMR and the inversion-based control to achieve the modeling and the control design of electric drives, is introduced. In the first section, different electric drives are summarized. In the second section, a generic EMR is described, from which other EMRs of some basic electric drives can be obtained. In the third section, the inversion-based controls of two different electric drives are presented.

Chapter III is dedicated to the modeling and control design of whole systems in a general way. The general approach used in chapter II, is extended to the whole system. In the first section, the common points of different HEVs, in terms of architectures and power flows, are discussed. In the second section, a common EMR is introduced to describe different HEVs. In the third section, a unified control scheme deduced from this common EMR can be applied to the study of series, parallel, and series-parallel HEVs.

Chapter IV deals with the validation and extended applications of the unified control scheme. In the first section, the validation is carried out both by simulation, and, in a real-time environment, by experimentation. In the second section, extended applications of this unified control scheme are discussed.

Chapter I

Hybrid Electric Vehicles and Control design

Introduction

Oil, also known as “black gold”, is a vital natural resource which will one day cease to exist. In recent decades, however, the oil consumption of the transportation sector has grown at a higher rate than any other sector. This growth has mainly come from new demands for personal use vehicles powered by conventional Internal Combustion Engines (ICEs). Given that some environmental problems, such as the green house effect, are directly related to ICE vehicle emissions, government agencies and organizations have developed more stringent standards for fuel consumption and emissions.

Battery-powered Electric Vehicles (BEVs) appear to be an ideal solution to deal with the energy crisis and climate change, since they have zero local oil consumption and zero local emissions. However, issues such as high cost, short driving range and long charging time have highlighted their limitations [Raskin 2006] [Chan 2010]. Hybrid Electric Vehicles (HEVs) were developed to overcome the limitations of ICE vehicles and BEVs.

One of the key issues of HEV development is the control design of such complex systems. Different modeling approaches can be used for the purpose of control design. Compared to other approaches, Energetic Macroscopic Representation (EMR) offers a more macroscopic energetic view, and emphasizes the way the system functions [Bouscayrol 2003]. Hence it contributes significantly to the control design and energy management of HEVs.

This chapter aims to present the state of the art of the modeling and control of HEVs in order to define the objective of this thesis.

Section one is dedicated to the emergence of HEVs. In the second section, different modeling approaches and control designs are discussed. In the third section, the objective of this thesis, within the framework of the national scientific network MEGEVH, is introduced.

I.1. Emergence of Hybrid Electric Vehicles

Today's transportation technology has brought human beings increased freedom of mobility. Nevertheless, a steady increase in energy demands, the limitation of fossil fuel sources, and environmental concerns, are huge challenges for the transportation sector [IEA 2009-b] [Hellgren 2007]. In this section, the emergence of Hybrid Electric Vehicles (HEVs) is introduced. First, the evolution of road transportation technology can be seen by examining the history of automotives. Second, the challenges of the transportation sector are mentioned. Among different possible solutions, HEVs have strong potential and are expected to become a mainstay in the automotive market [Raskin 2006]. In the third and final part, HEVs are discussed.

I.1.1. Automotive history

The definition of the term automotive is: an automobile is a wheeled, trackless, self-propelled vehicle for land transportation of normally as many as eight people [McGraw 2003]. This sub-section is dedicated to the evolution of this road transportation technology [Raskin 2006] [Bellis 2009] [Eshani 2005].

Early steam powered vehicles – In 1769, the first self-propelled road vehicle was invented by the French engineer, Nicolas Joseph Cugnot. This vehicle was powered by a steam-engine. Steam engines used boiling water heated by burning fuel to produce mechanical motion. Compared with horses, steam engines had many advantages, especially the ability to work in varied weather conditions without the need to rest. These engines, however, were too inefficient for transport, with less than 5% efficiency at the time.

Early Battery-powered Electric vehicles – Between 1832 and 1881, many names were associated with the invention of Battery-powered Electric Vehicles (BEVs): the Scot Robert Anderson, the Dutchmen Stratingh of Groningen and his assistant Christopher Becker, the American Thomas Davenport and the French Gustave Trouvé etc. BEVs were powered by batteries and electric machines. In 1897, the "Electric Carriage and Wagon Company" of Philadelphia in the USA commercialized their New York taxis. BEVs became popular because they were quieter, ran more smoothly and produced less odors than other vehicles. They required neither gear changes nor manual effort during ignition, unlike gasoline vehicles. The range of BEVs, however, was limited. The only satisfactory roads during this period were both short and located in town, which made this disadvantage of BEVs seem less important.

Internal Combustion Engine vehicles – In 1885, the German Karl Benz designed and built the first practical automotive powered by an Internal Combustion Engine (ICE). ICE vehicles use the explosive combustion of fuel to produce mechanical energy. The different kinds of fuel commonly used are gasoline, diesel and kerosene. ICE vehicles were more powerful, and had a longer range than BEVs. Given that longer roads had been constructed by the 1920s, longer driving ranges were required. With discovery of more and more oil, the price of gasoline became cheaper. In 1912, the electric starter was invented by the American Charles

Franklin Kettering. ICE vehicles no longer required a hand crank. The first automotive manufacturers in the world were the French Panhard and Levassor, and Peugeot. The mass production of the automobile began in 1901. The American Henry Ford invented an improved assembly line around 1913. This made ICE vehicles affordable. On the contrary, BEVs with very limited range were much more expensive than ICE vehicles with high range. By the early 1900s, gasoline vehicles outsold all other vehicles. Today, ICE vehicles play a leading role in the automobile market.

Hybrid Electric vehicles – In 1897, one of the earliest HEVs was built by the American Justus B. Entz. It was powered by an ICE assisted by an electric machine. Around the same time, Dr. Ferdinand Porsche introduced a HEV called "Mixt". In 1905, the American engineer Henri Piper built a petrol-electric HEV. Unlike today, the purpose of Piper's hybrid design was not to decrease fuel consumption or emissions. His idea was to make the vehicle accelerate faster than contemporary vehicles. Between 1902 and 1920, thousands of HEVs were produced by companies such as Krieger, Lohner-Porsche, and Auto-Mixte. By 1920, the development of assembly lines for ICE vehicles resulted in a rapid decline in HEV production.

Between the 1970s and the 1980s, in order to decrease the emissions from ICE vehicles and reduce oil dependency, many efforts were made to produce BEVs and HEVs. BEVs appear to be an ideal solution, given its zero local oil consumption and zero local emissions. However, the development of BEVs was limited by battery technology. In order to overcome the disadvantages of BEVs, such as short driving ranges and long charging times, HEVs became an important option. HEVs combine conventional propulsion systems with electric Energy Storage Systems (ESS) and electric machines. They have a longer range than BEVs and show improved fuel economy compared to conventional ICE vehicles.

In 1997, the first commercial mass-market hybrid car, the Toyota Prius, was sold in Japan. Two years later, the USA saw its first sale of a hybrid, the Honda Insight. Subsquently, over 20 models of passenger hybrids have been introduced to the auto market.

Interest in Plug-in Hybrid Electric Vehicles (PHEVs) has recently increased. PHEVs are HEVs with batteries that can be recharged by connecting a plug to an electric power source, for example the electricity grid. In 2003, Renault began selling the Elect'road, a series PHEV, in Europe. In September 2004, the California Cars Initiative (CalCars) converted a 2004 Toyota Prius into a prototype called the Prius +. With the addition of batteries, the Prius+ achieved roughly double the fuel economy of a standard Prius. As of September 2008, Toyota, General Motors, Ford, Chinese automaker BYD Auto, amongst others, have announced their intention to introduce production of PHEV automobiles. In March 2009, EDF and Toyota announced important trials, involving PHEVs and innovative charging infrastructures. About one hundred PHEVs will be leased in Strasbourg from the end of 2009, for a duration of three years.

Alternative fuel vehicles – There are more than a dozen alternative fuels, such as natural gas, biofuel and Hydrogen. Use of these fuels can reduce oil consumption and improve air quality.

A Natural Gas Vehicle (NGV) uses Compressed Natural Gas (CNG) or, less commonly, Liquefied Natural Gas (LNG). There are more than 7 million NGVs on the roads worldwide as of 2008. However, NGVs have the same problems as ICE vehicles, such as producing gas emissions involved in climate change. NGVs nonetheless emit fewer harmful emissions than other vehicles using classic fossil fuels.

Biofuel is material derived from living organisms, such as plants, animals and their by-products (manure, garden waste and crop residues etc). It is a renewable energy source based on the carbon cycle. Issues related to biofuels involve developing new feedstocks, production processes, land requirements and food crisis.

Hydrogen vehicles use hydrogen as their primary power source. These vehicles generally use hydrogen in one of two methods: combustion or fuel-cell conversion. In combustion, the hydrogen is "burned" in engines using fundamentally the same method as ICE vehicles. In fuel-cell vehicles (FCVs), the hydrogen is turned into electricity through fuel cells which then power electric machines. With either method, the only byproduct is water. Key issues for fuel cell vehicles include production of hydrogen, storage of hydrogen on-board, the development of refueling infrastructure, and efficiency improvement.

I.1.2. Challenges of transportation

The International Energy Agency (IEA) stated in 2008 that the future of human prosperity depends on how successfully we tackle the two energy challenges: securing the supply of reliable and affordable energy; and effecting a rapid transformation to a low-carbon, efficient and environmentally benign system of energy supply [IEA 2009-a]. The transportation sector, one of the largest energy sectors, must face these challenges.

Energy security – The impact of the 1973 oil crisis and the emergence of the OPEC (Organization of the Petroleum Exporting Countries) cartel prompted some countries to increase their energy security. The concerns related to energy security include oil and other fossil fuel depletion, secure supply of energy, etc.

Oil is a vital natural resource which will one day cease to exist. The oil supply growth has decreased, while the demand for oil has increased significantly. Global oil consumption has increased from 49 million barrels per day in 1971 to nearly 84 million barrels in 2005. In 2008, about 60% of all the oil was consumed by the transport sector [IEA 2009-b]. The transportation sector has the highest growth rate of oil consumption in recent decades. Within the transportation sector, the fastest growing category has been road transport, such as passenger vehicles, buses and commercial trucks, which accounted for about 40% of global oil consumption in 2003. It is estimated that the balance of oil supply and demand will be broken in 2030 [Eshani 2005].

Energy security is not to be confused with energy independence. The latter seeks to maximize energy self-sufficiency. In the context of globalization, energy security aims at maintaining a secure supply of energy, at reasonable prices, rather than zero imports [Makhijani

2006]. Diversification of energy types is important to improve energy security. Nuclear Energy has allowed France to diversify its energy supply, but it has not greatly reduced France's oil consumption, because oil is the principal fuel for France's transportation sector. Its consumption has steadily increased, in that sector, since 1973 and is expected to continue to do so in the future. Today, about 50% of the oil imported is used for road transportation in France [Syrota 2008].

Environmental impact – The link between global climate change and Green House Gasses (GHG) from the burning of fossil fuels has been recognized. The greenhouse effect keeps the Earth warm. Without it, the planet would be too cold for human life. Greenhouse gases in the atmosphere raise the earth's temperature by preventing the heat from the Sun from escaping back into space. The main greenhouse gases are water vapor, carbon dioxide (CO_2), ozone (O_3), methane (CH_4), nitrous oxide (N_2O) and chlorofluorocarbons (CFCs). The problems begin when there are more greenhouse gases than necessary to keep the planet at an ideal temperature. Today, the Earth's temperature is increasing with unprecedented speed. During the entire 20th century, the average global temperature increased by about 0.6°C. It has been forecasted that a further 1.5°C to 4.5°C increase could occur by 2050. Even a small increase in the global temperature would lead to significant climate changes. Weather changes could threaten human and animal life. In the European Union (EU), 19% of total EU greenhouse gas emissions and 28% of CO2 emissions in 2005 are linked to transport. More than 90% of total EU transport emissions are due to road transport. While total EU emissions declined, transport emissions increased continuously between 1990 and 2005 due to high growth in both passenger (28%) and freight transport (62%) [EC 2009].

ICE vehicle tailpipe emissions are also involved in concerns about air pollution. Air pollution endangers human health, causing breathing difficulties or longer-term damage through its effects on our planet's ecosystem. Pollutants include smoke and dust, sulfur oxides (SOx), nitrogen oxides (NOx), carbon monoxide (CO), carbon dioxide (CO_2) and so on. The main cause of acid rain is nitrogen and sulphur compounds from burning fossil fuels. Acid rain has a higher acid content than normal rain. Monument s can be damaged by acid rain. It is also harmful to plants, animals and human. Road transport is a major source of air pollution.

More stringent emission standards – Given the growing evidence of serious climate change, the Kyoto Protocol has been ratified. It is aimed at reducing emission of GHG. There is no current European Union (EU) law which limits the amount of CO_2 produced by vehicles. However, the European Commission reached a voluntary agreement with the European Automobile Manufacturers Association (in French: Association des Constructeurs Européens d'Automobiles; abbreviated ACEA) to reduce the average CO_2 emissions to 140 g/km by 2008 for all new vehicles sold in the EU with a possible second target of 120 g/km by 2012 [ADEME 2007]. The effect of tighter standards on vehicle emissions has been to promote greener vehicle technologies.

Many emissions standards focus on regulating pollutants released by vehicules and

also by industry. European emission regulations were first introduced in 1992. They define the acceptable limits for exhaust emissions of new vehicles sold in EU member states. These regulations become more stringent each year.

Possible Options – To meet these challenges, many options using different energy sources exist. Table 1.1 shows different energy sources. Gasoline or diesel is easy to store and use: gasoline or diesel vehicles have high energy density and great driving range. Sustainable transportation can not be achieved solely through the use of gasoline or diesel vehicles. BEVs have the best efficiency and zero local emissions. Nevertheless, high costs, low energy density and long charge times limit their application. It is not possible to avoid greenhouse gas emissions with natural gas vehicles. Hydrogen as an alternative energy source has to meet the challenges posed by the need to impose rigorous storage conditions. The efficiency of hydrogen vehicles, through combustion or fuel-cell conversion, is unsatisfactory.

Table 1.1 Different energy sources [Syrota 2008]

	gasoline	diesel	Battery	CNG	LNG	H2 gas	H2 liquid
Temperature (^{o}C)	ambient	ambient	ambient ~ 300 ^{o}C	ambi-ent	ambient	ambient	-253 ^{o}C
Storage pressure (Pa)	ambient	ambient	ambient	> 20M	0.5~2.5M	70M	0.5M
Energy density in Wh/kg	11 900	11 800	30-200	2 200	7 080	1 200	500-1 000
Charge time of 60 l (min.)	5	5	25 min – 6 h	5	5	5	5
Range of 60 l (km)	~ 900	~ 1000	30- 120	160	430	200-300	~180
Tank-to-wheel efficiency	12-40%	12-45%	80-85%	20-38 %	30-35%	40-50%	30-35%

LNG: Liquefied Natural Gas; CNG: Compressed Natural Gas

Each previous option has its advantages and drawbacks. Might it be possible to combine different energy sources, as is the case with HEVs, which marry both gasoline (or diesel) and batteries?

I.1.3. Hybrid Electric Vehicles

HEVs have shown great potential in meeting the challenges inherent in road transport regarding energy security and environmental impact. Different definitions of HEVs exist. In this thesis, a HEV combines two drivetrains:

- One unidirectional drivetrain which is based on fossil fuel powered ICE. Fossil fuels can be gasoline, diesel or natural gas.

- One bidirectional drivetrain which includes an ESS and Electric Machines (EMs). The traditional ESS of HEVs is a battery. Recently, new components in development such as supercapacitors have become new options for ESS [Burke 2000] [Rufer 2004] [Marie-Francoise 2005] [Cheng 2006] [Thounthong 2007]. Batteries have higher specific energy than supercapacitors. However, supercapacitors have higher specific power, faster power response, higher efficiency, and much longer life cycles.

I.1.3.1. HEV advantages

Energy consumption is a major criterion in evaluating different vehicles. The ICE of HEVs can be stopped if the vehicle is at standstill. The drivetrain based on EMs can optimize the efficiency of the ICE and thus reduce the oil consumption. The kinetic energy can be recovered during deceleration. Several authors have provided Well-to-Wheel analyses that assess the global energy consumption of different vehicles [Brinkman 2005] [Willamson 2005]. HEVs have been shown to achieve real fuel economy compared to ICE vehicles, even when the electricity is generated using oil. Moreover, using HEVs also leads to a global reduction of greenhouse gas emissions.

Furthermore, the on-board EMs of HEVs provide more flexibility and controllability of the vehicle control. Therefore, HEVs have the potential to enhance vehicle performance and safety. Compared to BEVs, HEVs have a wide driving range. Unlike alternative fuel vehicles, HEVs do not require special refueling infrastructure.

I.1.3.2. Classification

HEVs can be classified by architectures or by degree of hybridization.

A. Classification by architectures

Given different combinations of the two drivetrains, three kinds of HEVs are classified: series, parallel and series-parallel HEVs [Eshani 2005] [Ceraolo 2008] [Chan 2009].

Series HEVs – In a series HEV, all traction power is converted from electricity. The energy sum of the two power sources is in an electric node, commonly in a DC bus (Figure 1.1). The ICE has no mechanical connection with the traction load, meaning it never directly powers the vehicle. The ICE supplies power through an electric machine, generally called the generator. Because of the decoupling between the ICE and the driving wheels, it has the advantage of flexibility for locating the generating unit. For the same reason, the ICE can operate at its optimal region independently of the vehicle speed. Its control is relatively simple using the single torque source (electric traction machine) for the traction. Due to the inherent high performance of torque-speed characteristics of the electric machine drive, multi-gear transmissions and clutches are unnecessary. However, such cascade structures lead to relatively low efficiency and three machines are required.

Parallel HEVs – In a parallel HEV, the two drivetrains are combined only in mechanical way. The energy sum of two power sources is obtained, in terms of mechanical quan-

tities, via a mechanical coupling (Figure 1.2). The ICE and the EM can drive the vehicle independently or concurrently through a mechanical coupling. This mechanical coupling may be considered as a common shaft or the connection of two shafts by gears, pulley-belt units , etc. Parallel HEVs can be also Four Wheel Drive (4WD) HEVs (or called "parallel through-the-road"), where the front wheels are powered by the ICE, and the rear wheels by the EM. The EM of parallel HEV can operate as a generator to charge the battery by regenerative braking or absorbing power from the ICE. Parallel HEVs require only two machines (ICE and EM) rather than three for series HEVs. Moreover, smaller devices can be used to get the same dynamic performance. Owing to the mechanical coupling between the ICE and the transmission, however, the ICE can not always operate at its optimal region. Clutches and multi-gear transmissions are commonly necessary.

Series-Parallel HEVs – In a series-parallel HEV, the two drivetrains are combined in both electric and mechanical ways (Figure 1.3). The energy node can be found both in electrical couplings (generally, a DC bus) and mechanical couplings (for example, a planetary gear). The ESS powers the vehicle mainly through an EM (Electric Machine 1). The ICE energy supplied to this electrical coupling is generally done through another EM (Electric Machine 2). The ICE can also power the vehicle with Electric Machine 1 through the mechanical coupling. Due to the mechanical coupling, the ICE speed can be adjusted independently of the vehicle velocity by controlling Electric Machine 2. The ICE can thus operate at its optimal region. Despite possessing these features of both series and parallel HEVs, three machines are necessary, which makes the drivetrain somewhat complex and costly.

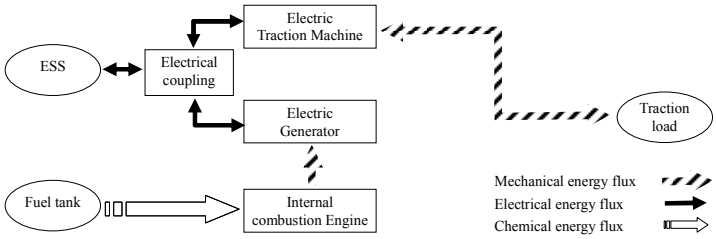

Figure 1.1 Series hybrid electric vehicle

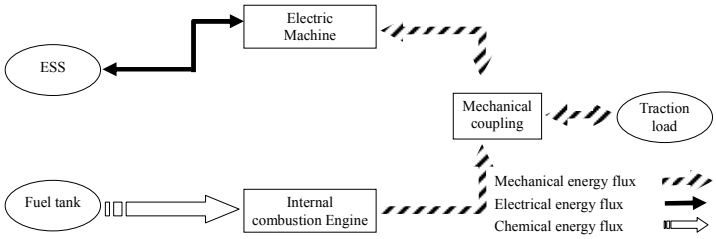

Figure 1.2 Parallel hybrid electric vehicle

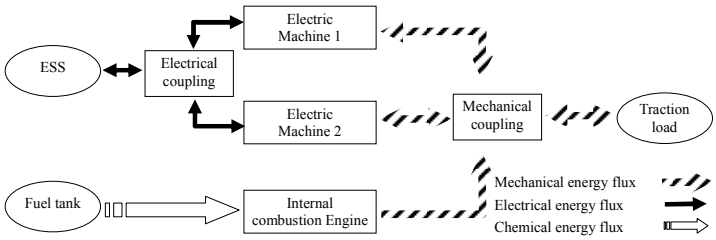

Figure 1.3 Series-parallel hybrid electric vehicle

B. Classification by degree of hybridization

HEVs can be classified by degree of hybridization. Degree of hybridization is the ratio of peak electric power to the sum of the peak fuel power and electric power [Maggetto 2000] (Figure 1.4). The larger the electrical components used, the greater the fuel economy obtained [Uhrig 2007] [Chan 2010].

Micro HEVs – In a micro HEV, a small EM is used as an starter-alternator [Sepe 2001]. The electric machine helps the ICE to achieve better operations at the start-up. Due to the fast dynamics of EM, micro HEVs ensure a stop and start function. The ICE propels the vehicle alone in cruise. In a conventional ICE vehicle, the ICE continues to run when the vehicle stops at traffic lights. Different from conventional ICE vehicles, the ICE is turned off by the starter-alternator to save fuel whenever the vehicle stops. Fuel economy improvements are estimated as ranging from 2% to 10% for urban drive cycles.

Mild HEVs – In addition to the stop-and-go function, mild HEVs have a boost function, which means they use a larger EM to boost the ICE during acceleration or braking by applying a supplementary torque. Compared with micro HEVs, the electrical components are larger and play a greater role in the vehicle operation. Fuel economy improvements are estimated as ranging from 10% to 20%.

Full HEVs – Full HEVs have a fully electric traction system, which means that the EM can power the vehicle alone. When such a vehicle operates in pure electric mode, it becomes a “zero emission vehicle” (ZEV) in urban centers. Fuel economy improvements are estimated as ranging from 20% to 50%.

Plug-in HEVs – The battery in a Plug-in HEV (PHEV) can be charged externally, for example, by plugging into the electrical grid. In some cases, the plug-in vehicle may simply be a BEV married with a limited-power ICE. In other cases, the driving range can be extended by charging the batteries from the ICE in order to extend the EV driving range. Fuel economy of P-HEVs can be improved by 100% if the ICE is not used to charge the battery (e.g., in urban drive cycles). Increasing the battery size allows ZEV operation for small trips and thus results in a significant reduction in fuel consumption and greenhouse gas emissions.

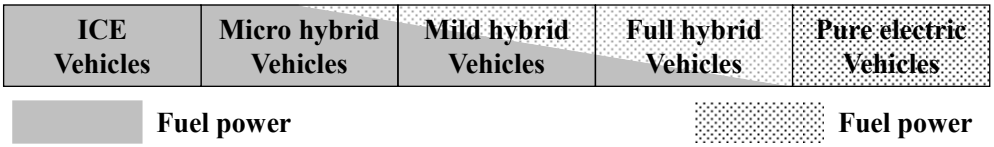

Figure 1.4 Classification by degree of hybridization

A Micro HEV is a kind of parallel HEV. Mild HEVs can be parallel or series-parallel HEVs. Full HEVs or PHEVs can be series, parallel, or series-parallel HEVs [Chan 2010].

I.1.3.3. Future for HEVs

HEVs have many advantages, such as achieving greater fuel economy, enabling cost-efficient CO_2 reductions, and increasing driving pleasure. However, they do not yet play a major role in the automotive market.

The most important reason is the high price of HEVs. A HEV has at least two propulsion systems, which makes it more expensive than a conventional vehicle. Batteries for electric vehicles are still expensive. It takes between five and twenty years to take back the investment, depending on oil prices and the amount of driving undertaken. In 2009, lower oil prices had an impact on public decisions. Another reason is that production and maintenance infrastructure is not yet in place. There is still a lack of public awareness and confidence regarding HEVs. Today's economic uncertainties may slow down the growth of the HEV market share. The economic crisis in 2009 caused a sharp decline in total vehicle sales [IEA 2009-b].

On the other hand, such a crisis may offer opportunities to change and implement new, better adapted technologies. In Italy, a measure to award a bonus to people who replace old vehicles by low-carbon vehicles was introduced. Germany and other European countries have also introduced a vehicle buy-back program for drivers who buy new, cleaner cars. The United States have introduced a new tax credit for plug-in hybrids on the road by 2015. France launched a 14-point plan to accelerate development of electric cars and PHEVs in 2009 - for example, a €2,000 bonus for the purchase of HEVs with CO2 emissions less than or equal to 135 g [Franceplan 2009].

Key issues in the development of HEVs involve the drivetrain design, battery or ESS design, and control design. This thesis is interested in the control design of HEVs. If no satisfactory controls for such complex systems can be obtained, good performance or fuel economy can not be achieved, even if very good drivetrain designs are applied.

I.2. Modeling and control design

One of the key issues related to HEV development is the control design of such complex systems, which are composed of multi-sources and multi-subsystems. Two challenges facing designers are shrinking development times and growing design complexity. The traditional text based approach is not efficient enough to deal with such complex systems. To meet these challenges, model-based control design processes provide an efficient way of carrying out control design. The general steps in a model-based control design process are: system modeling, system analysis, control tuning, system and control simulation, experimental validation, and finally control deployment.

For the system modeling step, different graphical modeling formalisms can be used, such as Bond Graph [Paynter 1961] [Karnopp 1975], Power Oriented Graph (POG) [Zanasi 1996], Causal Ordering Graph (COG) [Hautier 1996] [Hautier 2004] and Energetic Macroscopic Representation (EMR) [MMS 2000] [Bouscayrol 2003]. These approaches deal with the organization of models. Among these modeling formalisms, COG and EMR yield the control structure directly using the inversion-based rules. Compared with COG, EMR offers a more global energetic view. Therefore, EMR and its inversion-based control significantly contribute to the control structure and energy management.

In this section, the first part is dedicated to modeling and control design approaches. Energetic Macroscopic Representation (EMR) and its inversion-based control approach are introduced in the second part.

I.2.1. Modeling and control design approaches

Modeling is the first step for the control design in model-based design processes. Starting from the different objectives, various models and modeling approaches can be used for the same real system. Control design can be based on the modeling of the system, or independent of the modeling. Term definitions are first given to help the reader better understand [Gao 2007] [Chan 2010]. Modeling and control design approaches are then summarized.

I.2.1.1. Term definitions

Model – A model may be represented either by experimental data using look-up tables and efficiency maps, or by mathematical equations. The same system can be represented by different models. Depending on the study's objective (e.g., design, analysis, implementation or energy management), different levels of accuracy are required. The validity range of the various models depends on the simplification assumptions applied.

Modeling – Modeling is the act of construction of models.

Representation – Representation is a way to organize models according to specific rules and conventions. The same model can be described by different formalism in order to highlight different properties. Each representation has its own philosophy, representation notions and organization rules.

Simulation software – It is a computer software environment. Model programs and control program can be implemented and observed in this environment. It leads to rapid prototyping, testing and verification in function of the software constraints. The models established by the same modeling formalism can be implemented in different simulation software.

I.2.1.2. Model types

Steady state and dynamic models – Depending on the level of detail regarding how each component is modeled, vehicle models may be steady-state, quasi-steady-state or dynamic [Gao 2007]. Steady-state models consider that all transient effects are negligible. Steady-state models can be based on experiential data in the form of look-up tables, or simplified dynamic models. The main advantage of steady-state models is fast computation, but the disadvantage is inaccuracy. Dynamical models take the transient effects into account. They are more general, more accurate and more complex than steady state models, and they require more computation time. Quasi-static models consist of steady state models which are completed with the main equivalent dynamic of the system [Guzzella 1999]. For example, ICE engines are often modeled using a map (steady state model) associated with a first order system for control strategy purposes.

Structural and functional models – Structural models respect the topology of physical systems. Most simulation software is based on structural models: component libraries are available and the user need only "pick and place" to built the vehicle architectures. Functional models represent the system via interconnected system functions [MMS 2000]. The topology view is often lost, but system analysis is facilitated, because the physical behavior of the system is always respected.

For complex systems, one of the problems is the association of the various subsystems. For structural modeling software, specific solvers are required to solve the association problems. The quality of the simulation depends on the quality of the solvers. When using functional modeling software, the users have to solve the association problems before implementation, which means more physical knowledge of the system is required. However, functional approaches highlight the holistic constraints.

Forward and backward facing models – Depending on the direction of calculation, vehicle models can be classified as forward models or backward facing models [Wipke 1999] [Trigui 2004-a]. The forward approach is also called the engine-to-wheel or rear-to-front method. It starts from the ICE or another energy source and works "forward" using transmitted and reflected torque. The backward method is also called either the wheel-to-engine or front-to-rear method. It starts with the required traction effort at the wheels and "works backward" towards the ICE or the primary energy sources. Forward models better represent the real system setup and are useful for testing control algorithms. This kind of approach requires some kind of "driver model", because a reproduction of speed profiles is not possible without a speed controller. Powertrain System Analysis Toolkit (PSAT) models are forward models [PSAT]. Backward models require knowledge of an imposed speed cycle (impossible in real-time) to

calculate the forces acting on the wheels that rise to the primary energy sources. Backward models may be faster than forward models because they are often based on quasi-static models. Some approaches combine the two methods, such as ADVISOR [Wipke 1999].

Causal and acausal models – Causal models use cause and effect logic to describe the behavior of the system. Physical causality is based on integral causality [Iwasaki 1994] [Hautier 1996]. Integral causality indicates system inputs and outputs: output is always an integral function of input, which induces a time-delay from input to output. In acausal models, inputs and outputs are not fixed (floating inputs/outputs). Inputs or outputs can be defined according to the requirement of communication with other systems. For that reason, acausal models are often used for structural software. If the association problems are not highlighted during the modeling, they have to be taken into account by the solver of the software [Tiller 2003] [Dempsey 2006].

I.2.1.3. Different graphical formalisms

Bond Graph – Since the 1950s, Bond Graph has been developed by Professor H. M. Paynter of MIT and his team in the USA [Paynter 1961] [Karnopp 1975]. It is based on three types of analogies, namely, component, signal, and connection analogies. Bond Graph components include sources (for example, voltage sources), dissipations (e.g. R), storages (e.g. L or C), conversion (e.g. TR (transformer) and GY (gyrator)) elements, and so on. There are two basic signal categories: “effort” and “flow”. Two components can be connected by a power bond. Power is transmitted between connected components by a combination of “effort” and “flow”. Power bonds may join at one of two kinds of junctions: 0 and 1 junctions. At a 0 junction, the sum of the flows is zero and the efforts are equal. At a 1 junction, the sum of the efforts is zero. Using Bond Graph, integral causality is not mandatory. Bond Graph is a powerful and unified formalism to describe multiphysical systems [Karnopp 2006]. Bond Graph highlights the transfer of energy between system components. In fact, power is the universal currency of physical systems. The modeling of a parallel HEV has been achieved using Bond Graph [Filippa 2005].

Causal Ordering Graph – In 1996, Causal Ordering Graph (COG) was introduced by Professor J.-P. Hautier and his team in France to describe power electronics and electrical machines for control purposes [Hautier 1996] [Hautier 2004]. Two basic elements: causal and rigid elements. A causal element is depicted using an ellipse with a unidirectional arrow: the output (effect) is the integration of the input (cause). Integral causality is the only accepted causality. A rigid element is presented by an ellipse with a bi-directional arrow: the inputs and outputs are kinetic (flow in Bond Graph) or potential (effort in Bond Graph) variables. COG indicates where controllers have to be located and measurements have to be made. Cascaded loop controls can be systematically deduced from the process graphs using inversion rules [Barre 2006]. COG has already been used to study different types of electromechanical system controls, as in [Giraud 2004] for piezoelectric systems.

Energetic Macroscopic Representation – Energetic Macroscopic Representation

(EMR) has been developed to describe complex electromechanical systems at the University of Lille in France since the 2000s [MMS 2000] [Bouscayrol 2003]. It can be considered as an extension of COG for complex systems. Macro pictograms are defined to highlight energy properties of the system (source, accumulation, conversion and distribution of energy). EMR hence offers a more global energetic view than COG. The different EMR elements are introduced in I.2.2. Similar to Bond Graph, all EMR elements are connected according to the action and reaction principle. The product of the action and the reaction always yields the power. Like COG, control schemes can be systematically deduced from the model description due to the need to respect integration causality. Moreover, degrees of freedom for energy management are highlighted during the inversion process. The modeling and control of the design of different HEVs using EMR have been carried out, as in [Lhomme 2008-a] [Chen 2009-a].

Other graphical descriptions, such as Power Oriented Graph (POG) [Zanasi 1996] [Morselli 2006], Power Flow Diagram (PFD) [Schönfeld 2004] and so on, are also powerful graphical formalisms which have different notions and highlight different properties of multiphysical systems. Using these formalisms, designing and analyzing a system can often be undertaken by simply using pen and paper. Designers can thus focus on the interaction among components or subsystems rather than the implementation details of their particular software. Another advantage is to help users respect physical properties, which is very important for the control design of energy systems. The drawback of these descriptions is that they require prior vocabulary, semantic and graphical knowledge. They are often considered as requiring excessive work, as it is not always mandatory when the user is an expert. This supplementary step however can be very important and useful for advanced and complex systems.

I.2.1.4. Control design

To achieve satisfactory energy management of a HEV, two control levels can be considered [Bouscayrol 2003]. The first, local energy management must be ensured in real-time in each subsystem; however, the second, global energy management, must be ensured at the system level in order to coordinate the power flow of each subsystem.

Local control design – Two kinds of local control methods can be used: heuristic control or model-based control. Heuristic control is based on the prior knowledge of the designer. In this case, the expertise or experience of the designers is very important. Inversion-based control methods are based on causal models of systems [Hautier 2004] [Barre 2006]. The key idea is to locate controllers and degrees of freedom along the causal model of the system. The model is inverted according to the following rules:

- controllers are used for the inversion of components which have integral causality,

- supplementary inputs (degrees of freedom) are added for the inversion of components which have connection analogies [MMS 2003],

- direct inversions are used for other instantaneous relationships

Using this methodology a control scheme can be systematically deduced from the

causal model of the system. This control scheme indicates the number of controllers, measurements (or estimations) and degrees of freedom. Using specific inversion rules, the control scheme of the system can be obtained from COG or EMR of the system [MMS 2003] [Barre 2006].

Global control design (energy management strategies) – This supervision level generally yields references for local control loops. The energy management of HEVs can be classified into two types: rule-based solutions and optimization-based solutions [Salmasi 2007]. The energy management system should meet the driver's requirements regarding traction power, sustaining or depleting the battery charge, optimization of drivetrain efficiency, fuel consumption, and emissions. The main aspect involved in rule-based energy management approaches is their effectiveness in real-time supervisory control of power flows in a hybrid drive train. The rules are designed based on heuristics, intuition, human expertise, as well as mathematical models and, generally, without prior knowledge of a predefined driving cycle [Salmasi 2007]. These strategies can be classified into deterministic [Anderson 1995] and fuzzy rule-based methods [Lee 1998]. In optimization-based strategies, the optimal torque and gearbox ratios are calculated by minimization of a cost function associated with the consumption. If this optimization is performed over a fixed driving cycle, a global optimum solution can be found. To reach real-time energy management, definition of an instantaneous cost function is the key issue to obtain a real-time optimization-based control strategy [Sciarretta 2004].

I.2.1.5. EMR advantages for control design

The control design and energy management is one of the key issues for HEVs. Since HEVs are energetic systems, the energy consideration in HEVs should be emphasized. Bond Graph contributes significantly to the modeling of energetic systems, but it can not yield the control design directly. COG can yield control design directly using inversion-based control rules. The complexity of HEVs, however, requires a more macroscopic energetic view.

EMR is an energy-based graphical description, like Bond Graph and COG. Compared to COG, EMR has a more global energetic view. Differing from Bond Graph, EMR focuses on the system function but not only on the system structure [Gawthrop 2007]. Therefore EMR gives insights into the real energy operation of the system and allows a deep understanding of its potentialities from a dynamic point of view. Thanks to these features, inversion-based control can be deduced from EMR.

Specific inversion rules yield control schemes of systems from the EMR. This control scheme can ensure the local control. At the same time, the local control of each subsystem takes the whole system into account. This is because the EMR of the system, from which this control scheme is deduced, is established according to the whole system function, not only the structure of the system. In this way, the degrees of freedom of the system naturally appear where they act on the global energy management level.

This methodology has been successfully applied to different kinds of systems: wind

energy conversion systems [Delarue 2003-b] [Bouscayrol 2005-b], new AC/AC converters [Bouscayrol 2005-a], subway systems [Verhille 2007-a] [Allegre 2010], BEVs [Chen 2008-a] , HEVs [Lhomme 2007] [Boulon 2009-a], etc.

I.2.2. Energetic Macroscopic Representation

Using EMR and its inversion-based control, four steps are necessary to yield the control design [Bouscayrol 2003].

Step 1, Organize the system model according to EMR rules

EMR is a graphical description used to organize a model of real processes for control purposes. It is based on the action-reaction principle, which is used to organize the interconnection of sub-systems according to physical causality (i.e. integral causality). This description highlights energetic properties of the system (energy accumulation, conversion and distribution).

Action-reaction principle – Power is transmitted between connected elements or sources by a combination of "action" and "reaction". For example, a battery (a voltage source, s_1) is connected to an inductor (a current source, s_2) (Figure 1.5). The action variable for s_1 is the battery voltage v_{dc}. The current i_L is the reaction variable for s_1 by s_2. The transmitted instantaneous power is the product of the action variable v_{dc} and the reaction variable i_L. The variable direction assigned to an EMR is only a reference or convention.

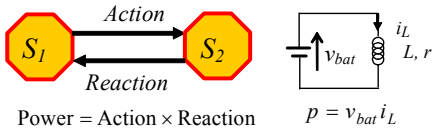

Figure 1.5 Action-reaction principle

Integral causality –EMR considers integral causality as the only allowable physical causality. In a real-time system, the surface before a given time (previous data) is calculted by integration, whereas the trends after this time (future data), which can not be determined beforehand, are calculated by derivation. Integral causality indicates what the inputs and the outputs of the system are. In other words, for a system modeled by an integral equation, integrands (cause) are inputs of the system and integrations (effect) are outputs. For example, as viewed from the equation of an inductor, the voltage is the cause (input), and the current is the effect (output), contrary to a capacitor. A resistor has no time-dependant behavior: voltage or current can be considered as input or output, depending on the system connected with it.

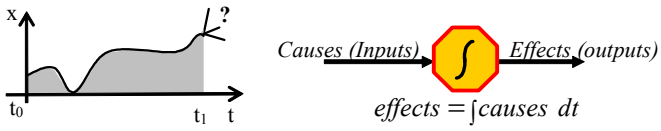

Figure 1.6 Integral causality principle

Elements – EMR has four basic kinds of elements: source elements, conversion elements, accumulation elements and coupling elements (Table 1.2).

Table 1.2 EMR basic elements

Element	Description			Example
Source element	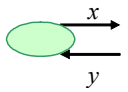			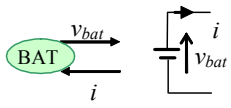
Accumulation Element	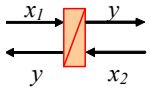			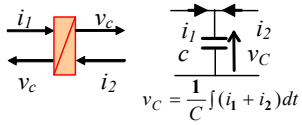
Conversion Element	Electrical conversion	Mechanical conversion	Electromechanical conversion	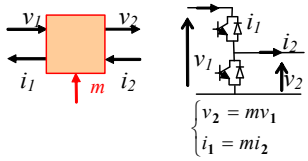
	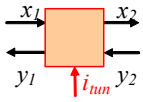	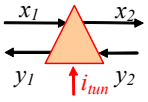	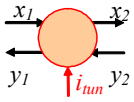	
Coupling Element	Electrical coupling	Mechanical coupling	Electromechanical coupling	Parallel electrical circuit
	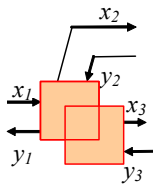	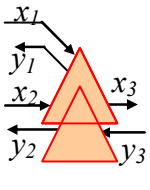	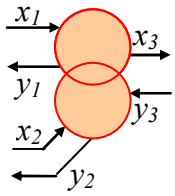	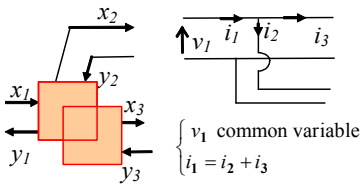

Source elements (ovals) are terminal elements, which deliver or receive energy (e.g. a battery).

Accumulation elements (rectangular pictograms with an oblique bar) store energy, which yields the state variables. For example, since the integrand (cause) is the sum of i_1 and i_2 of a capacitor (Table 1.2), the inputs are the two currents. The voltage v_C is the effect, so v_C is the output, namely the state variable. State variables represent the energy state of the system (e.g. $E = \frac{1}{2} C v_C^2$).

Conversion elements are considered as energy conversion without energy accumulation. They are described by squares for electrical conversions (e.g. chopper), circles for electromechanical conversions (e.g. electromechanical of an EM) and triangles for mechanical conversions (e.g. gearbox). Tuning inputs are involved if energy conversion is adjustable.

Coupling elements (overlapped pictograms) are introduced to distribute energy (e.g. parallel electrical circuits) [MMS 2000].

Other elements, such as switching sectors which allow switching among multimodels, can be found in IV.2.2 or in [Lhomme 2008-a].

These elements are interconnected through action-reaction principle. As EMR is a functional modeling approach, it can be different from the physical structure of the real processes. The physics of the system is nonetheless emphasized. For example, if some accumulation elements have the same state variables, or their state variables are not independent of each other, only one accumulation element will be used to respect the integral causality. This is called the merging rule, which is explained below.

Merging rule – Direct connection of two accumulation elements with the same output is not allowed in EMR. This association type basically corresponds to the resolution of the state variable conflict [Bouscayrol 2003]. For example, in the case of two inductors in series (Figure 1.7), there is only one and the same state variable (common current). Thus, the appropriate representation includes only a single accumulation element, which produces the common state variable. This accumulation element is an equivalent element representing the equivalent induction, which is the sum of two inductions.

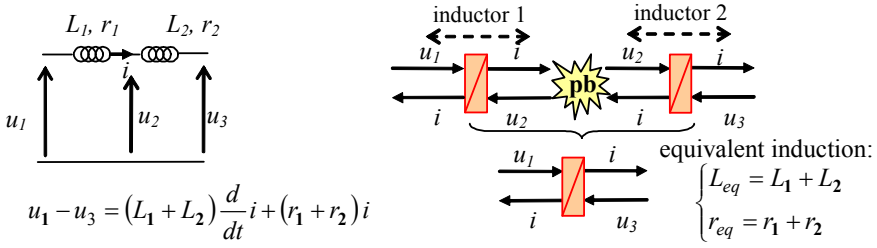

Figure 1.7 Example for merging rule [Bouscayrol 2003]

Permutation rule – Two conversion or accumulation elements with exchange variables having continuous evolutions can be permuted [Bouscayrol 2003]. The equivalent fictitious elements have to produce the same effect as the initial association (same global outputs) under the same requests (same global inputs). In that case, the parameters of the equivalent elements are defined based on the initial element parameters. For example, two shafts are connected together through an ideal gearbox (Figure 1.8). EMR of this system reveals two accumulation elements (shaft 1 and 2, kinetic energy accumulations) and a mechanical converter (gearbox). Since the speed of shaft 1 is proportional to the speed of shaft 2, only one state variable can represent the two speed variables. The two speeds can not be imposed independently. Only one accumulation element which represents an equivalent shaft is therefore considered.

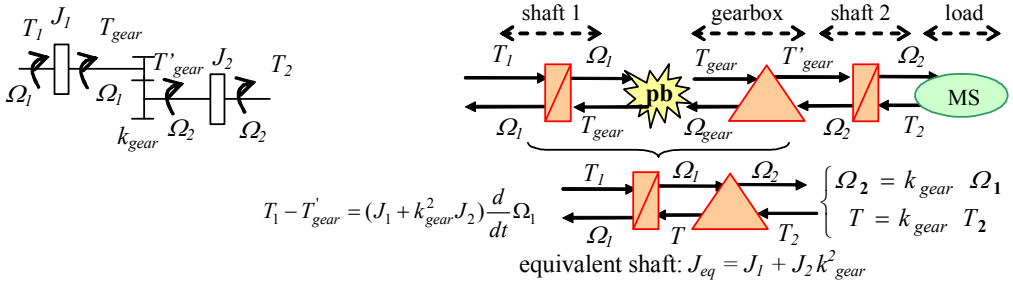

Figure 1.8 Example for permutation rule [Bouscayrol 2003]

Step 2, analyze and inverse the EMR of the system

An inversion-based control can be systematically deduced from EMR using specific inversion rules [Bouscayrol 2003] [Barre 2006]. First, tuning paths are defined according to the objectives and constraints of the system. Tuning paths start from tuning variables before moving towards the objective variables. Then, control paths are deduced by the inversion of the tuning paths. Control blocks are obtained through the inversion of elements by elements along the control paths. All control blocks are depicted by light blue parallelograms because they only handle information (Table 1.3).

Since accumulation elements (rectangles with an oblique bar) represent a time-dependence relationship, they cannot be inverted physically, therefore a controller is required. If the tuning path is chosen such that $x_1 \rightarrow y$, the control path is the paths from the y reference to *the* x_1 reference such that $x_{1\_ref} \leftarrow y_{ref}$ (Table 1.3). To deduce x_{1_ref} from y_{ref}, the y measurement y_{mea} is required. Small circles with measurement variables represent sensors. Continuous arrows with sensors mean mandatory measurements. The x_2 measurement can be compensated, or considered as a disturbance to be rejected. Therefore a dashed arrow is used to represent this measurement, which means it is not mandatory, but is considered at this stage. The controller (c_t in Table 1.3) type can be, for example, P controller, PI controller, or other kinds of controllers.

Conversion elements (squares) can be directly inverted if the element relationship is known, and it is linear and stationary. An electrical conversion element (converter) is shown in Table 1.3. The chosen tuning path of this EMR element starts from u_1 and moves to u_2. To obtain the modulation variable m_{tub} which deduces the switching function of this converter, the inversion is made directly according to the relationship of u_1 and u_2 [Delarue 2003-a]. The measurement of u_1 is not always mandatory if it is known. Another example is a reduction gear in Table 1.3. The chosen tuning path of this mechanical conversion element starts from T_1 and moves to T_2. It is inverted directly from the reference T_{2_ref} to T_{1_ref} assuming knowledge of the value of the gear ratio k_{red}.

Coupling elements (overlapped pictograms) may require supplementary inputs for inversion. One example is shown for the inversion of an electrical coupling element (parallel circuit in Table 1.3). The chosen tuning paths start from i_1 and move to i_2 and i_3. To obtain i_{1_ref} from i_{2_ref}, the measurement of i_{3_mea} (supplementary input) is required. Another example is presented for the inversion of a mechanical coupling element (Table 1.3). The torque T_t is the sum of the torques T_1 and T_2. The chosen tuning paths start from T_1 and T_2 and move towards T_t. To obtain the references T_{1_ref} and T_{2_ref} from T_{t_ref}, a distribution ratio k (supplementary input) is required.

Table 1.3 EMR and its inversion-based control

Element	Control blocks	Examples
Accumulation Element 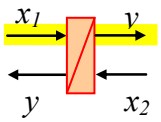	Controller 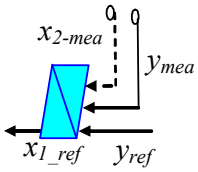	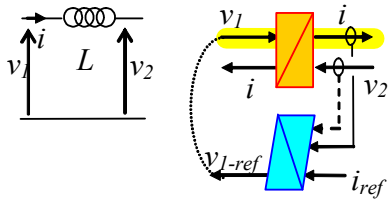 $i = \frac{1}{L}\int(v_1 - v_2)dt$ $v_{1\_ref} = C_i[i_{ref} - i_{mea}] + v_{2\_mea}$
Conversion Element 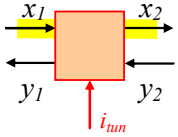	Inversion control block 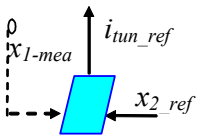	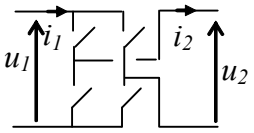 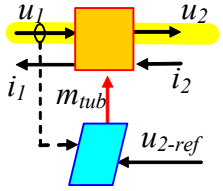 $\begin{cases} u_2 = m_{tun} u_1 \\ i_1 = m_{tun} i_2 \end{cases}$ $m_{tun\_ref} = \frac{u_{1\_ref}}{u_{2\_mea}}$
	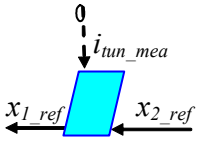	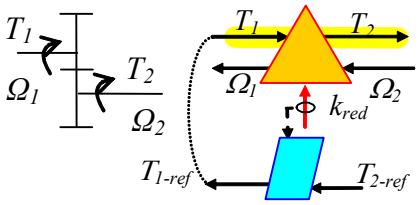 $\begin{cases} T_2 = k_{red} T_1 \\ \Omega_1 = k_{red} \Omega_2 \end{cases}$ $T_{1\_ref} = \frac{T_{2\_ref}}{k_{red}}$
Coupling Element 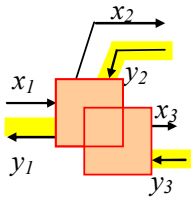	Inversion control block 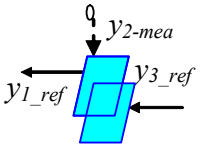	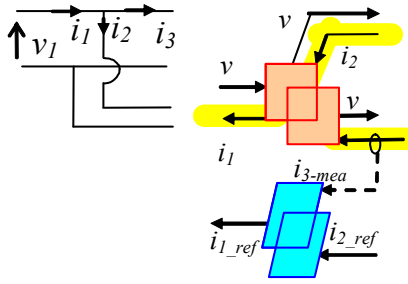 $\begin{cases} v_1 \text{ common variable} \\ i_1 = i_2 + i_3 \end{cases}$ $i_{1\_ref} = i_{2\_ref} + i_{3\_mea}$
Coupling Element 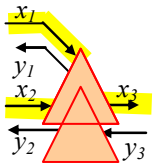	Inversion control block 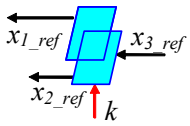	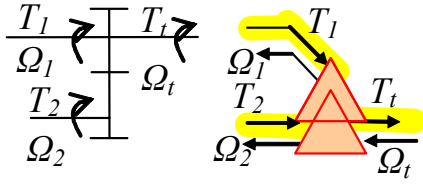 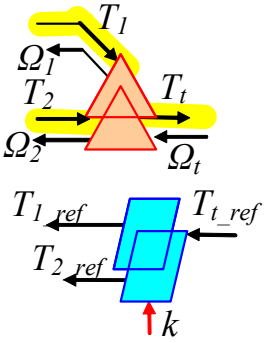 $\begin{cases} T_t = T_1 + RT_2 \\ \Omega_t = \Omega_1 = \frac{\Omega_2}{R} \end{cases}$ $\begin{cases} T_{1\_ref} = kT_{t\_ref} \\ T_{2\_ref} = \frac{(1-k)}{R} T_{t\_ref} \end{cases}$

More details can be found in [Bouscayrol 2003]. Examples can be found in chapters II and III. In this way, maximum control operations and measurements can be obtained under the assumption that all variables are measurable. This is called Maximum Control Structure (MCS).

Step 3, Simplification and estimation

Some simplifications can also be made based on the requirements and compromises. For Maximum Control Structures, despite the assumption that all variables are measurable, this is not always true, given that some of them are difficult to measure. Therefore some estimations are required. In order to obtain the required estimatiors, parts of the EMR can be copied directly. The estimation blocks have the same form as the EMR blocks but they are colored purple.

Step 4, Strategy

A strategy level, in dark blue, can be defined to manage the energy of the whole system. The control structure deduced from EMR is the local control level. The strategy level is the global management level.

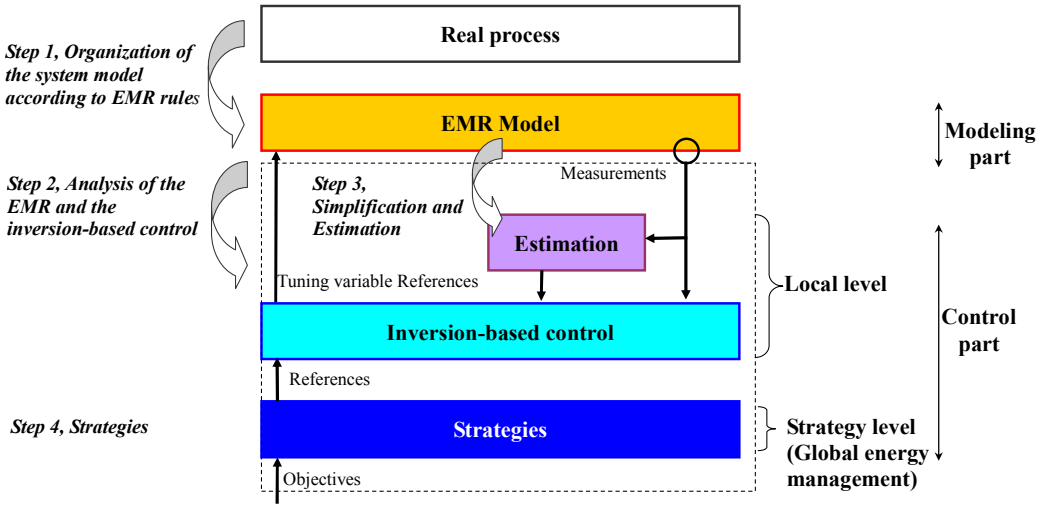

Figure 1.9 Steps necessary to obtain the control structure using EMR

Following the four steps (Figure 1.9), the control structure can be obtained using EMR and its inversion-based control principles. The control structure has two levels: the local level which deals with the control of the subsystems, and the strategy level which deals with the energy management of the whole system. Our focus is to establish the control structure for complex systems. Robust stability analysis and controller synthesis could be studied using different approaches [Ioannou 1988] [Sastry 1989] [Zhou 1999].

Before implementing this control prototype in the real process, it must be checked. It is firstly checked in a software simulation environment before being tested in a real-time environment.

Verification in software simulation environments

First, this control prototype can be checked in a software environment. The models organized using EMR (modeling part, Figure 1.9) and this control prototype (control part, Figure 1.9) are made into software programs (e.g. Matlab Simulink blocks). The two parts can run separately in software environments. The modeling program can be compared with the real process, which firstly needs to be validated, because the control is deduced from the modeling

part. Then both parts run together in the software simulation environment as a closed loop.

Verification in real-time environments

Simulation in a software environment is the first step. To be sure that this control prototype can run satisfactorily in real-time, it must be checked in a real-time environment. The control part is made into an Electronic Control Unit (ECU) and tested with a real process.

The real process or parts of the real process are not always available, or sometimes experiments using the real process are too costly or require too much time. Under such circumstances, real-time Hardware-In-the-Loop simulation (HIL) is required [Isermann 1999] [Bouscayrol 2008] [Bouscayrol 2010]. HIL simulation is characterized by the operation of real components in connection with real-time simulated components (Figure 1.10).

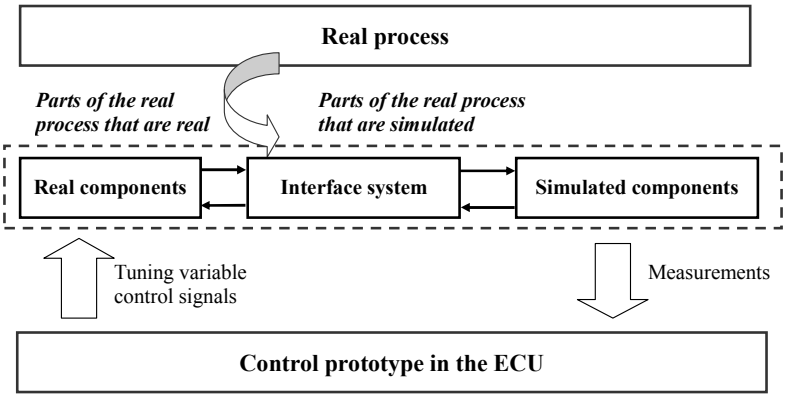

Figure 1.10 Control validation in a real-time environment using HIL simulation

An example of a BEV is given in Figure 1.11 [Bouscayrol 2006-b]. The traction machine of this BEV is an Induction Machine (IM) which is controlled by a Voltage-Source-Inverter (VSI) and fed by a battery (BAT). The parts from the Reduction Gear (RG) to the wheels are not available. To test its control prototype, these parts are simulated by a DC machine, a chopper and a DC source. The parts from the battery to the IM are real.

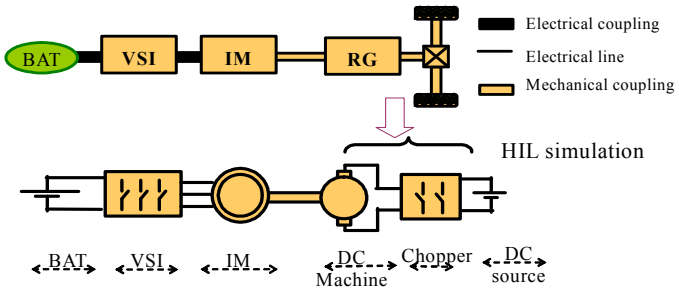

Figure 1.11 BEV and its HIL simulation test structure

This DC machine must have the same behavior as the real process parts which it simulates: it has to impose the same rotation speed as imposed by the mechanical power train. To provide the right set point for the DC machine rotation speed, the mechanical model is used with the IM torque as input (Figure 1.9). This mechanical model can be the same EMR model.

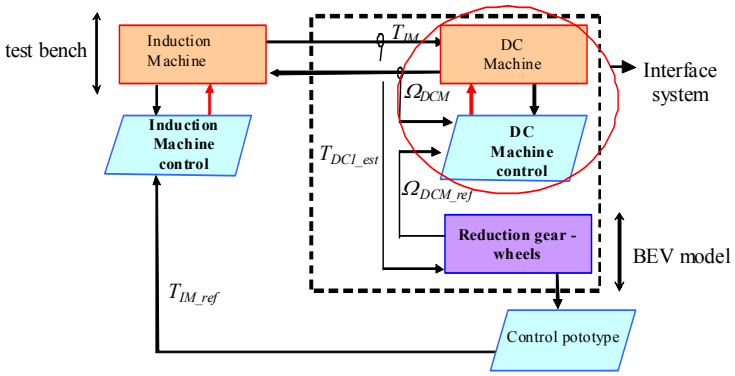

Figure 1.12 HIL simulation structure for a BEV [Bouscayrol 2006-a]

Different HIL simulations are summarized in [Bouscayrol 2008]. Studies of HIL simulations using EMR have been carried out [Bouscayrol 2009] [Allegre 2010]. One example for HEV is presented in IV.1.2

I.3. Ph. D background and objective

The distinct features of EMR include the fact that it respects physical causality and provides a functional modeling. EMR thus contributes significantly to the design of the control and energy management of HEVs. EMR and its inversion-based control are used in this Ph. D. This Ph. D is one of the projects of the research group "MEGEVH" (Modélisation Energétique et Gestion d'Energie de Véhicules Hybrides / Energy Modelling and Energy Management of Hybrid Vehicles). In this section, the background of MEGEVH is first introduced, and the objective of this thesis is discussed.

I.3.1. MEGEVH network and projects

Promotion of HEV research involves multiple skills. Electrical Engineering laboratories are playing a greater role in this field, as more and more electric components are used in HEVs. However, interdisciplinary collaboration with other disciplines, such as mechanical engineering, energy engineering, environmental engineering, chemical engineering, automatic control engineering, is required. Furthermore, timely exchange and cooperation between academic and industrial partners is essential. In this context, the national research group "MEGEVH" has been established [MEGEVH 2007]. MEGEVH is a thematic group of the inter-regional network "RT3" (Recherche Technologique sur les Transports Terrestres / Technological Research for Land Transport) of the French Ministry of Research. It is made up of academic institutions and industrial partners which work on HEVs in France (Figure 1.13) (http://l2ep.univ-lille1.fr/megevh/).

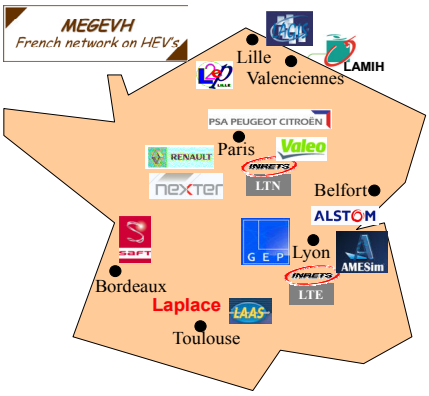

Figure 1.13 MEGEVH partners (2009)

I.3.1.1. Objective of MEGEVH

MEGEVH aims to foster collaboration regarding energetic modeling, energy management and energy optimization of HEVs. Unified methodologies have been developed to be used in research activities [MEGEVH 2007].

I.3.1.2. MEGEVH projects

MEGEVH projects are organized based on two levels: the theoretical level and the application level. The first level deals with the development of theoretical methodologies. It aims to develop generic methodologies for modeling energy management and energy optimization. There are currently three projects:

MEGEVH-macro: macroscopic modeling of HEVs (L2EP of Lille, FEMTO-ST of Belfort, LTE-INRETS of Lyon and Nexter Systems, 2 common PhD students)

MEGEVH-strategy: local energy management of HEVs (L2EP Lille, and LTE-INRETS, 2 common PhD students).

MEGEVH-optim: energy optimization of HEVs (LTE-INRETS and LAMIH Valenciennes, 1 common PhD student)

At the theoretical level, "component" subprojects focus on sensitive components. There are two "component" subprojects: MEGEVH-FC (Fuel Cells for HEVs) and MEGEVH-store (Batteries and Super capacitors for HEVs). At the application level, the theoretical methodologies are validated on real vehicles or sub-systems.

I.3.2. Ph. D objective

The aim of MEGEVH-macro is to establish the HEV modeling using energetic descriptions for control purposes. As part of this project, two parallel Ph. Ds have been carried out. These Ph. Ds involve cooperation between L2EP (Lille), FEMTO-ST (Belfort), LTE (INRETS) and Nexter Systems. One Ph. D focuses on energy sources of HEVs [Boulon 2009-a]. The other, which is the object of this thesis, focuses on different drivetrains of HEVs.

I.3.2.1. MEGEVH-macro

MEGEVH-macro deals with macroscopic modeling of HEVs for energy management purposes. Using different modeling approaches [Gao 2007], different vehicle architectures have been discussed [Wipke 1999] [Bogosyan 2007]. Most of the studies are based on structural approaches. Basic components are available in a library and are connected to represent the topology of a HEV. The interconnections of some components are not obvious and solving algorithms are therefore used. This kind of approach is very useful when the aim is to quickly build a HEV model. These structural approaches can not directly contribute to the control design. In order to obtain the control scheme systematically, causal and functional modeling approaches are necessary. Interconnection problems are solved by merging different components.

MEGEVH-macro first developed components of HEVs using the same graphical description and methodology in order to connect them based on causal considerations. During this first step, several graphical descriptions were studied, including bond-graph (BG), Power-oriented graph (POG), causal ordering graph (COG) and energetic macroscopic repre-

sentation (EMR) [Bouscayrol 2003] [Lhomme 2007] [Boulon 2009-a]. EMR and its inversion-based control, thanks to their advantages, are used in MEGEVH-macro studies.

Based on the previous work, the component library, including electrical machines, power electronics, batteries, supercapacitors, fuel cells and mechanical drivetrains, was further completed [Lhomme 2009] [Boulon 2008].

Different HEV topologies were then studied. EMR models have been established for different HEVs. From these models, control schemes have been deduced and different strategies have been used for global energy management [Lhomme 2007] [Boulon 2009-b].

Finally, some control schemes have been verified on real processes or on parts of real processes using Hardware-In-the-Loop simulations [Lhomme 2010].

I.3.2.2. EMR for HEVs

The first Ph. D applying EMR to HEVs was carried out from 2004 to 2007 [Lhomme 2007]. It involved cooperation between L2EP and LTE-INRETS. In this Ph. D, EMR and its inversion-based control were used to obtain the control design and energy management of three HEVs (series, parallel and series-parallel), each HEV being treated separately. Another Ph. D, as part of the CNRT Futurelec project in collaboration with VALEO, undertaken from 2005 to 2008, looked at modeling and control of multiphase starter-alternators for a Micro-hybrid automotive application [Bruyere 2009-a].

In these studies, each HEV or system was examined separately and independently. Each HEV has its own modeling and inversion-based control scheme. However, a HEV is a combination of two power sources: one unidirectional power source based on an ICE (gasoline or diesel fueled), and the other bidirectional based on batteries or electric energy storage subsystems, as well as electric machines. Regardless of how these two power sources are combined, a HEV has the same main power flows. From this point of view, just one modeling for different architectures can be developed. Thereby, it is possible to use just one and the same simulation program for different vehicles. This makes comparison of different vehicles easier.

From this common description for different HEVs, a unified control scheme can be achieved. In [Ceraolo 2008] [Chen 2009-a], the authors also describe how the control design of different HEVs could be achieved in a general way. Using a general approach, the time required for the control design of such complex systems can be significantly reduced. Moreover, it is easier to compare the different HEVs using the same control structure.

This Ph. D, which examines different drivetrains of HEVs, is part of MEGEVH-macro. It involves cooperation between L2EP, FEMTO-ST (Belfort) and LTE -INRETS. The purpose is to establish a common EMR which can describe different HEVs. Based on this common EMR, a unified control scheme is deduced, which can be used for different HEVs. Using a common EMR, the main power flows of different HEVs may be better understood. If the modeling and control design is achieved in a general way, the time required for the control design can be significantly reduced. Using the same control structure, the dif-

ferent HEVs can be compared easily. Based on this general approach, more efficient energy managements could be achieved. HEV manufacturing costs, fuel consumption and exhausting emissions can therefore be reduced without sacrificing vehicle dynamic performance.

Conclusion

In this chapter, the background and the objective of this Ph. D are discussed.

In the first section, the state of the art of HEVs is presented. To meet the challenges of the transportation sector - energy security, climate change and more stringent government regulations - HEVs are becoming more and more important.

In the second section, different modeling approaches and control design are discussed. One of the key issues related to HEV development is the control design of such complex systems. To efficiently obtain the control design, different modeling approaches for the control purpose can be used, such as Bond Graph, Causal Ordering Graph (COG) and Energetic Macroscopic Representation (EMR). COG and EMR can yield the control scheme using specific inversion rules. Compared to COG, EMR offers a more global energetic view. Therefore, EMR is suitable for the control design of HEVs. Four steps to obtain the control structure using EMR are presented. The validation of control prototypes is also summarized.

In the third section, the objective of this thesis has been introduced. This Ph. D, a part of MEGEVH-macro, is one of MEGEVHs projects. The national research group MEGEVH and its projects have been firstly introduced. The aim of MEGEVH is to foster collaboration between academic and industrial partners related to modeling and power management of HEVs. MEGEVH-macro deals with macroscopic modeling of HEVs for energy management purposes. It involves cooperation between L2EP (Lille), FEMTO-ST (Belfort), LTE –INRETS (Lyon) and Nexter Systems, and includes two Ph. Ds. One Ph. D focuses on energy sources of HEVs [Boulon 2009-a]. This thesis focuses on different drivetrains of HEVs.

The purpose of this Ph. D is to use these general approaches (EMR and its inversion-based control) to establish a common modeling of different HEVs, and to obtain a unified control scheme. Using a common EMR, the main power flows of different HEVs may be better understood. If the modeling and control design is achieved in a general way, the time required for the control design can be reduced. Using the same control structure, the different HEVs can be compared easily, and more efficient energy managements of HEVs could be achieved and compared. HEV manufacturing costs, fuel consumption and exhausting emissions can therefore be reduced.

Before examining the modeling and control design of whole systems, one of the most important subsystems – the electric drives- is studied in chapter II.

Chapter II

Modeling and control of electric drives

Introduction

Electric drives are one of the most important subsystems of Hybrid Electric Vehicles (HEVs). They mainly consist of electrical Energy Storage Systems (ESS), Power Electronics (PEs) and Electric Machines (EMs). Different types of EMs exist, including classical machines such as Direct Current Machines (DCMs), Induction Machines (IMs), Synchronous Machines (SMs) and Switched Reluctance Machines (SRMs), as well as some innovative EMs such as multiphase EMs and double-rotor EMs [Eshani 2005]. Many studies have been undertaken regarding the modeling and control design of these electric drive systems. EMR has been used to study different electric drives including a DCM drive [Delarue 2003-b], an IM drive [Bouscayrol 2006-a], a SM drive [Bouscayrol 2005-b], a standard Double Fed Induction Machine (DFIM) drive [Peng 2009], as well as other innovative electric drives [Locment 2006] [Bruyere 2009-a] [Cheng 2009-b].

In these studies, each system has been examined separately. In this chapter, the modeling and the control of different electric drives is proposed to be developed in a unified way, as each electric drive is a system to convert power from an electrical form to a mechanical form, and vice versa. In this way, the common points of different electric drives are revealed in terms of energy appropriates. The differences, such as possibilities for the energy management, are emphasized. Applying this general approach to electric drives can be considered as a first step for the study of the whole system. This general approach will be used in chapter III for different HEVs.

This chapter is dedicated to presenting the modeling and control design of various electric drive systems in a general way. In the first section, the possibility of establishing the modeling and control of different electric drives using a generic approach is discussed. The second section develops a generic EMR which, via some modifications, can represent certain basic electric drives. Based on this generic EMR, the modeling of some basic electric drives can be obtained by removing some elements. Furthermore, this generic EMR offers a base for other more complex electric drives. The third section deals with the control structure obtained by the inversion of this generic EMR. Two examples are presented and validated by experimentation.

II.1. Electric drives for HEVs

The purpose of this section is to discuss the possibility of using a general approach to establish the modeling and control design of different electric drives. In the first part of this section, the characteristics of EMs are mentioned. These characteristics meet the requirement of traction applications. The second part summarizes different studies which have been carried out related to the modeling and control design of some electric drives using EMR. These previous studies show that it is possible to achieve the modeling and control design of various electric drives in a generic way.

II.1.1. EMs for Traction applications

EMs are suitable for traction applications for the reasons detailed below:

1. The torque-speed profile of EMs is almost ideal for traction applications

The ideal characteristics of traction machines are high torque at low speeds for fast acceleration or hill climbing, and low torque at high speeds for normal driving. The ICE torque-speed profile does not fit this requirement. In ICE vehicles, multi-gear transmission is therefore used to ensure the traction force-speed profile corresponds to the above requirements[Eshani 2005], and also to increase the ICE efficiency. The maximum torque-speed profile of a well-controlled EM is similar to the ideal profile, as shown in Figure 2.1.

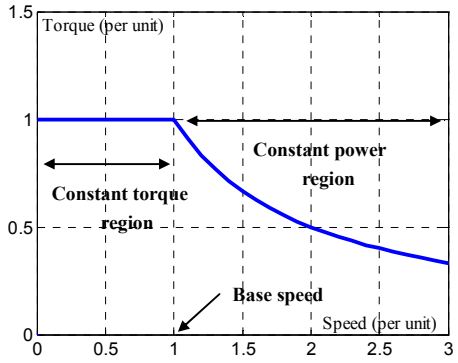

Figure 2.1 Torque-speed requirement for traction machines

This profile includes two distinguishable regions: a constant torque region and a constant power region. The corner speed is usually called the base speed. In the constant torque region, EMs have high torques at low speeds. This region can be used for starting, accelerating or hill climbing. Beyond the base speed, the flux is weakened. This region corresponds to the application of high power for high speed cruising. Moreover, EMs can have wide speed ranges. In the constant power region, the speed of the EMs can reach around 3-4 times the base speed [Zhu 2007].

2. High torque or power density

When designing a vehicle, one of the most important considerations is to reduce the volume and weight of the drivetrain for a given performance. The torque density or power

density of traction machine is one of the most important criteria. This criterion reflects the volume and weight of traction machines for a given torque. Table 2.1 lists typical torque densities for different EMs. IMs and SRMs have similar torque densities; however Permanent Magnet Synchronous Machines (PMSMs) have the highest torque densities [Lovelace 1998] [Makni 2007]. The reason is that the excitation of PMSM is provided by permanent magnets, which require little space and smaller mass. They therefore can potentially have lower weight for given torque and power ratings.

Table 2.1 Typical torque density values for different EMs [Eshani 2005]

	Torque/Volume (kNm/m3)	Torque/Mass(Nm/kg)
IM	about 4	about 7
PMSM	about 30	about 29-48
SRM	about 7	about 6

3. High efficiency over wide speed and torque ranges

High efficiency means lower consumption and pollution for a given driving cycle. The ICE efficiency is weak. Even when the ICE operates in the narrow optimal zone, the best efficiency possible is about 40%. EMs have much better efficiency (more than 90%) over wide speed and torque ranges, including at low torque operations. Like DCMs, IMs are also the most technically mature EMs. Compared with DCMs, IMs have higher power density and better efficiency. PMSMs exceed IMs in terms of efficiency because of the absence of rotor copper losses. SRMs are similar to PMSMs except that the rotors are made from “soft” magnetic materials. Therefore, SRMs have potentially high efficiency.

4. Control robustness and reliability

The first speed control of DCMs was obtained using a resistance in the armature circuits. By the development of PEs and microcontrollers, squirrel-cages IMs using volts/hertz control became popular [Leonard 1896]. Thereafter, based on the development of PEs, other control methods, such as Field-Orientation Control (FOC) [Hasse 1969], Direct Torque Control (DTC) [Takahashi 1986], and Direct Self Control (DSF) [Depenbrock 1988], have been developed. These efforts have highly improved the robustness and reliability of electric propulsion systems.

5. Summary

In addition, EMs have high overload capacities for short periods. Based on the growth of the various technologies involved, the cost of electric drives has become affordable. All these EMs have their advantages and drawbacks, which render them interesting in the design of HEVs. Early Battery-powered Electric Vehicles (BEVs) used DCMs because of their simplicity, for example the Peugeot 106. The Toyota Prius chose PMSMs due to their high efficiency, high power density, and fast dynamic response time.

Apart from these basic EMs, some innovative EMs have also been developed. Multi

phase EMs where the number of phases is greater than 3, have higher reliability and power density, and lower torque pulsations [Semail 2003] [Scuiller 2004] [Levi 2007]. Double-rotor IMs and double-rotor PMSMs are designed for Electric Continuously Variable Transmission (E-CVT) systems [Hoeijmakers 2006] [Cheng 2007] [Chau 2007]. These specific EMs offer a wider range of possibilities in the design of HEVs.

II.1.2. EM Modeling and control design using EMR

EMR is suitable to organize complex models in order to develop control schemes. The energetic properties of the system are highlighted using EMR. An inversion-based control can be deduced directly and systematically from the EMR of the system (See I.2.2). The degrees of freedom, which can act upon the energy management of the system, naturally appear. EMR has been successfully applied to different electric drives for different applications: DCM-based systems for wind energy conversion applications [Bouscayrol 2005-b], DCMs [Delarue 2003-b], IMs with squirrel-cages [Bouscayrol 2005-a], a standard DFIM for wind generator applications [Peng 2009], Synchronous Machines (SMs) for wind energy conversion systems [Bouscayrol 2005-a], PMSMs which take into account different losses for BEV applications [Chen 2007], Double field 7-phase machines [Locment 2006] [Bruyere 2009-a], 7 phase Starter-alternators for micro-hybrid automotive applications [Bruyere 2008], two arranged EM drives (split E-CVT) [Chen 2008-b] [Cheng 2009-a]. These control schemes deduced from their EMRs ensure the electric drive systems operate within wide speed and torque ranges. Depending on the degrees of freedom, the field of the EMs is well controlled and some strategies that improve efficiency have been proposed.

Looking through these very different EMRs and deduced control schemes, some common points emerge. In [Serrano-Iribarnegaray 2007], the authors evoked a question: is it possible to establish a general approach which allows the deduction and development of the control design for diverse electric drive systems in a unified and systematic way? The authors answered this question by using their own approach to the torque control methods. In this chapter, we will answer this question in another way. In [Chen 2009-a], a Double-Inverter-Fed Wound-Rotor Induction Machine (DIF-WRIM) was represented using EMR. In this drive system, the stator and the rotor are separately controlled by two inverters. This configuration is not, at the present time, a very good choice for HEV applications, because the use of two inverters for one EM makes the system expensive. The supplementary inverter does however offer new degrees of freedom for the system. Moreover, the EMR of this configuration can also be used to represent other basic electric drive systems by removing certain elements. Since EMR respects the power flows of systems, a complex system can be considered as interactions of subsystems through power flows. The EMR of DIF-WRIMs shows the interaction of the stator and the rotor in terms of power flows. Therefore, the EMR of DIF-WRIMs can be used to represent other basic electric drive systems. The EMR of DIF-WRIMs will be firstly introduced. In next section, the manner in which EMRs of other electric drives can be obtained will be outlined. In the third section, the inversion-based control of DIF-WRIMs will be discussed, and then, the con-

trol design of PMSM s will be detailed.

In this way, the modeling and control design of various electric drives can be carried out in a generic way. The control design cost and time can be reduced. In addition, these studies have established a base and are very helpful to analyze new systems; for example, SRMs or integrated double-rotor machines. Different from other alternative machines, the control of SRMs is more complex due to the high non-linearity of the determination of the current-switching angle [Yang 2000] [Kestelyn 2002] [Husain 2005] [Hilairet 2006] [Sozer 2007]. Compared to split E-CVTs, double-rotor machines have more complex couplings, both among the rotors and between the rotors and the stator [Nordlund 2002] [Martin 2004].

II.2. Generic EMR of different electric drives

In the previous section, it is mentioned that the EMR of DIF-WRIMs can be considered as a generic EMR which can represent various basic electric drives. In the first part of this section, the EMR of DIF-WRIMs is presented. In the second part, the reorganized EMRs for some basic electric drives are deduced from this generic EMR.

II.2.1. EMR of DIF-WRIMs

To achieve variable speeds, the stator of a standard IM is controlled by a converter fed by a DC bus. Its rotor is in short circuit or squirrel cage, as shown in Figure 2.2 [Caron 1995]. The DFIM is suitable for high power applications. Among different DFIMs [Lecocq 1993] [Tnani 1995] [Hopfensperger 2001] [Aimani 2003], the classic DFIM configuration is as in Figure 2.3. The stator is directly connected with the grid. The rotor is controlled by a converter which is fed by a DC bus. This DC bus is connected to another converter in order to exchange power between the DC bus and grid. The rotor is typically wound with a number of turns between 2 and 3 times the number of turns of the stator. This means that the rotor voltages are higher while the currents are lower. Thus in the typical operational speed range the rated current of the converter is accordingly lower. This leads to a lower cost for the converter. This is the reason that this configuration is widely used in high power wind systems [Tapia 2006] [Brekken 2007] [Bonnet 2007] [López 2008]. A more versatile configuration is one where the stator and the rotor of the machine are independently fed by two converters: DIF-WRIMs (Figure 2.4) [Kawabata 1999] [Datta 2000] [Poddar 2004] [Vidal 2007]. Compared with the classic DFIM, this system requires two converters instead of one. But the supplementary converter also supplies the new degrees of freedom. As we mentioned in the previous section, the EMR of DIF-WRIMs shows the power flows of the stator and of the rotor. This EMR can also be used as a general EMR for certain basic electric drives.

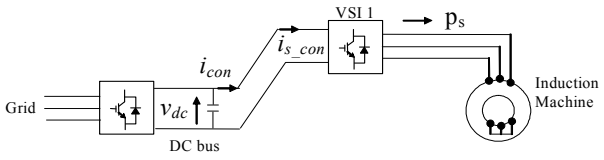

Figure 2.2 Standard IM

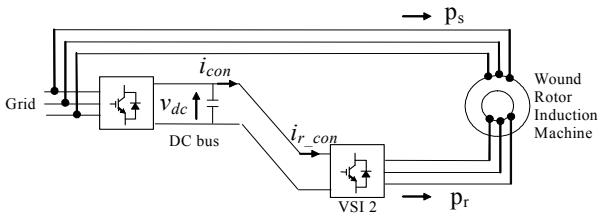

Figure 2.3 Classic DFIM

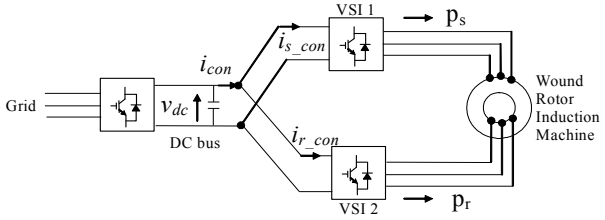

Figure 2.4 DIF-WRIM

II.2.2. Model of DIF-WRIMs

The WRIM is studied in a general *d-q* rotating reference frame (Figure 2.5). *d-q* transformation converts the three-phase stationary variables into a rotating coordinate system. In the *d-q* transformation, the rotating coordinate is defined relative to a fixed reference angle. When the reference is selected based on the location of the fixed alpha axis α_s for the stator, the transformation angle for the stator $\theta_{d/s}$ is the angle between the *d*-axis and the α_s-axis. Since the reference is selected based on the location of the fixed alpha axis α_r for the rotor, the transformation angle for the rotor $\theta_{d/r}$ is the angle between the *d*-axis and the α_r-axis.

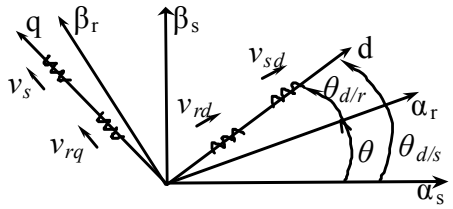

Figure 2.5 Reference frame

Both angles are linked to θ, the electrical angle between the rotor and the stator (Figure 2.5):

$$\theta_{d/s} = \theta_{d/r} + \theta \tag{2.1}$$

This angular relationship can be transformed into a frequency relationship with $\omega_{d/s}$ the stator angular frequency and $\omega_{d/r}$ the rotor angular frequency with respect to the *d*-axis:

$$\omega_{d/s} = \omega_{d/r} + \omega = \omega_{d/r} + p\Omega \tag{2.2}$$

with ω the electric pulsation, p the pole pair number and Ω the machine rotation speed.

Two classical Park transformations are used to obtain stator and rotor variables in the *d-q* frame [Caron 1995]:

$$\begin{cases} \underline{v}_{s\_dq} = [T(\theta_{d/s})]\begin{bmatrix} v_{sa} \\ v_{sb} \\ v_{sc} \end{bmatrix} = [T(\theta_{d/s})][T_{vu}]\underline{u}_s \\ \underline{i}_s = [T_i]\begin{bmatrix} i_{sa} \\ i_{sb} \\ i_{sc} \end{bmatrix} = [T_i][T(\theta_{d/s})]^{-1}\underline{i}_{s\_dq} \end{cases} \tag{2.3}$$

$$\begin{cases} \underline{v}_{r\_dq} = [T(\theta_{d/s})]\begin{bmatrix} v_{ra} \\ v_{rb} \\ v_{rc} \end{bmatrix} = [T(\theta_{d/r})][T_{vu}]\underline{u}_r \\ \underline{i}_r = [T_i]\begin{bmatrix} i_{ra} \\ i_{rb} \\ i_{rc} \end{bmatrix} = [T_i][T(\theta_{d/r})]^{-1}\underline{i}_{r\_dq} \end{cases} \tag{2.4}$$

with $\underline{v}_{s\_dq}=[v_{sd},\ i_{sq}]^{\mathrm{T}}$ the *d-q* stator voltage vector, $\underline{v}_{r\_dq}=[v_{rd},\ i_{rq}]^{\mathrm{T}}$ the *d-q* rotor voltage vector, $\underline{i}_{s\_dq}$ the *d-q* stator current vector, $\underline{i}_{r\_dq}$ the *d-q* rotor current vector, $\underline{u}_s=[u_{s13},\ u_{s23}]^{\mathrm{T}}$ the stator phase-to-phase voltage vector, $\underline{i}_s=[i_{s1},\ i_{s2}]^{\mathrm{T}}$ the stator current vector, $\underline{u}_r=[u_{r13},\ u_{r23}]^{\mathrm{T}}$ the rotor phase-to-phase voltage vector, $\underline{i}_r=[i_{r1},\ i_{r2}]^{\mathrm{T}}$ the rotor current vector. The Park transformation is given by:

$$[T(\theta_x)] = \sqrt{\frac{2}{3}}\begin{bmatrix} \cos\theta_x & \cos(\theta_x - \frac{2\pi}{3}) & \cos(\theta_x + \frac{2\pi}{3}) \\ -\sin\theta_x & -\sin(\theta_x - \frac{2\pi}{3}) & -\sin(\theta_x + \frac{2\pi}{3}) \end{bmatrix} \tag{2.5}$$

$$[T(\theta_x)]^{-1} = [T(\theta_x)]^T \text{ and } \theta_x = \theta_{d/s} \text{ or } \theta_{d/r}$$

The voltage transformation matrix $[T_{vu}]$ is used to convert the phase-to-phase voltages $\underline{u}$ to the phase-to-neutral voltages $\underline{v}$ (Figure 2.6):

$$\begin{bmatrix} v_a \\ v_b \\ v_c \end{bmatrix} = [T_{vu}]\begin{bmatrix} u_{13} \\ u_{23} \end{bmatrix} \text{ with } \begin{cases} \text{For Y connection}: [T_{vu}] = \frac{1}{3}\begin{bmatrix} 2 & -1 \\ -1 & 2 \\ 1 & -1 \end{bmatrix} \\ \text{For } \Delta \text{ connection}: [T_{vu}] = \begin{bmatrix} 0 & 1 \\ -1 & 0 \\ 1 & -1 \end{bmatrix} \end{cases} \tag{2.6}$$

The current transformation matrix $[T_i]$ is :

$$\begin{bmatrix} i_1 \\ i_2 \end{bmatrix} = [T_i]\begin{bmatrix} i_a \\ i_b \\ i_c \end{bmatrix} \text{ with } \begin{cases} \text{For Y connection}: [T_i] = \begin{bmatrix} 1 & 0 & 0 \\ 0 & 1 & 0 \end{bmatrix} \\ \text{For } \Delta \text{ connection}: [T_i] = \begin{bmatrix} 0 & -1 & 0 \\ 1 & 0 & 0 \end{bmatrix} \end{cases} \tag{2.7}$$

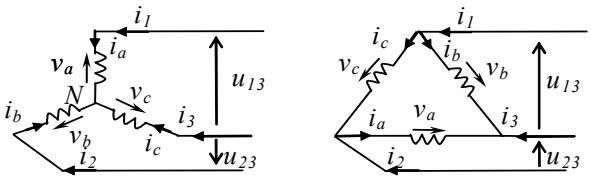

Figure 2.6 Y or Δ circuits

The voltage and flux relationships are obtained as follows:

$$\begin{cases} v_{sd} = R_s i_{sd} + \dfrac{d}{dt}\Phi_{sd} - \omega_{d/s}\Phi_{sq} \\ v_{sq} = R_s i_{sq} + \dfrac{d}{dt}\Phi_{sq} + \omega_{d/s}\Phi_{sd} \\ v_{rd} = R_r i_{rd} + \dfrac{d}{dt}\Phi_{rd} - \omega_{d/r}\Phi_{rq} \\ v_{rq} = R_r i_{rq} + \dfrac{d}{dt}\Phi_{rq} + \omega_{d/r}\Phi_{rd} \end{cases} \tag{2.8}$$

$$\begin{cases} \Phi_{sd} = L_s i_{sd} + M_{sr} i_{rd} \\ \Phi_{sq} = L_s i_{sq} + M_{sr} i_{rq} \\ \Phi_{rd} = L_r i_{rd} + M_{sr} i_{sd} \\ \Phi_{rq} = L_r i_{rq} + M_{sr} i_{sd} \end{cases} \tag{2.9}$$

with R_s, R_r the stator and rotor resistances, L_s, L_r the cyclic inductances and M_{sr} the mutual inductance. The electromagnetic torque T_{em} can be expressed in different ways, for example:

$$T_{em} = pM_{sr}(i_{rd}i_{sq} - i_{sd}i_{rq}) \tag{2.10}$$

Finally, the machine speed Ω is derived from the classical mechanical relationship:

$$J\frac{d}{dt}\Omega = -f\Omega + T_{em} - T_l \tag{2.11}$$

with T_l the load torque, J the total moment of inertia and f the viscous friction coefficient.

II.2.2.1. EMR of DIF- WRIM systems

The EMR of DIF-WRIMs is depicted in Figure 2.7.

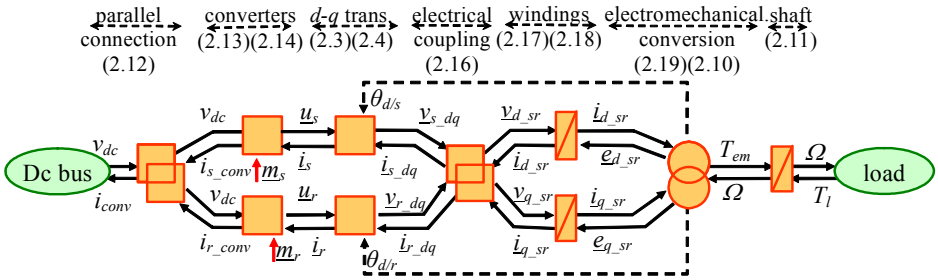

Figure 2.7 EMR of DIF-WRIM systems

Electrical Source – The DC bus is an electrical source (oval), which delivers the DC

voltage v_{dc} to the system and receives a current i_{conv}.

Converters – Firstly, an electrical coupling (overlapped square) is used to express the parallel connection of both converters:

$$\begin{cases} v_{dc} \text{ common variable} \\ i_{conv} = i_{s\_conv} + i_{r\_conv} \end{cases} \tag{2.12}$$

with i_{s_conv} and i_{r_conv} respectively the DC current of the stator and the rotor converters. Secondly, the two 3-leg converters are modeled in the same way using electrical conversion elements (squares):

$$\begin{cases} \underline{u}_s = \underline{m}_s v_{dc} \\ i_{s\_conv} = \underline{m}_s{}^t \underline{i}_s \end{cases} \tag{2.13}$$

$$\begin{cases} \underline{u}_r = \underline{m}_r v_{dc} \\ i_{r\_conv} = \underline{m}_r{}^t \underline{i}_r \end{cases} \tag{2.14}$$

with $\underline{m}_s=[m_{s1}, m_{s2}]^{\mathrm{T}}$, $\underline{m}_r=[m_{r1}, m_{r2}]^{\mathrm{T}}$ the stator and rotor converter modulations. Modulation functions can also be expressed by switching functions which represent the switching orders [Delarue 2003-a].

Wound-Rotor Induction Machine – First, the *d-q* transformations (2.3) (2.4) are described by electrical conversion elements (squares).

Second, relationships (2.8) and (2.9) are then rewritten to obtain the currents as state variables. Two classical subsystems are considered, one for the stator, and another for the rotor, with the following vectors:

$$\begin{cases} \underline{v}_{s\_dq} = \begin{bmatrix} v_{sd} \\ v_{sq} \end{bmatrix} \\ \underline{i}_{s\_dq} = \begin{bmatrix} i_{sd} \\ i_{sq} \end{bmatrix} \end{cases} \text{ and } \begin{cases} \underline{v}_{r\_dq} = \begin{bmatrix} v_{rd} \\ v_{rq} \end{bmatrix} \\ \underline{i}_{r\_dq} = \begin{bmatrix} i_{rd} \\ i_{rq} \end{bmatrix} \end{cases} \tag{2.15}$$

These two subsystems however are not decoupling because each current depends both on stator and rotor voltages. New vectors are defined to obtain two decoupling subsystems: one for the *d*-axis and another for the *q*-axis:

$$\begin{cases} \underline{v}_{d\_sr} = \begin{bmatrix} v_{sd} \\ v_{rd} \end{bmatrix} \\ \underline{i}_{d\_sr} = \begin{bmatrix} i_{sd} \\ i_{rd} \end{bmatrix} \end{cases} \text{ and } \begin{cases} \underline{v}_{q\_sr} = \begin{bmatrix} v_{sq} \\ v_{rq} \end{bmatrix} \\ \underline{i}_{q\_sr} = \begin{bmatrix} i_{sq} \\ i_{rq} \end{bmatrix} \end{cases} \tag{2.16}$$

Thus an electrical coupling element is used to change the stator and rotor based vectors to *d*- and *q*- based vectors (overlapped squares).

Third, two decoupling equivalent winding groups are obtained, the *d*-axis winding group and the *q*-axis winding group. The *d*-axis windings impose the currents $\underline{i}_{d\_sr}$ as state

variables:

$$[L_{eq}]\frac{d}{dt}\underline{i}_{d\_sr} = -[R_{eq}]\underline{i}_{d\_sr} + [K_{eq}]\underline{v}_{d\_sr} - \underline{e}_{d\_sr} \tag{2.17}$$

However, the *q*-axis windings impose the currents $\underline{i}_{q\_sr}$ as state variables:

$$[L_{eq}]\frac{d}{dt}\underline{i}_{q\_sr} = -[R_{eq}]\underline{i}_{q\_sr} + [K_{eq}]\underline{v}_{q\_sr} - \underline{e}_{q\_sr} \tag{2.18}$$

with the equivalent induction matrix $[L_{eq}]$, equivalent resistance matrix $[R_{eq}]$ and the gain matrix $[K_{eq}]$ as follows:

$$[L_{eq}] = \begin{bmatrix} R_s\sigma\tau_s & \mathbf{0} \\ \mathbf{0} & R_r\sigma\tau_r \end{bmatrix},\ [R_{eq}] = \begin{bmatrix} R_s & \mathbf{0} \\ \mathbf{0} & R_r \end{bmatrix}, \text{ and } [K_{eq}] = \begin{bmatrix} \mathbf{1} & -\dfrac{M_{sr}}{L_r} \\ \mathbf{1} & -\dfrac{M_{sr}}{L_s} \end{bmatrix}$$

with $\tau_s = L_s/R_s$ the stator electric time constant, $\tau_r = L_r/R_r$ the rotor electric time constant and $\sigma = (1-M^2_{sr}/(L_sL_r))$ the magnetic leakage factor between the stator and rotor windings. The two equivalent winding groups are depicted by two vectorial accumulation elements (rectangles with an oblique bar).

Fourth, the electromechanical conversion coupling element (overlapped circles) yields the machine torque T_{em} (2.10) and the equivalent e.m.f $\underline{e}_{d\_sr}$ and $\underline{e}_{q\_sr}$, as follows:

$$\begin{cases} \underline{e}_{d\_sr} = \begin{bmatrix} e_{sd} \\ e_{rd} \end{bmatrix} = \begin{bmatrix} \mathbf{0} & -\dfrac{M_{sr}R_r}{L_r} \\ -\dfrac{M_{sr}R_s}{L_s} & \mathbf{0} \end{bmatrix} \underline{i}_{d\_sr} + \begin{bmatrix} \dfrac{M^2_{sr}}{L_r}\omega_{d/r} - L_s\omega_{d/s} & M_{sr}(\omega_{d/r} - \omega_{d/s}) \\ M_{sr}(\omega_{d/s} - \omega_{d/r}) & \dfrac{M^2_{sr}}{L_s}\omega_{d/s} - L_r\omega_{d/r} \end{bmatrix} \underline{i}_{q\_sr} \\ \underline{e}_{q\_sr} = \begin{bmatrix} e_{sq} \\ e_{rq} \end{bmatrix} = \begin{bmatrix} L_s\omega_{d/s} - \dfrac{M^2_{sr}}{L_r}\omega_{d/r} & M_{sr}(\omega_{d/s} - \omega_{d/r}) \\ M_{sr}(\omega_{d/r} - \omega_{d/s}) & L_r\omega_{d/r} - \dfrac{M^2_{sr}}{L_s}\omega_{d/s} \end{bmatrix} \underline{i}_{d\_sr} + \begin{bmatrix} \mathbf{0} & -\dfrac{M_{sr}R_r}{L_r} \\ -\dfrac{M_{sr}R_s}{L_s} & \mathbf{0} \end{bmatrix} \underline{i}_{q\_sr} \end{cases} \tag{2.19}$$

Shaft – The shaft is an accumulation element (rectangle with an oblique bar) with the machine speed Ω as the state variable (output of the element) (2.11).

Load – A mechanical source (load, oval) is used to model the mechanical load [Bouscayrol 2006-a], delivering the load torque T_l and receiving the machine speed Ω.

II.2.3. Generic EMR

The EMR of DIF-WRIMs highlights the power flows of the electric drive system (see Figure 2.7). The total power of the system is distributed into two power flows using the parallel converters: one for the stator side, the other for the rotor side. Using the *d-q* transformations, two equivalent winding groups can be found, as is the case for the classic IM. But each winding

group is a two-dimensional element yielding two currents. Thus the electromechanical conversion yields the torque from 4 different currents. This property will be useful for control purposes. The electrical power flows are thus combined in a complex way to obtain the unique mechanical power flow.

This EMR shows the interaction between the stator power flow and the rotor power flow. It is a common point for all basic EMs. Therefore, this EMR can be used for the modeling of various basic electric drives in a generic way.

Separately excited DCM systems – In a separately excited DCM drive system, the armature winding is controlled by a chopper (converter 1); the field winding is controlled by another chopper (converter 2). The two choppers can be connected in parallel with a DC bus. Neither the *d-q* transformation, nor the "electrical coupling" element for the vector reorganization is necessary. The field winding voltage u_s, the field winding current i_s, the armature winding voltage u_r, the armature winding current i_r, and the two modulation variables of the two choppers m_s and m_r are all one dimensional variables. The electromechanical conversion yields the torque from the armature current i_s and the field current i_r. The same torque-speed relationship is used as in (2.11). This reduced EMR can represent the separately excited DCM drive system as shown in Figure 2.8. The equations are given in Appendix 1.

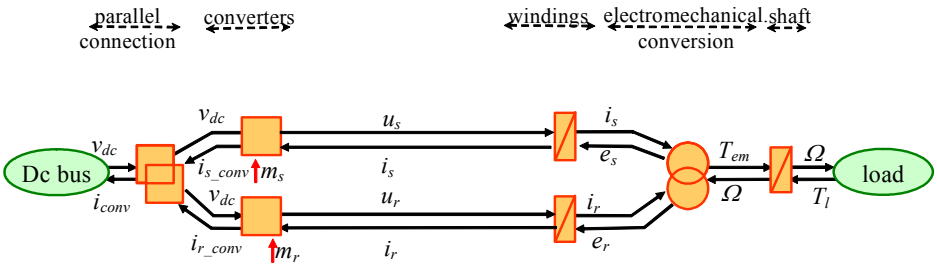

Figure 2.8 EMR of separately excited DCM drive systems

Standard IM systems – The difference between a DIF-WRIM and a standard IM (see Figure 2.2) is that there is only one converter for the stator, and the rotor is in short-circuit for a standard IM. The "parallel connection" element, the "converter" for the rotor and the "*d-q* trans." for the rotor are deleted from the generic EMR (see Figure 2.7). The rotor winding in short-circuits is represented by an equivalent electrical source "Rotor" which supplies the *d-q* rotor voltage vector $\underline{v}_{r\_dq}$ and receives the *d-q* rotor current vector $\underline{i}_{r\_dq}$. The *d-q* rotor voltage vector $\underline{v}_{r\_dq}$ is a zero vector. The EMR of standard IMs is obtained as shown in Figure 2.9. The equations in these EMR elements are the same as for DIF-WRIMs with $\underline{v}_{r\_dq} = [0, 0]^T$. In the same way, the EMR of classic DFIMs can also be deduced (Figure 2.9).

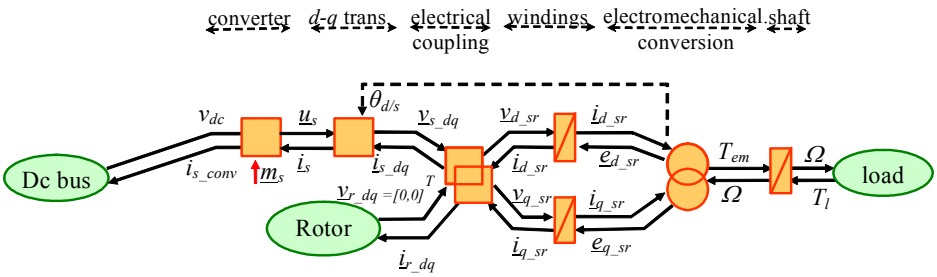

Figure 2.9 EMR of standard IM systems

PMSM systems – In a PMSM, the stator is controlled by a converter which is fed by a DC bus. The rotor is a permanent magnet that can be salient pole or non-salient pole. The "parallel connection" element, the "converter" for the rotor and the "*d-q* trans." for the rotor are deleted from the generic EMR (see Figure 2.7). In the "*d-q* trans." for the stator, the stationary reference is selected based on the location of the α-axis, the transformation angle is the rotor electrical position angle $\theta_{d/s}$:

$$\theta_{d/s} = p\theta = \int p\Omega dt \tag{2.20}$$

with $\theta_{d/s}$ the angle between the *d*-axis and the α-axis, and θ the rotor potion.

The mathematical model of a PMSM drive is defined in the rotation reference frame *d-q* by 2-phase voltage equations:

$$\begin{cases} v_{sd} = R_s i_{sd} + \dfrac{d}{dt}\Phi_{sd} - \omega\Phi_{sq} \\ v_{sq} = R_s i_{sq} + \dfrac{d}{dt}\Phi_{sq} + \omega\Phi_{sd} \end{cases} \tag{2.21}$$

The flux relationships are:

$$\begin{cases} \Phi_{sd} = L_{sd} i_{sd} + \Phi_f \\ \Phi_{sq} = L_{sq} i_{sq} \end{cases} \tag{2.22}$$

with R_s the stator resistance, Φ_f the permanent magnet flux linkage, L_{sd}, L_{sq} the cyclic inductances of the *d-q* axis.

The equation of the stator converter is the same as in (2.13). The *d-q* transmission for the stator is as in (2.3). The *d-q* stator voltage vector $\underline{v}_{s\_dq}$ and the *d-q* stator current vector $\underline{i}_{s\_dq}$ can be expressed separately. Therefore, the "electrical coupling" element can be used to convert the vector variable to scalar variables. Then, two scalar accumulation elements ("windings") represent the *d* and *q* windings separately:

$$L_{sd}\frac{d}{dt}i_{sd} = -R_s i_{sd} + v_{sd} - e_d \tag{2.23}$$

$$L_{sq}\frac{d}{dt}i_{sq} = -R_s i_{sq} + v_{sq} - e_q \tag{2.24}$$

The e.m.f. of the *d*-axis and *q*-axis are defined as follows:

$$\begin{cases} e_d = -L_{sq} i_{sq} \omega \\ e_q = (L_{sd} i_{sd} + \Phi_f)\omega \end{cases} \tag{2.25}$$

The two *d*-*q* stator currents yield the mechanical torque as below:

$$T_{em} = p i_q [\Phi_f + (L_{sd} - L_{sq}) i_{sd}] \tag{2.26}$$

The shaft equation is as in (2.11). The EMR of PMSMs is obtained from this generic EMR as in Figure 2.10.

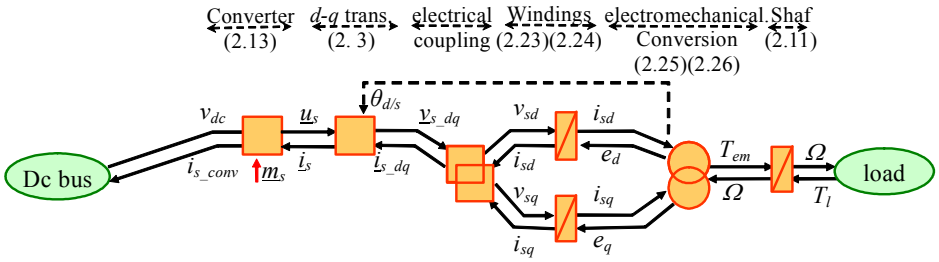

Figure 2.10 EMR of PMSM systems

In conclusion, the modeling of different basic EM systems can be organized in a general way. The EMR of DIF-WRIMs can be considered as a kind of generic EMR. By modifying certain elements, other EMRs for different basic EM electric drives, such as DCMs, standard IMs, standard DFIMs and PMSMs, can be deduced.

II.3. Control of electric drive subsystems

In section two, the EMR of DIF-WRIMs can be considered as a generic EMR. Other EMRs for some basic electric drive systems can be obtained based on this generic EMR. This section reveals a general approach for the control design of different EM systems. In the first part, a control scheme of DIF-WRIMs is deduced from the generic EMR using specific inversion rules. In the second part, based on the control scheme of DIF-WRIMs, a control scheme of PMSM systems is developed. Both control schemes are validated by experimentation.

II.3.1. Control scheme of DIF-WRIM systems

Compared to standard IM systems or standard DFIM systems, the supplementary converter of DIF-WRIMs brings more degrees of freedom which can be used to optimize the system. Some controls of DIF-WRIMs have already been discussed [Kawabata 1999] [Poddar 2005] [Vidal 2007]. All these studies have demonstrated the control possibilities of DIF-WRIMs. However, the degrees of freedom of this system are not highlighted and all optimization possibilities are not used. By inverting the EMR of DIF-WRIMs, a control structure can be deduced. This control structure highlights the degrees of freedom of the system which can be fully used to optimize the system at the strategy level. Two strategies are proposed and used simultaneously. The first strategy defines the active power distribution between the stator and rotor sides, as in [Vidal 2007]. A second new strategy leads to the minimization of copper losses for the same power distribution. This strategy is based on the minimization of stator and rotor copper losses [Chen 2010]. Loss-minimization strategies have already been proposed for standard DFIM systems where there is only one converter [Rabelo 2006]. In our case, a loss-minimization strategy is developed for DIF-WRIMs with two converters.

II.3.1.1. Tuning and Control paths

There are 4 tuning variables, $\underline{m}_s = [m_{s1}, m_{s2}]$ and $\underline{m}_r = [m_{r1}, m_{r2}]$ which act on the system. One objective which must be achieved is the control of the machine speed Ω. Therefore, the 3 remaining degrees of freedom should be used in the energy management of the system. By going from the tuning variables $\underline{m}_s$ and $\underline{m}_r$ towards the objective Ω, the tuning paths can be found, as in Figure 2.11. The control paths are obtained by an inversion of the tuning paths, as in Figure 2.12.

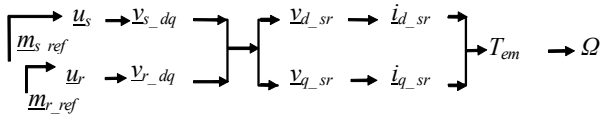

Figure 2.11 Tuning paths of DIF-WRIMs

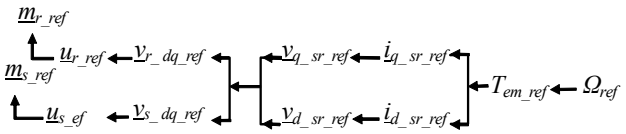

Figure 2.12 Control paths of DIF-WRIMs

II.3.1.2. Inversion-based control scheme

Along the tuning path, the inversion-based control scheme is obtained from the EMR of the system (Figure 2.13).

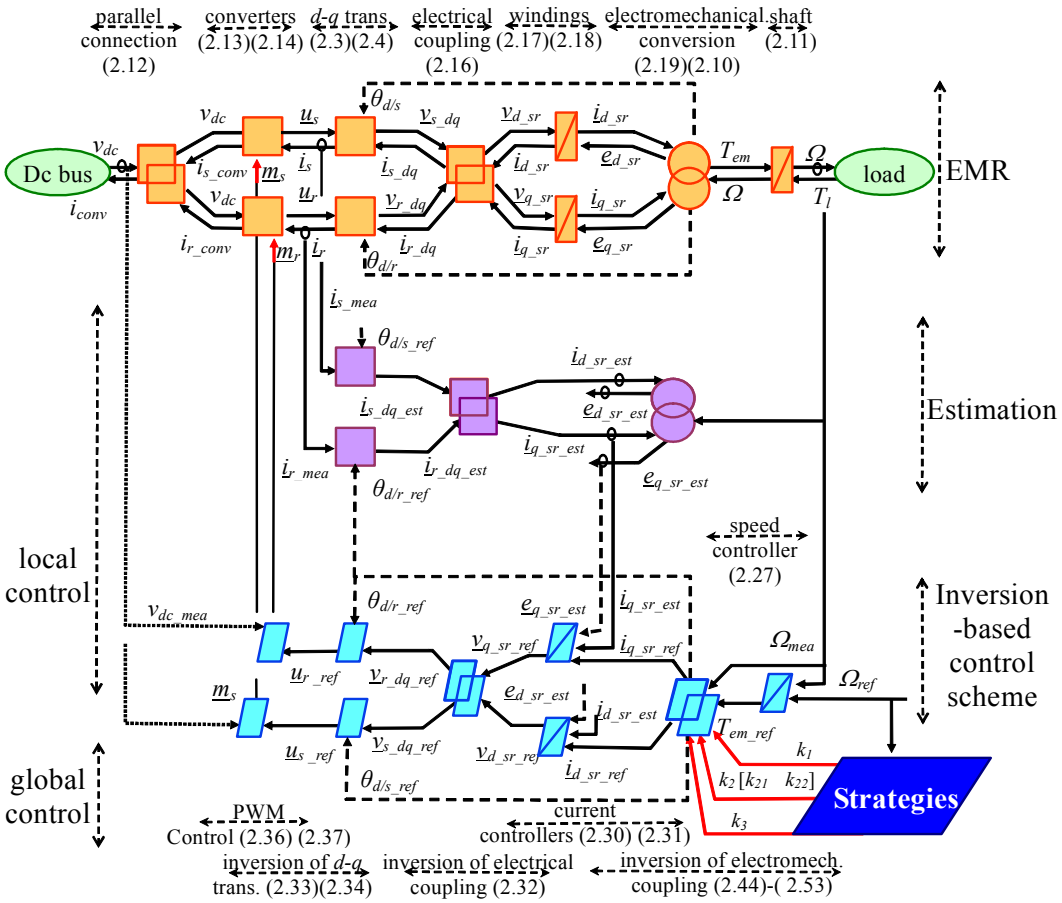

Figure 2.13 Control scheme of DIF-WRIMs

Inversion of the shaft – In order to invert (2.11), a controller is required to yield the reference T_{em_ref} from the measured and reference speeds, Ω_{mea} and Ω_{ref}:

$$T_{em\_ref} = C_s(t)[\Omega_{ref} - \Omega_{mea}] + T_{l\_mea} \qquad (2.27)$$

where $C_s(t)$ is the speed controller which may be a PI type or another type. In theory, a compensation of the load torque T_{l_mea} can be made.

Inversion of the electromechanical coupling – From (2.1), (2.2) and the machine speed Ω, the angle references θ_{d/s_ref} and θ_{d/r_ref} can be obtained using one supplementary input k_1 is required. To invert the electromechanical coupling, there are 4 inputs (i_{sd}, i_{sq}, i_{rd} and i_{rq}) and 1 output (T_{em}) for this EMR element, according to the chosen tuning paths. In this case, 3 other supplementary inputs, k_2 (two dimensions: k_{21} and k_{22}), and k_3 are required (Figure 2.14) [Bouscayrol 2005-b]. In this way, the degrees of freedom are highlighted. They are defined at the strategy level (see II.3.1.4).

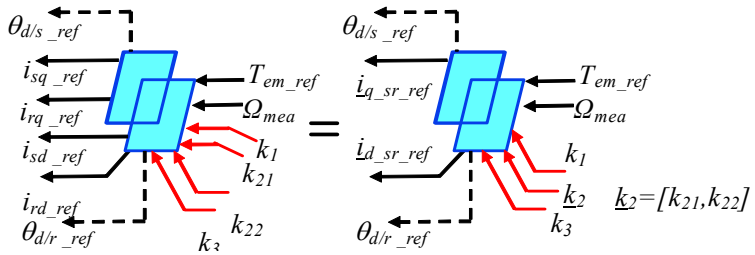

Figure 2.14 Inversion of the electromechanical coupling of DIF-WRIMs

Current Controllers – The inversion of (2.17) and (2.18) requires current controllers from the current measurement and references, $\underline{i}_{d\_sr\_mea}$, $\underline{i}_{q\_sr\_mea}$, $\underline{i}_{d\_sr\_ref}$ and $\underline{i}_{q\_sr\_ref}$, to obtain the *d*-axis and *q*-axis voltages $\underline{v}_{d\_sr\_ref}$ and $\underline{v}_{q\_sr\_re.}$ (2.17) and (2.18) can be written in Laplace form:

$$\underline{i}_{d\_sr} = [T_{ST}]([K_{eq}]\underline{v}_{d\_sr} - \underline{e}_{d\_sr}) \tag{2.28}$$

$$\underline{i}_{q\_sr} = [T_{ST}]([K_{eq}]\underline{v}_{q\_sr} - \underline{e}_{q\_sr}) \tag{2.29}$$

with $[T_{ST}] = \begin{bmatrix} \frac{1/R_s}{1+\sigma\tau_s S} & 0 \\ 0 & \frac{1/R_r}{1+\sigma\tau_r S} \end{bmatrix}$

The current controllers can be written as:

$$\underline{v}_{d\_sr\_ref} = C_c(t)[\underline{i}_{d\_sr\_ref} - \underline{i}_{d\_sr\_mea}] - [K_{eq}]\underline{v}_{d\_sr\_est} + \underline{e}_{d\_sr\_est} \tag{2.30}$$

$$\underline{v}_{q\_sr\_ref} = C_c(t)[\underline{i}_{q\_sr\_ref} - \underline{i}_{q\_sr\_mea}] - [K_{eq}]\underline{v}_{q\_sr\_est} + \underline{e}_{d\_sr\_est} \tag{2.31}$$

where $C_c(t)$ is the current controller which may be a PI type or other type controllers. The $C_c(t)$ parameters can be calculated from the matrix $[T_{ST}]$. At this point, $[K_{eq}]\underline{v}_{d\_sr\_est}$, $[K_{eq}]\underline{v}_{q\_sr\_est}$, $\underline{e}_{d\_sr\_est}$ and $\underline{e}_{q\_sr\_est}$ can be compensated.

Inversion of the *sr_dq* coupling – Since there are 4 inputs and 4 outputs in the chosen tuning paths, no supplementary input is needed. A simple inversion of (2.16) is made:

$$\begin{cases} \underline{v}_{s\_dq\_ref} = \begin{bmatrix} v_{sd\_ref} \\ v_{sq\_ref} \end{bmatrix} \\ \underline{v}_{r\_dq\_ref} = \begin{bmatrix} v_{rd\_ref} \\ v_{rq\_ref} \end{bmatrix} \end{cases} \tag{2.32}$$

Inversions of the *d-q* transformations – The inversion of (2.3) and (2.4) yield the final stator and rotor phase-to-phase voltage references:

$$\underline{u}_{s\_ref} = [T_{uv}][T(\theta_{d/s})]^T \underline{v}_{s\_dq\_ref} \tag{2.33}$$

$$\underline{u}_{r\_ref} = [T_{uv}][T(\theta_{d/r})]^T \underline{v}_{r\_dq\_ref} \tag{2.34}$$

The voltage transformation matrix $[T_{uv}]$, which converts the phase-to-neutral voltages $\underline{v}$ to the phase-to-phase voltage $\underline{u}$ (see Figure 2.6), is given as:

$$\begin{bmatrix} u_{13} \\ u_{23} \end{bmatrix}_{ref} = [T_{uv}] \begin{bmatrix} v_a \\ v_b \\ v_c \end{bmatrix}_{ref} \quad \text{with} \quad \begin{cases} \text{For Y connection}: [T_{uv}] = \begin{bmatrix} 1 & 0 & -1 \\ 0 & 1 & -1 \end{bmatrix} \\ \text{For } \Delta \text{ connection}: [T_{uv}] = \begin{bmatrix} 0 & -1 & 0 \\ 1 & 0 & 0 \end{bmatrix} \end{cases} \tag{2.35}$$

Inversions of the inverters – The modulation vectors $\underline{m}_{s\_ref}$ and $\underline{m}_{r\_ref}$ are obtained by inverting (2.13) and (2.14) :

$$\underline{m}_{s\_ref} = \frac{1}{v_{dc\_mea}} \underline{u}_{s\_ref} \tag{2.36}$$

$$\underline{m}_{r\_ref} = \frac{1}{v_{dc\_mea}} \underline{u}_{r\_ref} \tag{2.37}$$

The measurement of the DC bus voltage v_{dc_mea} is usually necessary considering its variable value. A pulse width modulation (PWM) can be used to define the switching functions from the modulation functions [Delarue 2003-a].

II.3.1.3. Simplifications and estimations

In reality, some variables are difficult or impossible to measure. Thereby, estimations or simplifications can be made. For the speed controller, the measurement of the load torque T_{l_mea} is difficult. It can be considered as disturbance to be rejected. For the current controllers, the *d-q* axis currents can not be measured directly, but can be estimated from the measurement of currents $\underline{i}_{s\_mea}$ and $\underline{i}_{r\_mea}$ using the *d-q* transformation:

$$\underline{i}_{s\_dq\_est} = \begin{bmatrix} i_{sd\_est} \\ i_{sq\_est} \end{bmatrix} = [T(\theta_{d/s})][T_{ii}]\underline{i}_{s\_mea} \tag{2.38}$$

$$\underline{i}_{r\_dq\_est} = \begin{bmatrix} i_{rd\_est} \\ i_{rq\_est} \end{bmatrix} = [T(\theta_{d/r})][T_{ii}]\underline{i}_{r\_mea} \tag{2.39}$$

The current transformation matrix $[T_{ii}]$ is :

$$\begin{bmatrix} i_a \\ i_b \\ i_c \end{bmatrix} = [T_{ii}] \begin{bmatrix} i_1 \\ i_2 \end{bmatrix} \quad \text{with} \quad \begin{cases} \text{For Y conncetion s}: [T_{ii}] = \begin{bmatrix} 1 & 0 \\ 0 & 1 \\ -1 & -1 \end{bmatrix} \\ \text{For } \Delta \text{ conncetion s}: [T_{ii}] = \frac{1}{3} \begin{bmatrix} 1 & 2 \\ -2 & -1 \\ 1 & -1 \end{bmatrix} \end{cases} \tag{2.40}$$

The *d-q* transformation requires knowledge of the angles $\theta_{d/s}$ and $\theta_{d/r}$. These angles can be determined at the strategy level (see II.3.1.4). Similarly, the estimation of the electro-magnetic forces (e.m.f.) $\underline{e}_{d\_sr\_est}$ and $\underline{e}_{q\_sr\_est}$ can be carried out using (2.19). The estimation can be established by reusing the EMR models. The same blocks as for the EMR (but in purple) represent the estimation model (see Figure 2.13). $\underline{v}_{d\_sr\_est}$ and $\underline{v}_{q\_sr\_est}$ can be replaced by the their reference values.

II.3.1.4. Strategies for the DIF-WRIM control

To invert the coupling element, some supplementary inputs are required. In fact, these supplementary inputs reveal the degrees of freedom. There are generally several possibilities at the strategy level. Two of them are explicitly used in [Vidal 2007] (one for machine flux regulation, another for power distribution between the stator and the rotor). The supplementary inputs, k_1 (with Ω), $\underline{k}_2$ (k_{21} and k_{22}) and k_3 are chosen as follows:

1. k_1 and Ω is used for the power distribution between the stator and the rotor, as shown in [Vidal 2007]. This means that k_1 is used to calculate $\omega_{d/s}$ and $\omega_{d/r}$, then to determine the angles $\theta_{s/d}$ and $\theta_{r/d}$, and finally to define the power ratio between the stator and the rotor;

2. k_{21} and k_{12} are used for the choice of field orientation (stator or rotor field orientation);

3. k_3 is used to determine the current ratios that minimize the copper losses

This is one possibility proposed in this thesis. Other possibilities can be proposed using different strategies.

(1) Stator and rotor power ratio k_1

The stator power p_s and the rotor power p_r can be calculated by:

$$\begin{aligned} p_s &= v_{sd} i_{sd} + v_{sq} i_{sq} \\ &= R_s (i_{sd}^2 + i_{sq}^2) + \omega_{d/s} M_{sr} (i_{rd} i_{sq} - i_{sd} i_{rq}) \\ &= copper\ losses + \frac{\omega_{d/s}}{p} T_{em} \end{aligned} \tag{2.41}$$

$$\begin{aligned} p_r &= v_{rd} i_{rd} + v_{rq} i_{rq} \\ &= R_r (i_{rd}^2 + i_{rq}^2) + \omega_{d/r} M_{sr} (i_{rd} i_{sq} - i_{sd} i_{rq}) \\ &= copper\ losses + \frac{\omega_{d/r}}{p} T_{em} \end{aligned} \tag{2.42}$$

The positive power direction is defined as in Figure 2.4. Neglecting the copper losses, the power ratio k_1 can be defined as:

$$\frac{p_s}{p_r} \approx -\frac{\omega_{d/s}}{\omega_{d/r}} = k_1 \tag{2.43}$$

According to the position relationship (2.2), $\omega_{d/s}$ and $\omega_{d/r}$ are deduced from Ω and k_1:

$$\begin{cases} \omega_{d/s} = \dfrac{k_1}{k_1 + 1} p\Omega \\ \omega_{d/r} = \dfrac{-1}{k_1 + 1} p\Omega \end{cases} \tag{2.44}$$

$\theta_{s/d}$ and $\theta_{r/d}$ can thus also be determined by integration of these frequencies. From (2.43), k_1 and Ω can be used to ensure the active power distribution between both sides of the machine (2.43), thereby determining the two converter sizes [Vidal 2007].

(2) Choice of field orientation

$\underline{k}_2$ ([k_{21}, k_{21}]) is used to choose the field orientation, as shown in Table 2.2 ((2.46) or (2.47)). For the stator field orientation, Φ_{sd_ref} is imposed on the rated value of the stator flux (or is weakened when necessary), and Φ_{sq_ref}=0. These two stator flux are imposed through k_{21} and k_{22}. For the rotor field orientation, Φ_{rd_ref} and Φ_{rq_ref} are imposed by k_{21} and k_{22}. Φ_{rd_ref} is set to its rated value of the rotor flux (or is weakened when necessary), and Φ_{rq_ref}=0.

(3) Minimum-copper-loss

The different equations concerning k_3, which depend on the field orientations, are given in Table 2.2. If the stator field is oriented, k_3 is introduced as in (2.48). From the flux equation (2.9) and torque equation (2.10), the current references $\underline{i}_{d\_sr\_ref}$ are deduced as in (2.50) and $\underline{i}_{q\_sr\_ref}$ as in (2.52). If the rotor field is oriented, k_3 is introduced as in (2.49), the current references $\underline{i}_{d\_sr\_ref}$ are deduced as in (2.51) and $\underline{i}_{q\_sr\_ref}$ as in (2.53). Under the same power distribution condition (same value of k_1), the copper losses can be minimized using k_3. The optimal k_3 is obtained as follows:

$$\frac{\partial(R_s(i_{sd}^2 + i_{sq}^2) + R_r(i_{rd}^2 + i_{rq}^2))}{\partial k_3} = 0 \tag{2.45}$$

The value of k_3 for the minimum copper losses is calculated on-line using (2.54) or (2.55). The evolution of k_3 is a function of T_{em} (Figure 2.15). This allows the copper losses to be reduced.

(4) Operation summary

The angles $\theta_{s/d}$ and $\theta_{r/d}$ can be determined using k_1 and Ω, ensuring the power distribution between the stator and the rotor sides. The size of both converters can therefore be determined. k_2 is considered as the choice of the field orientation. Either the stator field oriented control or rotor oriented control can be used. Depending on the field orientation chosen, k_3 is determined in such a way that the copper losses are reduced. In this way, the degrees of freedom are highlighted and fully used.

Table 2.2 k_2 and k_3 for stator field orientation or for rotor field orientation

Stator field orientation	Rotor field orientation
$\begin{cases} k_{21} = \Phi_{sd\_ref} \\ k_{22} = \Phi_{sq\_ref} \end{cases}$ (2.46)	$\begin{cases} k_{21} = \Phi_{rd\_ref} \\ k_{22} = \Phi_{rq\_ref} \end{cases}$ (2.47)
$i_{sd\_ref} = k_3 i_{sq\_ref}$ (2.48)	$i_{rd\_ref} = k_3 i_{rq\_ref}$ (2.49)
$\begin{cases} i_{sd\_ref} = \dfrac{k_3 T_{em\_ref}}{p\Phi_{sd\_ref}} \\ i_{rd\_ref} = \dfrac{\Phi_{sd\_ref} - L_s i_{sd\_ref}}{M_{sr}} \end{cases}$ (2.50)	$\begin{cases} i_{sd\_ref} = \dfrac{\Phi_{rd\_ref} - L_r i_{rd\_ref}}{M_{sr}} \\ i_{rd\_ref} = -\dfrac{k_3 T_{em\_ref}}{p\Phi_{rd\_ref}} \end{cases}$ (2.51)
$\begin{cases} i_{sq\_ref} = \dfrac{T_{em\_ref}}{p\Phi_{sd\_ref}} \\ i_{rq\_ref} = -\dfrac{L_s i_{sq\_ref}}{M_{sr}} \end{cases}$ (2.52)	$\begin{cases} i_{sq\_ref} = -\dfrac{L_r i_{rd\_ref}}{M_{sr}} \\ i_{rq\_ref} = -\dfrac{T_{em\_ref}}{p\Phi_{rd\_ref}} \end{cases}$ (2.53)
$\begin{cases} \text{If } T_{em} = \mathbf{0} \text{ then } k_3 = 0 \\ \text{Else } k_3 = \dfrac{1}{T_{em\_ref}} \dfrac{pL_s R_r \Phi_{sd\_ref}^2}{(R_s M_{sr}^2 + R_r L_s^2)} \end{cases}$ (2.54)	$\begin{cases} \text{If } T_{em} = \mathbf{0} \text{ then } k_3 = 0 \\ \text{Else } k_3 = -\dfrac{1}{T_{em\_ref}} \dfrac{pL_r R_s \Phi_{rd\_ref}^2}{(R_r M_{sr}^2 + R_s L_r^2)} \end{cases}$ (2.55)

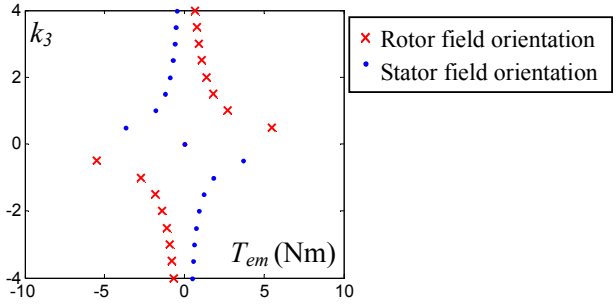

Figure 2.15 k_3 in relation of T_{em}

II.3.1.5. Experimental results

The simulation was firstly carried out with the help of the EMR and the inversion-based control. The experimentation was subsequently conducted through a dSPACE 1103 controller board to check the control in a real-time environment. In this part, only the experimentation results are presented. In Appendix 2, the simulation results are compared with some of the experimental results. The simulation is validated, as the simulation results coincide with the experimental ones.

The experimental set-up (Figure 2.16) is composed of one 1.5 kW WRIM (Table 2.3) and a DC machine. The stator of the WRIM and the rotor of this WRIM are separately fed by

two 3-leg IGBT inverters, VSI1 and VSI2. A DC bus of 250 V supplies both inverters. The DC machine has the same shaft as the WRIM. This DC machine is controlled with a chopper to impose different load torques on the tested drive.

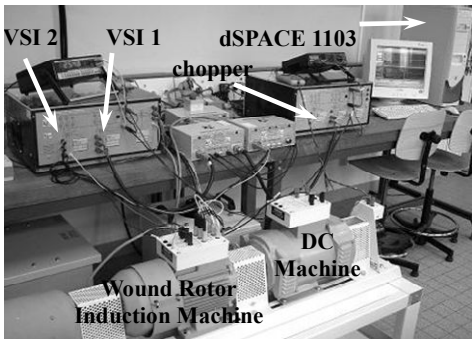

Figure 2.16 Experimental set-up of the DIF-WRIM

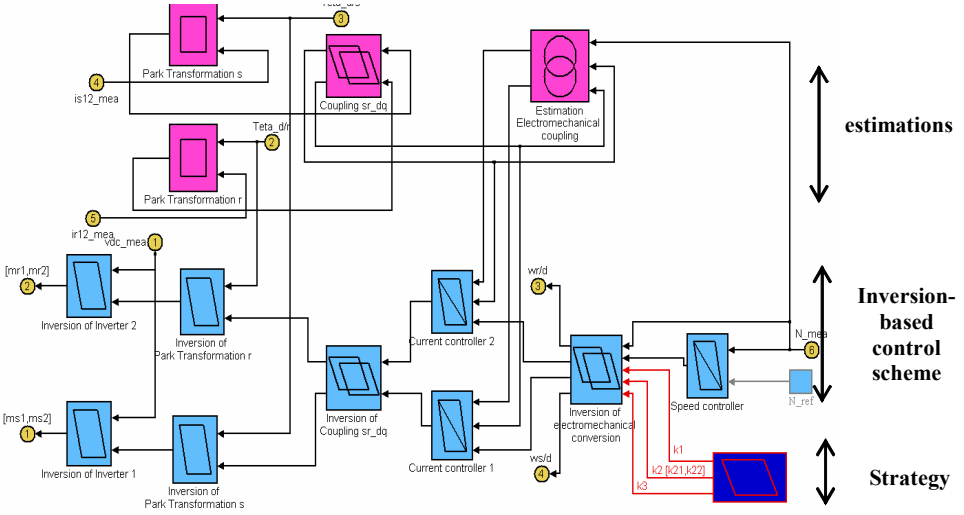

Figure 2.17 Experimental control model of DIF-WRIMs(Matlab-Simulink^{TM})

Table 2.3 WRIM specifications

Rated speed (rpm)	1410	Cyclic stator inductance (H)	0.7090
Rated active power (W)	1500	Cyclic rotor inductance (H)	0.0189
Number of pole pairs	2	Mutual inductance between stator and rotor (H)	0.1061
Stator resistance per phase (Ω)	7.7	Moment of inertia (kg.m2)	4.32e-2
Rotor resistance per phase (Ω)	0.264	Friction coefficient (Nms)	5.35e-3

The control scheme is directly transposed from the EMR into Matlab-Simulink^{TM} (Figure 2.17). The purple blocks are estimations, as is the case in the EMR. The light blue blocks are the inversion-based control blocks deduced from the EMR. The same control scheme will be kept, but the strategy level will be changed in order to compare the stator field orienta-

tion and rotor field orientation. All controllers are PI controllers. The switching frequency for the rotor side is 10 kHz and 2 kHz for the stator side. Due to the limits imposed by the dSPACE 1103, two interruption levels are used. The sampling period of the first interruption is fixed at 50 μs to manage securities, send modulation references to PWM circuits and calculate the phase references θ_{sd_ref} and θ_{rd_ref} from the frequency references ω_{sd_ref} and ω_{rd_ref}. The second interruption is focused on the inversion-based control and its sampling period is fixed at 500 μs. Many tests have been done to check this control in the real-time environment. In this part, some of them are presented. Other experimental results can be found in Appendix 2.

A. Trapezoidal speed reference

Figure 2.18 shows the results when the stator field orientation is chosen (case 1). Figure 2.19 shows the results when the rotor field orientation is chosen (case 2). In both cases, k_1 is fixed at 1.

In case 1, k_2 is used to determine the stator field orientation. Φ_{sd_ref} is set at its rated value (1.8 Wb) upto and including the base speed (500 rpm), and is weakened beyond the base speed. Φ_{sq_ref} is set at zero. k_3 is calculated on line using (2.54).

In case 2, k_2 is used to determine the rotor field orientation. Φ_{rd_ref} is set at its rated value (1.8 Wb) upto and including the base speed, and is weakened beyond the base speed. Φ_{rq_ref} is set at zero. k_3 is calculated on line using (2.55).

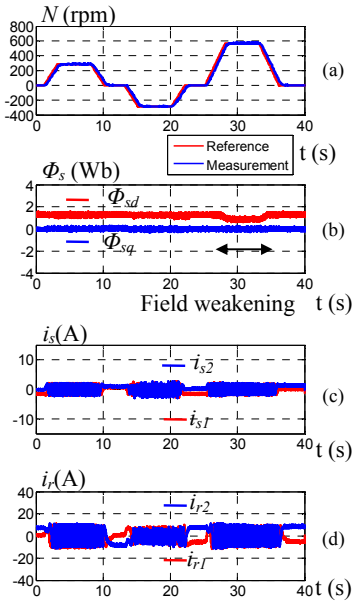

Figure 2.18 Experimental results of the stator field oriented control with trapezoidal speed reference (case 1)

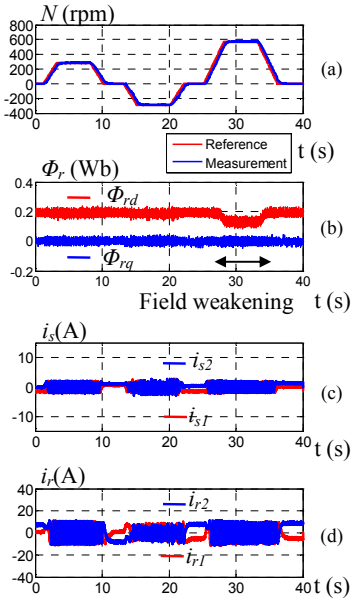

Figure 2.19 Experimental results of the rotor field oriented control with trapezoidal speed reference (case 2)

(a) Machine speed (b) Estimated flux in the d-q axis (c) Stator currents (d) Rotor currents

Under the same trapezoidal speed reference, the speed measurements closely follow

the reference in both cases (Figure 2.18.a and Figure 2.19.a). In case 1, Φ_{sd} and Φ_{sq} are estimated using (2.9), and show that the stator field orientation is achieved. In case 2,Φ_{rd} and Φ_{rq} are estimated using (2.9), and show that the rotor field orientation is achieved. The current measurements in the stator field oriented control (Figure 2.18, c and d) are the same as those in the rotor field oriented control (Figure 2.19, c and d). Since the load torque is positive in this test, the motor and generator operations are validated.

B. Constant speed reference when k_1 is varied

A constant speed is maintained, as shown in Figure 2.20 (a). k_1 is varied, as shown in Figure 2.20 (b). The estimated active power ratio p_s/p_r, which varies according to the value of k_1, evolves in the same way in both the stator field oriented control and rotor field oriented control (2.43). If the currents are zoomed, it can be seen that the stator current frequency is k_1 times that of the rotor current frequency: for example, the stator frequency is half that of the rotor when k_1=0.5 (Figure 2.20. c and d); the stator frequency is three times that of the rotor when k_1=3 (Figure 2.20. e and f).

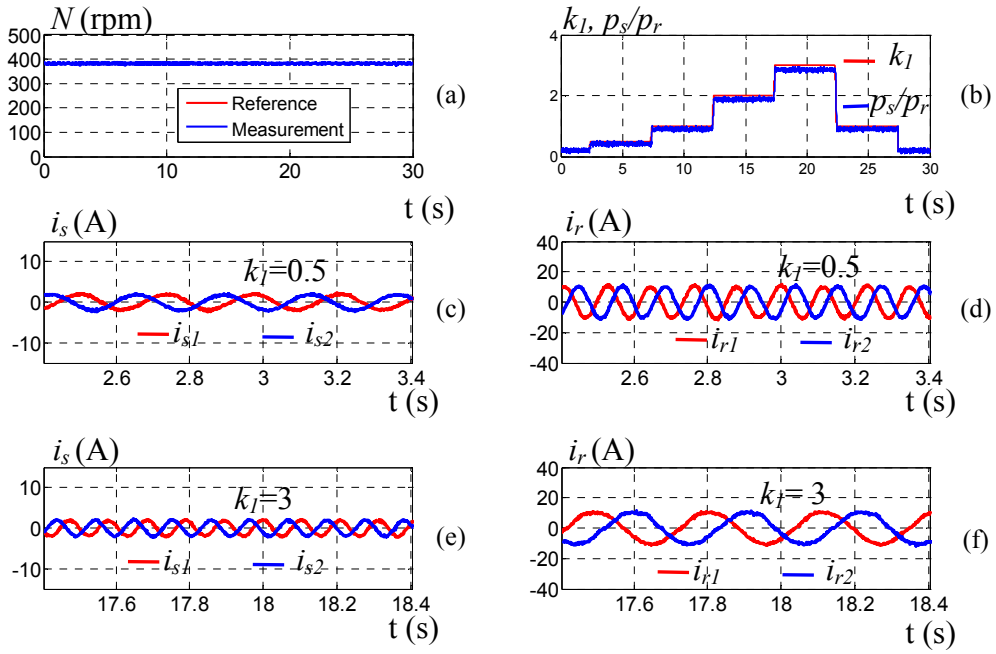

Figure 2.20 Experimental results of constant speed with variable k1 (experimental results)
(a) Machine speed (b) k1 and ps/pr
(a) Stator current measurement when k1=0.5 (d) Rotor current measurement when k1=0.5
(e) Stator current measurement when k1=3 (f) Rotor current measurement when k1=3

C. Validation of the minimum copper-loss strategy

Finally, to validate the minimum copper-loss strategy, two tests are carried out. In the first test, different values of k_3, which vary in steps of 0.2, are set, as shown in Table 2. After the

transient state, the copper losses are estimated using the measured current for a constant load torque of 1.7 Nm. It can be noted that $k_3 = -1$ yields the minimum copper losses of 22.1 W. In the second test, k_3 is calculated on line using (2.54) under the stator field orientation condition. The estimated copper losses are 22 W, which is close to the minimum copper losses in the first test. This means that the on-line calculation yield the minimization of the copper losses. Other operating tests can be found in Appendix 2.

Table 2.4 Experimental copper losses versus k_3 (N=500 rpm, T_l=1.7 Nm)

First test	k3	0	-0.2	-0.4	-0.6	-0.8	-1	-1.2	-1.4
	Ploss(W)	47.1	35.3	29.2	25.3	23.5	22.1	25.3	30.2
Second test	k3	On-line calculation using (2.54)							
	Ploss(W)	22.0							

II.3.1.6. Conclusion

In this subsection, the control structure has been deduced from the EMR of DIF-WRIMs. The use of a supplementary converter of DIF-WRIMs yields new degrees of freedom for the energy management. This control scheme highlights the degrees of freedom and indicates where they can be used. This methodology offers a different way to visualize the system. Hence the method illustrates and details how the degrees of freedom can be fully used.

This control achieves an important objective (rotation speed or desired torque). Three degrees of freedom are thus available. Keeping the same control scheme deduced from the EMR, different control possibilities are discussed. The first degree of freedom is used for the power distribution between the stator side and rotor side, as in [Vidal 2007]. The second is used to manage the flux: either stator field orientation or rotor field orientation can be used. The last one is used to implement the minimum copper-loss strategy depending on the chosen field orientation. Experimental results show that both the stator and rotor field oriented control have been achieved. Other tests could be conducted to study the differences between both controls, especially in terms of robustness [Drid 2007]. Other strategies could be developed by acting on these 3 degrees of freedom. The control scheme would be the same, only the strategy blocks would have to be changed.

II.3.2. Control scheme of PMSMs

Since the EMR of PMSMs (see Figure 2.10) can be considered as a reduced description of the generic EMR of DIF-WRIMs (see Figure 2.7), the inversion-based control structure of PMSMs (Figure 2.21) can be very similar to the DIF-WRIM control structure (see Figure 2.13).

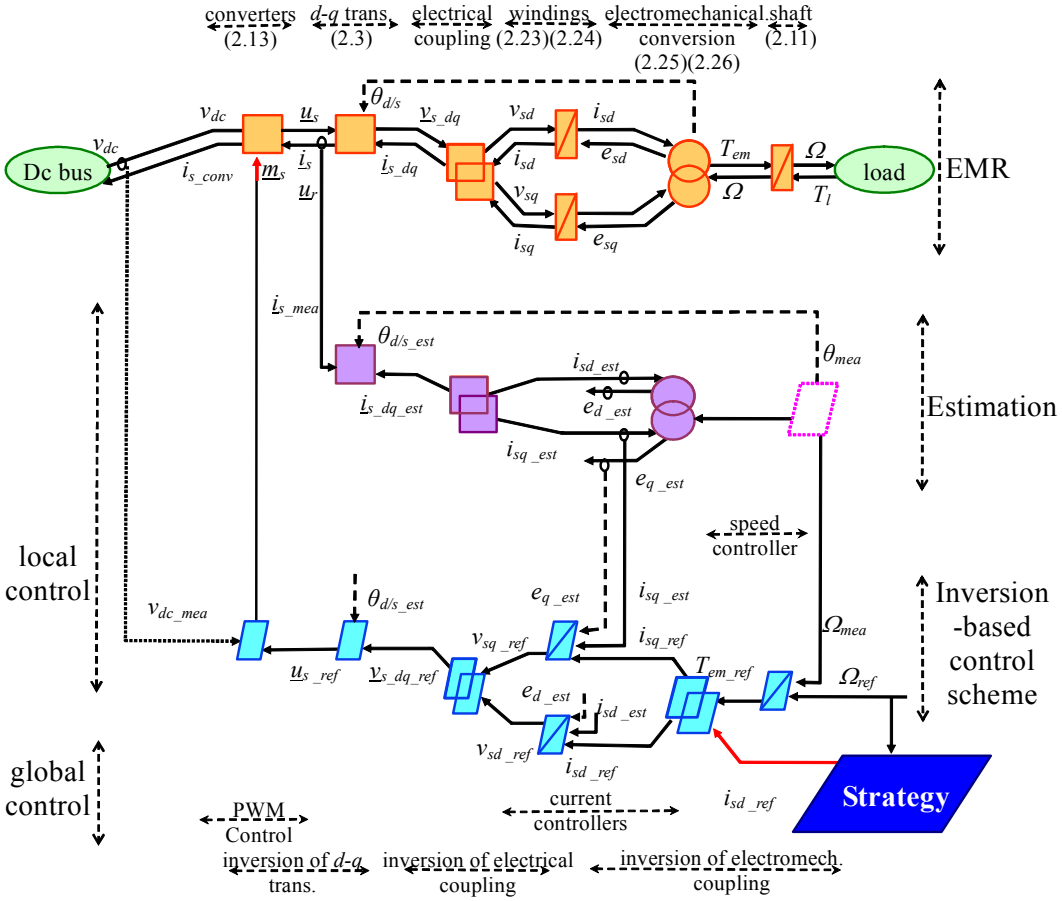

Figure 2.21 Control scheme of PMSM systems

The differences are:

1. Since only one converter (converter 1) is used, there is no PWM control block of converter 2.

2. There is no inversion of the *d-q* transformation for the rotor windings, as the rotor is made up of permanent magnets.

3. The current controllers are one-dimensional controllers. The current controllers can be written as:

$$v_{sd\_ref} = C_c(t)[i_{sd\_ref} - i_{sd\_mea}] + e_{d\_est} \tag{2.56}$$

$$v_{sq\_ref} = C_c(t)[i_{sq\_ref} - i_{sq\_mea}] + e_{q\_est} \tag{2.57}$$

where $C_c(t)$ is the current controller which may be a PI type or another type. The $C_c(t)$ parameters can be calculated from L_{sd}, L_{sq} and R_s. Using (2.25), e_{d_est} and e_{q_est} can be compensated.

4. The rotor position $\theta_{d/s}$ can be measured or be estimated as in [Boussak 2005]. Then Ω_{mea} can be obtained from the rotor position, which is measured or estimated.

5. The inversion of the electromagnetic coupling requires only one supplementary input. For the chosen tuning paths, there are two inputs and one output. To invert the electromagnetic coupling, only one supplementary input is necessary. From (2.26), one possibility is to consider the reference i_{sd_ref} as this supplementary input. It is defined at the strategy level (see II.3.2.1). The q-axis current reference i_{sq_ref} thus can be obtained when the torque reference T_{em_ref} and d-axis current reference i_{sd_ref} are known.

6. A different strategy is used to determine this supplementary input for the inversion of the electromechanical coupling (see II.3.2.1).

II.3.2.1. Strategies for PMSMs considering field weakening

At the strategy level, the supplementary input for the inversion of the electromechanical coupling i_{sd_ref} is defined. For a non-salient pole PMSM, the stator d-axis inductance L_d and q-axis inductance L_q are identical. For a salient pole PMSM,

$$L_d \neq L_q \tag{2.58}$$

In this thesis, only a salient pole PMSM is discussed. The non-salient pole PMSM strategy can be established in the same way. When no field weakening is required (when PMSM runs slower than its base speed), i_{sd_ref} is set to zero to minimize copper losses; When field weakening is required, i_{sd_ref} is negative, in the accordance with the system limitations.

There are two limitations related to field weakening. The first limitation is the voltage limitation. When field weakening is required, the term ω is large enough to neglect the R term; the steady state of (2.21) with (2.22) is

$$\begin{cases} v_{sd} \approx -\omega \Phi_{sq} = -\omega L_{sq} i_{sq} \\ v_{sq} \approx \omega \Phi_{sd} = \omega (L_{sd} i_{sd} + \Phi_f) \end{cases} \tag{2.59}$$

The machine stator voltage v is then limited, as below:

$$v_s = \sqrt{v_{sd}^2 + v_{sq}^2} \leq V_{s\_\max} \tag{2.60}$$

The maximum voltage V_{s_max} which is limited by the DC bus voltage v_{dc} and the PWM strategy, can be written as:

$$V_{s\_\max} = R_{PWM} v_{dc} \tag{2.61}$$

The coefficient R_{PWM} depends on the PWM strategy. (2.59) and (2.60) show that PMSM can not operate at higher speeds with its rated flux because of this voltage limitation. From (2.59) and (2.60),

$$\left(i_{sd}+\frac{\Phi_f}{L_{sd}}\right)^2+\left(\frac{L_{sq}}{L_{sd}}i_{sq}\right)^2\le\left(\frac{V_{s\_\max}}{\omega L_{sd}}\right)^2 \tag{2.62}$$

(2.62) expresses the ellipses in the *d-q* current plane, of which the minor radius is $V_{max}/(\omega L_{sd})$, and the center ($-\Phi_f/L_{sd}$, 0), as "the ellipses of voltage limitation" in Figure 2.22. These ellipses limit the *d-q* currents due to the voltage limitation.

The second limitation is the current limitation. The maximum current I_{s_max} is determined by the inverter current rating and machine limitation, as below:

$$i_{sd}^2+i_{sq}^2\le I_{s\_\max}^2 \tag{2.63}$$

(2.63) expresses the circle in the *d-q* current plane, of which the radius is I_{s_max}, and the center (0, 0), as "the circle of current limitation" in Figure 2.22. This circle limits the *d-q* currents due to the maximum current I_{s_max}.

From (2.62), the maximum stator electric pulsation ω_{lim} (absolute value) without field weakening (i_{sd}=0) is a function of the maximum voltage V_{s_max} and the *q*-axis current reference i_{sq_ref},

$$\omega_{\lim}=\sqrt{\frac{V_{s\_\max}^2}{(\Phi_f^2+L_{sq}^2 i_{sq\_ref}^2)}} \tag{2.64}$$

$$\text{with}\quad \sqrt{\frac{V_{s\_\max}^2}{(\Phi_f^2+L_{sq}^2 I_{s\_\max}^2)}}\le\omega_{\lim}<\frac{V_{s\_\max}}{\Phi_f} \tag{2.65}$$

When the machine reaches ω_{lim}, the field-weakening is achieved through a negative *d*-axis current reference i_{sd_ref}. Since the field is reduced, the machine can thus reach higher speeds than ω_{lim}. The *d*-axis current i_{sd} is in the range as:

$$-\frac{\Phi_f}{Lsd}\le i_{sd}\le 0 \tag{2.66}$$

because the flux of *d*-axis is increased again after the center ($-\Phi_f/L_d$, 0).

Figure 2.22 shows that the minor radius of the voltage limitation ellipses decreases as the speed increases. When field weakening is not necessary, the i_{sd} is equal to zero, however i_{sq} is proportional to the torque. The points of i_{sd} and i_{sq} are located on the *q*-axis. When field weakening is required, the points of i_{sd} and i_{sq} are located on the voltage limitation ellipses. The higher the EM speed, the smaller the ellipse.

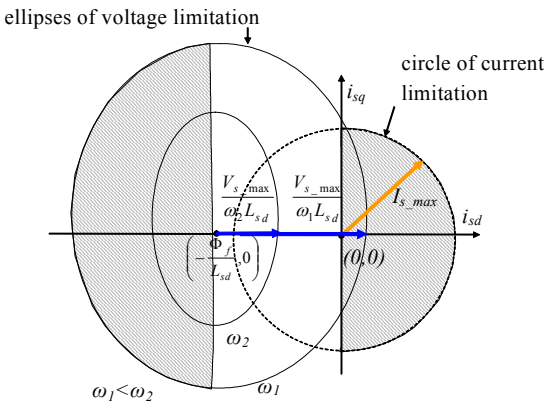

Figure 2.22 Limitation ellipses and circles for the d-q currents of salient-pole PMSMs

Different field-weakening methods for salient-pole PMSMs have been used [Kim 1997] [Schaible 1999] [Zordan 2000]. In this thesis, one field-weakening method, which takes into account the minimum copper losses, is used. Similar to non-salient pole PMSMs, i_{sd}=0 can be used when field-weakening is not necessary. From (2.64) and (2.26), the maximum stator electric pulsation ω_{lim} is a function of the maximum voltage V_{s_max}, the torque reference T_{em_ref} and q-axis current reference i_{sq_ref},

$$\omega_{\lim} = \sqrt{\frac{V_{s\_\max}^2}{(\Phi_f^2 + L_{sq}^2\left(\frac{T_{em\_ref}}{p[\Phi_f + (L_{sd} - L_{sq})i_{sd\_ref}]}\right)^2)}} \tag{2.67}$$

When ω reaches ω_{lim}, the d axis current reference i_{sd_ref} becomes negative to reduce the field. From (2.26),

$$i_{sd} = \frac{1}{(L_{sd} - L_{sq})}(\frac{T_{em}}{pi_{sq}} - \Phi_f) \tag{2.68}$$

The square of the stator current is then

$$i_s{}^2 = i_{sd}^2 + i_{sq}^2 = \left(\frac{1}{(L_{sd} - L_{sq})}(\frac{T_{em}}{pi_{sq}} - \Phi_f)\right)^2 + i_{sq}^2 \tag{2.69}$$

In order to achieve the minimum copper losses [Vaclavek 2008],

$$\frac{\partial i_s{}^2}{\partial i_{sq}} = 0 \tag{2.70}$$

For salient-pole PMSMs at the strategy level, the d-axis current reference i_{sd_ref} is

$$\begin{cases} \text{If } |\omega| < \omega_x, i_{sd\_ref} = \mathbf{0}; \\ \text{If } |\omega| \geq \omega_x, i_{sd\_ref} = f_{fieldw}(\Omega_{ref}) \end{cases} \tag{2.71}$$

with

$$f_{fieldw}(\Omega_{ref}) = \frac{-\left(2L_{sd}\Phi_f + \frac{\Phi_f L_{sq}^2}{(L_{sd}-L_{sq})}\right) + \sqrt{\left(2L_{sd}\Phi_f + \frac{\Phi_f L_{sq}^2}{(L_{sd}-L_{sq})}\right)^2 + 4(L_{sd}^2+L_{sq}^2)\left(-\Phi_f^2 + \left(\frac{V_{s\_\max}}{p\Omega_{ref}}\right)^2\right)}}{2(L_{sd}^2+L_{sq}^2)} \quad (2.72)$$

The calculation is detailed in Appendix 3.

Therefore, the inversion of the electromechanical coupling (Figure 2.23) uses the equation:

$$i_{sq\_ref} = \frac{T_{em\_ref}}{p[\Phi_f + (L_{sd} - L_{sq})i_{sd\_ref}]} \quad (2.73)$$

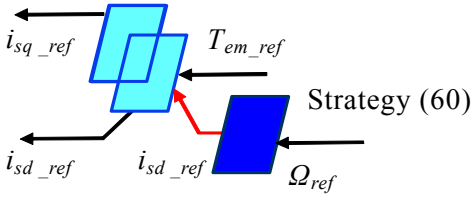

Figure 2.23 Inversion of the electromechanical coupling of PMSM systems

Using several different speed cycles and load profiles, Figure 2.24 shows the *d-q* axis currents in the *d-q* plane during simulation. When field weakening is not necessary, i_{sd} is equal to zero, however i_{sq} is proportional to the torque. These points form a straight line in the *d-q* plane. When field weakening is required, i_{sd} and i_{sq} move to the voltage limitation ellipses. The higher the EM speed required, the smaller the minor radius of the voltage limitation ellipses.

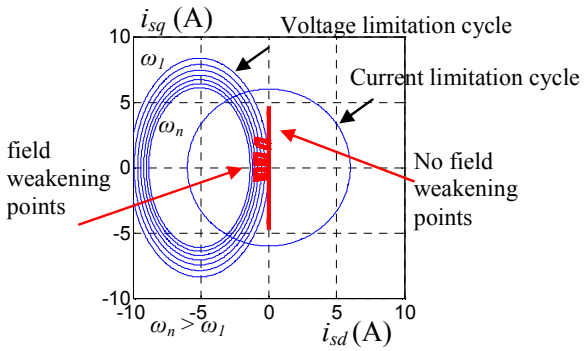

Figure 2.24 Stator currents of the Interior PMSM in the d-q current plane

II.3.2.2. Experimental results

The simulation was firstly carried out. The experimentation was subsequently conducted through a dSPACE 1103 controller board to check the control in a real-time environment. In this part, only the experimentation results are presented.

The experimental set-up (Figure 2.25) is composed of one 1.5 kW salient-pole synchronous machine (Table 1.1) and one induction machine. This salient-pole synchronous ma-

chine is not a permanent magnet synchronous machine. The rotor is excited uing a DC circuit to replace the permanent magnet. The stator of this salient-pole synchronous machine is fed by a 3-leg IGBT inverter (VSI). A DC bus of 300 V supplies this inverter. The stator of the induction machine is fed by another 3-leg IGBT inverter (VSI_im). Another DC bus supplies this inverter. The induction machine has the same shaft as the synchronous machine which simulates a mechanical load. This induction machine is controlled in order to impose different load torques on the tested drive. The control scheme is directly transferred to Matlab-Simulink^{TM} (Figure 2.26). This control runs through a dSPACE 1103 controller board. All controllers are PI controllers. The switching frequency is 1.2 kHz. The sampling period of the first interruption is fixed at 50µs to manage securities, send modulation references to PWM circuits, and measure the rotor electrical position angle $\theta_{d/s}$. The second interruption is focused on the inversion-based control and its sampling period is fixed at 500µs.

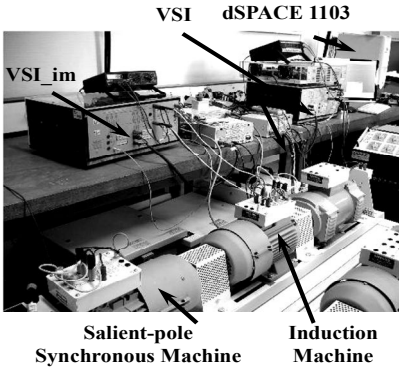

Figure 2.25 Experimental set-up of the salient-pole Synchronous Machine

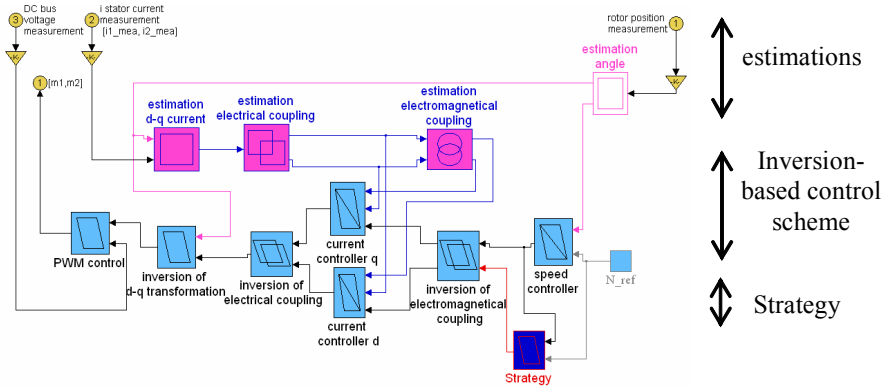

Figure 2.26 Control of the salient-pole synchronous machine

Table 2.5 SM specifications

Number of pole pairs	2	Stator q axis inductance (H)	0.22
Stator resistance per phase (Ω)	4.65	Moment of inertia (kg.m2)	4.32e-2
permanent magnet flux linkage	1.84	Friction coefficient (Nms)	5.35e-3
Stator d axis inductance (H)	0.36	Nominal power (W)	1500

A. Four quadrant validation

The machine speed reference is given as shown in Figure 2.27. (a). The load torque is given through the induction machine, as shown in Figure 2.27 (b). The measurement of the machine speed closely follows the reference (Figure 2.27. a). When the machine runs beyond its base speed (absolute value: about 800 rpm), the *d*-axis flux is weakened using i_{sd} negative to make the machine operate at higher speeds. The estimated value of Φ_{sd} using (2.22) is shown in Figure 2.27 (c). The *q*-axis flux is proportional to the i_{sq} which depends on the machine torque. The estimated value of Φ_{sq} using (2.22) is shown in Figure 2.27(d). These results show that this control can run in the real-time environment in the four quadrants. In Appendix 4, the simulation results, which are close to the experimental ones, can be found. Other experimental results can be found in Appendix 4.

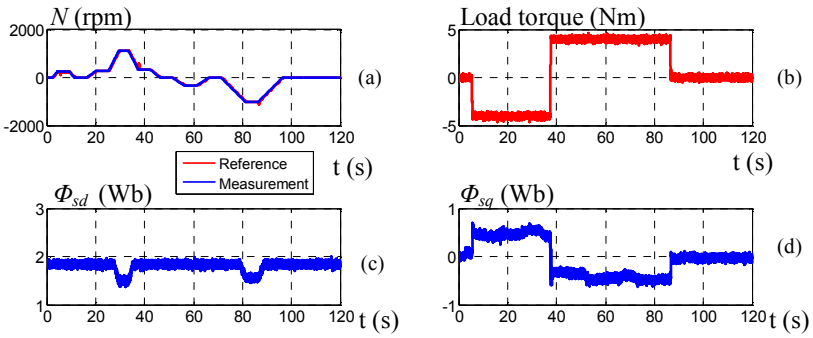

Figure 2.27 Experimental results of the salient pole SM

(a) Measurement and reference of the speed (b) Load torque (c) Estimated Φsd (d) Estimated Φsq

B. Validation of field-weakening taking into account the minimum copper losses

In this thesis, (2.72) and (2.71) are used to ensure the field-weakening in such a way that the copper losses are taken into account. In order to check this strategy, the stator copper losses are compared using three field weakening methods in steady state. P_u is the measurement output power.

Method 1: the *d*-axis current reference i_{sd_ref} can be calculated on line using (2.72) and (2.71).

Method 2: a table is generated from (2.72) and (2.71) off line. When the control program runs on line, i_{sd_ref} will be found in this table according to the machine speed.

Method 3: a simplified equation is obtained from (2.72) and (2.71) because the values of other terms are relatively weak in this case, as below:

$$\begin{cases} \text{If } |\omega| < \omega_{\lim}, i_{sd\_ref} = \mathbf{0}; \\ \text{If } |\omega| \geq \omega_{\lim}, i_{sd\_ref} = \dfrac{-\left(\mathbf{2}L_{sd}\Phi_f + \dfrac{\Phi_f L_{sq}^2}{(L_{sd} - L_{sq})}\right) + \sqrt{\mathbf{4}(L_{sd}^2 + L_{sq}^2)\left(\dfrac{V_{s\_\max}}{p\Omega_{ref}}\right)^2}}{\mathbf{2}(L_{sd}^2 + L_{sq}^2)} \end{cases} \quad (2.74)$$

Table 2.6 shows the stator copper losses using different field-weakening methods. In case 1 and case 2, the same copper losses are achieved, because when the synchronous machine runs at 500 rpm or 600 rpm, no field weakening is required (i_{sd} = 0). The same stator copper losses are obtained using method 1 and method 2. In fact, the same equation is used. When the table is used, different values can be obtained if the table precision is not adequate. When field weakening is required, a significant difference can be found between method 1 and method 3.

Table 2.6 Comparison of stator copper losses using different field weakening methods

	Stator copper losses (W)					
	Case 1: N=500 rpm Tl=-6Nm	Case 2: N =600 rpm Tl=-8Nm	Case 3: N =900 rpm Tl=-6Nm	Case 4: N =900 rpm Tl=-8 Nm	Case 5: N =1000 rpm Tl=-6Nm	Case 6: N =1000 rpm Tl=-8Nm
Method 1	14.5 W	25 W	18.50 W	29W	21 W	33.5 W
Method 2	14.5 W	25 W	19 W	29.5W	21 W	34 W
Method 3	14.5 W	25W	35 W	49 W	43 W	61 W

II.3.2.3. Conclusion

In this subsection, the control scheme of PMSMs has been obtained from the control structure of DIF-WRIMs. For salient-pole PMSMs, a strategy of field weakening minimizing copper losses has been proposed. To check this control design and the strategy, experimental verifications have been carried out. The experimental results show this salient pole synchronous machine can run in four quadrants with field weakening. A comparison of the stator copper losses using different field weakening methods shows that this strategy minimizes the copper losses. Since real PMSMs are not available for experimentation, a salient-pole synchronous machine, where the rotor is excited by a DC circuit, was used to verify the control. Issues related to demagnetization using the above field weakening could be studied in future research. Other control methods using other converter, for example, DTC using Matrix Converter [Ortega 2010], could be studied.

Conclusion

This chapter deals with the modeling and control design of electric drives in a general way using EMR. The EMR of DIF-WRIMs is considered as a generic EMR. From this generic EMR, other EMRs for various basic electric drives can be deduced by modifying certain elements, such as DCMs, standard IMs, standard DFIMs, and PMSMs. The energy property and degrees of freedom for the energy management of these electric drives are therefore emphasized. EMR illustrates and details how the degrees of freedom can be fully used.

By inverting these EMRs, the control schemes can be deduced. The inversion-based control schemes for DIF-WRIMs and PMSMs have been presented separately. Both of them are validated by experimentation in real-time. Their proposed strategies have been also discussed.

In the future, more complex models could be used to estimate different losses. Saturation or nonlinearity could be taken into account. From the inversion-based control, the controller synthesis and robustness could be studied.

In the next chapter, this general approach will be used to establish the modeling and control structure of whole HEV systems. Different HEVs are studied in a general way in order to propose a common EMR and a unified control scheme.

Chapter III

Common EMR and unified control scheme of different HEVs

Introduction

One of the key issues related to HEVs is the control design of such complex systems, which are composed of multi-sources and multi-subsystems. Many studies have been done on different HEVs, but generally, different HEVs are studied separately [Lhomme 2007]. For example, in [Barsali 2004] [He 2006] [Yoo 2008], various series HEVs have been studied. In [Delprat 2004] [Sciarretta 2004] [Won 2005], different controls of parallel HEVs have been introduced. In [Liu 2008] [Syed 2009] [Vinot 2008], the modeling and control of series-parallel HEVs have been established. In [Ceraolo 2008], the possibility to obtain the control design of different HEVs in a general way has been discussed, despite the fact that HEVs can be very different from each other in terms of structure.

The objective of this chapter is to achieve a unified control structure for different HEVs. The general approach used in chapter II for electric drives can be used in this chapter for the whole system study. This unified control has two levels: first, a local level that deals with each subsystem, second, a strategy level, which is generally called the global energy management of the whole system. Many studies about global energy management have been carried out [Jong-Seob 2005] [Pisu 2007] [Salmasi 2007] [Kessels 2008], generally under the assumption that each subsystem is already well controlled. However, a subsystem has to take into account the interactions with other subsystems. Furthermore, the global energy management and the local control should be mutually considered. To obtain this unified control structure, EMR and its inversion-based control are used. A common EMR is firstly established. This EMR may offer a better understanding of the main power flows of different HEVs. Using the general approach, the time required for the control design of such complex systems can be significantly reduced. Then, the different HEVs can be compared more easily: the common points are revealed, and differences are highlighted.

In the first section of this chapter, the common points of various HEVs are discussed. In the second section, EMR is used to organize the models of some HEVs. Due to the common points of various HEVs in terms of energy flow, the same EMR is used to describe these HEVs. Setting different values for certain parameters, this common EMR can be used to represent series, parallel or series-parallel HEVs. In the third part, a unified control scheme is deduced from this common EMR. This unified control scheme can be applied to different HEV architectures. This is one way to develop HEV control schemes. It must however be compared to other classic methods.

III.1. Architectures and power flows of HEVs

This section discusses the common points of different HEVs from two viewpoints: architectures, and power flows. Part one is dedicated to the different architectures. Part two deals with the main power flows. From these two aspects, the possibility of establishing a common representation for different HEVs is then explored.

III.1.1. Different architectures

A HEV combines two power sources: one unidirectional based on fuel tanks and ICEs (gasoline or diesel fueled), the other bidirectional based on electric Energy Storage Systems (ESSs), Electric Machines (EMs), and Power Electronics (PEs) [Ehsani 2010]. ESSs can be batteries (BAT) or batteries combined with supercapacitors, and their relevant converters. Transmissions (Trans.) can be discrete gearboxes with clutches, Continuously Variable Transmissions (CVTs) or fixed reduction gears.

1. Series-parallel HEVs

In series-parallel HEVs, power-split devices allow power to be exchanged between the two power sources and the wheels. These power-split devices can be either mechanical (e.g. planetary gears [Miller 2006] [Ehsani 2007]), or mechanical and electromechanical (e.g. two concentric arranged EMs, or EMs with two rotors [Hoeijmakers 2006] [Chau 2007] [Zheng 2007]). The most popular type of series-parallel HEVs (Toyota Prius type) uses a planetary gear as its power split device, as shown in Figure 3.1. The planetary gear is composed of the ring gear (R), the carrier gear (C) and the sun gear (S). This planetary gear is the mechanical coupling, while the DC bus is the electrical coupling. The energy node can be found both in the mechanical coupling and in the electrical coupling. The transmission (Trans.) is a fixed reduction gear. This kind of HEV can be considered to be composed of all the basic components, from which other architectures can be derived by removing some components and couplings. For this reason, these classic architectures are drawn in a specific way [Chen 2009-a].

2. Series HEVs

In series HEVs (Figure 3.2), there is no mechanical connection between EM1 and the other machines. All traction power is converted from electricity and supplied through EM1. The energy node is in the DC bus. The mechanical energy node in series-parallel HEVs is removed. The mechanical coupling between EM2 and the ICE can be a belt, a mechanical gear or a common shaft. The transmission (Trans.) is a fixed reduction gear.

3. Parallel HEVs

In parallel HEVs (Figure 3.3), there is no EM1-based drivetrain. The energy node is located in the mechanical coupling between EM2 and the ICE. The transmission (Trans.) can be a discrete gearbox with a clutch or CVT. Between the ICE and the transmission, a cut-out clutch is usually used to uncouple the ICE from the transmission shaft. 4WD parallel HEVs (or parallel through-the-road) [Pusca 2004] [Letrouve 2009] are not presented here.

4. Other vehicles

Other vehicles can also be derived, by deleting some components or couplings [Chen 2009-a] . A BEV results when only the EM1 drivetrain remains (Figure 3.4). An ICE vehicle is obtained when only the ICE drivetrain remains (Figure 3.5).

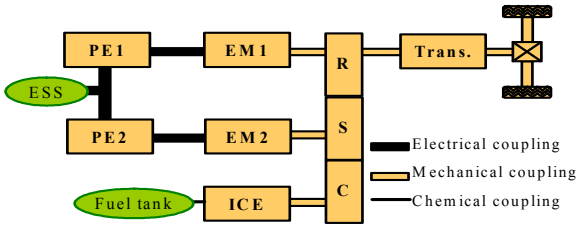

Figure 3.1 Series-parallel HEV using a planetary gear unit

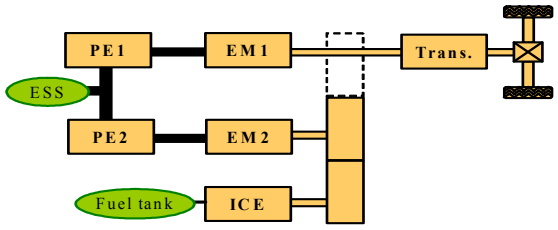

Figure 3.2 Series HEV

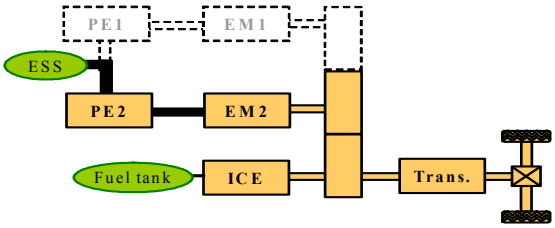

Figure 3.3 Parallel HEV

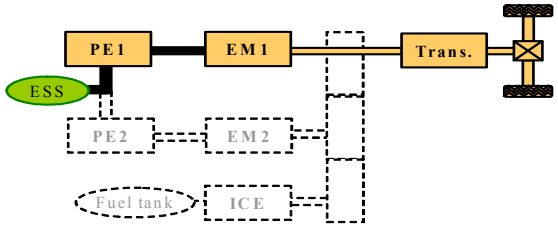

Figure 3.4 BEV

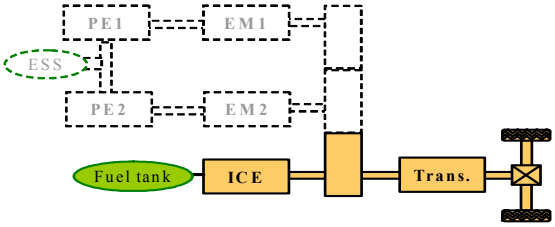

Figure 3.5 ICE vehicle

III.1.2. Power flows

Several basic power flows between the two power sources (ESS and Fuel tank) and the traction load (Traction Load) for these typical HEVs are considered in Figure 3.6 [Ehsani 2007]. The main criteria needed to evaluate a HEV is the energy in the ESS (e.g. State Of Charge (SOC)) and the fuel consumption under the given driving cycle, namely under the given traction load. The power flows with regard to the mechanical braking and the auxiliaries are not discussed in this chapter. Furthermore, the auxiliary powers are normally very low compared to the propulsion power. Figure 3.6 shows 4 basic power flows:

1, Pure electric traction: the traction power is only delivered by the ESS. The engine is turned off.

2, Regenerative braking: the ESS is charged only by the braking energy. There is no fuel injection for the ICE.

3, Pure engine traction: the traction power is only delivered by the ICE. The ESS neither supplies nor draws any power from the driven wheels.

4, ESS charging only by the ICE: the ESS is charged only by the ICE. No power is recovered from the traction.

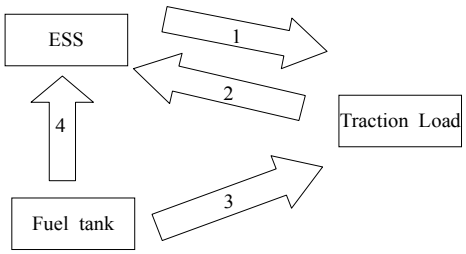

Figure 3.6 Basic power flows

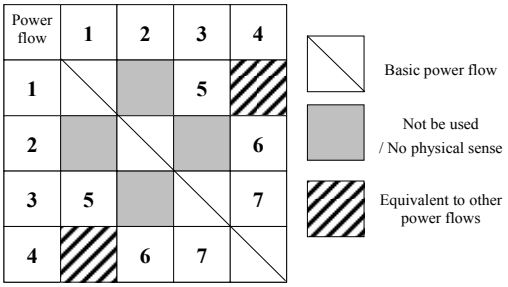

Figure 3.7 Combination power flows

There are 3 possible combinations of power flows (Figure 3.7):

5, Hybrid traction: traction power is drawn from both the fuel tank and the ESS. The energy in the ESS decreases. It is a combination of power flow 1 and power flow 3.

6, Hybrid charging: the ESS is charged both by the braking energy and the ICE. It is a combination of power flow 2 and power flow 4.

7, Engine traction and ESS charging: the ICE supplies the traction power and at the same time charges the ESS. It is a combination of power flow 3 and power flow 4.

Other combinations can be considered to be no physical sense, or to be equivalent to some of the above power flows. For example, the combination of power flow 1 and power flow 4 (Figure 3.7) is analyzed as follows. If the energy in the ESS is constant, this combination is equivalent to power flow 3, as all the traction power is indeed delivered only by the fuel tank through the ICE. If the energy in the ESS decreases, this combination can be considered to be equivalent to power flow 5 (power flow 1 + power flow 3). The traction power is delivered both from the fuel tank and the ESS. If the energy in the ESS increases, this combination is the same as power flow 7 (power flow 3 + power flow 4). This means that the ICE supplies the traction power, and the ESS is charged by the ICE at the same time. Therefore, in fact, there are only 3 combinations of power flows.

Table 3.1 Power flows of HEVs

1	ESS→Load	Pure electric traction
2	Load →ESS	Regenerative braking
3	Fuel tank→Load	Pure engine traction
4	Fuel tank → ESS	ESS charging
5	1+3	Hybrid traction
6	2+4	Hybrid charging
7	3+4	Engine traction and ESS charging

A summary of the main power flows is listed in Table 3.1. No matter how the two power sources are combined (ESS and Fuel tank), different HEVs generally have these main power flows. But not all architectures have all of these power flows. For example, a micro-parallel HEV has no power flow 1.

III.1.3. Modeling and control design of HEVs using EMR

Using different approaches [Gao 2007], modeling for different HEVs has been studied [Wipke 1999] [Mierlo 2004] [Onoda 2004] [Syed 2006] [Bogosyan 2007]. Generally, considering the different combinations of components, each architecture has its own modeling. EMR has also been applied to the modeling of different HEVs: series HEVs [Lhomme 2004] [Boulon 2009-a] [Boulon 2009-b], micro parallel HEVs [Bruyere 2008] [Bruyere 2009-a], parallel HEVs with clutches [Lhomme 2007], series-parallel HEVs [Lhomme 2007] [Cheng 2009-a], BEVs [Bouscayrol 2006-b] [Chen 2007], ICE vehicles [Lhomme 2010], and other vehicles [Lhomme 2008-b] [Letrouve 2009]. Different combinations of the two power sources of HEVs lead to different architectures. EMR highlights these energy couplings.

Since HEVs have the same main power flows, a single common representation for different architectures is possible. Based on these previous works, one common EMR can be used to describe various vehicles [Chen 2009-a]. In [Rizzoni 1999], a unified modeling approache has been introduced for HEV drivetrains. The authors have been proposed a framework for the generic classification of HEV components. However, no unique model for diiferent HEV architectures has been proposed. Based on our common EMR, one simulation program has been established for different HEV architectures.

Using the specific inversion rules, a unified control structure for different HEVs has been established [Chen 2009-b]. In this way, the control design of such complex systems can be achieved in a general way. This reduces the time required for the control design. .

III.2. Common EMR of different HEVs

The purpose of this part is to develop a common EMR which can represent various typical HEVs. Since this thesis focuses on power flows (or the global energy), lateral motions, curve roads and slip phenomena are not taken into account. The modeling of series-parallel HEVs using EMR is firstly detailed, because this architecture is considered to be composed of all the basic components. The modeling of series HEVs and of parallel HEVs is then successively treated. Finally, a common EMR is proposed, which describes series, parallel and series-parallel HEVs.

III.2.1. Modeling of Series-parallel HEVs

In the most popular series-parallel HEV architecture (Toyota Prius type) (Figure 3.8), a planetary gear is used as the power-split device [Eshani 2005] [Miller 2006]. The mechanical part of EM1, the ring gear and the transmission shaft (Trans.) are connected together. The mechanical part of EM2 is connected to the sun gear.

The ICE is connected to the carrier. The ICE can be controlled to operate in its optimal region by choosing the appropriate torque and speed. The ICE torque can be directly achieved using its control. Due to the planetary gear, the ICE speed is a weighted average of the EM1 and the EM2 speeds. Since the mechanical part of EM1 is connected directly to the transmission, the EM1 speed is proportional to the vehicle velocity. At a given vehicle velocity, the EM2 speed can be controlled to adjust the ICE speed. Therefore, the ICE speed can be chosen independently of the vehicle velocity in such a way that it operates in its optimal region.

The two stators are fed separately by two Voltage Source Inverters (VSIs) which have a common DC bus. The DC bus is supplied by the ESS.

Since the speed ratio between the ICE and transmission is continuous and variable, the systems can replace the well-known CVT [Chau 2007]. This is why they are, sometimes, called Electrical Continuous Variable Transmissions (E-CVTs or EVTs). The transmission (Trans.) is thus a fixed reduction gear.

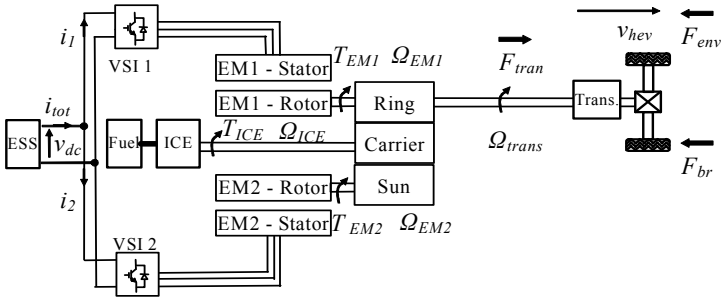

Figure 3.8 Series-parallel HEVs using a planetary gear unit

ESS – The ESS can be batteries, or batteries plus supercapacitors with their relevant PEs [Burke 2007]. This subsystem can be considered as an electrical source (Figure 3.9, green oval, ESS) which delivers a DC bus voltage v_{dc} and receives a current i_{tot} in reaction. If only the

batteries are used, the source is non controllable. If PEs are added, the source can be controllable. The second Ph. D thesis of MEGEVH-macro mainly deals with this area [Boulon 2009-a] [Boulon 2009-b]. More details about the modeling of batteries, supercapacitors and their PEs can also be found in [Chau 2007] [Lhomme 2009] [Boulon 2008] [Marie-Francoise 2006].

Parallel connection – The two PEs of the EMs (PEs, in this case, two VSIs) are connected in parallel across the DC bus (Figure 3.8). An electrical coupling element (Figure 3.9, overlapped square) is used to express the parallel connection of both inverters:

$$\begin{cases} v_{dc} \text{ common variable} \\ i_{\text{tot}} = i_1 + i_2 \end{cases} \tag{3.1}$$

with i_1 and i_2 the PEs' currents on the DC bus side.

EMs with their PEs – Each EM with its PE can be considered as a controllable electromechanical conversion (Figure 3.9, circles), which delivers the machine torque (T_{EM1}, T_{EM2}) and receives its corresponding speed (Ω_{EM1}, Ω_{EM2}) [Trigui 2004-b] [Lhomme 2007]. More details about the EMR of EMs can be found in Chapter II or in [Bouscayrol 2003] [Bouscayrol 2006-a].

ICE – This can be considered as a controllable source (Figure 3.9, green oval, ICE) which delivers the ICE torque T_{ICE} and receives its speed Ω_{ICE} [Lhomme 2007]. It can be described by means of maps [Waltermann 1996] (in particular, the consumption map) using experimental data [Kessels 2007] [Vinot 2008].

Environment – This is a mechanical source (Figure 3.9, green oval, Env.) [Ehsani 1997] [Bouscayrol 2003] which delivers the environmental resistance force F_{env} and receives the vehicle velocity v_{hev} in reaction:

$$F_{env} = F_0 + a v_{\text{hev}} + b v_{\text{hev}}^2 + Mg \sin\alpha \tag{3.2}$$

with F_0 the initial rolling force, a the rolling coefficient, b the drag coefficient, α the slope rate and g the gravity.

Mechanical brake – According to the EMR philosophy, this is generally considered as a controllable mechanical source which delivers the mechanical braking force F_{br} and receives the vehicle velocity v_{hev} [Bouscayrol 2003] [Lhomme 2007]. Since the lateral motions, curve roads and the slip phenomena are not taken into account in this thesis, the mechanical braking force which acts on the wheels is considered as an equivalent torque that acts on the transmission shaft. From this point of view, the mechanical braking part can be considered as a controllable mechanical source (Figure 3.9, green oval, Brake) which delivers the mechanical braking torque T_{br} and receives the transmission speed Ω_{tran} in reaction. The transmission speed Ω_{tran} is the speed on the planetary gear side.

Transmission to wheels – The part of HEVs from the transmission to the wheels can be represented by mechanical conversion elements (Figure 3.9, triangle). Using this equivalent one-wheel model, the environment force F_{env} acting on the wheels is converted to a resistance

torque T_{res} acting on the transmission shaft:

$$\begin{cases} T_{res} = \dfrac{R_{wh}}{k_{trans}} F_{env} \\ v_{hev} = \dfrac{R_{wh}}{k_{trans}} \Omega_{tran} \end{cases} \tag{3.3}$$

with k_{trans} the ratio of the transmission, and R_{wh} the radius of the wheels. Since the transmission is a fixed reduction gear in series-parallel HEVs, k_{trans} is fixed. Since the ratio k_{trans} may be adjustable for other transmission types, k_{trans} is represented as a tuning variable in the general case. In the case of fixed reduction gears, k_{trans} is constant. The modeling of tire-road interaction using EMR can be found in [Verhille 2007-b] [Grossi 2009].

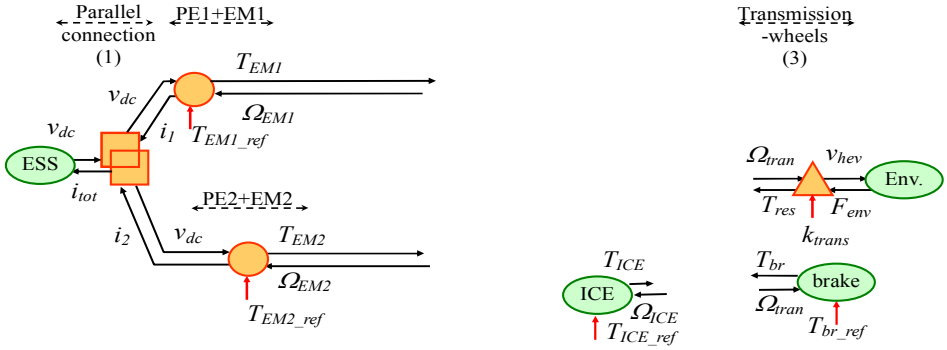

Figure 3.9 EMR of the sources and EMs in a series-parallel HEV using a planetary gear

Planetary gear – If losses are not taken into account, the power sum using the motor convention on the planetary gear (Figure 3.10) is as below:

$$T_C \Omega_{ICE} + T_R \Omega_{EM1} + T_S \Omega_{ICE} = 0 \tag{3.4}$$

with T_R, Ω_{EM1} the ring torque and speed, T_C, Ω_{ICE} the carrier torque and speed, and T_S, Ω_{EM2} the sun torque and speed. The efficiency of planetary gears is very high (more than 96%). The planetary gear is thus expressed using the Willis equation [Syed 2006] [Miller 2006]:

$$\begin{cases} \Omega_{ICE} = k_R \Omega_{EM1} + k_S \Omega_{EM2} \\ T_R = -k_R T_C \\ T_S = -k_S T_C \end{cases} \quad \text{with} \quad k_R = \frac{R_R}{2R_C}, \; k_S = \frac{R_S}{2R_C} \tag{3.5}$$

with R_R the ring radius, R_C the carrier radius, and R_S the sun radius. A mechanical coupling element can be used to describe the planetary gear (Figure 3.11, overlapped triangle).

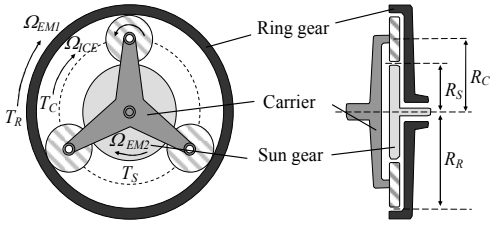

Figure 3.10 Planetary gear unit (figure from [Kessels 2007])

Shafts –The force-velocity relationship of the vehicle (Figure 3.8) is:

$$F_{tran} - (F_{env} + F_{br}) = M \frac{d}{dt} v_{hev} \tag{3.6}$$

with F_{tran} the transmission force, F_{env} the resistance force from (3.2), F_{br} the mechanical braking force and M the vehicle mass. From (3.3), using the merging rule (see chapter I), (3.6) can be expressed as:

$$T_{tran} - (T_{res} + T_{br}) = J_{eq} \frac{d}{dt} \Omega_{tran} \quad \text{with} \quad J_{eq} = M \frac{R_{wh}^2}{k_{trans}^2} \tag{3.7}$$

with T_{tran} the transmission torque, T_{res} the resistance torque from (3.3) and T_{br} the mechanical braking torque. The torque-speed relationship of the EM1 shaft (Figure 3.9) is:

$$T_{EM1} - T_R - T_{tran} = J_{EM1} \frac{d}{dt} \Omega_{EM1} + f_{EM1} \Omega_{EM1} \tag{3.8}$$

The other torque-speed relationships (Figure 3.9) are:

$$T_{EM2} - T_S = J_{EM2} \frac{d}{dt} \Omega_{EM2} + f_{EM2} \Omega_{EM2} \tag{3.9}$$

$$T_{ICE} - T_C = J_{ICE} \frac{d}{dt} \Omega_{ICE} + f_{ICE} \Omega_{ICE} \tag{3.10}$$

with J_{EM1}, J_{EM2}, J_{ICE} the moments of inertia, and f_{EM1}, f_{EM2}, f_{ICE} the viscous frictions coefficients. The four torque-speed relationships (3.7)-(3.10) can be described by accumulation elements which receive torques and yield speeds (Figure 3.11, rectangles with an oblique bar).

Figure 3.11 shows that there is an association problem among the EMR elements "Machine shafts" and "Planetary gear", because the outputs of "Machine shafts" (Ω_{EM1}, Ω_{EM2} and Ω_{ICE}) can not be connected with the input of "Planetary gear" T_C. Therefore, the merging rule is used (see chapter I). The relationship between the transmission shaft speed Ω_{tran} and other machine speeds depends on the vehicle architecture. In this architecture, the EM1 shaft is connected directly to the transmission shaft, and Ω_{tran} is equal to the EM1 speed Ω_{EM1}:

$$\Omega_{tran} = \Omega_{EM1} \tag{3.11}$$

From (3.7), (3.8) and (3.11):

$$T_{EM1} - (T_R + T_{res} + T_{br}) = (J_{EM1} + J_{eq}) \frac{d}{dt} \Omega_{EM1} + f_{EM1} \Omega_{EM1} \tag{3.12}$$

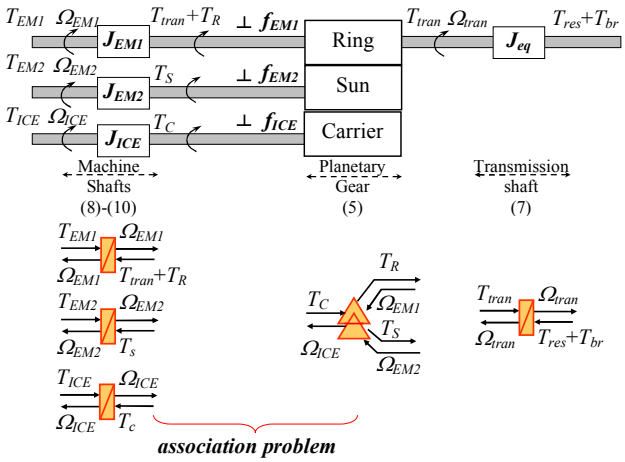

Figure 3.11 Shafts on the planetary gear set

(3.12), (3.9), and (3.10) can be written in matrix form as:

$$\begin{bmatrix} J_{EM1}+J_{eq} & 0 & 0 \\ 0 & J_{ICE} & 0 \\ 0 & 0 & J_{EM2} \end{bmatrix} \frac{d}{dt} \begin{bmatrix} \Omega_{EM1} \\ \Omega_{ICE} \\ \Omega_{EM2} \end{bmatrix} = -\begin{bmatrix} f_{EM1} & 0 & 0 \\ 0 & f_{ICE} & 0 \\ 0 & 0 & f_{EM2} \end{bmatrix} \begin{bmatrix} \Omega_{EM1} \\ \Omega_{ICE} \\ \Omega_{EM2} \end{bmatrix}$$

$$+\begin{bmatrix} 1 & -1 & -1 & -1 & 0 & 0 & 0 & 0 \\ 0 & 0 & 0 & 0 & 1 & -1 & 0 & 0 \\ 0 & 0 & 0 & 0 & 0 & 0 & 1 & -1 \end{bmatrix} \begin{bmatrix} T_{EM1} \\ T_R \\ T_{res} \\ T_{br} \\ T_{ICE} \\ T_C \\ T_{EM2} \\ T_S \end{bmatrix} \tag{3.13}$$

This matrix equation is transformed into a simplest matrix equation (see Appendix 5). Among the three speed variables, there are only 2 basic state variables [Verhille 2007-a] [Lhomme 2007]. In other words, if two of these variables (Ω_{EM1}, Ω_{EM2} and Ω_{ICE}) are known, the third one can be deduced. There are 9 possibilities [Lhomme 2007], using different basic state variable combinations. For example, one possibility is:

$$\begin{bmatrix} J_{EM1}+J_{eq}+k_R^2 J_{ICE} & k_R k_S J_{ICE} \\ k_R k_S J_{ICE} & k_S^2 J_{ICE}+J_{EM2} \end{bmatrix} \frac{d}{dt} \begin{bmatrix} \Omega_{EM1} \\ \Omega_{EM2} \end{bmatrix}$$

$$= -\begin{bmatrix} f_{EM1}+k_R^2 f_{ICE} & k_R k_S f_{ICE} \\ k_R k_S f_{ICE} & k_S^2 f_{ICE}+f_{EM2} \end{bmatrix} \begin{bmatrix} \Omega_{EM1} \\ \Omega_{EM2} \end{bmatrix} + \begin{bmatrix} T_1 \\ T_2 \end{bmatrix} - \begin{bmatrix} T_3 \\ T_4 \end{bmatrix} \tag{3.14}$$

A vectorial accumulation element describes all the torque-speed relationships in the system (Figure 3.12, rectangle with an oblique bar) using (3.14). In this case, the EM1 and EM2 speeds depend on all the torque vector inputs.

Two mechanical coupling elements are required to constitute the torque vector inputs (Figure 3.12, overlapped triangles). Mechanical coupling ① is given by:

$$\begin{cases} \begin{bmatrix} T_1 \\ T_2 \end{bmatrix} = \begin{bmatrix} 1 & -1 & 0 \\ 0 & 0 & 1 \end{bmatrix} \begin{bmatrix} T_{EM1} \\ T_{br} \\ T_{EM2} \end{bmatrix} \\ \begin{bmatrix} \Omega_{EM1} \\ \Omega_{tran} \\ \Omega_{EM2} \end{bmatrix} = \begin{bmatrix} 1 & 0 \\ 1 & 0 \\ 0 & 1 \end{bmatrix} \begin{bmatrix} \Omega_{EM1} \\ \Omega_{EM2} \end{bmatrix} \end{cases} \tag{3.15}$$

Mechanical coupling ② uses the equation:

$$\begin{cases} \begin{bmatrix} T_3 \\ T_4 \end{bmatrix} = \begin{bmatrix} 1 & -k_R \\ 0 & -k_S \end{bmatrix} \begin{bmatrix} T_{res} \\ T_{ICE} \end{bmatrix} \\ \begin{bmatrix} \Omega_{tran} \\ \Omega_{ICE} \end{bmatrix} = \begin{bmatrix} 1 & 0 \\ k_R & k_S \end{bmatrix} \begin{bmatrix} \Omega_{EM1} \\ \Omega_{EM2} \end{bmatrix} \end{cases} \tag{3.16}$$

In this way, the EMR of series-parallel HEVs using a planetary gear is established (Figure 3.12).

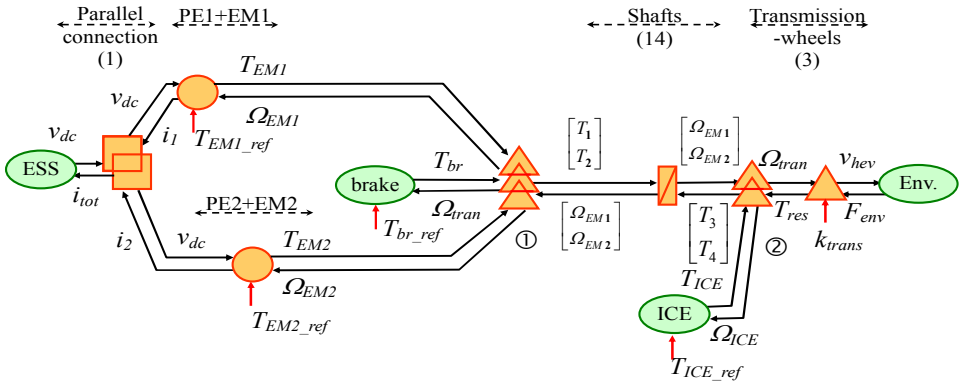

Figure 3.12 EMR of series-parallel HEVs using a planetary gear

III.2.2. Modeling of Series HEVs

Contrary to series-parallel HEVs, there is no mechanical coupling between EM1 and the ICE in series HEVs (Figure 3.13). The ICE is connected with EM2 through a mechanical coupling.

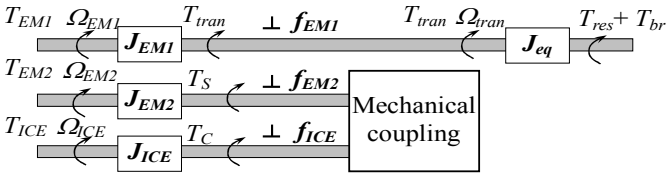

Figure 3.13 Shafts of series HEVs

If the motor convention is used, the mechanical coupling (Figure 3.13) is expressed as follows:

$$\begin{cases} \Omega_{ICE} = k_S \Omega_{EM2} \\ T_S = -k_S T_C \end{cases} \tag{3.17}$$

k_S depends on the radius of this mechanical coupling. Thus, the planetary gear equation (3.5) can be reused with k_R=0. In this way, the parameter k_R signifies the mechanical connection between EM1 and the other machines. If there is no mechanical connection between EM1 and the other machines, k_R=0; otherwise, k_S depends on the radius of the mechanical coupling which is used to connected EM1 with the other machines.

The transmission shaft is connected mechanically with EM1. The transmission speed Ω_{tran} is equal to the EM1 speed Ω_{EM1} (3.11). Using the merging rule, the two independent equations are:

$$(J_{EM1}+J_{eq})\frac{d}{dt}\Omega_{EM1} = -f_{EM1}\Omega_{EM2} + T_1 - T_3 \tag{3.18}$$

$$(k_S^2 J_{ICE} + J_{EM2})\frac{d}{dt}\Omega_{EM2} = -(k_S^2 f_{ICE} + f_{EM2})\Omega_{EM2} + T_2 - T_4 \tag{3.19}$$

with $T_1 = T_{EM1} - T_{br}$, $T_2 = T_{EM2}$, $T_3 = T_{res}$ and $T_4 = k_S T_{ICE}$

As is the case with series-parallel HEVs, (3.18) and (3.19) can be written as:

$$\begin{bmatrix} J_{EM1}+J_{eq} & 0 \\ 0 & k_S^2 J_{ICE} + J_{EM2} \end{bmatrix}\frac{d}{dt}\begin{bmatrix}\Omega_{EM1}\\ \Omega_{EM2}\end{bmatrix} = -\begin{bmatrix} f_{EM1} & 0 \\ 0 & k_S^2 f_{ICE} + f_{EM2} \end{bmatrix}\begin{bmatrix}\Omega_{EM1}\\ \Omega_{EM2}\end{bmatrix} + \begin{bmatrix}T_1\\ T_2\end{bmatrix} - \begin{bmatrix}T_3\\ T_4\end{bmatrix} \tag{3.20}$$

Thereby, the same EMR in Figure 3.12 can represent series HEVs using k_R=0. Since there is no mechanical coupling between EM1 and the other machines in series HEVs, the torque-speed vectorial matrix equation is diagonal (3.20). The equations of the mechanical couplings are the same in series HEVs and series-parallel HEVs.

III.2.3. Modeling of parallel HEVs

In parallel HEVs (Figure 3.3), there is neither the EM1-based drivetrain, nor the electrical coupling between EM1 and the other machines. The ICE and EM2 are connected through a mechanical coupling. To detach the ICE from the transmission shaft, a cut-out clutch is generally used. It can be located between the mechanical coupling and the ICE (Figure 3.14), or between the mechanical coupling and the transmission (Figure 3.15). The transmission can be a discrete gearbox or a CVT. If a discrete gearbox is chosen, two clutches are usually used (Figure 3.16). p_{cl} represents the position (in percentage) of the clutch release bearing.

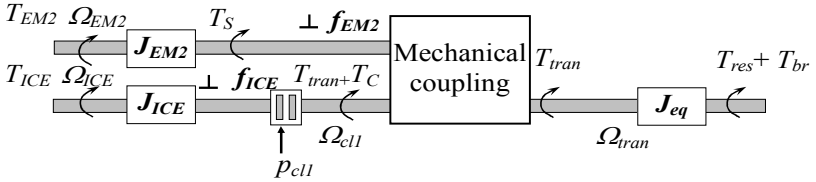

Figure 3.14 Shafts of parallel HEVs with a clutch between the ICE and the mechanical coupling

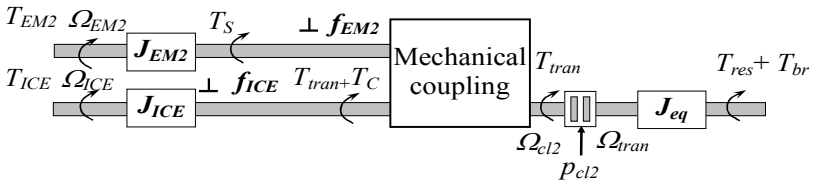

Figure 3.15 Shafts of parallel HEVs with a clutch between the mechanical coupling and the transmission

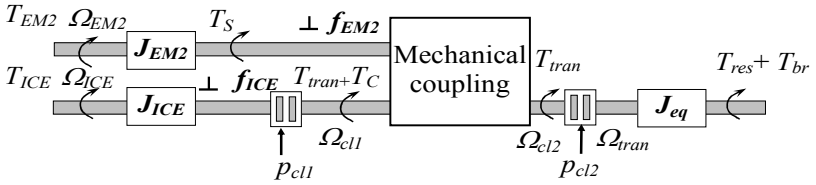

Figure 3.16 Shafts of parallel HEVs with two clutches

From these different possibilities of parallel HEVs, a common architecture can be found when all the clutches are locked (Figure 3.17). The cut-out clutch is open only when the ICE is required to be separated from the transmission shaft. For the discrete gearbox case, clutches are open only when the gear ratio is changed. 4WD parallel HEVs are not discussed here.

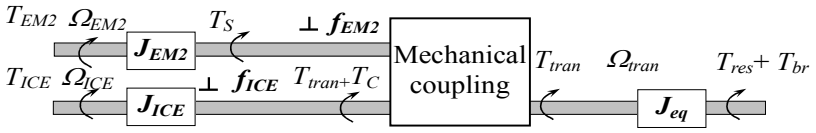

Figure 3.17 Shafts of parallel HEVs with all clutches locked

Using some simplifications, (3.3) can be used for the modeling of CVTs or discrete gearboxes with the ratio of the transmission k_{trans} which is variable. More details about the modeling of CVTs can be found in Appendix 6.

When all clutches are locked, the ICE is connected mechanically with EM2 through the mechanical coupling. Since there is no electrical coupling between EM1 and the other machines (because there is no EM1 based drivetrain), k_R=0. The planetary gear equation (3.5) can be reused with k_R=0 to represent the mechanical coupling between the ICE and EM1. The transmission shaft is connected mechanically with the ICE, and the transmission speed on the mechanical coupling side is:

$$\Omega_{tran} = \Omega_{ICE} = k_R \Omega_{EM1} + k_S \Omega_{EM2} \quad \text{with} \quad k_R = 0 \tag{3.21}$$

The torque-speed equations on the shafts of Figure 3.17 are:

$$T_{EM2} - T_S = J_{EM2} \frac{d}{dt} \Omega_{EM2} + f_{EM2} \Omega_{EM2} \tag{3.22}$$

$$T_{ICE} - (T_C + T_{tran}) = J_{ICE} \frac{d}{dt} \Omega_{ICE} + f_{ICE} \Omega_{ICE} \tag{3.23}$$

$$T_{tran} - (T_{res} + T_{br}) = J_{eq} \frac{d}{dt} \Omega_{tran} \tag{3.24}$$

Using the merging rule, (3.21)-(3.24) become:

$$(k_S^2 J_{ICE} + k_S^2 J_{eq} + J_{EM2}) \frac{d}{dt} \Omega_{EM2} = -(k_S^2 f_{ICE} + f_{EM2}) \Omega_{EM2} + T_1 - T_3 \quad (3.25)$$

with $T_1 = T_{EM2} - k_S T_{br}$ and $T_3 = -k_S T_{ICE} + k_S T_{res}$

The scalar relationship (3.25) can be also written in matrix form as:

$$\begin{bmatrix} 0 & 0 \\ 0 & k_S^2 J_{ICE} + k_S^2 J_{eq} + J_{EM2} \end{bmatrix} \frac{d}{dt} \begin{bmatrix} \Omega_{EM1} \\ \Omega_{EM2} \end{bmatrix} = -\begin{bmatrix} 0 & 0 \\ 0 & k_S^2 f_{ICE} + f_{EM2} \end{bmatrix} \begin{bmatrix} \Omega_{EM1} \\ \Omega_{EM2} \end{bmatrix} + \begin{bmatrix} T_1 \\ T_2 \end{bmatrix} - \begin{bmatrix} T_3 \\ T_4 \end{bmatrix} \quad (3.26)$$

Therefore, the EMR in Figure 3.12 can represent parallel HEVs when all clutches are locked. The differences are:

1. There is neither the EM1-based drivetrain nor the electrical coupling between EM1 and EM2;

2. k_{trans} is adjustable.

3. In the vectorial accumulation element, (3.26) is used. It represents a scalar relationship using a matrix form.

4. The equation of mechanical coupling ① is given by:

$$\begin{cases} \begin{bmatrix} T_1 \\ T_2 \end{bmatrix} = \begin{bmatrix} 0 & 0 & 0 \\ 0 & -k_S & 1 \end{bmatrix} \begin{bmatrix} T_{EM1} \\ T_{br} \\ T_{EM2} \end{bmatrix} \\ \begin{bmatrix} \Omega_{EM1} \\ \Omega_{tran} \\ \Omega_{EM2} \end{bmatrix} = \begin{bmatrix} 1 & 0 \\ 0 & 1 \\ 0 & 1 \end{bmatrix} \begin{bmatrix} \Omega_{EM1} \\ \Omega_{EM2} \end{bmatrix} \end{cases} \quad (3.27)$$

5. The equation of mechanical coupling ② is given by :

$$\begin{cases} \begin{bmatrix} T_3 \\ T_4 \end{bmatrix} = \begin{bmatrix} 0 & 0 \\ 1 & -k_S \end{bmatrix} \begin{bmatrix} T_{res} \\ T_{ICE} \end{bmatrix} \\ \begin{bmatrix} \Omega_{tran} \\ \Omega_{ICE} \end{bmatrix} = \begin{bmatrix} k_R & k_S \\ k_R & k_S \end{bmatrix} \begin{bmatrix} \Omega_{EM1} \\ \Omega_{EM2} \end{bmatrix} \end{cases} \quad \text{with} \quad k_R = 0 \quad (3.28)$$

When one clutch is open or slipping, more state variables should be considered, because, for example, the clutch speed on the mechanical coupling side Ω_{cl1} is no longer equal to the speed on the ICE side Ω_{ICE}, as shown in Figure 3.15. From the EMR point of view, two causal switching models are considered for the clutch: locked clutch (model 1) and slipping or open clutch (model 2) [Lhomme 2008-a]. In this way, the EMR in Figure 3.12 will be modified to adapt to different types of parallel HEVs by taking into account the state of the clutches. One example can be found in Chapter IV, where a parallel HEV uses a CVT with one cut-out clutch.

III.2.4. Common EMR and power flows using EMR

The EMR in Figure 3.12 can be considered as a common EMR using a generic matrix equation. By setting different values for certain parameters, the same EMR can describe: series-parallel, series, and parallel HEVs when all clutches are locked. The product of action and reaction between the EMR elements yields the power. Therefore the power flows of different HEVs are presented through EMR, which gives an intuitive vision of different HEVs.

III.2.4.1. Common EMR using a generic matrix equation

In series HEVs or series-parallel HEVs, the transmission speed on the mechanical coupling side Ω_{tran} is equal to the EM1 speed Ω_{EM1}, because the EM1 shaft is connected directly with the transmission shaft. In parallel HEVs with all clutches locked, Ω_{tran} is equal to the ICE speed Ω_{ICE}, as the ICE shaft is connected directly with the transmission shaft. From the above, the following equation can be introduced:

$$\Omega_{tran} = k_T \Omega_{EM1} + (1-k_T)\Omega_{ICE} \tag{3.29}$$

where k_T=1 for series HEVs and series-parallel HEVs, and k_T=0 for parallel HEVs.

From (3.14), (3.20) and (3.26), a generic matrix equation is used in the vectorial accumulation element (Figure 3.12) to represent the torque-speed relationship of systems as:

$$[J]\frac{d}{dt}\begin{bmatrix}\Omega_{EM1}\\ \Omega_{EM2}\end{bmatrix} = -[f]\begin{bmatrix}\Omega_{EM1}\\ \Omega_{EM2}\end{bmatrix} + \begin{bmatrix}T_1\\ T_2\end{bmatrix} - \begin{bmatrix}T_3\\ T_4\end{bmatrix} \tag{3.30}$$

with $[J] = \begin{bmatrix} k_T(J_{EM1} + J_{eq} + k_R^2 J_{ICE}) & k_R k_S J_{ICE} \\ k_R k_S J_{ICE} & k_S^2 J_{ICE} + J_{EM2} + (1-k_T)k_S^2 J_{eq}\end{bmatrix}$

and $[f] = \begin{bmatrix} k_T(f_{EM1} + k_R^2 f_{ICE}) & k_R k_S f_{\mathrm{ICE}} \\ k_R k_S f_{\mathrm{ICE}} & k_S^2 f_{ICE} + f_{EM2}\end{bmatrix}$

where [J] represents the coefficients of the matrix of the moments of inertia, and [f] is the viscous friction coefficient matrix. k_R represents the mechanical coupling between EM1 and other machines. If there is no mechanical coupling between EM1 and other machines, $k_R = 0$. If there is a mechanical coupling between EM1 and other machines, $k_R \neq 0$ and depends on the radii of the mechanical coupling. k_S represents the mechanical coupling between EM2 and the ICE. If there is no mechanical coupling between EM1 and the ICE, k_S=0. If there is a mechanical coupling between EM1 and the ICE, $k_S \neq 0$ and its value depends on the radii of the mechanical coupling between EM2 and the ICE. Since there is always a mechanical coupling between EM2 and the ICE in these architectures, $k_S \neq 0$ for these three HEV types. Different values for k_T and k_R are set for different architectures, as shown in Table 3.2.

Table 3.2 Different HEVs in function of the value of k_T and k_R

	k_T	k_R
Series-parallel HEVs using a planetary gear	$k_T = \mathbf{1}$	$k_R \neq \mathbf{0}$
Series HEVs	$k_T = \mathbf{1}$	$k_R = \mathbf{0}$
Parallel HEVs with clutches locked	$k_T = \mathbf{0}$	$k_R = \mathbf{0}$

From (3.15) and (3.27), the equation which represents mechanical coupling ① is:

$$\begin{cases} \begin{bmatrix} T_{\mathbf{1}} \\ T_{\mathbf{2}} \end{bmatrix} = \begin{bmatrix} k_T & -k_T & \mathbf{0} \\ \mathbf{0} & (\mathbf{1}-k_T)k_S & \mathbf{1} \end{bmatrix} \begin{bmatrix} T_{EM\mathbf{1}} \\ T_{br} \\ T_{EM\mathbf{2}} \end{bmatrix} \\ \begin{bmatrix} \Omega_{EM\mathbf{1}} \\ \Omega_{tran} \\ \Omega_{EM\mathbf{2}} \end{bmatrix} = \begin{bmatrix} \mathbf{1} & \mathbf{0} \\ k_T & \mathbf{1}-k_T \\ \mathbf{0} & \mathbf{1} \end{bmatrix} \begin{bmatrix} \Omega_{EM\mathbf{1}} \\ \Omega_{EM\mathbf{2}} \end{bmatrix} \end{cases} \tag{3.31}$$

From (3.16), (3.28) and (3.29), the equation for mechanical coupling ② is given by:

$$\begin{cases} \begin{bmatrix} T_{\mathbf{3}} \\ T_{\mathbf{4}} \end{bmatrix} = \begin{bmatrix} k_T & -k_T k_R \\ \mathbf{1}-k_T & -k_S \end{bmatrix} \begin{bmatrix} T_{res} \\ T_{ICE} \end{bmatrix} \\ \begin{bmatrix} \Omega_{tran} \\ \Omega_{ICE} \end{bmatrix} = \begin{bmatrix} k_T + (\mathbf{1}-k_T)k_R & (\mathbf{1}-k_T)k_S \\ k_R & k_S \end{bmatrix} \begin{bmatrix} \Omega_{EM\mathbf{1}} \\ \Omega_{EM\mathbf{2}} \end{bmatrix} \end{cases} \tag{3.32}$$

III.2.4.2. Power flows using EMR

The differences between these typical HEVs are mainly related to the vectorial accumulation element and the mechanical coupling elements. Due to these differences, the seven main power flows (see III. 1.2) of the different HEVs do not have the same paths. Since the main power flows are defined as the power flows between the ESS, the fuel tank (the ICE in EMRs) and the traction load (Env. in EMRs), the mechanical braking is not emphasized at this stage (see III.1.2).

A. Power flows for series-parallel HEVs

The power flows for a Toyota Prius type HEV are shown in Table 3.3.

Power flow 1: Only EM1 supplies the traction power. This happens when the vehicle velocity or vehicle power is low, and at the same time the energy in the ESS is within its allowable range.

Power flow 2: The ESS is only charged by the braking energy. When the vehicle is decelerating or braking, the ESS is charged by EMs if the ESS is within its allowable range. EM1 is connected directly to the transmission shaft. However EM2 is connected with EM1 through the planetary gear. The braking energy is therefore regenerated by EM1, but not by EM2, through the planetary gear. There is no fuel injection for the ICE. The ICE is at zero speed, and imposes a resistance torque.

Power flow 3: The energy in the ESS is constant and the ICE supplies all the traction power. This power flow is only between the ICE and traction load. Since the ICE is controlled to operate in its optimal region, EMs are involved. Therefore, the power from the ICE is separated into 2 parts. One part is from the ICE directly to the wheels. The other part is from the ICE through the EMs to the wheels. There are two possibilities for this other part. The first possibility (Table 3.3, power flow 3, first possibility) is that the ICE delivers its power to EM2, then EM2 generates electrical power for EM1, and finally EM1 assists the ICE for propulsion. Since the power generated by EM2 is equal to the EM1 power, the energy in the ESS is constant. This situation occurs during light acceleration or possibly during low-speed cruising [Ehsani 2010]. The second possibility (Table 3.3, power flow 3, second possibility) is that the ICE delivers its power to EM1, and then EM1 generates electrical power for EM2. This situation occurs frequently in EUDC (Extra Urban Driving Cycle), because maintaining constant energy in the ESS is reasonable in this situation.

Power flow 4: The ESS is charged only by the ICE. If the energy in the ESS is under its lowest allowable value when the vehicle is not moving, the ICE charges the ESS through EM2.

Power flow 5: The traction power comes from two sources: the ESS and the ICE. Since there are two possibilities with respect to power flow 3, there are also two possibilities for power flow 5: power flow 1 + the first possibility for power flow 3, and power flow 1 + the second possibility for power flow 3. Power flow 5 generally occurs during full acceleration.

Power flow 6: The ESS is charged by both the ICE and the braking energy through EM1 (power flow 2 + power flow 4)

Power flow 7: The ICE supplies the traction power and charges the ESS at the same time. There are two possibilities: the first possibility for power flow 3 + power flow 4, and the second possibility for power flow 3 + power flow 4.

Table 3.3 Power flows for series-parallel HEVs

1	ESS→Load Pure electric traction		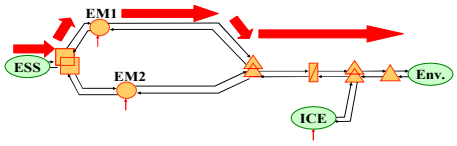
2	Load →ESS: Regenerative braking		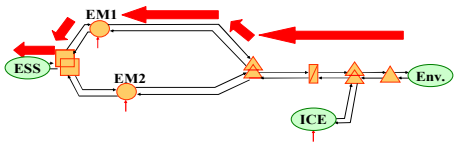
3	Fuel tank→Load: Pure engine	First possibility	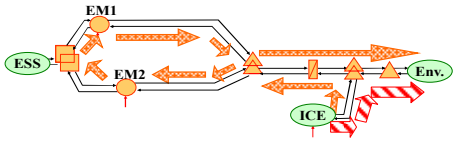
		Second possibility	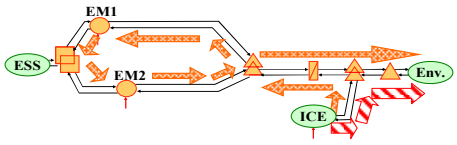
4	Fuel tank → ESS: ESS charging only by ICE		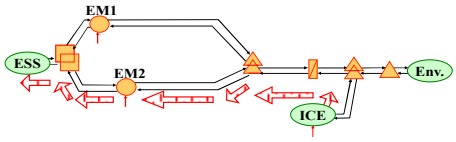
5	Hybrid traction	Power flow 1+ Power flow 3 (first possibility)	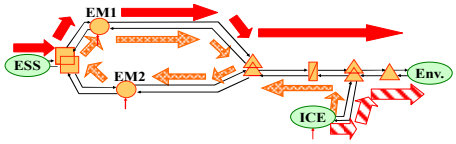
		Power flow 1 + Power flow 3 (second possibility)	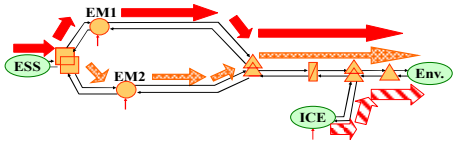
6	Hybrid charging	Power flow 2 + Power flow 4	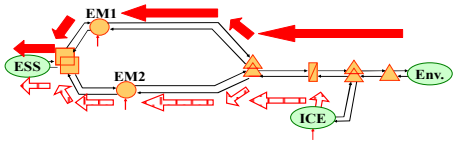
7	Engine traction and battery charging	Power flow 3 (first possibility) + Power flow 4	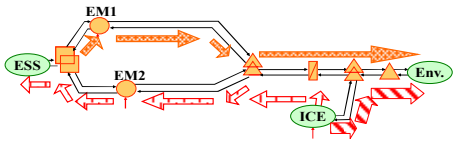
		Power flow 3 (second possibility) + Power flow 4	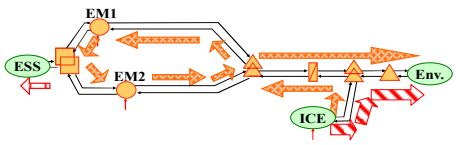

B. Power flows for series HEVs

Since (3.30) is diagonal for series HEVs, the vectorial accumulation element in Figure 3.12 can be replaced by two scalar accumulation elements in Figure 3.18 using (3.18) and (3.19). The coupling related to EM2 for mechanical coupling ① in Figure 3.12 is deleted, and (3.31) is replaced by:

$$\begin{cases} T_{\mathbf{1}} = T_{EM\mathbf{1}} - T_{br} \\ \Omega_{tran} = \Omega_{EM\mathbf{1}} \end{cases} \tag{3.33}$$

Mechanical coupling ② in Figure 3.12 (3.32) becomes two mechanical conversion elements, as shown in Figure 3.18:

$$\begin{cases} T_{\mathbf{3}} = T_{res} \\ \Omega_{tran} = \Omega_{EM\mathbf{1}} \end{cases} \tag{3.34}$$

$$\begin{cases} T_{\mathbf{4}} = -k_S T_{ICE} \\ \Omega_{ICE} = k_S \Omega_{EM\mathbf{2}} \end{cases} \tag{3.35}$$

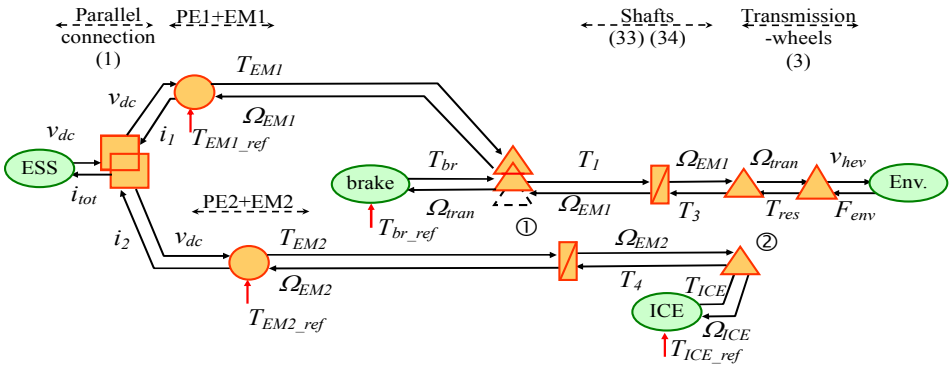

Figure 3.18 Reorganized EMR of series HEVs using two scalar accumulation elements

The power flows for series HEVs are shown in Table 3.4. Contrary to series-parallel HEVs, power flow 3 shows that the ICE supplies all of the traction, starting from EM2, then to the DC bus, subsequently to EM1, and finally to the wheels. There is no mechanical coupling between EM1 and the ICE.

Table 3.4 Power flows of series HEVs

1	ESS→Load Pure electric traction	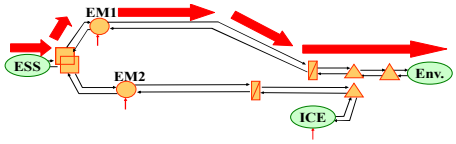
2	Load →ESS: Regenerative braking	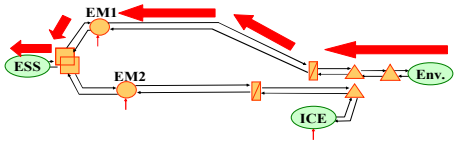
3	Fuel tank→Load: Pure engine Fist possibility	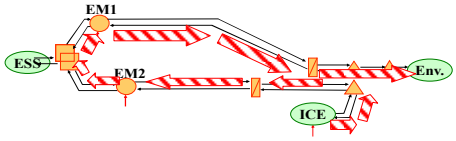
4	Fuel tank → ESS: ESS charging only by ICE	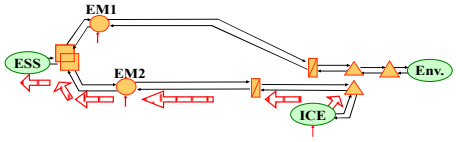
5	Hybrid traction Power flow 1+ Power flow 3	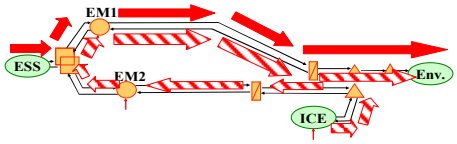
6	Hybrid charging Power flow 2 + Power flow 4	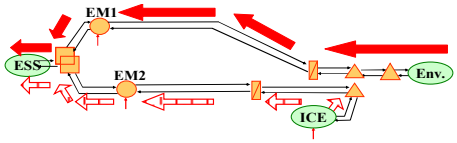
7	Engine traction and battery charging Power flow 3 + Power flow 4	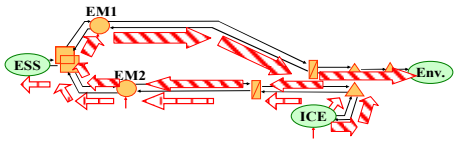

C. Power flows for parallel HEVs

Since there is no EM1 in parallel HEVs, the EM1 based drivetrain and the electrical coupling in Figure 3.12 can be deleted. (3.1) therefore becomes:

$$\begin{cases} v_{dc} \text{ common variable} \\ i_{\text{tot}} = i_2 \end{cases} \tag{3.36}$$

From (3.26), the vectorial accumulation element in Figure 3.12 is replaced by one scalar accumulation element, as shown in Figure 3.19. (3.25) is used in this scalar accumulation element. The coupling related to EM1 in mechanical coupling ① is deleted, and (3.31) is replaced by:

$$\begin{cases} T_2 = T_{EM2} - k_S T_{br} \\ \Omega_{tran} = k_S \Omega_{EM2} \end{cases} \tag{3.37}$$

The mechanical coupling ② (3.32) is replaced by:

$$\begin{cases} T_4 = -k_S T_{ICE} + k_S T_{res} \\ \Omega_{ICE} = k_S \Omega_{EM2} \\ \Omega_{tran} = \Omega_{ICE} \end{cases} \quad (3.38)$$

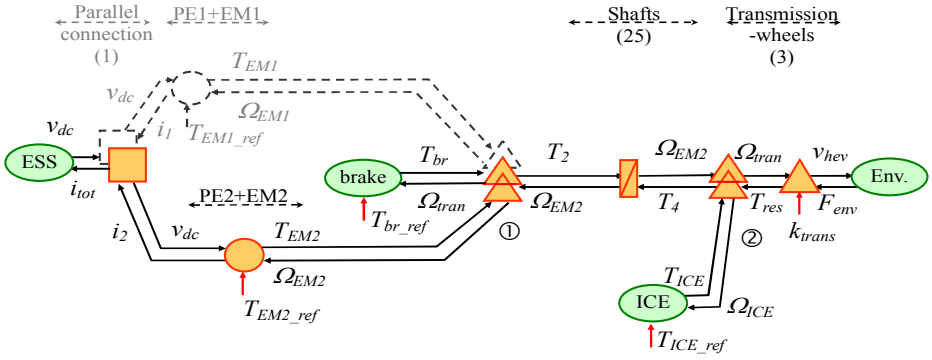

Figure 3.19 Reorganized EMR of parallel HEVs using a scalar accumulation element

Table 3.5 shows the power flows for full parallel HEVs. Since there is no EM1 based drivetrain, there is no power flow through EM1. Contrary to other HEVs related to power flow 3, EM2 is turned off and the ICE supplies the traction power. Not all parallel HEVs have all these power flows. To achieve these power flows, clutches are required.

III.2.4.3. Modeling Summary

By setting different values for certain parameters, a unique EMR describes series-parallel HEVs, series HEVs, and parallel HEVs when all clutches are locked. The common points for different HEVs are therefore shown through this common EMR. Their differences are mainly related to the vectorial accumulation element and the mechanical coupling elements. This common EMR can also be reorganized to show the power flow paths for different HEVs.

In this way, a unique simulation model can be established to study different HEV architectures by just changing certain parameter values.

Table 3.5 Power flows of parallel HEVs

1	ESS→Load Pure electric traction	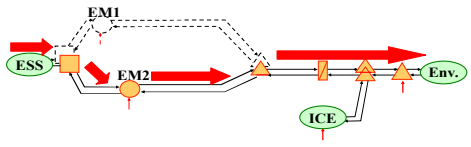
2	Load →ESS: Regenerative braking	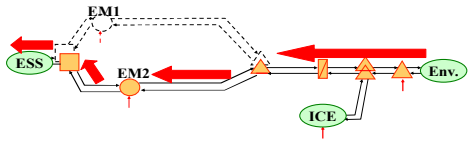
3	Fuel tank→Load: Pure engine Fist possibility	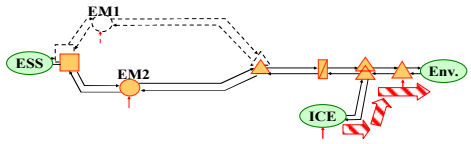
4	Fuel tank → ESS: ESS charging only by ICE	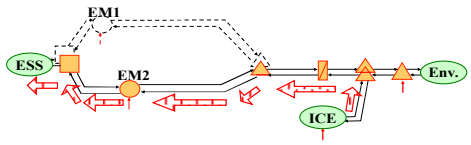
5	Hybrid traction Power flow 1+ Power flow 3	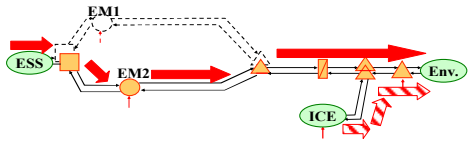
6	Hybrid charging Power flow 2 + Power flow 4	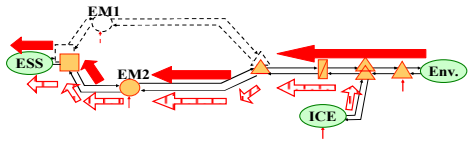
7	Engine traction and battery charging Power flow 3 + Power flow 4	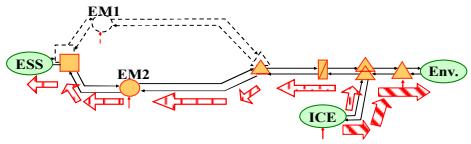

III.3. Unified control scheme for different HEVs

In the previous section, a common EMR was introduced to represent series-parallel, series, and parallel HEVs when all clutches are locked. Using the inversion principles, a unified control scheme can be deduced from this common EMR. This control scheme is organized into two levels: a local level and a strategy level (global energy management). First, the tuning and control paths are analyzed. Second, the inversion-based control scheme is detailed.

III.3.1. Tuning and Control paths

From the common EMR (Figure 3.12), there are a maximum of 5 tuning variables: the EM1 torque reference T_{EM1_ref}, the EM2 torque reference T_{EM2_ref} , the ICE torque reference T_{ICE_ref}, the mechanical braking torque reference T_{br_ref} and the transmission ratio k_{trans}.

In series or series-parallel HEVs, the transmission ratio k_{trans} is fixed because a fixed reduction gear is used. There are only 4 tuning variables: T_{EM1_ref}, T_{EM2_ref}, T_{ICE_ref}, and T_{br_ref}.

In parallel HEVs, there is no EM1 based drivetrain. The tuning variable T_{EM1_ref} can not be counted. The transmission ratio k_{trans} can be adjusted by the drivers or automatically by the control. In this case, there are also 4 tuning variables: T_{EM2_ref}, T_{ICE_ref}, T_{br_ref}, and k_{trans}. With regard to the clutches, the clutch position p_{cl} will not be discussed at this stage.

The control objective is to control the HEV velocity v_{hev}. The tuning variable T_{br_ref} is used to achieve the mechanical braking. Two optimization variables can therefore be defined at the strategy level to ensure fuel economy by choosing the appropriate values for T_{ICE_ref} and Ω_{ICE_ref} such that the ICE operate in its optimal region. Contrary to series or series-parallel HEVs, Ω_{ICE_ref} in parallel HEVs is obtained through the adjustment of the transmission ratio k_{trans}. If the transmission is a discrete gearbox, given that the transmission ratio is limited (a discrete gearbox typically offers between four and six gear choices), the optimum value for Ω_{ICE_ref} can not be achieved. The 4 tuning variables are fully used.

The tuning paths are chosen (Figure 3.20) according to these objectives, and the control paths are obtained (Figure 3.21) using the mirror effect.

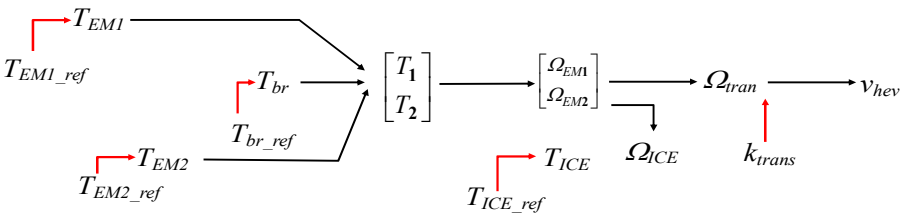

Figure 3.20 Tuning paths of the common EMR

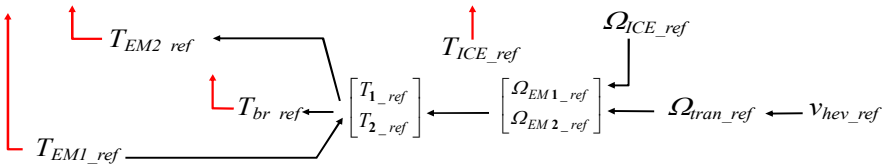

Figure 3.21 Control paths of the unified control scheme

III.3.2. Inversion-based control scheme

Along the control paths, an inversion-based control scheme can be deduced from the common EMR. These typical HEVs have the same inversion-based control structure. This control structure is composed of two levels, which operate mutually:

• a local level which is obtained by the inversion of the common EMR.

• a strategy level which deals with the global energy management of the whole system.

Inversion of "Transmission-wheels" – Along the control paths, from left to right, the first element (Transmission-wheels) is a mechanical conversion element. From (3.3), it can be inverted directly as follows (lower part of Figure 3.22, parallelogram):

$$\Omega_{tran\_ref} = \frac{k_{trans}}{R_{wh}} v_{hev\_ref} \tag{3.39}$$

In series or series-parallel HEVs, k_{trans} is fixed and known because of fixed reduction gears. In parallel HEVs, a discrete gear box (manual or automatic), or a CVT can be used, as the transmission. k_{trans} is adjustable and can be modified by the driver or calculated by the control. In the CVT case, the value of k_{trans} can be obtained at the strategy level from the ICE speed Ω_{ICE_mea}, with all clutches blocked, using:

$$k_{trans} = \frac{R_{wh}}{v_{hev\_mea}} \Omega_{ICE\_mea} \tag{3.40}$$

because the transmission speed Ω_{tran} is equal to the ICE speed Ω_{ICE} when the clutches are blocked (3.29). The ICE speed is chosen in its optimal zone. In this way, the transmission ratio k_{trans} can be adjusted according to the ICE speed relative to the vehicle speed.

Inversion of mechanical coupling ② – There are two inputs and one output according to the chosen tuning paths in mechanical coupling ②. The inversion of mechanical coupling ② (lower part of Figure 2.21, overlapped parallelogram) requires one supplementary input. From (3.32), the supplementary input is the ICE speed reference Ω_{ICE_ref} which is delivered at the strategy level. In series or series-parallel HEVs ($k_T = \mathbf{1}$), (3.32) can be inverted directly as below:

$$\begin{bmatrix} \Omega_{EM\mathbf{1}\_ref} \\ \Omega_{EM\mathbf{2}\_ref} \end{bmatrix} = \begin{bmatrix} \mathbf{1} & \mathbf{0} \\ k_R & k_S \end{bmatrix}^{-1} \begin{bmatrix} \Omega_{tran\_ref} \\ \Omega_{ICE\_ref} \end{bmatrix} = \begin{bmatrix} \Omega_{tran\_ref} \\ -\frac{k_R}{k_S}\Omega_{tran\_ref} + \frac{\mathbf{1}}{k_S}\Omega_{ICE\_ref} \end{bmatrix} \tag{3.41}$$

In parallel HEVs ($k_T = \mathbf{0}$ and $k_R = \mathbf{0}$), (3.32) can not be inverted directly. The speed equation of (3.32) becomes:

$$\begin{bmatrix} \Omega_{tran} \\ \Omega_{ICE} \end{bmatrix} = \begin{bmatrix} \mathbf{0} & k_S \\ \mathbf{0} & k_S \end{bmatrix} \begin{bmatrix} \Omega_{EM\mathbf{1}} \\ \Omega_{EM\mathbf{2}} \end{bmatrix} \text{ thus } \Omega_{tran} = \Omega_{ICE} = k_S \Omega_{EM2} \tag{3.42}$$

Since there is no EM1 based drivetrain, the EM1 speed can be set to zero. The speed

vector reference can be obtained as shown:

$$\begin{bmatrix} \Omega_{EM1\_ref} \\ \Omega_{EM2\_ref} \end{bmatrix} = \begin{bmatrix} \mathbf{0} \\ \dfrac{\mathbf{1}}{k_S}\Omega_{tran\_ref} \end{bmatrix} = \begin{bmatrix} \mathbf{0} \\ \dfrac{\mathbf{1}}{k_S}\Omega_{ICE\_ref} \end{bmatrix} \tag{3.43}$$

Vectorial speed controller – The "shafts" element is a vectorial accumulation element. A vectorial controller (lower part of Figure 3.22, parallelogram with an oblique bar) is required to define the torque vector reference $[T_{1\_ref}, T_{2\_ref}]^T$ from the speed vector reference $[\Omega_{EM1\_ref}, \Omega_{EM2\_ref}]^T$ and the speed measurements Ω_{EM1_mea} and Ω_{EM2_mea}. From (3.30),

$$\begin{bmatrix} T_{\mathbf{1}\_ref} \\ T_{\mathbf{2}\_ref} \end{bmatrix} = [J]\begin{bmatrix} C_{s\mathbf{1}}(t)(\Omega_{EM\mathbf{1}\_ref} - \Omega_{EM\mathbf{1}\_mea}) \\ C_{s\mathbf{2}}(t)(\Omega_{EM\mathbf{2}\_ref} - \Omega_{EM\mathbf{2}\_mea}) \end{bmatrix} + [f]\begin{bmatrix} \Omega_{EM\mathbf{1}\_mea} \\ \Omega_{EM\mathbf{2}\_mea} \end{bmatrix} + \begin{bmatrix} T_{\mathbf{3}\_mea} \\ T_{\mathbf{4}\_mea} \end{bmatrix} \tag{3.44}$$

$C_{s1}(t)$ and $C_{s2}(t)$ may be PI type controllers or other types of controllers. Different values of k_T, k_R and k_S are set for different architectures, as shown in Table 3.2. The torques T_{3_mea} and T_{4_mea} (3.32), which are composed of the resistance torque measurement T_{res_mea} and the ICE torque measurement T_{ICE_mea}, are compensated in this vectorial controller. Measurement of the resistance torque T_{res} and the ICE torque T_{ICE} are difficult. In practical controls, the T_{res} is usually considered as a disturbance to be rejected. The reference value of T_{ICE} may be used instead of its measurement value for the compensation in the controller.

Inversion of mechanical coupling ① –There are three action inputs and two outputs (a two dimensional vector) according to the chosen tuning paths in mechanical coupling①. To invert the mechanical coupling, one supplementary distribution input k_d is required. The supplementary input k_d is defined at the strategy level to distribute the power between the mechanical braking and the electrical braking. From (3.31), in series or series-parallel HEVs ($k_T = \mathbf{1}$),

$$\begin{cases} T_{EM1\_ref} = k_d T_{1\_ref} \\ T_{br\_ref} = -(1 - k_d)T_{1\_ref} \\ T_{EM2\_ref} = T_{2\_ref} \end{cases} \tag{3.45}$$

In parallel HEVs ($k_T = \mathbf{0}$), there are only two real inputs (T_{br} and T_{EM2}) and one output T_2 according to the chosen tuning paths in parallel HEVs. To invert the coupling, k_d is also required:

$$\begin{cases} \text{no } T_{EM\mathbf{1}\_ref} \\ T_{br\_ref} = -\dfrac{\mathbf{1}}{k_S}(\mathbf{1} - k_d)T_{\mathbf{2}\_ref} \\ T_{EM\mathbf{2}\_ref} = k_d T_{\mathbf{2}\_ref} \end{cases} \tag{3.46}$$

Since there is no EM1 based drivetrain, there is no EM1 torque reference T_{EM1_ref}.

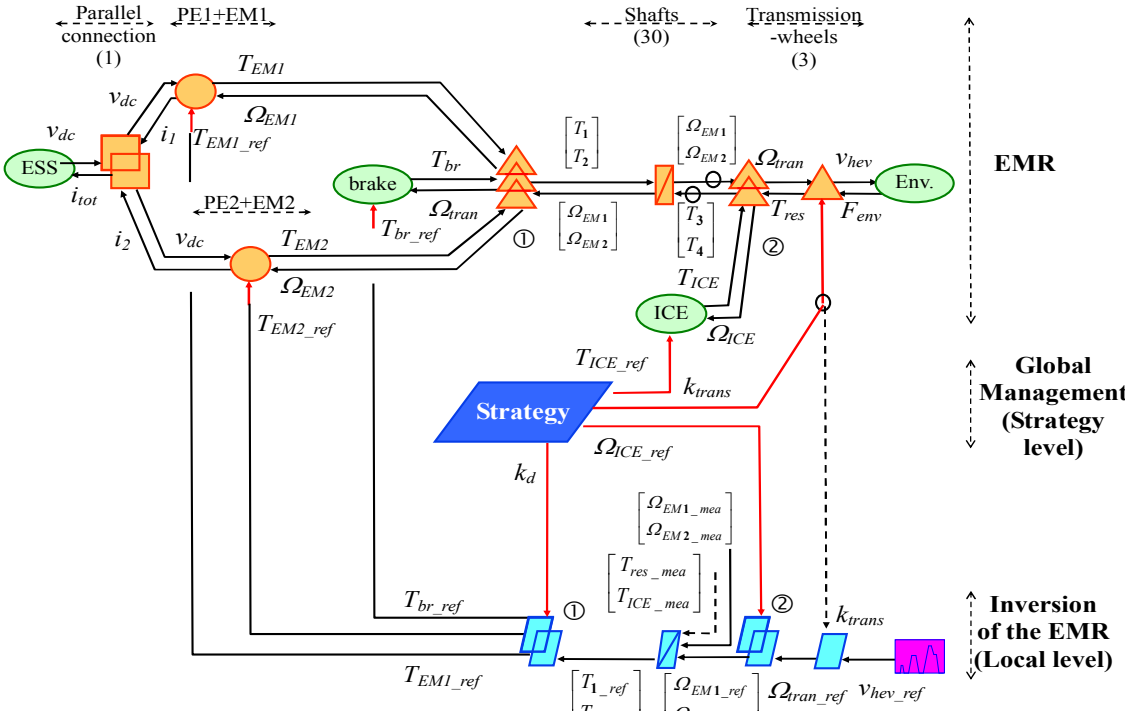

Figure 3.22 Unified control scheme of different HEVs

More details about the control of EMs to obtain the torque reference can be found in Chapter II.

III.3.3. Discussion of the unified control scheme

Following this procedure, a unified inversion-based control scheme (Figure 2.21) has been established, which can be used for series HEVs, series-parallel HEVs and parallel HEVs when all clutches are blocked. This control scheme shows the common points of control schemes among these HEVs. The differences are emphasized. They are located both at the local and strategy levels. Since the common EMR for series HEVs or parallel HEVs can be reo-ganized (see Figure 3.18 and Figure 3.19), this unified control scheme can be also modified according to the application. In this way, classical control schemes can be found for these typical HEVs from this unified control.

At the local level, the main differences concern the inversion of mechanical couplings and the vector controllers. In the inversion of the two mechanical couplings, different equations are used for different HEVs. In this unified control scheme, one vectorial controller is used for these three types. In series-parallel HEVs, the vectorial controller outputs T_{1_ref} and T_{2_ref} de-pend on both inputs Ω_{EM1_ref} and Ω_{EM2_ref} . In series HEVs, T_{1_ref} depends only on Ω_{EM1_ref}, and T_{2_ref} depends only on Ω_{EM2_ref}. In parallel HEVs, only T_{2_ref}, which depends on Ω_{EM2_ref}, is useful. Therefore, simpler controllers can be used for series HEVs and parallel HEVs.

At the strategy level, the maximum outputs are the ICE torque reference T_{ICE_ref}, the ICE speed reference Ω_{ICE_ref}, the power distribution between the mechanical braking and the electrical braking k_d, and the transmission ratio k_{trans}. In series, or series-parallel HEVs, k_{trans} is fixed; as a fixed reduction gear is used. k_{trans} can not be considered as an output of the strategy

block for these vehicles. In parallel HEVs, k_{trans} can be adjusted by the driver or the control. Different strategies can be used for various HEVs. For the same architecture, different strategies can be also used [Salmasi 2007] [Kessels 2007]. This part is generally called global energy management or supervision. The inputs of the strategy level are not shown in Figure 2.21, because they depend on the strategy used. Concrete examples can be found in Chapter IV.

III.3.3.1. Simplification of this control scheme

Since it is possible to reorganize this common EMR for each architecture, the control scheme can be presented in another way. Possible simplifications for Toyota Prius type HEVs will be discussed in chapter IV in order to find the classical control for series-parallel HEVs [Vinot 2008].

A. Series HEVs

In series HEVs, the vectorial accumulation element in Figure 3.12 can be replaced by two scalar accumulation elements (see Figure 3.18) (3.18) and (3.19). The vectorial controller (Figure 2.21) can also be replaced by the two independent controllers (Figure 1.12). The first one is used to obtain the EM1 speed (3.47). The second one is used to adjust the EM2 speed (3.48). Through the EM2 speed, the optimum ICE speed can be ensured.

$$T_{1\_ref} = J_{11} C_{s1}(t)(\Omega_{EM1\_ref} - \Omega_{EM1\_mea}) + f_{11}\Omega_{EM1\_mea} + T_{3\_mea} \tag{3.47}$$

$$T_{EM2\_ref} = J_{22} C_{s2}(t)(\Omega_{EM2\_ref} - \Omega_{EM2\_mea}) + f_{22}\Omega_{EM2\_mea} + T_{4\_mea} \tag{3.48}$$

with $J_{11} = J_{EM1} + J_{eq}$, $J_{22} = k_S^2 J_{ICE} + J_{EM2}$, $f_{11} = f_{EM1}$,
$f_{22} = k_S^2 f_{ICE} + f_{EM2}$, $T_{3\_mea} = T_{res\_mea}$ and $T_{4\_mea} = -k_S T_{ICE\_mea}$

The mechanical coupling ② in Figure 3.12 becomes two mechanical conversion elements in Figure 3.18. From (3.34) and (3.35), they can be inverted directly using:

$$\Omega_{EM1\_ref} = \Omega_{tran\_ref} \tag{3.49}$$

$$\Omega_{EM2\_ref} = \frac{1}{k_S}\Omega_{ICE\_ref} \tag{3.50}$$

The coupling related to EM2 in mechanical coupling ① of Figure 3.12 is deleted in Figure 3.18. From (3.33), it can be inverted using a supplementary input k_d:

$$\begin{cases} T_{EM1\_ref} = k_d T_{1\_ref} \\ T_{br\_ref} = -(1-k_d)T_{1\_ref} \end{cases} \tag{3.51}$$

Thereby, the control scheme obtained in Figure 1.12 is the classical control scheme of series HEVs [Jalil 1997] [Barsali 2004] [Lhomme 2004].

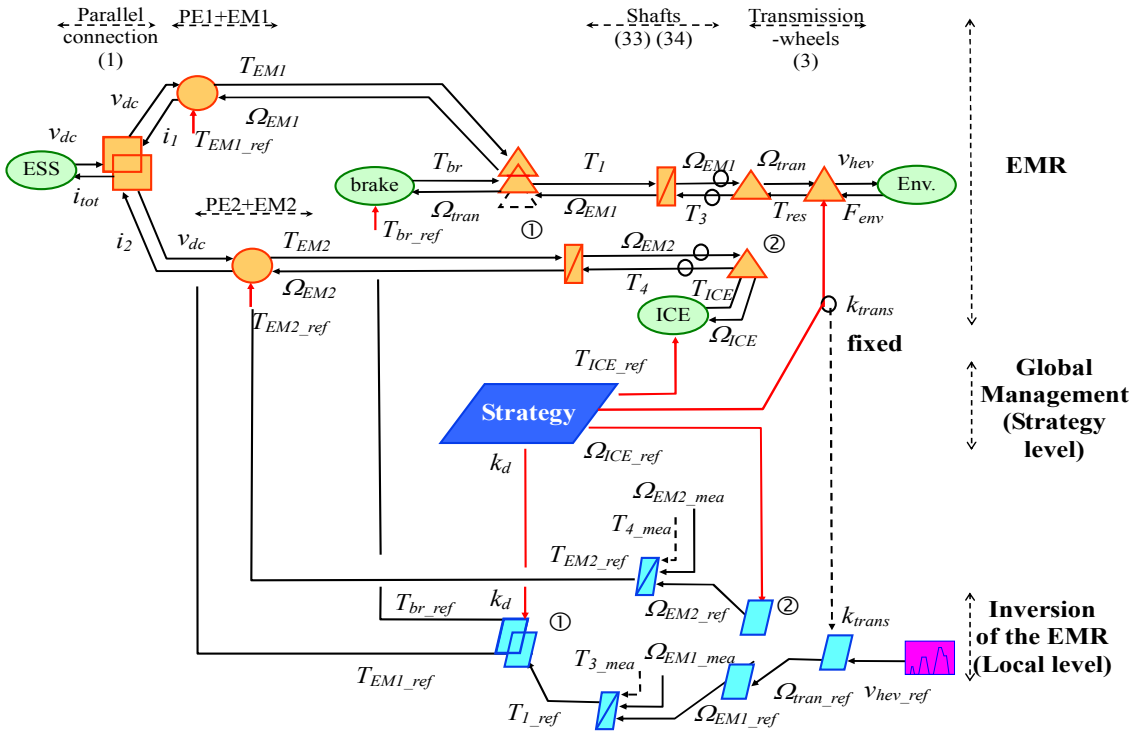

Figure 3.23 Classical control scheme for series HEVs

B. *Parallel HEVs*

Concerning parallel HEVs, the EM2 based drivetrain and the electrical coupling in Figure 3.12 are deleted in Figure 3.19. The vectorial accumulation element in Figure 3.12 is replaced by one scalar accumulation element in Figure 3.19 using (3.25). The vectorial controller (Figure 2.21) can also be replaced by one scalar controller (Figure 3.24) using (3.48),

with $J_{22} = k_S^2 J_{ICE} + k_S^2 J_{eq} + J_{EM2}$, $f_{22} = k_S^2 f_{ICE} + f_{EM2}$, and $T_{4\_mea} = -k_S T_{ICE\_mea} + k_S T_{res\_mea}$

The transmission ratio k_{trans} can be adjusted by the drivers or automatically by the control. If a CVT is used as the transmission, k_{trans} is obtained by choosing the appropriate ICE speed Ω_{ICE_ref} using (3.40). From (3.38), the inversion of mechanical coupling ② is given by:

$$\Omega_{EM2\_ref} = \frac{1}{k_S}\Omega_{ICE\_ref} = \frac{1}{k_S}\Omega_{tran\_ref} \tag{3.52}$$

No supplementary input is required. (3.46) is used in the inversion of mechanical coupling①. The control scheme in Figure 3.24 is the classical control scheme of parallel HEVs [Delprat 2004] [Trigui 2007] [Lhomme 2007].

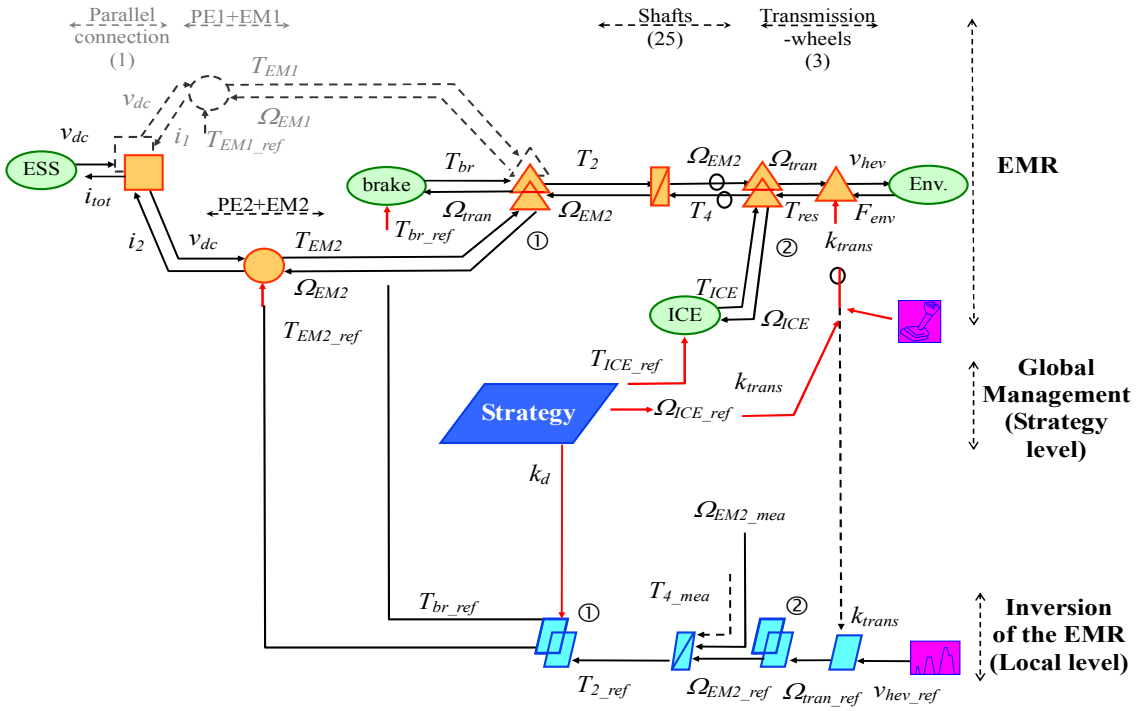

Figure 3.24 Classical control scheme for parallel HEVs

III.3.3.2. Control scheme summary

A unified control scheme has been deduced from the common EMR, which can be used for the study of some series-parallel, series, and parallel HEVs when all clutches are closed. In this way, the control design of such complex systems can be achieved in a general way, which can significantly reduce the time required for control design. Moreover, the differences among different HEVs are emphasized, both at the local and strategy levels. Through some equivalent modifications of this unified control scheme, classical control schemes for some HEVs can be found.

This section focuses on the inversion-based control structure. Based on this control structure, more control design details such as controller synthesis and robust stability could be developed [Ioannou 1988] [Sastry 1989] [Zhou 1999].

Conclusion

In this chapter, the modeling and control design of different HEVs have been achieved in a general way, while HEVs can be very different from each other in terms of structure.

A common EMR has been firstly presented. By setting different values for certain parameters, the same EMR describes series-parallel, series and parallel HEVs when all clutches are locked. This common EMR shows the points which are similar and different for these HEVs. A unique simulation model program can be therefore established based on the common EMR, and can be applied to study different HEVs simply by setting different parameter values. In the literature, no common simulation model for different HEVs has been presented.

Using the inversion principles, one unified control scheme has been deduced from this common EMR. This unified control scheme reveals the manner in which the control schemes of such complex systems can be achieved using the general approach. Thus, the time required for control design can be greatly reduced. Furthermore, this unified control scheme shows the differences related to different HEVs. This unified control has two levels: a local level, which deals with each subsystem, and a strategy level. The differences are emphasized both at the local and strategy levels. The use of EMR and the inversion-based control imply that the two levels must operate mutually. This point is seldom mentioned in the control design of HEVs. In the literature, generally, the strategy level, called energy management or supervision strategy is the only focus studied. The local level, the interaction between subsystems, as well as the interaction between the local and strategy levels are often briefly discussed or completely ignored. They are all important, however, for the control design.

Equivalent modifications can be made from this unified control scheme for each HEV. A classical control scheme for each HEV can therefore be obtained from this common control scheme.

This common EMR offers a macroscopic energetic view on different HEVs. More detailed models could be studied. The wheels can be modeled separately, instead of using an equivalent one wheel model. The tire-road interaction could be also added using EMR as in [Verhille 2007-b] [Grossi 2009]. Further control design details, including controller synthesis, robustness, and stability, could be studied in future research on whole HEV systems [Ioannou 1988] [Sastry 1989] [Zhou 1999].

In chapter IV, this common EMR and the unified control structure will be validated both by simulation and by experimentation in real-time. The extension of the common EMR and the unified control structure will be discussed.

Chapter IV

Validation of the unified control scheme and extended applications

Introduction

In the literature, many interesting control prototypes have been proposed. However, not all of them can run in real-time environment. The control prototype can be firstly checked in a software environment. Simulation in a software environment is the first step. To be sure that this control prototype can run satisfactorily in real-time, it must be checked in a real-time environment.

The previous chapter proposed a unified control scheme for three popular HEVs: series-parallel HEVs using a planetary gear, series HEVs and parallel HEVs (the clutches are not taken into account). The objective of this chapter is to validate this unified control. The extension of the common EMR and this unified control structure will be discussed.

This unified control scheme will be validated in this chapter by simulation and experimentation. A simulation program is established in MATLAB-Simulink^{TM} with the help of the common EMR and the unified control. Setting different values, this common program can be used in the simulation of the three types of HEVs. If the simulation results of the common program are close to another simulation which has already been validated by real HEVs, the common EMR and the unified control are thus validated by simulation. Second, the unified control is implemented in a DSP chip based dSPACE system to control a HEV. Hardware-In-the-Loop simulation (HIL) is used [Bouscayrol 2006-b] to replace parts of the real process. Thereby, the unified control is validated in a real-time environment by experimentation.

The common EMR and the unified control can not be used for all HEVs. But by modifying some parts of the common EMR and the unified control, new applications can be obtained. The extended applications of the common EMR and the unified control are developed.

The first section is dedicated to the validation of the unified control. The simulation for a Toyota Prius II is firstly compared with another simulation which has been validated by the measurement of a real HEV [Vinot 2008]. In the second subsection, the unified control is verified for a series HEV using HIL simulation in a real-time environment. The second section develops the extended applications of the common EMR and the unified control. Two examples are introduced: one is a series-parallel HEV using two arranged EMs; the other is a parallel HEV using a CVT and a clutch. These two examples show how the modified common EMR and the unified control can be used in other HEVs.

IV.1. Validation of the unified control scheme

The common EMR and the unified control scheme are first validated by simulation. The simulation program is compared with another simulation program which has already been validated by experimentation. Then, the unified control is implemented in the real-time environment for experimental validation.

IV.1.1. Simulation validation

The simulation program using the common EMR and the unified control are established in MATLAB-Simulink^{TM} (Figure 4.1). In this part, this simulation program is called the common simulation program. It is composed of two parts: the EMR based common model, and the inversion-based control. The two parts can run separately and independently. The same common model program can be used for the modeling of some HEVs by simply setting different values for certain parameters. Similarly, the same control part can be used to control some HEVs using different parameter values. For example, setting k_T=1, k_R=0.7222; k_S=0.2778 and using other component parameters of Toyota Prius II, this common simulation program can be used in the simulation of the Toyota Prius II. Setting different values for k_T, k_R and k_S, the same simulation program can be applied to other HEVs.

In this subsection, the simulation validation is conducted for the Toyota Prius II by comparing it with VEHLIB, a simulation program which has been validated. First, the improvement of the Toyota Prius II relative to the Toyota Prius I is introduced. Second, VEHLIB is presented, and its philosophy is compared with the EMR philosophy. Third, this common simulation program is validated in three steps. The first step involves validation of the EMR based common model. In the second step, the simulation results using the unified control are compared with those of VEHLIB. Finally, other simulation results of this common simulation program are discussed.

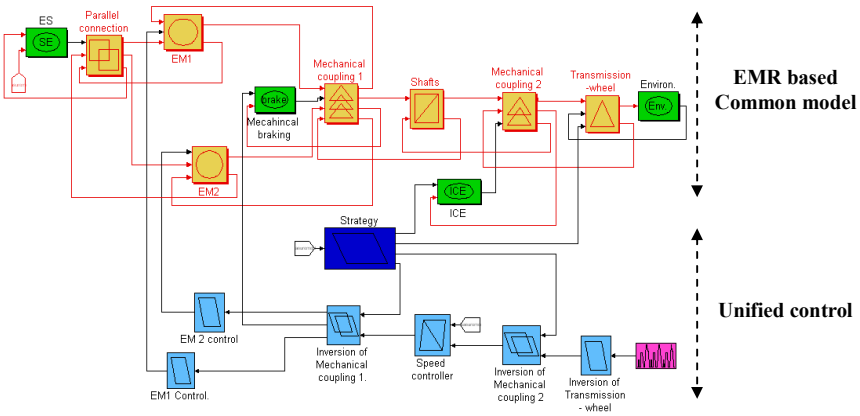

Figure 4.1 Common simulation program based on the common EMR and the unified control

IV.1.1.1. Toyota Prius II

Toyota Prius first went on sale in Japan in 1997 and was subsequently introduced worldwide in 2001 (Toyota Prius I). The second generation (Toyota Prius II) was released in 2004. Toyota Prius architecture has been discussed in Chapter III. The Toyota Prius II was significantly improved compared to the Toyota Prius I [Sasaki 1998] [Olszewsky 2006] [Vinot 2008] [Ehsani 2010]. The ESSs in the two versions are different (Table 4.1). In the Toyota Prius II, a buck boost converter is added between the battery and the DC bus. The EMs' voltage can be greater than in the first version, using fewer battery modules. In the Toyota Prius I, 38 battery modules are connected in series. Each module is composed of six 1.2 V cells in series. The rated DC bus voltage is 273.6 V. In the Toyota Prius II, 28 battery modules are connected in series for a rated voltage of 201.6 V. This new boost converter increases the DC bus voltage to the maximum value of 500 V.

In both versions, the type of EM is PMSM, and the ICE type is 1NE-FXE, which is a four-cylinder gasoline engine with Electric Throttle Control Systems - Intelligence (EFCS-i). The power of the EMs and that of the ICE are increased in the Toyota Prius II (Table 4.2).

Table 4.1. ESS comparison of Toyota Prius I and II [Vinot 2008] [Ehsani 2010]

		Toyota Prius I	Toyota Prius II
ESS	Battery type	Ni-MH	Ni-MH
	Cell voltage	1.2 V	1.2 V
	Module voltage	7.2 V	7.2 V
	Number of cell in a module	6 cells in series	6 cells in series
	Number of module in the pack	38	28
	Rated battery pack voltage	273.6 V	206.6 V
	Boost converter	No	Maximum voltage: 500V

Table 4.2. Machine comparison of Toyota Prius I and II

		Toyota Prius I	Prius II
EM1	Machine type	PMSM	PMSM
	Maximum power	30 kW	50 kW
	Maximum voltage	275 V	500 V
	Maximum speed	6000 rpm	6000 rpm
	Maximum torque	300 Nm (0-940 rpm)	400Nm (0-1200 rpm)
EM2	Machine type	PMSM	PMSM
	Maximum power	15 kW	30 kW
	Maximum voltage	275 V	500 V
	Maximum speed	8000 rpm	10000 rpm
	Maximum torque	145 Nm (0-940 rpm)	160 Nm (0-1800 rpm)
ICE	Engine type	1NE-FXE, four-cylinder	1NE-FXE, four-cylinder
	Maximum power	52 kW at 4500 rpm	57 kW at 5000 rpm

In both versions, the numbers of ring gear teeth, planet gear teeth and sun gear teeth are the same: 78/23/30 respectively. The fixed reduction gear ratio is 3.905 in the first version, but 4.113 in the second version.

IV.1.1.2. VEHLIB simulation

VEHLIB (Hybrid Electric Vehicle Library) is a simulation software program developed in 2000 by the LTE (Environment and Transport Laboratory) at INRETS (The French National Institute for Transport and Safety Research) (Figure 14.2) [Paganelli 1999][Trigui 2004-a] [Trigui 2004-b] [Scordia 2004]. It allows the simulation of existing or new vehicles using a complete library of components and architectures.

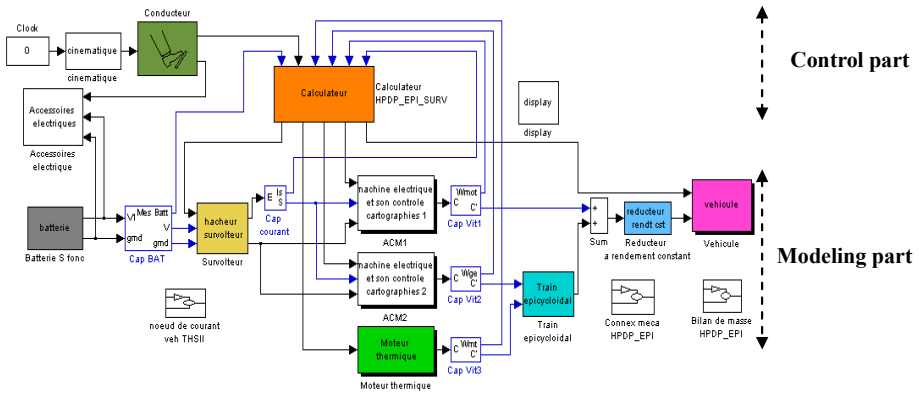

Figure 14.2 VEHLIB for the Toyota Prius II

The VEHLIB simulation for the Toyota Prius II has already been validated by experimentation [Vinot 2008], both for each main component and the whole system. Specific test benches are used for the validation of the main components of the Toyota Prius II, including the battery, boost converter. the ICE, and the two EMs. A real Toyota Prius II vehicle is also available for experimental validation.

The simulation results of the main components closely match the measurements. Fuel consumption comparisons between the simulation and the measurements have been conducted on Japanese 10-15, urban use, road use and motorway use cycles. The maximum error is 2.6% which is of the same order as the measurement precision (less than 5%). The instantaneous experimental validation for VEHLIB has been carried out on Japanese 10-15 cycles. The evolutions of the instantaneous consumption and of the battery SOC correspond to those obtained through experimentation using the real Toyota Prius II. Therefore, we can conclude that the VEHLIB simulation for the Toyota Prius is acceptably accurate.

These simulation results have been made available for the MEGEVH-macro project. Thereby, these simulation results can be compared with those of the EMR based simulation. If the simulation results of the EMR based simulation program are consistent with those of VEHLIB, the EMR based simulation program can subsequently be validated.

IV.1.1.3. VEHLIB simulation and EMR based simulation

VEHLIB and EMR do not have the same philosophies.

A. VEHLIB and EMR philosophies

VEHLIB – This is a simulation software program which is implemented in MATLAB-Simulink. It is also composed of two parts: the modeling part and the control part (Figure 14.2). The modeling part is based on a systemic representation. The vehicle is viewed as a set of subsystems. The subsystems and the whole system are not organized in the same way. At the subsystem level, the modeling of sub-systems is based on Bond Graph (See Chapter I). The subsystems use effort and flux input/output variables and respect the energy conversion law. At the whole system level, the Bond Graph method is replaced by a systemic representation [Vinot 2008] to make the whole system correspond to the system structure. Compared with EMR, which is a functional representation, VEHLIB uses a structural modeling approach. The control part in VEHLIB is not built upon the modeling of system, but established using heuristic approaches.

EMR based simulation program – The EMR based simulation program respects the EMR principles, both at the subsystem and whole system levels. Since EMR is a graphical representation, the simulation program using EMR can also be implemented in MATLAB-Simulink, or other software environments. Contrary to VEHLIB programs, the control schemes are deduced from the EMRs. Therefore, the control design is based on modeling.

B. Two simulation programs for the Toyota Prius II

The main differences between the VEHLIB and the common EMR-based simulation program for the Toyota Prius II are:

1. Because VEHLIB respects the system structure, to solve the association problem among components, some simplifications are made. Since EMR focuses on system functions, not only the system structures, a vectorial accumulation element is used to solve the association problem (see III.2.1).

2. The control used in VEHLIB for Toyota Prius II has been developed using expertise and experimentation. Two scalar independent controllers in VEHLIB are used: one is used for the vehicle velocity control; the other is used for the EM2 speed control to achieve the ICE speed. Since the unified control is deduced from the common EMR, a vectorial controller is used in the common simulation program, which was introduced in Chapter III.

Because the product of k_R and k_S is relatively small (k_R=0.7222; k_S=0.27780) for the Toyota Prius, the term $k_R k_S J_{ICE}$ in the generic matrix (3.30), which is used in the vectorial accumulation element, is relatively small. This generic matrix equation in the common EMR can be simplified as a decomposed matrix equation as shown:

$$\begin{bmatrix} J_{EM1}+J_{eq}+k_R^2 J_{ICE} & 0 \\ 0 & k_S^2 J_{ICE}+J_{EM2} \end{bmatrix} \frac{d}{dt}\begin{bmatrix} \Omega_{EM1} \\ \Omega_{EM2} \end{bmatrix} = -\begin{bmatrix} f_{EM1}+k_R^2 f_{ICE} & 0 \\ 0 & k_S^2 f_{ICE}+f_{EM2} \end{bmatrix}\begin{bmatrix} \Omega_{EM1} \\ \Omega_{EM2} \end{bmatrix} + \begin{bmatrix} T_1 \\ T_{EM2} \end{bmatrix} - \begin{bmatrix} T_3 \\ T_4 \end{bmatrix} \tag{4.1}$$

The vectorial accumulation element in the common EMR can therefore be replaced by two scalar accumulation elements using (4.1) (Figure 4.3). The coupling related to EM2 in mechanical coupling ① is deleted:

$$\begin{cases} T_1 = T_{EM1} - T_{br} \\ \Omega_{tran} = \Omega_{EM1} \end{cases} \tag{4.2}$$

The equation in mechanical coupling ② is the same as in the common EMR presented in chapter III.

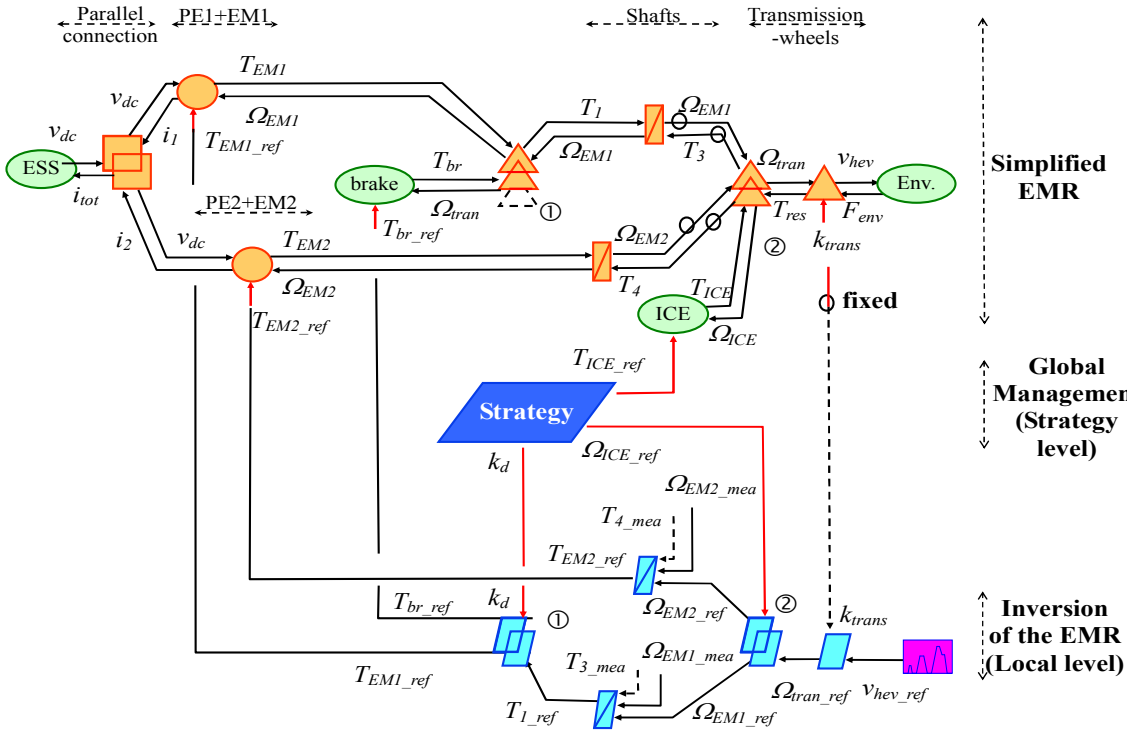

Figure 4.3 Simplified control scheme for series-parallel HEVs (Toyota Prius)

If this simplification is made as in (4.1), the vectorial controller in the unified control scheme can also be replaced by the two independent controllers (Figure 4.3). The first one is used to obtained the EM1 speed (4.3). This controller can be considered as a driver. The second one is used to adjust the EM2 speed (4.4). Through the EM2 speed, the optimum ICE speed can be ensured.

$$T_{1\_ref} = J_{11} C_{s1}(t)(\Omega_{EM1\_ref} - \Omega_{EM1\_mea}) + f_{11}\Omega_{EM1\_mea} + T_{3\_mea} \tag{4.3}$$

$$T_{EM2\_ref} = J_{22} C_{s2}(t)(\Omega_{EM2\_ref} - \Omega_{EM2\_mea}) + f_{22}\Omega_{EM1\_mea} + T_{4\_mea} \tag{4.4}$$

with $J_{11} = J_{EM1} + J_{eq} + k_R^2 J_{ICE}$, $J_{22} = k_S^2 J_{ICE} + J_{EM2}$, $f_{11} = f_{EM1} + k_R^2 f_{ICE}$, $f_{22} = k_S^2 f_{ICE} + f_{EM2}$, $T_{3\_mea} = -k_R T_{ICE\_mea} + T_{res\_mea}$ and $T_{4\_mea} = -k_S T_{ICE\_mea}$

The inversion of mechanical coupling ② is not changed. From (4.2), to invert mechanical coupling ①,

$$\begin{cases} T_{EM1\_ref} = k_d T_{1\_ref} \\ T_{br\_ref} = -(1 - k_d) T_{1\_ref} \end{cases} \tag{4.5}$$

In this way, the two scalar controllers used in the VEHLIB simulation are found. This explains why there is no great difference in both simulation programs. It should be noted that this simplification is not always valid in other cases.

IV.1.1.4. Comparison and validation by simulation

The two parts of the common simulation program, the EMR based common model and the inversion-based control, can run separately. The common model must be firstly checked, as the control part is deduced from the EMR. First, the EMR based common model is validated by comparing it with VEHLIB using Japanese 10-15 cycles. Second, the unified control is validated by comparing it with VEHLIB using Japanese 10-15 cycles. Finally, the comparison is made using New European Driving Cycles (NEDC).

A. Validation of the EMR based common model by simulation

To validate the EMR based common model, the modeling part runs simultaneously with the control part of VEHLIB (Figure 4.4). The simulation results are compared with those obtained using the simulation program of VEHLIB for the Toyota Prius II.

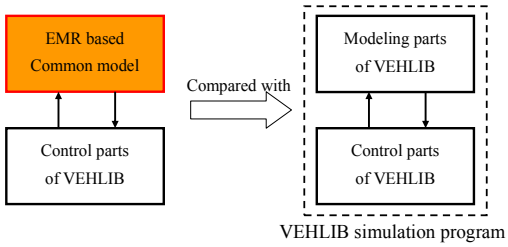

Figure 4.4 Validation for the EMR based common model by simulation

In [Vinot 2008], the instantaneous experimental validation of VEHLIB has been validated on Japanese 10-15 cycles (Figure 4.5). Three cases were presented: initial SOC of 55.8%, initial SOC of 70% and initial SOC of 20%. In each case, the VEHLIB simulation concerning the SOC and instantaneous fuel consumption were compared with the measurements of a real Toyota Prius.

The simulation results using the EMR based modeling part and the control part of VEHLIB are similar to those of VEHLIB. The ICE specific fuel consumption map is obtained by measurement [Vinot 2008]. The lines numbered 400, 300, 275, 250 and 220 represent the ICE specific fuel consumption in g/kWh. An ICE has an optimal operating region in which fuel consumption is minimal. For example, the best specific fuel consumption of the Toyota Prius II is 225 g/kWh. The ICE operating points of both simulations are the same, as shown in Figure 4.6.

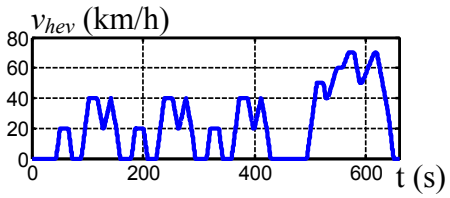

Figure 4.5 Japanese 10-15 driving cycle

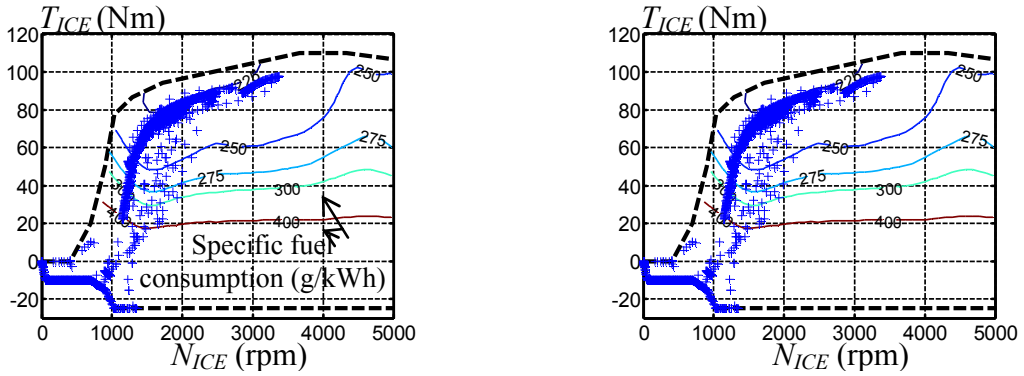

(a) VEHLIB Simulation (b) EMR-based common EMR simulation

Figure 4.6 ICE operation of the Toyota Prius II

B. Validation of the unified control by simulation

In this step, the common simulation program, which is based on the common EMR and the unified control, is validated. The simulation results are compared with those of VEHLIB (Figure 4.7).

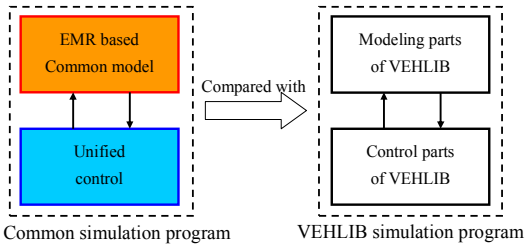

Figure 4.7 Validation of the unified control in simulation

To compare the two simulation programs, the same strategy is used. This strategy is not the one used in a real Toyota Prius II. However, it is strongly based on the Toyota Prius control principle [Sasaki 1998] [Jeanneret 1999], and deduced through specific experimentation from a real Toyota Prius II [Vinot 2008], thus approaching the strategy of the Toyota Prius II. The overview of this strategy is given in Figure 4.8.

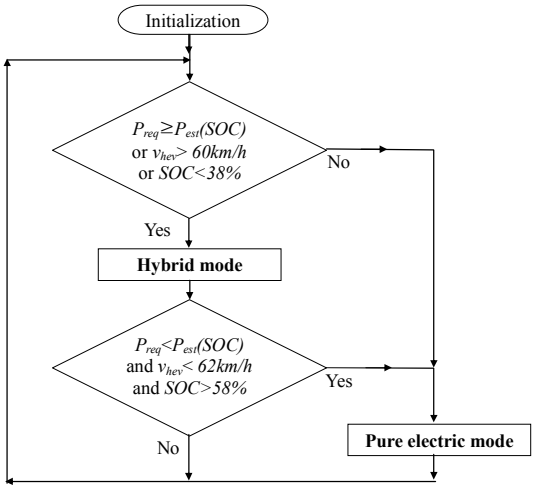

Figure 4.8 Strategy overview used in the simulation of the Toyota Prius II

According to the operation modes in this flowchart, the strategy level (Figure 4.9) defines the ICE torque reference T_{ICE_ref} and the ICE speed reference Ω_{ICE_ref}.

Hybrid mode - The required vehicle power P_{req} is calculated as follows:

$$P_{req} = P_{trac\_req} + P_{bat\_req} \tag{4.6}$$

with P_{trac_req} the required traction power and P_{bat_req} the required battery power, which depends on the SOC, defined by the Battery Management System (BMS). The function P_{est}(SOC) is the available battery power based on the SOC [Vinot 2008]. When the ESS can not supply the traction power ($P_{req} \geq P_{est}$(SOC)), or the vehicle velocity is higher than 60km/h (v_{hev}>60km/h), or the ESS needs to be recharged (SOC<38%), the HEV runs in hybrid mode. The ICE power reference P_{ICE_ref} is given by:

$$P_{ICE\_ref} = P_{req} + P_l = P_{trac\_req} + P_{bat\_req} + P_l \tag{4.7}$$

with P_l the estimated system losses. The ICE torque reference T_{ICE_ref} and the ICE speed reference Ω_{ICE_ref} are obtained using an optimal torque/speed characteristic.

Pure electric mode - When the ESS can supply the traction power ($P_{req} < P_{est}$(SOC)), or the vehicle velocity is lower than 60km/h (v_{hev}>60km/h), or the ESS does not need to be recharged (SOC>58%), the HEV runs in pure electric mode. There is no fuel injection for the ICE. The ICE speed Ω_{ICE_ref} is zero, and it imposes a resistance torque.

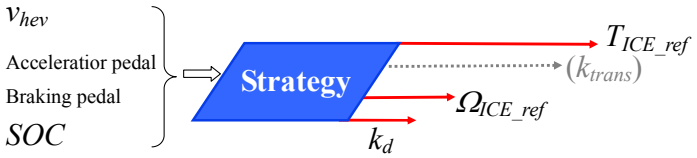

Figure 4.9 Strategy level of the unified control

The output of the transmission ratio k_{trans} is not used in series-parallel HEVs, because a fixed reduction gear is used. The distribution between mechanical braking and propulsion machines is defined by k_d. The braking forces distributed on different wheels vary according to

the vehicle's driving conditions [Ehsani 2010]. Since the common EMR uses only one equivalent wheel model, the braking forces distribution on different wheels is not taken into account. When only the electric braking is used (as soon as the accelerator pedal is released), k_d=1. When the hybrid braking is used (more rapid deceleration is required, or the braking pedal is added) , $0<k_d<1$.When only mechanical braking is used, k_d=0.

Comparisons of the SOC and the instantaneous consumption are given below. Three cases are presented: initial SOC of 55.8% in Figure 4.10, initial SOC of 70% in Figure 4.11, and initial SOC of 20% in Figure 4.12. The SOC difference (ΔSOC) is calculated by:

$$\Delta SOC = \frac{SOC_{EMR} - SOC_{VEHLIB}}{SOC_{VEHLIB}} \tag{4.8}$$

with SOC_{VEHLIB} calculated using VEHLIB, and SOC_{EMR} calculated using the common simulation results. In the three cases, the SOC difference is less than 5% (Figure 4.10, Figure 4.11 and Figure 4.12, b).

With respect to the instantaneous fuel consumption, differences occur during transient states (Figure 4.10, Figure 4.11, Figure 4.12, c). They are caused firstly by the use of different controllers in the two simulation programs, and secondly by issues related to accuracy regarding the fuel consumption map (g/s). Two scalar independent controllers are used in the VEHLIB simulation program. However, one vectorial controller is used in the common simulation program (see IV.1.1.3.B).

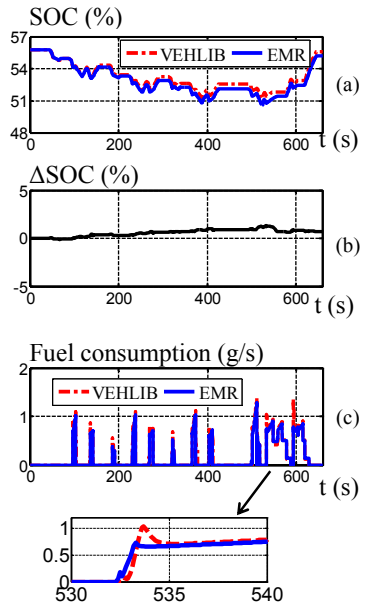

Figure 4.10 SOC and instantaneous consumption for 1015 cycle with initial SOC of 55.8%

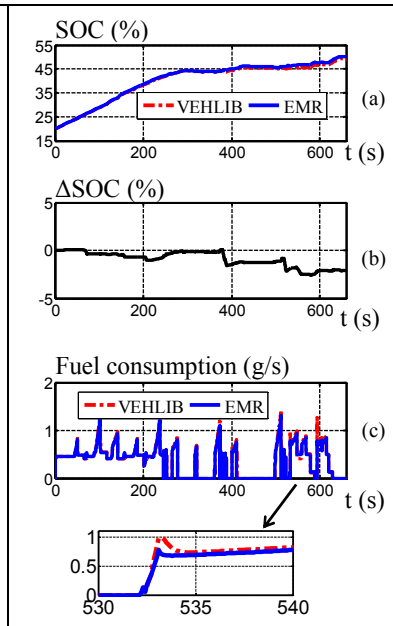

Figure 4.11 SOC and instantaneous consumption for 1015 cycle with initial SOC of 20%

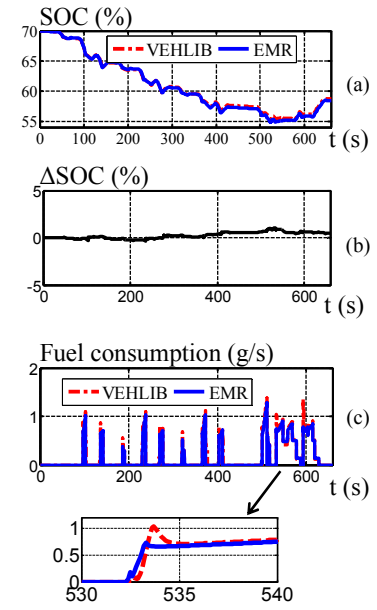

Figure 4.12 SOC and instantaneous consumption for 1015 cycle with initial SOC of 70%

(a) SOC (b) SOC differences between the two simulations (c) Instantaneous fuel consumption (d) Zoom of instantaneous fuel consumption

C. Validation for NEDC

A simulation based on the common EMR and the unified control for New European Driving Cycles (NEDC) ((Figure 4.13. a) has been also carried out. The SOC, the machines' power, and the mechanical braking are shown in Figure 4.13. The maximum SOC difference between the common program simulation and the VEHLIB simulation is 3.45%. The final fuel consumption is 0.35 liters using the common program, compared to 0.36 liters using the VEHLIB simulation. In both simulations, the auxiliary consumption is removed. Most of power flows mentioned in Chapter III can be found. For example, during the EUDC (between 800s-1100s), the SOC is constant (Figure 4.13. b). The ICE supplies all the traction power through the two paths: the first path is from the ICE to the driven wheels; the second path starts at the ICE, and continues to EM1 (EM1 power negative, Figure 4.13. d), and finally to EM2 (EM2 power positive, Figure 4.13. e) through the DC bus.

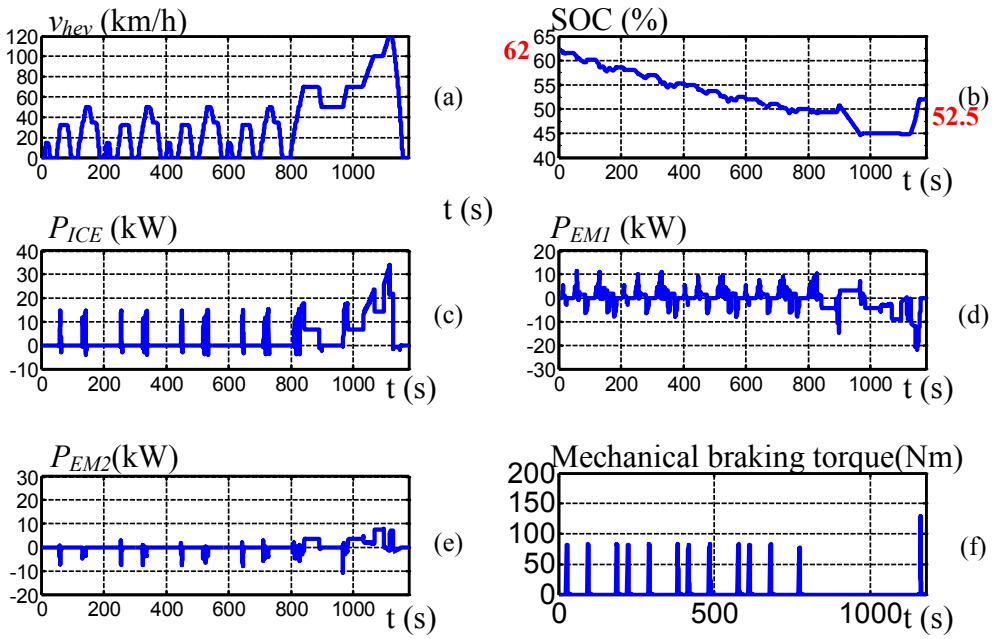

Figure 4.13 Simulation results of the common simulation program for the Toyota Prius II during a NEDC (a) New European Driving Cycle (NEDC), (b) SOC, (c) ICE power, (d) EM1 power, (e) EM2 power, (f) Mechanical braking torque

IV.1.1.5. Conclusion

In this part, the common EMR and the unified control scheme have been validated by simulation in the case of the Toyota Prius II. The simulation results in MATLAB-Simulink™ have been compared with those of VEHLIB. The VEHLIB simulation results are very close to the measurements of a real Toyota Prius II [Vinot 2008]. Therefore, our simulation program has been validated by comparing it with the VEHLIB simulation results. The comparison between the two simulations shows good coherence.

In the next subsection, the unified control scheme will be implemented in a dSPACE

system to be checked in a real-time environment. A series HEV using Hardware-In-the-Loop (HIL) simulation will be discussed.

IV.1.2. Real-time validation

In the first subsection, a MATLAB-Simulink™ program has been established with the help of the common EMR and the unified control scheme. Setting different values for certain parameters, the same program can be used for the simulation of three types of HEVs. It has already been validated by simulation for the Toyota Prius II (see IV.1.1). In this subsection, the unified control will be validated in a real-time environment. It is implemented in a dSPACE 1103 control board for a series HEV using Hardware-In-the-Loop (HIL) simulation.

IV.1.2.1. Test bench for a series HEV

The unified control is implemented in a dSPACE system to control a series HEV. This experimentation is done on the L2EP test bench (see Appendix 7).

Because parts of the real process are not available, HIL simulation is used [Isermann 1999] [Bouscayrol 2008] [Bouscayrol 2010]. The HIL principle can be found in Chapter I.

The traditional ESS of HEVs uses batteries. The batteries are replaced by a supercapacitor-based ESS (Scaps in Figure 4.14). Since supercapacitors have a much longer life cycle and faster power responses than batteries, they can be used to test the unified control scheme in real time. Moreover, the charge and discharge of the ESS will be better highlighted. For security reasons, a braking resistor is usually required in the supercapacitor-based ESS. This is not discussed here. The control of this ESS can be found in [Lhomme 2009].

Since the vehicle part from the transmission to the wheels is not available, an Induction Machine (IM1) and its Voltage-Source-Inverter (VSI1) are used for the HIL simulation of those components from the transmission to the wheels. The ICE and EM2 are connected by a mechanical coupling in the series HEV. This mechanical coupling can be a common shaft, a gear or a belt. The ICE and this mechanical coupling are simulated by using another Induction Machine (IM2) and its Voltage-Source-Inverter (VSI2).

DC machine 1 (DCM1) and its chopper (chopper 1) are considered as the traction machine EM1 and its Power Electronics (PE 1) in the series HEV. DC machine 2 (DCM 2) and its chopper (chopper 2) are considered as the generator machine EM2 and its Power Electronics (PE 2). Since the machines (1.5 kW) in this test bench are much smaller than the real ICE, EM1 and EM2 (about 20 kW), power adaptations are used [Bouscayrol 2006-b] [Allegre 2010]. The purpose of the power adaptations is to reduce the torque and speed of the real process. This method allows the model and control, which have the same power as the real vehicle using reduced power devices, to be tested. Figure 4.15 illustrates the test bench for the series HEV.

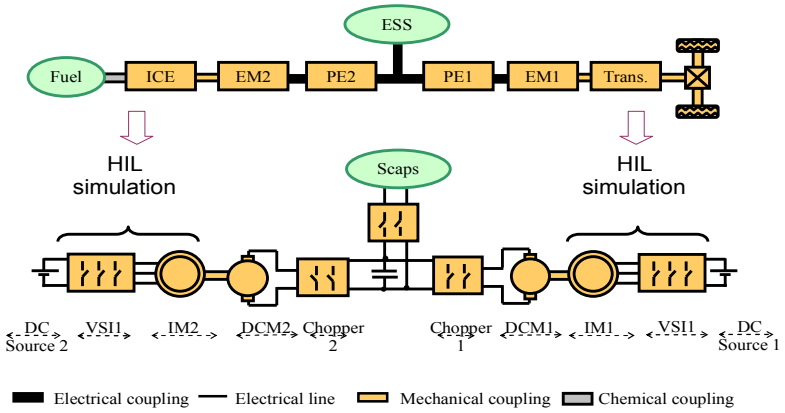

Figure 4.14 series HEV and its HIL simulation test structure

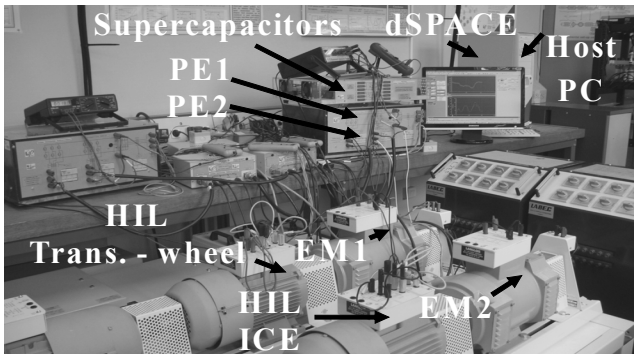

Figure 4.15 Test bench for Series HEV

IV.1.2.2. Real-time implementation

A. Program organization

The HIL simulation structure is shown in Figure 4.16. Its implementation in the dSPACE control board is shown in Figure 4.17. The unified control tested in the DSPACE control board is shown in (Figure 4.18). The models for HIL simulation (Figure 1.12, purple blocks) are established with the help of the reorganized EMR for series HEVs (see Figure 3.18). The HIL simulation parts must have the same characteristics as the real components of the process (for example, impose the same torque with the same dynamics).

Because of the limits of dSPACE 1103, two interruption levels are used. The sampling period of the first interruption is fixed at 50 μs to manage securities, send modulation references to PWM circuits and treat measurements. The second interruption deals with the unified control, and HIL simulation programs. Its sampling period is fixed at 500 μs.

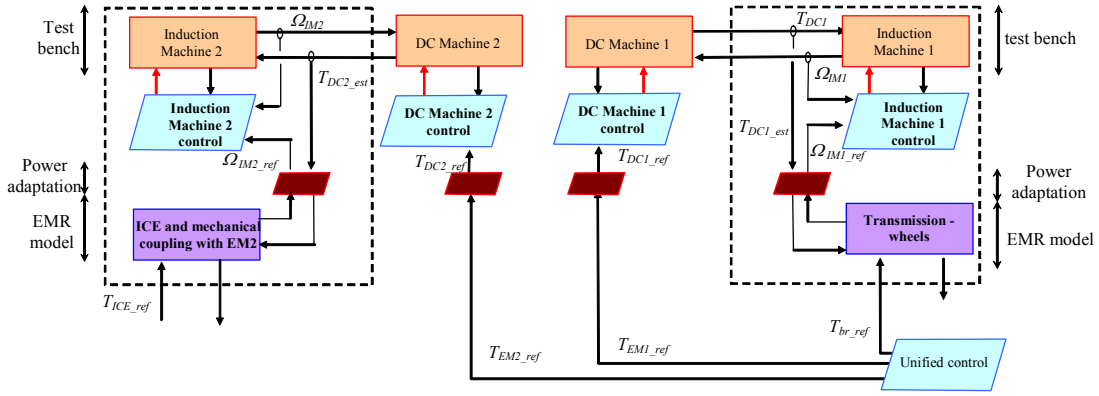

Figure 4.16 HIL simulation structure for the series HEV

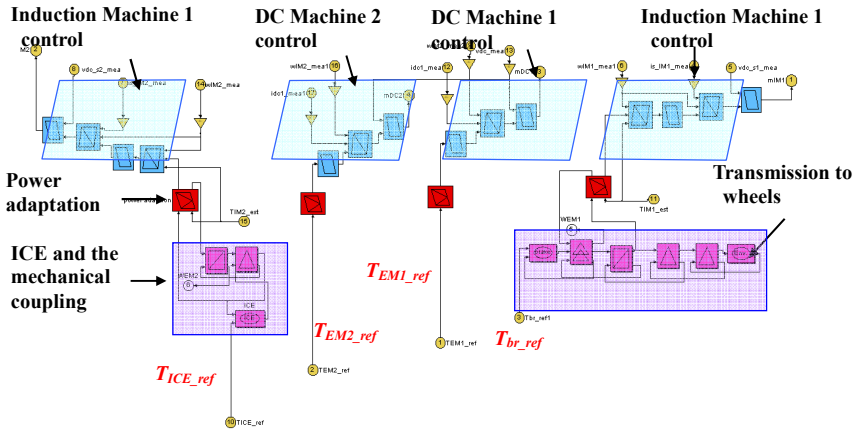

Figure 4.17 HIL simulation in the dSPACE control board

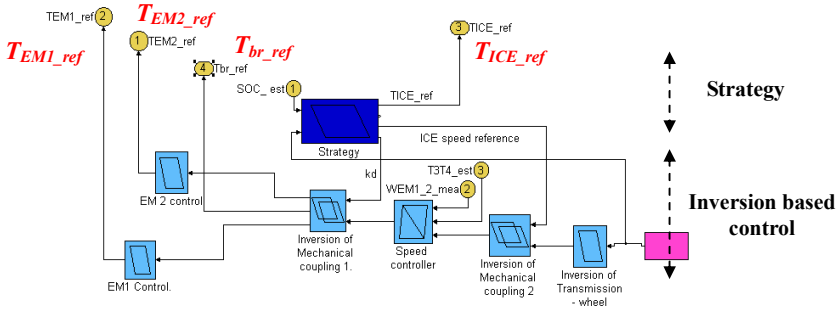

Figure 4.18 Unified control in the dSPACE control board

IV.1.2.3. Experimental results

The objective of this part is to study the main power flows in a real-time environment (see III.2.4.2).

Two repeated UDCs are used (Figure 4.19, a). The DC bus voltage is controlled such that it remains constant (250V) to ensure the EMs' torque and speed (Figure 4.19. b). The

control and energy management of the supercapacitor-based ESS has been established in [Lhomme 2009]. Since the supercapacitor voltage u_{SC} represents the supercapacitor energy state ($E_{SC} = \frac{1}{2} C_{SC} u_{SC}^2$), the supercapacitor voltage replaces the SOC for batteries. The supercapacitor voltage u_{sc} is kept between 130V and 140 V (Figure 4.19. d). The range used here (only 10V) is simply to check the unified control in the real-time environment.

In this study, the ICE is turned on or off based on the supercapacitor voltage. When the supercapacitor voltage reaches its lowest value (u_{SC_l} =130V), the ICE operates in order to charge the supercapacitor to its highest value (u_{SC_h} =140V).

Contrary to the classical Thermostat strategy [Anderson 1995] [Hochgraf 1996] [Jalil 1997], here, the ICE speed and torque references are given to find all main power flows, not to achieve the energy management. The ICE speed reference is constant (Figure 4.19. e), however the ICE torque reference is variable for the power flow study purpose.

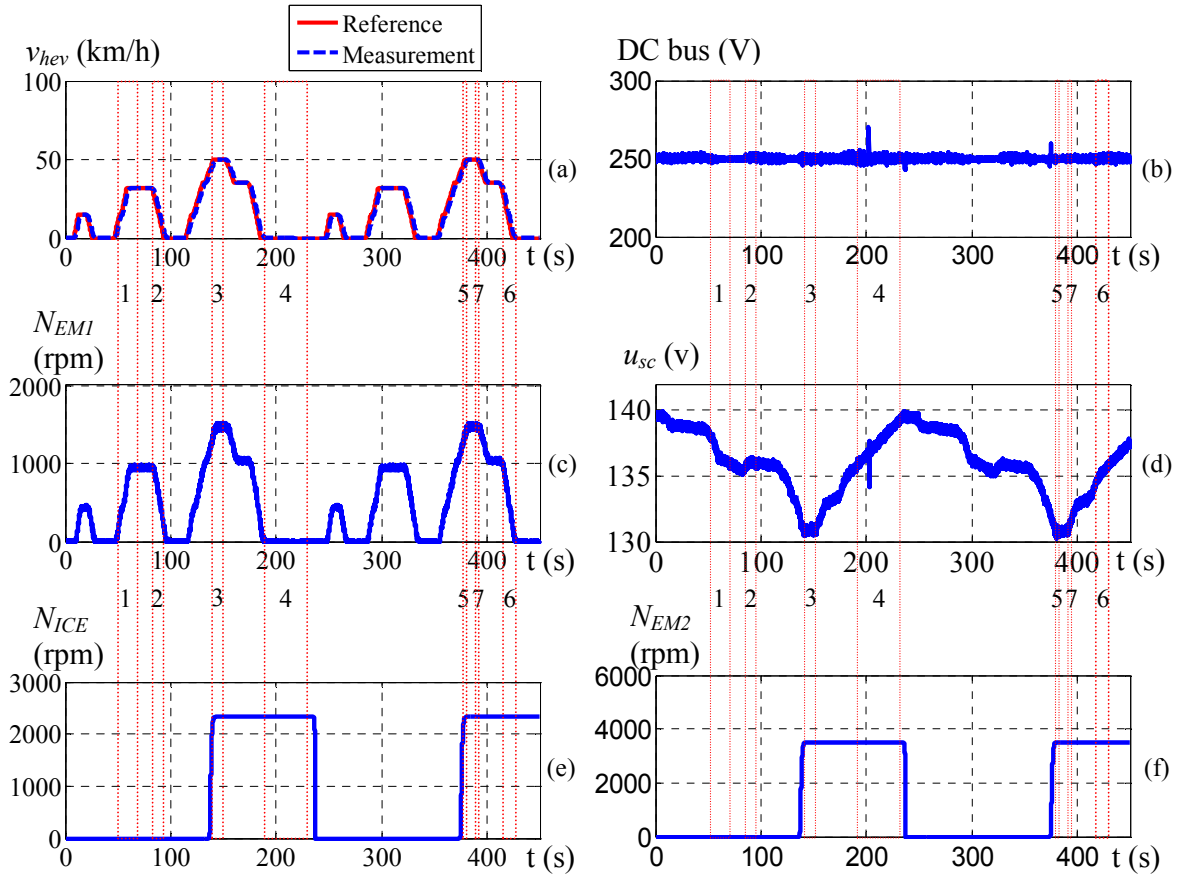

Figure 4.19 Experimental results for the power flow study
(a) Vehicle velocity, (b) DC bus voltage, (c) EM1 speed, , (d) Supercapacitor voltage, (e) ICE speed, (e) EM2 speed

The EM1 speed is proportional to the vehicle velocity (Figure 4.19, c), because the EM1 is connected directly to the transmission shaft in series HEVs. The EM2 speed is proportional to the ICE speed (Figure 4.19, d), as the ICE and EM2 are connected by a mechanical coupling.

The experimental results show the 7 main power flows discussed in chapter III (Figure 4.19). Different power flows can be found several times. Only one example for each power flow is numbered in Figure 4.19. For example, between 48s and 84s, the power flow is pure electric traction power flow (power flow 1): the ICE is shut down; all traction power comes from the ESS; the supercapacitor voltage decreases. Between 420s and 430s, power flow 6 (Hybrid charging) occurs: the vehicle decelerates; the ICE operates; the supercapacitor voltage increases; the ESS is charged through two paths: one by the electrical braking, another by the ICE.

IV.1.2.4. Different strategies

The objective of this part is to show that different strategies can be easily conducted and compared in the real-time environment using the unified control.

The unified control, as is the case for all inversion-based controls deduced from EMR, is composed of two parts: the inversion-based control part (local level) and the strategy level (energy management of the whole system). The same control structure is kept. The local level parts are the same. At the strategy level, different strategies are used. The strategy level defines the ICE torque reference T_{ICE_ref}, the ICE speed reference Ω_{ICE_ref}, and k_d which distributes the power between the mechanical braking and EM1 (Figure 4.9).

Three different strategies are checked in the real-time environmental for the same driving cycle (UDC). Since the vehicle velocity is not high for this cycle, the vehicle velocity will not be considered for the ICE operating condition. Regarding all these strategies, the DC bus voltage is maintained at 250V.

Simple thermostat strategy – This is a classical thermostat strategy [Anderson 1995] [Hochgraf 1996] [Jalil 1997]. The only difference between this strategy and the previous strategy used in the power flow study is the ICE torque reference. In the previous power flow study, the ICE operates at constant speed but variable torque in order to find all main power flows. Using this simple thermostat strategy, the ICE operates at constant power using constant speed and torque references (Figure 4.21, b). This optimal power point can be defined using different methods considering the forecasted drive power, the required battery charging power and minimum specific fuel consumption [Barsali 2002]. The ICE is simulated by Induction Machine 2 of the test bench. The ICE power is reduced using a power adaptation block.

When the required braking torque is low and the supercapacitor voltage is within its allowable range, the ESS is charged by the braking energy using k_d=1. When the required braking torque is greater than certain values, the mechanical braking is added ($0 \leq k_d < 1$). Between 176s and 188s, the vehicle decelerates. At this moment, the supercapacitor voltage reaches its highest value. The ESS can not absorb the braking energy. The mechanical braking is used (Figure 4.21. c).

The initial supercapacitor voltage is 140V, and the final value is 139 V. The fuel consumption of the HIL simulation is 0.033 liters.

Improved thermostat strategy – This is an improved thermostat strategy. Different from the simple thermostat strategy, the ICE disengagement condition is not a fixed value u_{SC_h}, but a variable one u_{SC_m} (Figure 4.20) which is a function of the vehicle velocity v_{hev}.

If the vehicle decelerates after t_2 (Figure 4.20, possibility 1), the maximum braking energy E_{br_est} is estimated by:

$$E_{br\_est} = \frac{1}{2} M v_{hev\_mea}^2 \tag{4.9}$$

with M the vehicle mass and v_{hev_mea} the vehicle velocity measurement. This equation estimates the maximum braking energy at the speed v_{hev_mea}. If this braking energy can be totally aborbed to increase the supercapacitor voltage to its highest value u_{SC_h} (considering losses and system limitations):

$$R_{est} E_{br\_est} = \frac{1}{2} C_{SC} u_{SC\_h}^2 - \frac{1}{2} C_{SC} u_{SC\_m}^2 \tag{4.10}$$

with R_{est} the estimated reduction coefficient which depends on the system losses and the system limitation. The ICE disengagement condition u_{SC_m} is therefore defined as:

$$u_{SC\_m} = \sqrt{u_{SC\_h}^2 - \frac{R_{est}}{C_{SC}} \frac{1}{2} M v_{hev\_mea}^2} \tag{4.11}$$

In this way, the ICE stops to "make a reservation" for the supercapacitor to be charged by the electric braking.

If vehicle accelerates after t_2 (Figure 4.20, possibility 2), the supercapacitor voltage decreases because the ICE is shut down. The ICE will restart when the supercapacitor voltage reaches u_{SC_l}.

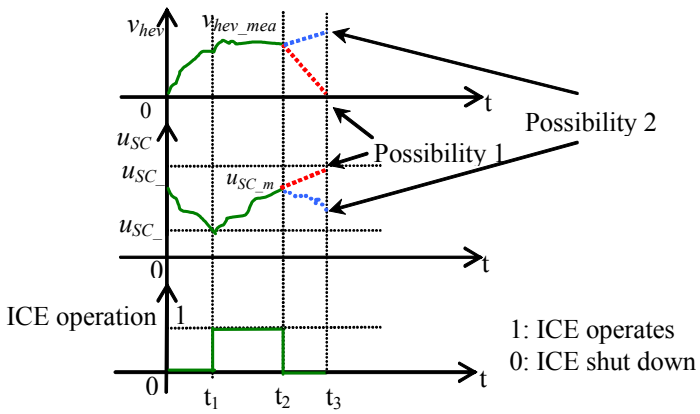

Figure 4.20 Improved thermostat strategy

As is the case for the simple thermostat strategy, the ICE operates at one optimal point (constant ICE power) (Figure 4.22, b). Contrary to the simple thermostat strategy, the ICE does not stop at u_{SC_h} (Figure 4.22, a). Thus, at the end of this cycle, the supercapacitor is charged by the electrical braking. During this cycle, there is no mechanical braking ((Figure 4.22, c). This strategy ensures the maximum electrical braking. The initial supercapacitor voltage is 140V,

and the final value 139 V. The fuel consumption of the HIL simulation is 0.027 liters.

"Power thermostat" strategy – The ICE operation condition depends on the required power P_{req} using (4.6), which is composed of the required traction power and the required ESS charging power. If the required power P_{req} is greater than its highest value P_{req_h} , the ICE operates. When the required power is less than its lowest value $P_{req\_l,}$ the ICE is shut down, and the vehicle is in all electric mode. According to the required power P_{req}, the ICE operates at its optimal characteristics (Figure 4.23.d). Contrary to the simple thermostat strategy and improved thermostat strategy, the ICE power is not constant. The initial supercapacitor voltage is 140V, and the final value 139 V. The fuel consumption of the HIL simulation is 0.03 liters.

A summary of the three strategies is given in Table 4.3. Concerning the supercapacitor voltage, the three strategies have the same final voltage with the same initial voltage. But the total consumptions are not the same. The improved thermostat strategy has the best fuel economy. Concerning the supercapacitor voltage, the "Power thermostat" strategy has the smallest voltage change.

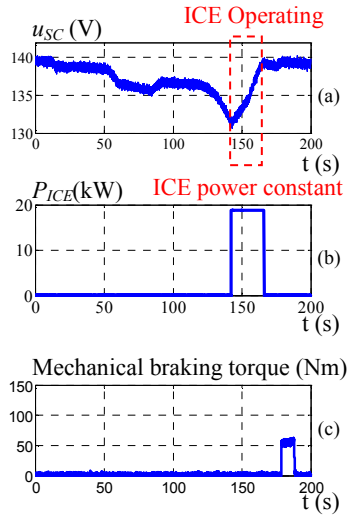

Figure 4.21 Simple thermostat

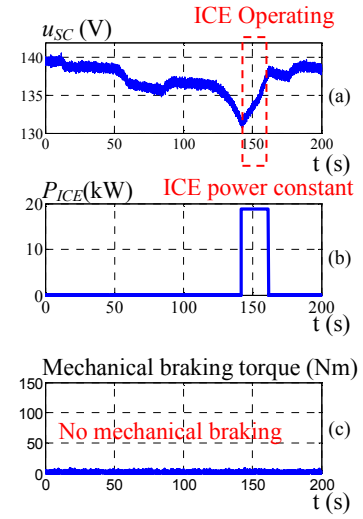

Figure 4.22 Improved thermostat

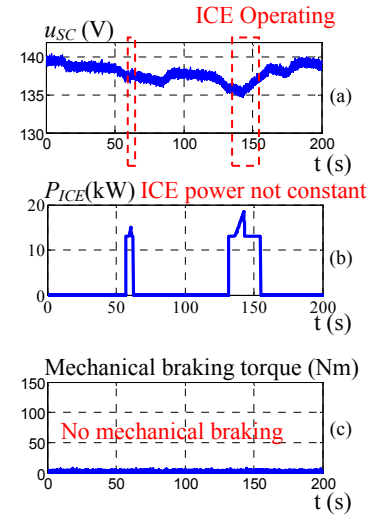

Figure 4.23 "Power thermostat"

(a) Supercapacitor voltage, (b) ICE power, (c) Mechanical braking torque

Table 4.3. Strategy comparisons for a series HEV using HIL simulation during UDC

Strategy	Initial u_{SC} (V)	Final u_{SC} (V)	Δu_{SC} (V)	Total fuel consumption (liters)
Simple thermostat	140	139	10	0.033
Improved thermostat	140	139	10	0.027
"Power thermostat"	140	139	5	0.03

The objective of this part is simply to show different strategies can be implemened

and compared in a real-time environment using this unified control. Other studies can be found which deal with optimal strategies [Barsali 2004]. For example, the DC bus is maintained constant in all experimentations here. But the DC bus voltage can be variable. Using a variable DC bus strategy, the Toyota Prius II can reduce by about 3% the converter losses [Olszewsky 2006]. In the case of supercapacitor-based ESSs, another advantage of using a variable DC bus is the potential to resolve the supercapacitor stability problem. The maximum voltage ratio (v_{dc}/u_{SC}) depends on the traction current required by the vehicle [Lhomme 2009]. The DC bus can be variable, depending on the stability and losses. For example, one IGBT can be blocked when the vehicle brakes at relatively low velocity. In this case, the voltages on both sides of the converter are close to being equal (v_{dc}/u_{SC} is close to 1), then the system is within its stable zone. At the same time, the switching losses are reduced.

IV.1.2.5. Conclusion

The unified control scheme has been implemented in a dSPACE 1103 control board. It was tested for a series HEV. Since parts of the real process are not available, a HIL simulation was used. Despite the use of many control blocks in the experimentation, the main power flows of series HEVs have been studied in the real-time environment. Using this unified control, different strategies have been checked and compared. The developed unified control can really be implemented in the real-time environment.

To validate the ESS control part in a real time environment, a real battery based ESS can replace this supercapacitor based ESS. These two kinds of electrical energy storage sources can also be mixed in order to study them [Allegre 2009] [Camara 2008] [Camara 2010].

It should be note that relative simple models are used for the mechanical parts and the ICE in the HIL simulation. More detailed models could be used for the robustness and stability study in the future research. The driver is included in the vectorial controller of the unified control scheme in this thesis. The driver behavior could be also taken into account.

In this section, the common EMR and the unified control scheme have been validated both by simulation and in a real-time environment by experimentation. In the next section, extensions of the common EMR and the unified control will be discussed.

IV.2. Extension to other applications

In the first section of this chapter, the common EMR and the unified control have been validated both by simulation and by experimentation. In this section, applications of the common EMR and the unified control will be extended to other HEVs. Two examples are discussed: first, a series parallel HEV using two arranged EMs; second, a parallel HEV using a Continuously Variable Transmission (CVT) and a clutch.

IV.2.1. Extension to two arranged EM type HEVs

In this part, the extension of the common EMR and the unified control is discussed in the case of series-parallel HEVs using two arranged EMs. First, a series-parallel HEV using two arranged EMs is presented. Second, the extension of the application on this HEV is detailed. By simply changing certain parameter values, the common EMR and the unified control scheme can be adapted to this HEV. Third, using the common simulation program based on the common EMR and the unified control, a comparison between this HEV and the Toyota Prius type HEV is conducted.

IV.2.1.1. Series-parallel HEVs using two arranged EMs

Rather than using a planetary gear, some special EMs can be used as power-split devices for series-parallel HEVs, such as EMs with double rotors [Hoeijmakers 2006] [Chau 2007] [Zheng 2007]. A simpler option is to use a combination of two concentrically arranged EMs [Cheng 2007] (Figure 4.24, EM1 and EM2). EM1 is a classical machine, whereas EM2 is a special machine: the EM2 stator is internal and can rotate; the EM2 rotor is external. The rotors of both EMs and the transmission have a common shaft.

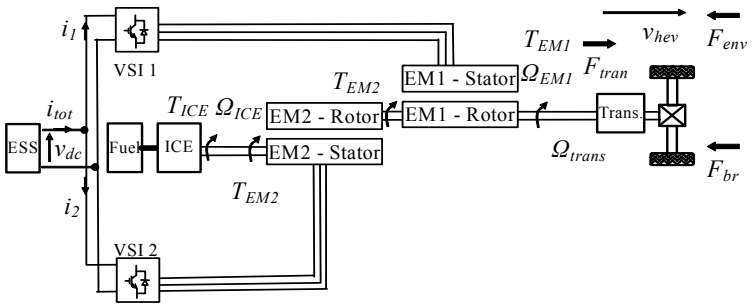

Figure 4.24 Series-parallel HEVs using two concentrically arranged EMs

Like series-parallel HEVs using a planetary gear, the two stators are fed separately by two Voltage Source Inverters (VSIs) which have a common DC bus. The DC bus is supplied by the ESS. While different power split devices are used in both series-parallel HEVs, the energy nodes are located both in the electric coupling (the DC bus) and in the mechanical coupling (planetary gear set or the mechanical coupling of the two rotors). The EM1 speed in both HEVs is proportional to the vehicle velocity. The ICE speed can be chosen independently of the vehicle velocity. This is the reason why this system is also called an Electrical Continuously Variable Transmission (E-CVT or EVT), as is also the case for Toyota Prius type HEVs. The

transmission (Trans.) is therefore a fixed reduction gear. At a given vehicle velocity, the EM2 speed can be controlled to adjust the ICE speed. The ICE can thus operate within its optimal region.

IV.2.1.2. EMR and control scheme of two arranged EM type HEVs

The main difference between the two series-parallel HEVs is in the mechanical couplings. The speed of an EM is the difference between the rotor speed and its stator speed. The EM2 rotor speed Ω_{EM2_r} is equal to the EM1 speed Ω_{EM1}, because the EM2 rotor and the EM1 rotor are connected together. Since the EM2 "rotating" stator is connected to the ICE, the EM2 stator speed Ω_{EM2_s} is equal to the ICE speed Ω_{ICE}. So the EM2 speed is the difference between the EM1 speed and the ICE speed [Cheng 2007][Cheng 2009-a]:

$$\Omega_{EM2} = \Omega_{EM2\_r} - \Omega_{EM2\_s} = \Omega_{EM1} - \Omega_{ICE} \tag{4.12}$$

The shaft torque-seed relationships can be calculated in the same way as for the Toyota Prius type HEVs. If the inertia of the EM2 "rotating" stator is ignored, the shaft equations are (Figure 4.25) [Cheng 2007]:

$$(J_{EM1} + J_{eq} + J_{EM2})\frac{d}{dt}\Omega_{EM1} = -(f_{EM1} + f_{EM2})\Omega_{EM1} T_{EM1} + T_1 - T_3 \tag{4.13}$$

$$J_{ICE}\frac{d}{dt}\Omega_{ICE} = -f_{ICE}\Omega_{ICE} + T_2 - T_4 \tag{4.14}$$

$$\text{with } T_1 = T_{EM1} + T_{EM2} - T_{br},\ T_2 = -T_{EM2},\ T_3 = T_{res} \text{ and } T_4 = -T_{ICE} \tag{4.15}$$

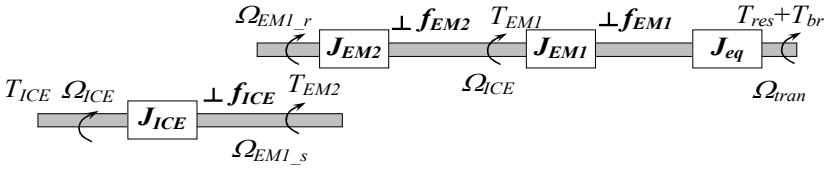

Figure 4.25 Shafts in HEVs using two arranged EMs

A. EMR of two arranged EM type HEVs

Since the EM1 is connected directly to the transmission shaft, equation (3.29) in chapter III describes this relationship using k_7=1.

Similar to series-parallel HEVs using a planetary gear, 2 basic speed variables are enough to represent all speed variables. If the Ω_{EM1} and Ω_{EM2} are chosen as basic state variables, (4.13) and (4.14) can be rewritten in matrix form. The generic matrix equation (3.30) for the common EMR can represent HEVs using two arranged EMs. The different values of *[J]* and *[f]* are used as follows:

$$[J] = \begin{bmatrix} J_{EM1} + J_{EM2} + J_{eq} & \mathbf{0} \\ J_{ICE} & -J_{ICE} \end{bmatrix} \text{ and } [f] = \begin{bmatrix} f_{EM1} + f_{EM2} & \mathbf{0} \\ f_{ICE} & -f_{ICE} \end{bmatrix} \tag{4.16}$$

Since the torque combinations are different in the two series-parallel HEVs, the matrices in the equation of mechanical coupling ① are different:

$$\begin{cases} \begin{bmatrix} T_1 \\ T_2 \end{bmatrix} = \begin{bmatrix} 1 & -1 & 1 \\ 0 & 0 & -1 \end{bmatrix} \begin{bmatrix} T_{EM1} \\ T_{br} \\ T_{EM2} \end{bmatrix} \\ \begin{bmatrix} \Omega_{EM1} \\ \Omega_{tran} \\ \Omega_{EM2} \end{bmatrix} = \begin{bmatrix} 1 & 0 \\ 1 & 0 \\ 0 & 1 \end{bmatrix} \begin{bmatrix} \Omega_{EM1} \\ \Omega_{EM2} \end{bmatrix} \end{cases} \tag{4.17}$$

The EM1 is connected directly to the transmission shaft. The matrices in the equation of mechanical coupling ② are different:

$$\begin{cases} \begin{bmatrix} T_3 \\ T_4 \end{bmatrix} = \begin{bmatrix} 1 & 0 \\ 0 & -1 \end{bmatrix} \begin{bmatrix} T_{res} \\ T_{ICE} \end{bmatrix} \\ \begin{bmatrix} \Omega_{tran} \\ \Omega_{ICE} \end{bmatrix} = \begin{bmatrix} 1 & 0 \\ 1 & -1 \end{bmatrix} \begin{bmatrix} \Omega_{EM1} \\ \Omega_{EM2} \end{bmatrix} \end{cases} \tag{4.18}$$

In this way, the common EMR (see Figure 3.22) describes this HEV. Only the values of *[J]*, *[f]* and the matrices in the mechanical coupling elements are different to the case of series-parallel HEVs using a planetary gear. The EMR can be reorganized by choosing different state variables (for example, choosing Ω_{EM1} and Ω_{ICE}). Thereby, the vectorial accumulation element of the common EMR can be replaced by two independent scalar accumulation elements [Chen 2008-b].

B. Control scheme of two arranged EM type HEVs

The two types of series-parallel HEVs have many common points. The common EMR can describe both series-parallel HEVs using different parameter values. Thereby, the unified control scheme (see Figure 3.22) can also be applied to series-parallel HEVs using two arranged EMs.

The vectorial speed controller of the unified control scheme is the same (3.44), whereas the values of [*J*] and [*f*] are different and calculated by (4.16) here. The torque T_{3_mea} and T_{4_mea} can be compensated using (4.15). The matrices in the mechanical couplings are different from those in series-parallel HEVs using a planetary gear. From (4.18), the inversion of mechanical coupling ② is:

$$\begin{bmatrix} \Omega_{EM1\_ref} \\ \Omega_{EM2\_ref} \end{bmatrix} = \begin{bmatrix} 1 & 0 \\ 1 & -1 \end{bmatrix}^{-1} \begin{bmatrix} \Omega_{tran\_ref} \\ \Omega_{ICE\_ref} \end{bmatrix} = \begin{bmatrix} 1 & 0 \\ 1 & -1 \end{bmatrix} \begin{bmatrix} \Omega_{tran\_ref} \\ \Omega_{ICE\_ref} \end{bmatrix} \tag{4.19}$$

From (3.15), the inversion of mechanical coupling ① is:

$$\begin{cases} T_{EM1\_ref} = k_d (T_{1\_ref} + T_{2\_ref}) \\ T_{br\_ref} = -(1 - k_d)(T_{1\_ref} + T_{2\_ref}) \\ T_{EM2\_ref} = -T_{2\_ref} \end{cases} \tag{4.20}$$

The supplementary input k_d is defined at the strategy level to distribute the power between the mechanical braking and EM1. In this way, using different parameter values in the inversion of mechanical couplings, the unified control can be used in this type of HEVs.

Since the EMR can be reorganized by choosing different state variables, other control schemes can be used for this HEV. For example, in [Chen 2008-b], two simple scalar controllers are used, instead of one complex vectorial controller.

IV.2.1.3. Simulation results

Modifying the common simulation program mentioned in IV.1.1, the simulation in MATLAB-Simulink™ is carried out for series-parallel HEVs using two arranged EMs. There is no real commercial series-parallel HEV using 2 arranged EMs available. The same parameter values for the two EMs, ICE, transmission ratio k_{trans} and wheel radius R_{wh} are used in the simulation of both types (Toyota Prius type and two arranged EM type). Since both series-parallel HEVs have many common points, as shown by the common EMR, the power flow comparisons are carried out first [Chen 2009-c]. Second, the simulation results during a NEDC are shown using a strategy similar to that for the Toyota Prius II. Lastly, the limitations of both HEVs are discussed.

A. Simulation of power flows in both series-parallel HEVs

The simulations of the two series-parallel HEVs are made using the same cycle: an Extra Urban Driving Cycle (EUDC) as in Figure 4.26. Since the objective of the first stage is to find the main power flows in both HEVs, the same ICE power reference (Figure 4.27) is achieved by providing the same ICE torque T_{ICE_ref} and ICE speed references Ω_{ICE_ref}. These references are not relevant to the energy management, but are needed to check all the main power flows (See Chapter III.1.2). The same ICE power reference curve enables all the main power flows to be found. If the same ICE speed reference curve and the ICE torque reference curve are controlled, the ICE powers have the same form in the two cases. This means the same fuel consumption in both HEVs is achieved.

The evolution of the EM1 speeds in both HEVs is the same (Figure 4.28) and is proportional to the vehicle velocity, as the same transmission ratio k_{trans} and wheel radius are used. Since different speed equations are used in the two HEVs, the EM2 speeds are different. For HEVs using a planetary gear, Willis equation is used (Figure 4.28). For HEVs using two arranged EMs, (4.12) is used (Figure 4.30).

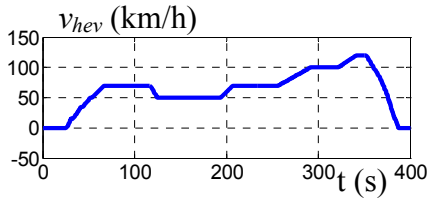

Figure 4.26 Extra-Urban Driving Cycle (EUDC)

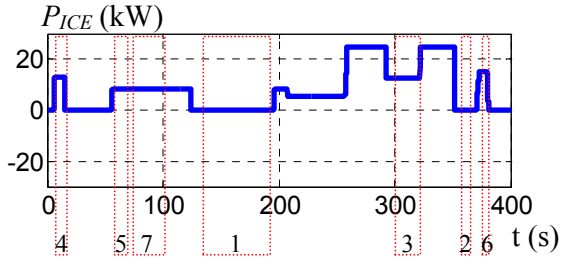

Figure 4.27 ICE power

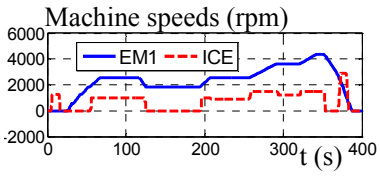

Figure 4.28 EM1 and ICE speeds

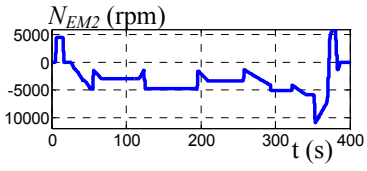

Figure 4.29 EM2 speed of Toyota Prius HEVs

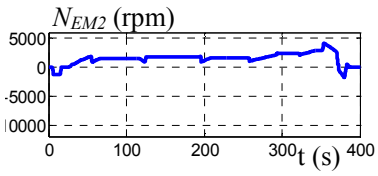

Figure 4.30 EM2 speed of HEVs using two arranged EMs

Both HEVs have the same basic power flows during this cycle using the same ICE power reference curve. Different power flows can be found several times. Only one example for each power flow is numbered (power flow 1-7, see III.2.4.2) [Chen 2009-c]. The power of the EMs and the SOC for HEVs using a planetary gear are shown in Figure 4.31, and for HEVs using two arranged EMs in Figure 4.32.

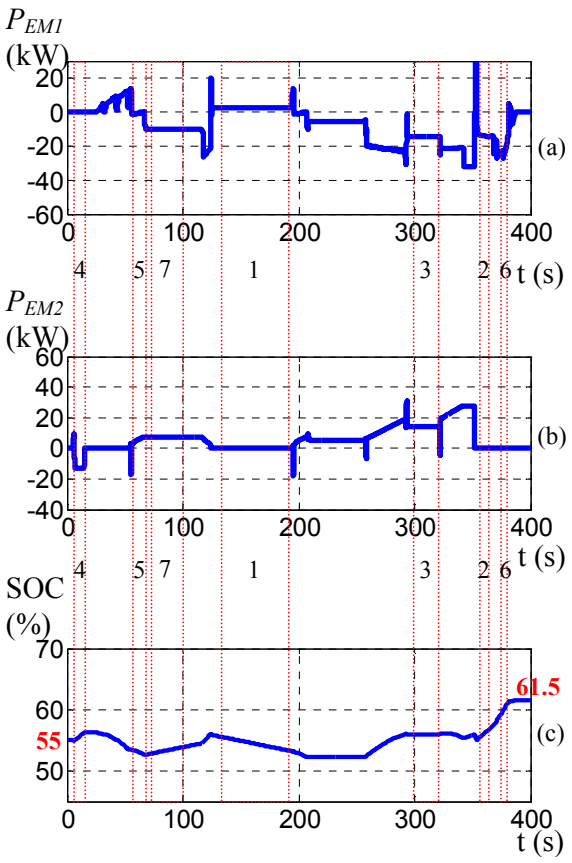

Figure 4.31 EMs' power and SOC for Toyota Prius type HEVs

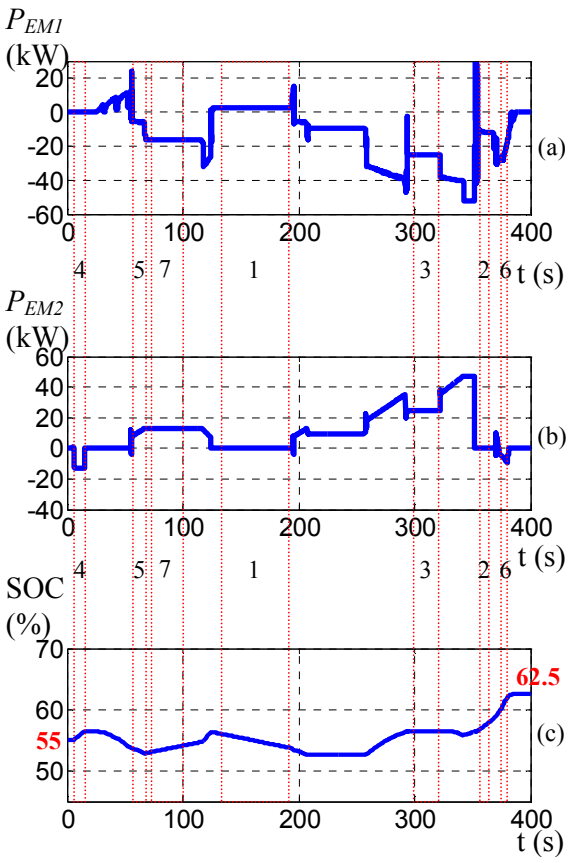

Figure 4.32 EMs' power and SOC for HEVs using two arranged EMs

(a) EM1 power (b) EM2 power (c) SOC

Given the same initial SOC (55%), the final SOC of both HEVs (61.5% for the Toyota Prius type, and 62.5% for the type using two arranged EMs) are very close. Simulation results for both series-parallel HEVs show that the two types have the same main power flows.

B. Simulation during a NEDC

Using the strategy presented in Chapter IV.1, the simulation results are shown in Figure 4.33 during a NEDC. The same parameters are used for the main components (EM1, EM2, ICE), the transmission ratio, wheel radius and vehicle mass as those for the Toyota Prius II. The auxiliary consumption is not taken into account. The same initial SOC (62%) is used. The final SOC is different: 56% for the two arranged EM type, and 52.5% for the Toyota Prius II. However the final fuel consumption is 0.41 liters for the two arranged EM type, and 0.36 liters for the Toyota Prius II. These differences are caused by the mechanical coupling differences. The ICE operation (Figure 4.34) shows that the ICE runs in its optimal region. Other strategies can be also used [Cheng 2009-b] [Salmasi 2007].

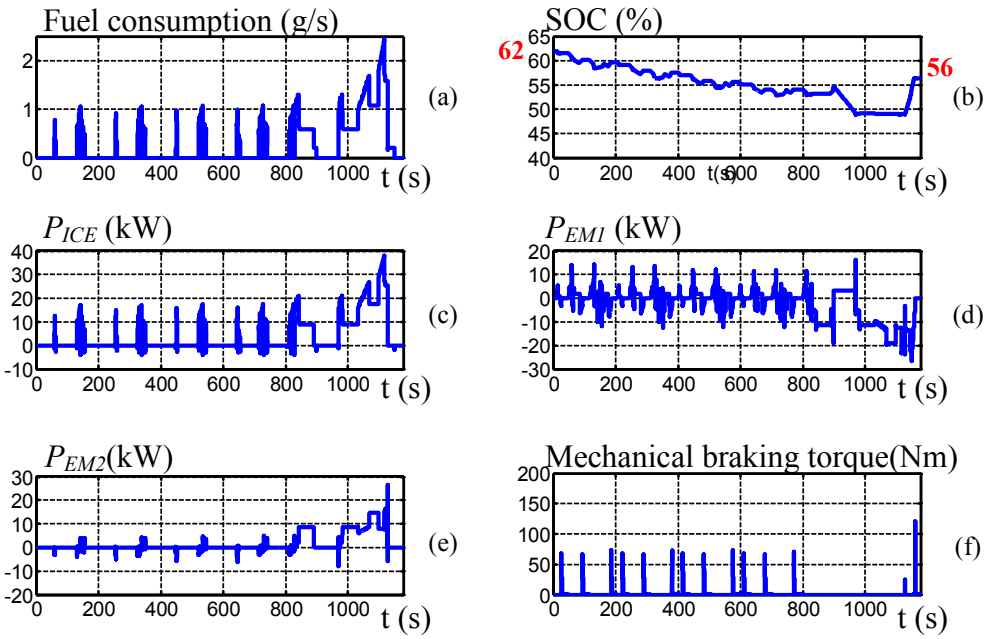

Figure 4.33 Simulation results for series-parallel HEVs using two arranged EMs during a NEDC
(a) Instantaneous fuel consumption (b) SOC (c) ICE power (d) EM1 power (e) EM2 power (f) Mechanical braking torque

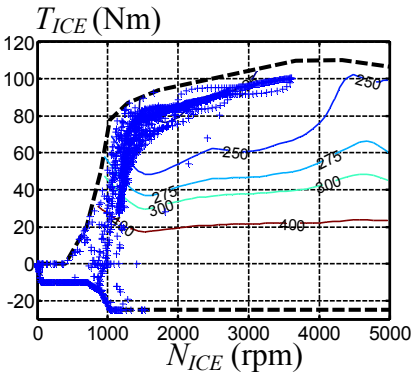

Figure 4.34 ICE operation of the two arranged EM type during a NEDC

C. *Discussion of the limitations of both series-parallel HEVs*

(1) ICE Speed limitation

For the Toyota Prius II, the EM2 speed is limited to 10,000 rpm (N_{EM2_max}=10,000 rpm). Using the planetary gear speed equation, the ICE speed range [Vinot 2008] is:

$$k_R N_{EM1} - k_S N_{EM2\_\max} < N_{ICE} < k_R N_{EM1} + k_S N_{EM2\_\max} \tag{4.21}$$

with k_R=0.7222 and k_S=0.2778. The EM1 speed is proportional to the vehicle velocity v_{hev} (km/h):

$$N_{EM1} = \frac{k_{trans}}{R_{wh}} \frac{\mathbf{1000}}{\mathbf{3600}} v_{hev} \frac{\mathbf{60}}{\mathbf{2\pi}} = \mathbf{36.2873}\, v_{hev} \tag{4.22}$$

with transmission ratio k_{trans}=4.113 and wheel radius R_{wh} = 0.3. The ICE speed range of the Toyota Prius II is:

$$\mathbf{26.2067} v_{hev} - \mathbf{2778} < N_{ICE} < \mathbf{26.2067} v_{hev} + \mathbf{2778} \tag{4.23}$$

The ICE speed limitation is considered at the strategy level.

If the same values of N_{EM2_max}, k_{trans} and R_{wh} are used in both series-parallel HEVs, from (4.12), the ICE of HEVs using two arranged EMs (type 2) is

$$N_{EM1} - N_{EM2\_\max} < N_{ICE} < N_{EM1} + N_{EM2\_\max} \tag{4.24}$$

$$\mathbf{36.2873}\, v_{hev} - \mathbf{10000} < N_{ICE} < \mathbf{36.2873}\, v_{hev} + \mathbf{10000} \tag{4.25}$$

From (4.23) and (4.25), the ICE speed ranges relative to the vehicle velocity of both HEVs are shown in Figure 4.35. It can be noted that the type using two arranged EMs has a greater ICE speed range than that of the Toyota Prius II, if the same parameters are used for N_{EM2_max}, k_{trans} and R_{wh} in both cases.

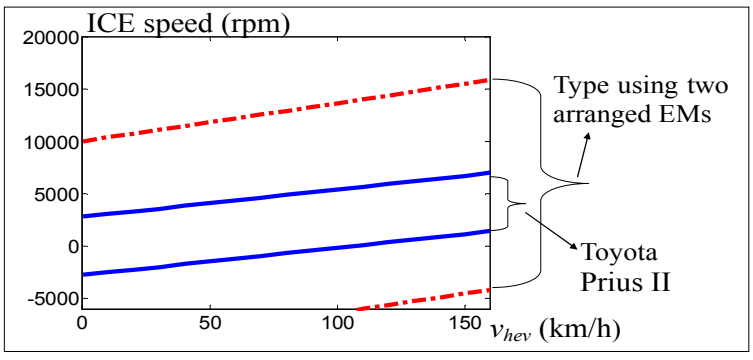

Figure 4.35 ICE speed ranges relative to the vehicle velocities

(2) Electric mode

For the Toyota Prius type, if no clutch is used between the ICE and the planetary gear, there is always a mechanical coupling between the ICE and EM1. When the vehicle operates in electric mode, the EM1 always has to overcome the resistance force from the ICE. For the type

using two arranged EMs, the ICE has neither mechanical coupling with EM1, nor with the transmission shaft. In electric mode, EM2 and the ICE are shut down. No energy is wasted in overcoming the ICE resistance, as for the Toyota Prius type. The efficiency of EMs is not discussed here.

(3) Machine dimension

Since there are no real commercial series-parallel HEVs using two arranged EMs, the simulations in this thesis use the same EM1, EM2 and ICE as for the Toyota Prius II. In fact, given the differences related to mechanical coupling for both series-parallel HEVs, machine dimensions should be different. For example, since EM2 and the ICE have a common shaft, the EM2 torque dimension should take into account the ICE torque, which is greater than the EM2 torque dimension for the Toyota Prius type. Such conception and optimization issues are studied to a greater degree by the MEGEVH-EVT project.

IV.2.1.4. Conclusion

Setting different values for certain parameters of the mechanical coupling elements and the vectorial accumulation element, the common EMR can describe series-parallel HEVs using two arranged EMs. The unified control scheme can therefore be used for this type of HEV given the corresponding parameter values. In this way, the common EMR and the unified control scheme are extended to new applications, such as series-parallel HEVs using two arranged EMs.

By simply modifying certain parameter values of the common simulation program mentioned in Chapter IV.1.1, simulations of this HEV type have been carried out in MATLAB-Simulink^{TM}. The power flow simulation results show the same main power flows are found for the two HEV types, i.e. the Toyota Prius type and the HEV type using two arranged EMs. Another simulation, during a NEDC, has also been conducted. The limitations of both HEVs have been briefly discussed. Given that the same control scheme is used, it is easier to compare the Toyota type and the two arranged EM type. The objective of this section is to extend the application of the common EMR and the unified control; more detailed comparisons are being undertaken by the MEGEVH-EVT project.

IV.2.2. Extension to a Parallel HEV using a CVT and a clutch

In this subsection, the extension of the common EMR and the unified control to a parallel HEV is discussed. This parallel HEV uses a CVT and a cut-out clutch. First, this parallel HEV is presented, along with a parallel HEV using two clutches. Second, the extended application of the common EMR and the unified control on this HEV is detailed. Third, using the modified common simulation program based on the common EMR and the unified control, a simulation of the parallel HEV using a CVT is carried out. The simulation results are compared with those for the parallel HEV using a discrete gearbox and two clutches.

IV.2.2.1. Parallel HEVs using a CVT and a clutch

For parallel HEVs, EM2 and the ICE based drivetrains are connected by a mechanical coupling, which can be a belt, a mechanical gear or a common shaft. Between the mechanical coupling and the ICE, a clutch (clutch 1) is usually required to cut out the ICE when necessary (Figure 4.36). The transmission can be a discrete gearbox or a CVT. A discrete gearbox, manual or automatic, typically offers between four and six gear choices. However, a CVT provides an infinite number of transmission gear ratios within its range. A CVT therefore offers great potential to increase the fuel economy by choosing an appropriate ratio between the ICE speed and the vehicle velocity.

If a discrete gearbox is used, a clutch (clutch 2) between the mechanical coupling and the transmission is generally required to adapt the change of transmission gear ratio (Figure 4.36). This discrete gearbox with clutch 2 can be replaced by a CVT (Figure 4.37).

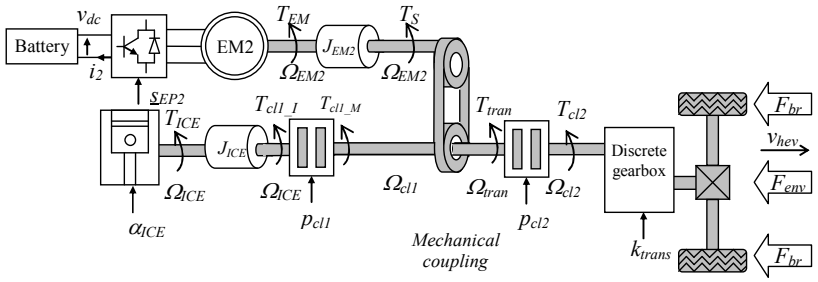

Figure 4.36 Parallel HEV using a discrete gearbox (figure from [Lhomme 2007])

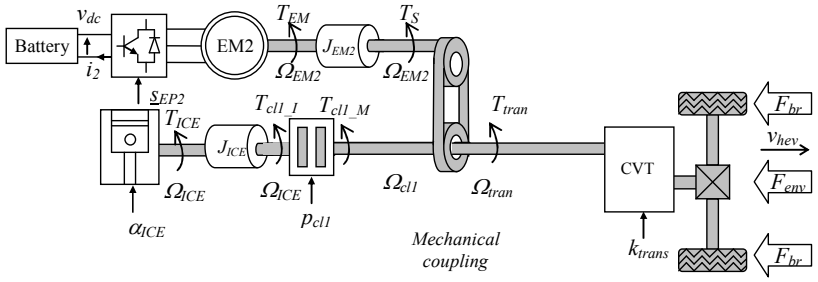

Figure 4.37 Parallel HEV using a CVT

IV.2.2.2. EMR and control scheme for the parallel HEV using a CVT

The common EMR introduced in chapter III can describe parallel HEVs with all clutches locked. By modifying certain elements, this modified EMR can represent the parallel HEV using a CVT. In the same way, the modified unified control can be used for this parallel HEV. Finally the control strategy is discussed.

A. EMR for the parallel HEV using a CVT and a clutch

For a parallel HEV using a CVT and a clutch, this clutch (clutch 1) and the ICE together can be considered as a controllable source which delivers the clutch 1 torque on the mechanical coupling side T_{cl1_M} and receives the clutch 1 speed on the mechanical coupling side Ω_{cl1}. Therefore, the common EMR can be used in this case subject to the modifications outlined below:

1. The original ICE source in the common EMR presented in chapter III is replaced by a source which represents the ICE with its clutch (Figure 4.39). The state variable Ω_{ICE} is replaced by Ω_{cl1}, and T_{ICE} is replaced by T_{cl1_M}. This source is controlled by the ICE torque reference T_{ICE_ref} and the control of the clutch p_{cl1} which represents the position of the clutch 1 release bearing (in percentage).

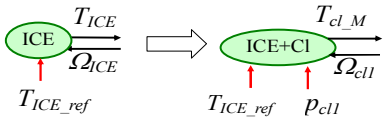

Figure 4.38 Modification of the ICE based source

2. In the equation of mechanical coupling ② (3.32), the variable Ω_{ICE} is also replaced by Ω_{cl1}, and T_{ICE} by T_{cl1_M} as:

$$\begin{cases} \begin{bmatrix} T_3 \\ T_4 \end{bmatrix} = \begin{bmatrix} k_T & -k_T k_R \\ 1-k_T & -k_S \end{bmatrix} \begin{bmatrix} T_{res} \\ T_{cl1\_M} \end{bmatrix} \\ \begin{bmatrix} \Omega_{tran} \\ \Omega_{cl1} \end{bmatrix} = \begin{bmatrix} k_T + (1-k_T)k_R & (1-k_T)k_S \\ k_R & k_S \end{bmatrix} \begin{bmatrix} \Omega_{EM1} \\ \Omega_{EM2} \end{bmatrix} \end{cases} \tag{4.26}$$

where $k_T = 0$, $k_R = 0$ and k_S depends on the mechanical coupling between the ICE and EM2.

3. The behavior of clutches is non-linear and two causal switching models have to be considered [Lhomme 2008-a]. When the clutch is locked, only one single equivalent inertia ($k_S^2 J_{ICE} + J_{EM2} + k_S^2 J_{eq}$) is considered, which is discussed in Chapter III. However, when it is slipping (or open), two inertias (J_{ICE}, and $J_{EM2} + k_S^2 J_{eq}$) must be taken into account.

Locked clutch (model 1) – When the clutch is locked, the friction plate is rigidly coupled with the primary and secondary plates. There is only one independent state variable:

$$\Omega_{ICE} = \Omega_{cl1} = \Omega_{tran} = k_S \Omega_{EM2} \tag{4.27}$$

If the clutch losses are ignored, the clutch 1 torque on the mechanical coupling side

T_{cl1_M} and the clutch 1 speed on the mechanical coupling side Ω_{cl1} are:

$$\begin{cases} T_{cl\mathbf{1}\_T} = T_{ICE} \\ \Omega_{cl\mathbf{1}} = \Omega_{ICE} \end{cases} \tag{4.28}$$

The above relationship is represented by a mechanical conversion element (Figure 4.39, triangle). The generic matrix equation of the vectorial accumulation element in the common EMR represents the torque-speed relationship with respect to the state variable Ω_{EM2}, where

$$[J] = \begin{bmatrix} \mathbf{0} & \mathbf{0} \\ \mathbf{0} & k_S^2 J_{ICE} + k_S^2 J_{eq} + J_{EM\mathbf{2}} \end{bmatrix} \text{ and } [f] = \begin{bmatrix} \mathbf{0} & \mathbf{0} \\ \mathbf{0} & f_{EM\mathbf{2}} \end{bmatrix} \tag{4.29}$$

Slipping or open clutch (model 2) – When the clutch slips or is open, there are two independent state variables:

$$\begin{cases} \Omega_{cl\mathbf{1}} = \Omega_{tran} = k_S \Omega_{EM\mathbf{2}} \\ \Omega_{ICE} \neq \Omega_{cl\mathbf{1}} \end{cases} \tag{4.30}$$

The torque-speed relationship concerning the first independent state variable Ω_{ICE} is:

$$J_{ICE} \frac{d}{dt} \Omega_{ICE} + f_{ICE}\ \Omega_{ICE} = T_{ICE} - T_{cl\mathbf{1}\_I} \tag{4.31}$$

with T_{cl1_I} the clutch 1 torque on the ICE side (4.31) represented by an accumulation element (Figure 4.39, rectangle with an oblique bar).The two side torques of clutch 1 T_{cl1_I} and T_{cl1_T} are:

$$T_{cl\mathbf{1}\_I} = T_{cl\mathbf{1}\_M} = \mathbf{2}\, F_n\ R_{cl\mathbf{1}}\ \mu\ sign\left(\Omega_{ICE} - \Omega_{cl\mathbf{1}}\right) \tag{4.32}$$

$$\text{with}\quad F_n = F_{\max}\left[\mathbf{1} - \sqrt{\mathbf{1} - \left(\frac{p_{cl\mathbf{1}}}{\mathbf{100}} - \mathbf{1}\right)^2}\right] \quad \text{and} \quad \mu = \mu_{stat} - \alpha_{dyn}\left|\Omega_{ICE} - \Omega_{cl\mathbf{1}}\right| \tag{4.33}$$

where F_n is the normal actuation force; R_{cl1} is the average radius of the clutch 1 friction plate; μ is the total friction coefficient, with μ_{stat} the static friction coefficient and α_{dyn} the dynamic friction coefficient. (4.32) is represented by a nonlinear mechanical conversion element (Figure 4.39, rectangle with an internal rectangle). The generic matrix equation of the vectorial accumulation element in the common EMR represents the torque-speed relationship with respect to this state variable Ω_{EM2} using different values for *[J]* and *[f]*:

$$[J] = \begin{bmatrix} \mathbf{0} & \mathbf{0} \\ \mathbf{0} & k_S^2 J_{eq} + J_{EM\mathbf{2}} \end{bmatrix} \text{ and } [f] = \begin{bmatrix} \mathbf{0} & \mathbf{0} \\ \mathbf{0} & f_{EM\mathbf{2}} \end{bmatrix} \tag{4.34}$$

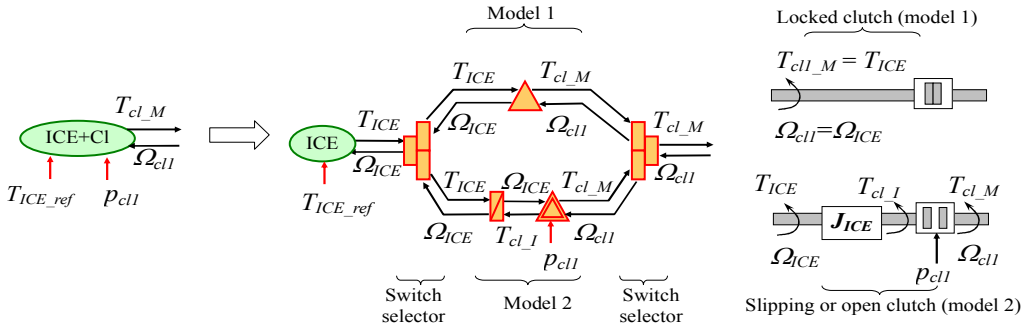

Figure 4.39 Two modes for clutches

In this new source (ICE+Cl), the two models of the clutch are represented separately. Both models are connected through a couple of switch selectors (Figure 4.39) to ensure the power energy flow required during commutation between both models. In the vectorial accumulation element of the common EMR in Chapter III, the different values of *[J]* and *[f]* are used according to the clutch states. The switching between the two modes concerning the clutch states is performed using a Petri net (Figure 4.40). Since the static friction coefficient is similar to the dynamic friction coefficient for the material used in the clutch plate [Armstrong-Helouvry 1994], the maximal torque T_{cl_max} is defined by:

$$T_{cl\_\max} = \mathbf{2}\, F_n\ R_{cl\mathbf{1}}\ \mu_{stat} \tag{4.35}$$

More details about clutch modeling and control can be found in [Lhomme 2007] [Lhomme 2008-a].

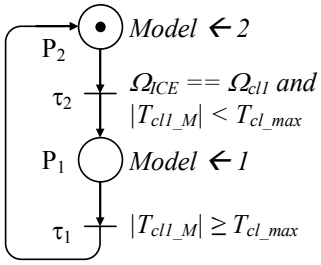

Figure 4.40 Petri net for switching clutch modes

B. Control scheme of the parallel HEV using a CVT and a clutch

The unified control scheme (see Figure 3.22) can be used in this HEV subject to the modification as below:

1. Concerning the speed controller parameters, different values for *[J]* and *[f]* are used with respect to different clutch states: when the clutch is closed (mode 1), (4.29) is used; when the clutch slips or is open (model 2), (4.34) is used. The torques T_{3_mea} and T_{4_mea}, which are composed of the resistance torque measurement T_{res_mea} and clutch torque measurement on the mechanical coupling side $T_{cl1\_M\_mea}$, are compensated using (3.32).

2. The control of the clutch p_{cl1} is added at the strategy level (Figure 4.42).

C. Strategy for the parallel HEV using a CVT

(1) Strategy overview

Many different strategies can be considered for parallel HEVs [Sciarretta 2004] [Pisu 2007] [Trigui 2007] [Won 2005]. In order to compare the parallel HEV using a CVT with a parallel HEV using a discrete box and two clutches, a similar rule-based strategy as the one detailed in [Lhomme 2007] can be used. An overview of this strategy is given in Figure 4.8.

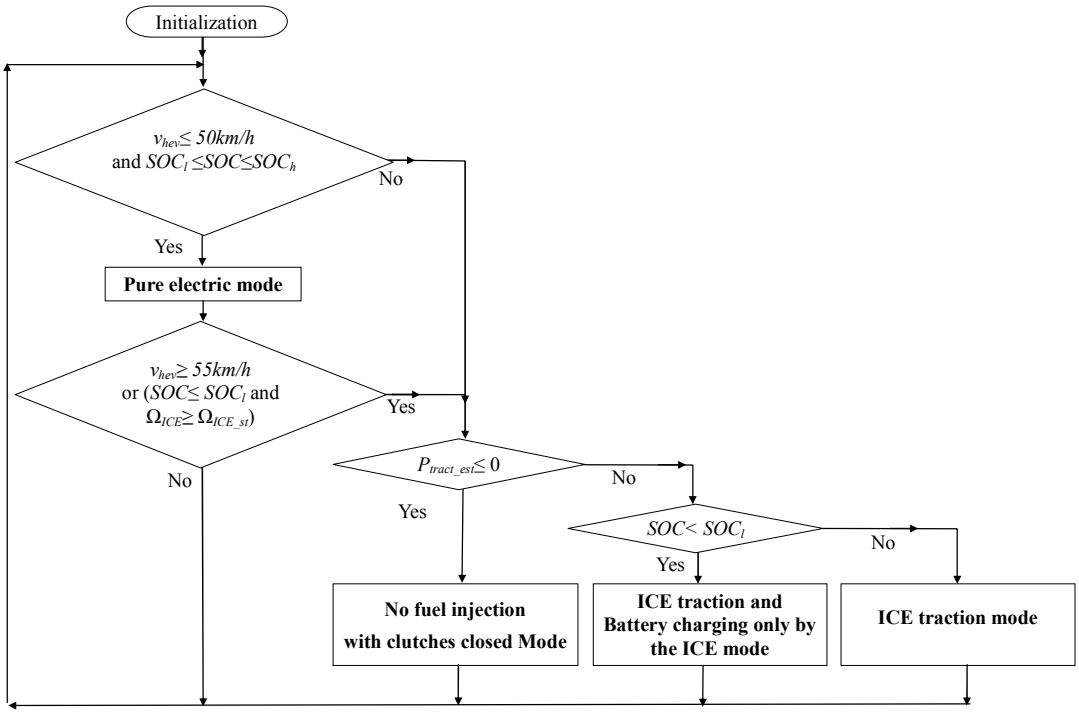

Figure 4.41 Strategy overview used in the simulation of both parallel HEVs

According to the operating modes of this flowchart, the strategy level (Figure 4.42) defines the control of the clutch p_{cl1}, the ICE torque reference T_{ICE_ref}, the ICE speed reference Ω_{ICE_ref}, and the speed ratio k_{trans}. The distribution between the mechanical braking and propulsion machines is defined by k_d which is determined in the same way as for other HEVs in this thesis.

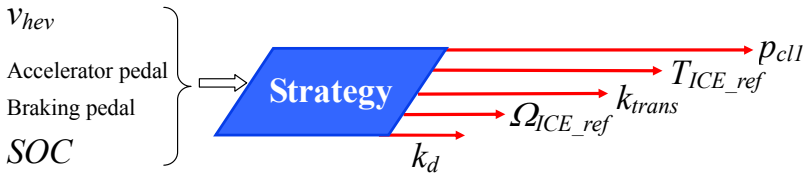

Figure 4.42 Strategy level for the parallel HEV using a CVT

Pure electric mode - HEVs drive in electric mode during an Urban Driving Cycle (UDC) if the battery SOC is within its preferable range ($SOC_l \leq SOC \leq SOC_h$). Within this range, the efficiency of batteries concerning charge and discharge are better. SOC_l is the lowest value and SOC_h is the highest value in this range. In this mode, clutch 1 is open ($p_{cl1} = 100\%$). The ICE is shut down ($T_{ICE\_ref} = 0$ and $\Omega_{ICE\_ref} = 0$). The speed ratio k_{trans} is fixed and equal to the initial value of the CVT k_{trans_el} in pure electric mode.

No fuel injection with clutches closed mode - The ICE operates in the following two situations: one, when the SOC decreases to SOC_l and the ICE is higher than its start speed ($\Omega_{ICE} \geq \Omega_{ICE\_st}$); or when the vehicle velocity is higher than 55 km/h ($v_{hev} \geq 55$ km/h). If the traction power is negative or zero ($P_{tract\_ref} \leq 0$), there is no fuel injection to the ICE. In this mode, clutch 1 is closed ($p_{cl1}=0\%$). The ICE speed is proportional to the transmission speed $\Omega_{trans.}$ The ICE

imposes a resistance torque.

ICE traction and Battery charging only by the ICE mode - If the traction power is positive (P_{tract_ref} >0) and the SOC decreases to SOC_l when the ICE operates, the ICE charges the battery and supplies the traction power.

ICE traction mode - If the traction power is positive (P_{tract_ref} >0) and the SOC is in within its preferable range, the ICE only supplies the traction power.

In the three latter modes, the ICE torque reference T_{ICE_ref}, the ICE speed reference Ω_{ICE_ref} and speed ratio k_{trans} are obtained as shown in Figure 4.43. The required power P_{req} is composed of the required traction power P_{trac_req} and the required battery power P_{bat_req} (4.6).

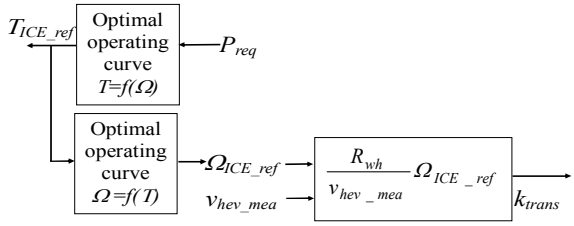

Figure 4.43 ICE torque and speed references and speed ratio k_{trans} when the ICE operates

(2) Differences for the two parallel HEVs

The differences for the two parallel HEVs are:

Parallel HEV using a discrete gearbox - The speed ratio of the parallel HEV using a discrete gearbox k_{trans} is adjusted by the driver. The evolution of the discrete gear choices can be optimized empirically. For example, the optimized gear evolution during a NEDC is shown in Figure 4.44, a. The corresponding speed ratio evolution (k_{trans}) is shown in Figure 4.44, b. However, the transmission gear choices are limited (6 choices: 5 different ratios and Neutral 0). Therefore, the speed ratio k_{trans} has discrete and limited values. The ICE speed is determined by the vehicle velocity and limited owing to the fact that there are only 6 choices. When the vehicle is in EUDC, all traction power comes from the ICE. The ICE operation is expected to follow its optimal curve. This objective however can not be achieved in this case. The reason is that the ICE power which corresponds to the determinate ICE speed along the optimal curve is higher than the required traction power [Lhomme 2007]. But when the battery needs to be charged, the ICE follows this curve. One part of this optimal ICE power is used for the traction, and the other part is used to charge the battery.

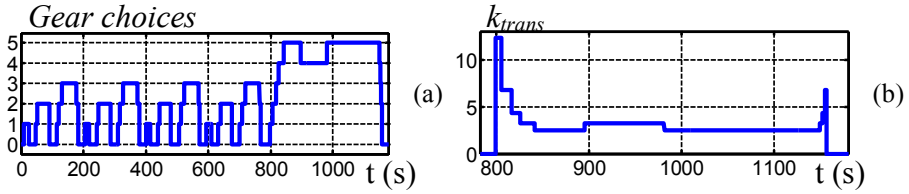

Figure 4.44 Gears and speed ratios of the parallel HEV using a discrete gearbox during a NEDC
(a) Gear choices (b) Speed ratios

Parallel HEV using a CVT – Because of the CVT, k_{trans} has infinite continuous values within its range. For a given power, it is calculated to ensure that the ICE follows this optimal operating curve. The ICE which operates along this curve can have better efficiency. Better fuel economy can therefore be obtained.

(3) Power flows of both parallel HEVs using a similar strategy during a NEDC

During a NEDC (Figure 4.13, a), power flow 4 (battery is recharged only by the ICE when the vehicle stops), and power flow 5 (hybrid traction), are not taken into account for both parallel HEVs.

IV.2.2.3. Simulation results

Modifying the common simulation program based on the common EMR and the unified control, the simulation for the parallel HEV using a CVT and a clutch (Figure 4.37) in MATLAB-Simulink™ is established. These simulation results are compared with those of the parallel HEV using a discrete gearbox and two clutches (Figure 4.36), during a NEDC (Figure 4.13, a). The simulation results for the parallel HEV using a discrete gearbox and two clutches can be found in [Lhomme 2007].

Using the discrete gearbox profile shown in Figure 4.44.a, the ICE operating points of the first parallel HEV during a NEDC are shown in Figure 4.45. The operating points are composed of two groups. The first group follows the optimal curve when the ICE supplies the traction power and charges the battery. The second group is lower than this optimal curve when the ICE supplies the traction power only. The second group of operating points occurs during a EUDC (Figure 4.26). Because of the limitations of the discrete gearbox (only 6 discrete choices), the ICE can not always follow this optimal curve.

Figure 4.46 shows the ICE operating points for the parallel HEV using a CVT during a NEDC. The ICE mainly follows this optimal curve. Other points outside of this optimal curve represent those that are in transient states.

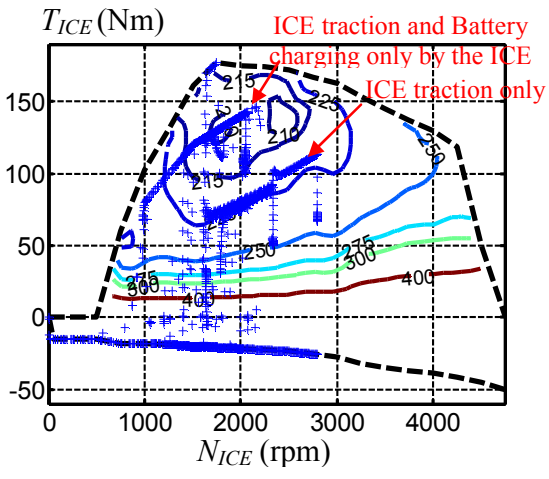

Figure 4.45 ICE operating points of the parallel

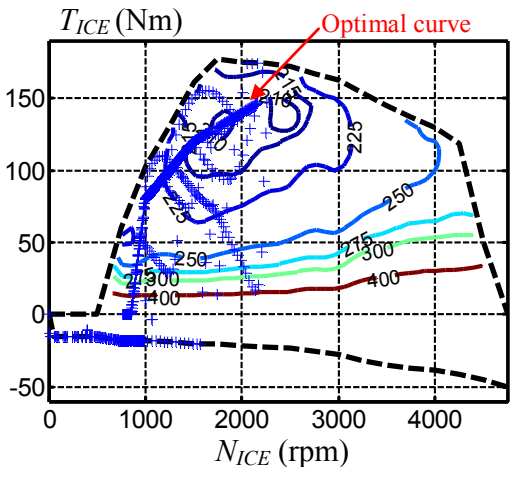

Figure 4.46 ICE operating points of the parallel

HEV using a discrete gearbox and two clutches HEV using a CVT

The main difference between the two vehicles occurs during EUDC. The speed ratios k_{trans} and the ICE speed of the parallel HEV using a discrete gearbox during EUDC are shown in Figure 4.47. The speed ratios and the ICE speed of the second vehicle during EUDC are shown in Figure 4.48. Contrary to the first vehicle, the speed ratios k_{trans} of the second vehicle are calculated at the strategy level using the infinite continuous values of the CVT (Figure 4.43). This is the reason why CVT offers great potential for fuel economy.

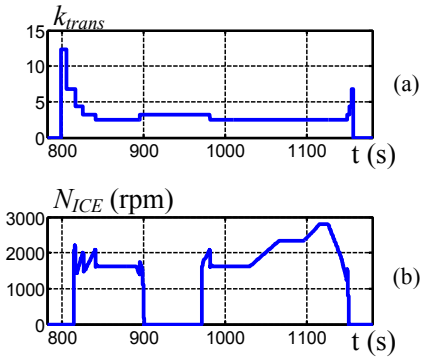

Figure 4.47 Speed ratios and ICE speeds of the parallel HEV using a discrete gearbox and two clutches during a EUDC
(a) Speed ratios (b) ICE speeds

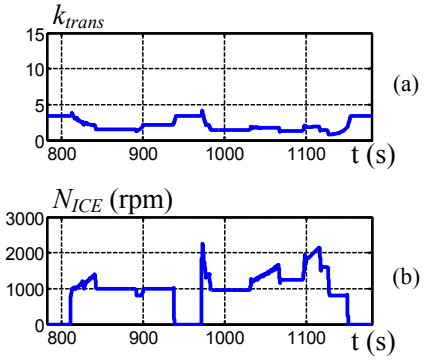

Figure 4.48 Speed ratios and ICE speeds of the parallel HEV using a CVT during a EUDC
(a) Speed ratios (b) ICE speeds

The fuel consumption of the parallel HEV using a CVT is lower than the parallel HEV using a discrete gearbox (0.37 liters for the double clutch parallel HEV, and 0.34 liters for the CVT parallel HEV).

Figure 4.49 illustrates the SOC of the parallel HEV using a discrete gearbox. Figure 4.50 shows the SOC of the parallel HEV using a CVT. The initial SOC of both vehicles is the same (55%). At the end of the driving cycle, the SOC of the parallel HEV using CVT is higher than the one using a discrete box (53.6% for the two clutches parallel HEV, and 56% for the CVT parallel HEV).

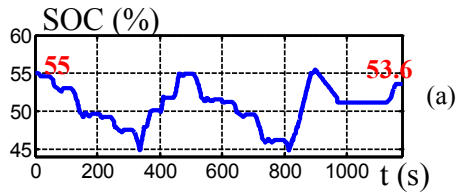

Figure 4.49 SOC of the parallel HEV using a discrete gearbox

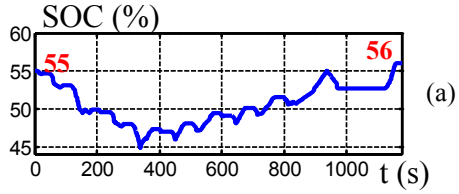

Figure 4.50 SOC of the parallel HEV using a CVT

The parallel HEV using CVT achieves higher SOC and lower consumption than the parallel HEV using a discrete gear box. Figure 4.50 shows that the battery is charged smoothly in the CVT case. Thereby, the mechanical braking is used less frequently in the CVT case than in the discrete gearbox case, because the SOC in CVT case reaches its limitation value less frequently. More braking energy is therefore recovered to charge the battery in the CVT case.

To further validate CVTs, the strategy is changed to use only the mechanical braking without the electrical braking.

To use only mechanical braking, the strategy is changed as follows: if P_{trac_req} is negative, only mechanical braking is used (k_d=0); if P_{trac_req} is positive, k_d=1. In this way, there is no electrical braking. Almost the same frequency for the mechanical braking is achieved for both HEVs (almost the same values are obtained for k_d in Figure 4.51 and Figure 4.52, e).

In this case, the fuel consumptions of both parallel HEVs are the same (0.4 liters). But the final SOC of the parallel HEV using a discrete box is 6% less than that of the parallel HEV using a CVT (Figure 4.52 and Figure 4.52, a). The CVT potential to achieve fuel economy is thereby proven in another way.

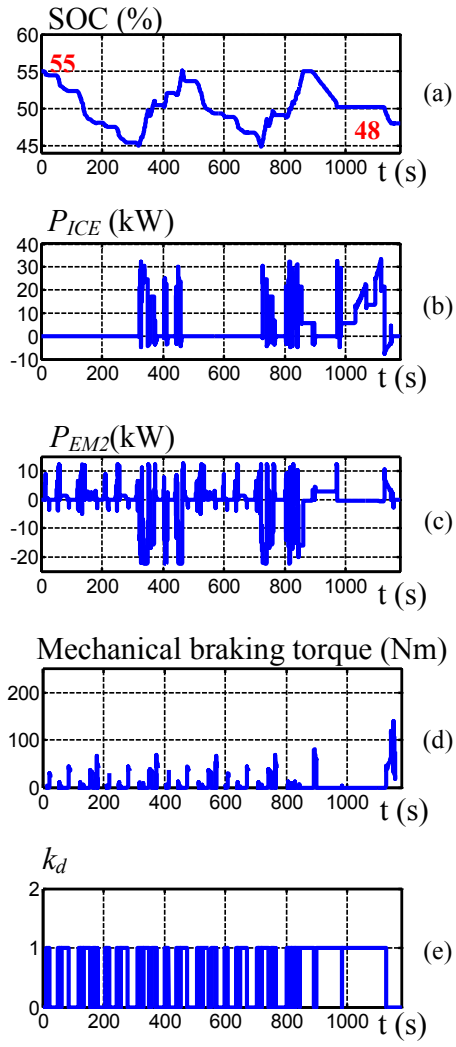

Figure 4.51 Simulation results for the parallel HEV using a discrete gearbox (the modified strategy)
(a) SOC (b) ICE power (c) EM2 power (d) Mechanical braking torque (e) k_d

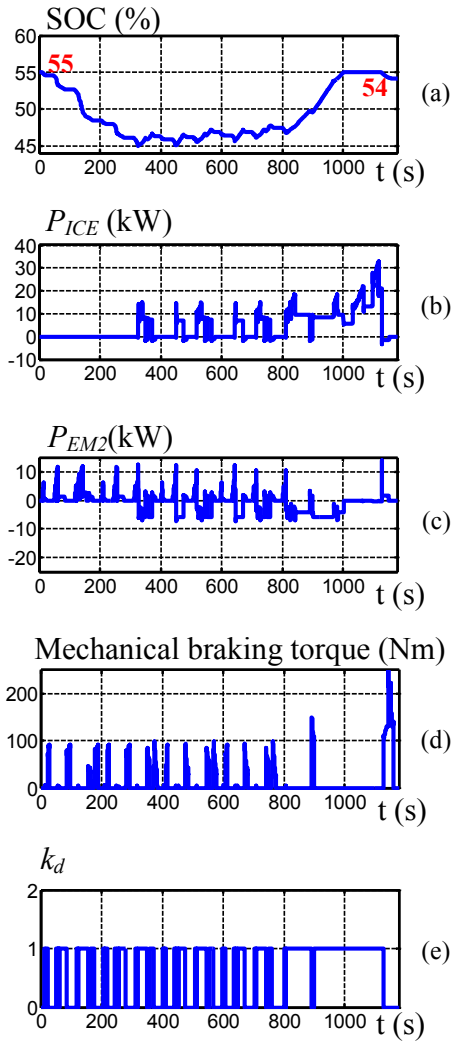

Figure 4.52 Simulation results for the parallel HEV using a CVT (the modified strategy)
(a) SOC (b) ICE power (c) EM2 power (d) Mechanical braking torque (e) k_d

IV.2.2.4. Conclusion

By modifying the common simulation program in MATLAB-Simulink™, the simulation of a parallel HEV using a CVT and a clutch has been carried out. The common EMR and the unified control scheme are conveniently applied to new applications. They ensure the comparison between different HEV more easily.

The simulation results of the parallel HEV using a CVT have been compared with those of a parallel HEV using a discrete gearbox with two clutches. In order to genuinely compare the two parallel HEVs, a similar strategy is used in both parallel HEVs. This modified common EMR and the unified control scheme allow studying the possibilities offered by the CVT for fuel economy. The objective here is to introduce an extension of the unified control. The strategy used in this instance is just for the comparison of the two HEVs, and could be improved by taking into account the required power. Other strategies also can be used, as listed in [Salmasi 2007].

The vehicle part from the transmission to the wheels is represented by an equivalent one-wheel model in the common EMR, and the mechanical braking is only described as a simple controllable source. This part could be further detailed in future research. For example, more complex models for CVTs can be used [Roell M. van 2001] [Setlur 2003]. More control details therefore could be studied [Lu 2001].

Conclusion

The unified control scheme has been validated both by simulation and by experimentation in real time.

First, the common simulation program has been established in MATLAB-Simulink™. This common program is composed of two parts: the modeling part based on the common EMR, and the control part based on the unified control scheme. The two parts can run separately. Setting different values for certain parameters, this common program can be used in the simulation of series, parallel (clutches not taken into account), and series-parallel HEVs.

The simulation for the Toyota Prius II has been compared with another simulation (VEHLIB) which has already been validated by experimentation using a real Toyota Prius II. Both the modeling part and the control part of the common program have been verified by simulation. Since the simulation results of the common program are very close to those of VEHLIB, the common EMR and the unified control have been validated by simulation.

Second, the unified control has been implemented in dSPACE controller board. It has been verified in a real-time environment using HIL simulation for a series HEV. The main power flows have been studied by experimentation. Different strategies have been used and compared. These experimental results show that the unified control can be implemented in real-time environment. Moreover, keeping the same control scheme, different strategies can be conducted and compared easily.

In the second section, the extension of the common EMR and the unified control for other HEVs has been discussed. Two examples have been introduced. The first example is the extension to a series-parallel HEV using two arranged EMs. The simulation results have been compared with the Toyota Prius type HEV. The second example is the application for a parallel HEV using a CVT and a cut-out clutch. Using a similar strategy, this parallel HEV has been compared with a parallel HEV using a discrete gearbox and two clutches. Both examples show that the common EMR and the unified control scheme can be extended easily to new applications. Furthermore, using the extended unified control scheme, the comparison of different HEVs can be made easily.

It should be noted that the vehicle part from the transmission to the wheels is represented by an equivalent one-wheel model in the common EMR, and the mechanical braking is only described as a simple controllable source. More complex models could be used in future research in order to study control robustness and stability [Ioannou 1988] [Sastry 1989] [Zhou 1999].

In the future, further extended applications could be proposed and validated by experimentation. In this thesis, certain rule-based strategies have been discussed, but real-time optimal strategies should be studied [Salmasi 2007] [Kermani 2009].

Conclusion

Generally, in the literature, each HEV has its own model. Using structural modeling approaches, models can be established very quickly, and these models correspond to the system structure. However, these approaches can not directly yield the control design. Energetic Macroscopic Representation (EMR), an energy based graphical description, respects physical laws, emphasizes system functions, and highlights the possible degrees of freedom for energy management. Thanks to these advantages, the inversion-based control structure can be deduced from the EMR of the systems. EMR and the inversion-based control therefore contribute significantly to the control design and energy management of HEVs. EMR has been successfully applied to the study of different HEVs. The modeling and control schemes of these different HEVs in previous studies have been achieved on a case-by-case basis.

The objective of this thesis - establishing a common energetic description for different Hybrid Electric Vehicles (HEVs) - has been achieved. By setting different parameter values, a unique common model based on EMR has been developed to describe different HEVs. From this common EMR, a unified control scheme has been deduced, which can be used for the study of series-parallel, series, and parallel HEVs. Thus, the control design of such complex systems, which are composed of multiple sources and subsystems, can be obtained in a general way, despite the fact that HEVs can be very different from each other in terms of structure.

The common EMR offers a macroscopic energetic view for different HEVs, especially in terms of power flows. Using this unified approach, the time required for the control design is therefore significantly reduced. Given the same control structure, different HEVs can be easily compared.

In chapter I, the thesis objective has been discussed. This study involves cooperation between L2EP, FEMTO-ST (Belfort) and LTE –INRETS, within the framework of MEGEVH-macro.

In chapter II, before establishing the modeling and control structure of a whole system, the unified approach has been proposed firstly for electric drives, one of the most important subsystems. The EMR of Double-Inverter-Fed Wound-Rotor Induction Machine systems (DIF-WRIMs) has been initially presented. DIF-WRIMs are not an interesting option for HEV applications due to the supplementary converter required. However, the EMR of DIF-WRIMs can be considered as a generic description, from which other basic electric drive systems have been deduced. By inverting the EMRs of the systems, the control schemes of two electric drives have been deduced. These control schemes highlight the degrees of freedom and ensure that these degrees of freedom are fully used for energy management. Experimental results of two electric drives have validated their inversion-based control schemes in real-time.

In chapter III, the modeling and control design of different HEVs have been achieved

in a general way. A common EMR has therefore been established, which highlights the main power flows of different HEVs. With the help of this common EMR, a unique simulation model program has been applied to different HEVs. By simply setting different parameter values according to HEV architectures, this common model describes classical series-parallel, series and parallel HEVs. Using the inversion principles, one unified control scheme has been deduced from this common EMR. Like other control schemes deduced from EMRs, this unified control has two levels: a local level which deals with each subsystem, and a strategy level. In the literature, generally, the strategy level, called the energy management or supervision control, is the only focus studied. However, both levels, and the interaction between them, are all important for the control design.

In the first section of chapter IV, the common EMR and the unified control have been validated both by simulation, and, in a real-time environment, by experimentation. The simulation validation has been conducted by comparing the EMR-based common program with VEHLIB, which has been validated by experimentation using a real Toyota Prius II. The unified control has been also checked in a real-time environment for a series HEV using Hardware-In-the-Loop (HIL) simulation. Despite the use of many control blocks in the experimentation, the unified control scheme can be implemented in the real-time environment. Keeping the same control scheme, different strategies have been checked and compared by experimentation.

In the second section of chapter IV, extended applications of this unified control scheme have been discussed. Two examples were given - one is a series-parallel HEV using two arranged Electric Machines (EMs), and the other is a parallel HEV using a Continuously Variable Transmission (CVT). The simulation results show that new applications can be obtained by modifying the common EMR and the unified control scheme. Using the unified control scheme, comparisons between different HEVs can be easily carried out.

In conclusion, using EMR and the inversion-based control, the modeling and control design of HEVs have been achieved in a general way. This work can now be extended in other MEGEVH projects. More efficient energy managements of HEVs could be achieved and compared, and thus to reduce HEV costs, fuel consumption and CO2 emissions.

The vehicle part, from the transmission to the wheels, is represented by an equivalent one-wheel model in the common EMR, and the mechanical braking is only described as a simple controllable source. More complex models could be studied. For example, the braking force distribution on different wheels should be taken into account. Thus, the brake distribution control could be developed. The tire-road interaction could be also added using EMR as in [Verhille 2007-b] [Grossi 2009]. The vehicle stability could thus be studied.

Based on this unified control scheme, the controller synthesis, robustness and stability

could be detailed in the future research. Sensitivity analysis for nonlinear elements could be carried out. Different approaches can be used to ensure the control robustness and stability. In order to ensure the control robustness and stability, it may be preferable to carry out these studies on a case-by-case basis. For example, in the case of supercapacitor-based ESSs, a floating DC bus strategy could be proposed, depending on the supercapacitor stability range and converter losses.

Control prototypes could be tested in a real vehicle. Electromagnetic interference (EMI) should be taken into account and attempts made to reduce it [Balcells 2005]. Further extended applications could be proposed and validated by experimentation. Since the control scheme of HEVs has been established, different optimization strategies could be studied and compared, specifically real-time global strategies.

In this thesis, two series-parallel HEVs, the Toyota Prius II and a HEV using two arranged electric machines, have been compared by simulation. More detailed comparisons, such as losses and operation limits, are being undertaken by the MEGEVH-EVT project. A real double rotor electric machine could be used in series-parallel HEVs.

Appendix

Appendix 1
Equations of separately excited DC Machine drives

Table App. 1 Equations of separately excited DCM systems

parallel connection		$\begin{cases} v_{dc} \text{ common variable} \\ i_{conv} = i_{s\_conv} + i_{r\_conv} \end{cases}$	(App. 1)
converters	chopper of the field winding	$\begin{cases} u_s = m_s v_{dc} \\ i_{s\_con} = m_s i_s \end{cases}$	(App. 2)
	chopper of the armature winding	$\begin{cases} u_r = m_r v_{dc} \\ i_{r\_con} = m_r i_s \end{cases}$	(App. 3)
windings	field winding	$L_s \frac{d}{dt} i_s = -r_s i_s + u_s - e_s$	(App. 4)
	armature winding	$L_r \frac{d}{dt} i_r = -r_r i_r + u_r - e_r$	(App. 5)
electromagnetical conversion	torque:	$T_{em} = k_e i_s i_r$	(App. 6)
	e.m.f of the armature winding	$e_s = k_e i_r \Omega$	(App. 7)
	e.m.f of the field winding	$e_r = 0$	(App. 8)
shaft		$J \frac{d}{dt} \Omega = -f\Omega + T_{em} - T_l$	(App. 9)

In Table App. 1, r_s and L_s are the resistance and the cyclic inductance of the field winding, r_r and L_r the resistance and cyclic inductance of the armature winding, i_s and u_s the current and voltage of the field winding, i_r and u_r the current and voltage of the armature winding, i_{s_conv} the current of the field winding chopper on the DC bus side, i_{r_conv} the current of the armature winding chopper on the DC bus side, v_{dc} the DC bus voltage, T_l the load torque, J the total moment of inertia and f the viscous friction coefficient.

Appendix 2
Other results for the DIF-WRIM

1. Step speed reference

Figure App. 1 and Figure App. 2 show the simulation results for the stator field oriented control (case 1) and the rotor field oriented control (case 2) using the same step references. In both cases, k_1 is fixed at 1. Figure App. 3 and Figure App. 4 show the experimental results for both cases. The simulation is validated, as the simulation results coincide with the experimental results.

In case 1, k_2 is used to obtain the stator field orientation. Φ_{sd_ref} is set at its rated value (1.7 Wb) upto and including the base speed (500 rpm), and is weakened beyond the base speed. Φ_{sq_ref} is set to zero. k_3 is calculated on line using (2.54).

In case 2, k_2 is used to obtain the rotor field orientation. Φ_{rd_ref} is set at its rated value (0.2 Wb) upto and including the base speed, and is weakened beyond the base speed. Φ_{rq_ref} is set to zero. k_3 is calculated on line using (2.55).

Using the same step speed reference, the speed measurements closely follow the reference curve in both cases (Figure App. 3. a and Figure App. 4. a). In case 1, the estimated Φ_{sd} and Φ_{sq} show that the stator flux achieves the stator field orientation (Figure App. 3, b) under experimentation. In case 2, the estimated Φ_{rd} and Φ_{rq} show that the stator flux achieves the rotor field orientation (Figure App. 4, b) under experimentation.

2. Constant speed reference

Figure App. 5 shows the simulation results using a constant speed in both the stator field oriented control and the rotor field oriented control. k_1 is varied, as shown in Figure App. 5 (b). The active power ratio p_s/p_r is close to k_1 (see (2.43)) . If the currents are zoomed, it can be seen that the stator current frequency is k_2 times that of the rotor current frequency: for example, the stator frequency is 0.25 times that of the rotor when k_1=0.25 (Figure 2.20. c and d); the stator frequency is 2 times that of the rotor when k_1=2 (Figure 2.20. e and f). Figure App. 6 shows the experimental results using the same constant speed and the same values for k_1 as in the simulation. The experimental results closely match the simulation results.

3. Constant speed reference with the variation of load

Figure App. 7 and Figure App. 8 show the experimental results for the two orientation controls with the varied load. In both cases, k_1 is fixed at 1.

In case 1, k_2 is used to obtain the stator field orientation. Φ_{sd} is weakened (Figure App. 7.b, Φ_{sd}=1 Wb whereas its rated value is 1.7 Wb), because the machine speed (600rpm) is greater than its base speed (500 rpm). The load is variable and its estimated value is shown in Figure App. 7. c.

In case 2, k_2 is used to obtain the rotor field orientation. Φ_{sd} is weakened (Figure App.

8. b, Φ_{rd}= 0.17 Wb whereas its rated value is 0.2Wb). The load is variable and its estimated value is shown in Figure App. 8. c.

Under the same constant reference (600 rpm), the speed measurements closely follow the reference in both cases (Figure App. 7. a and Figure App. 8. a).

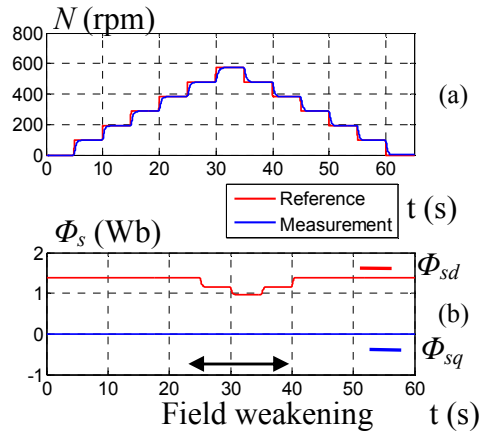

Figure App. 1 Simulation results of the stator field oriented control with the step speed reference and k1 = 1 (Simulation case 1)

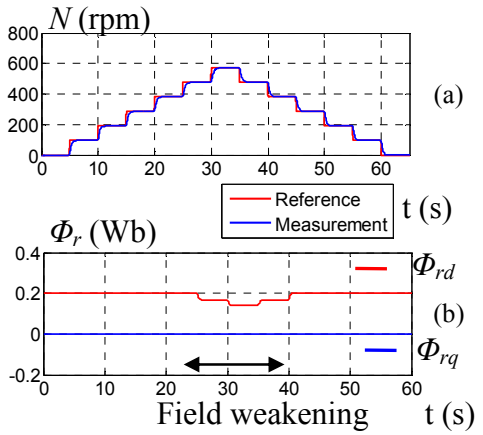

Figure App. 2 Simulation results of the rotor field oriented control with the step speed reference k1 = 1 (Simulation case 2)

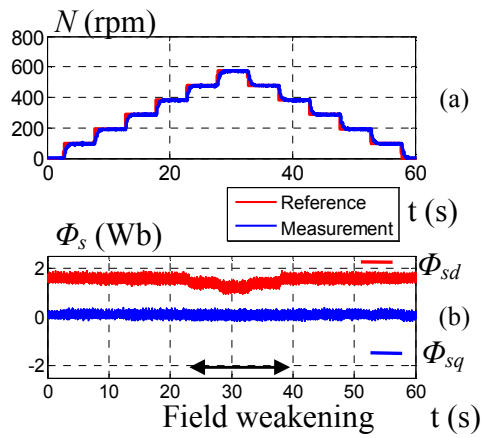

Figure App. 3 Experimental results of the stator field oriented control with the step speed reference and k1 = 1 (Experimentation-case 1)

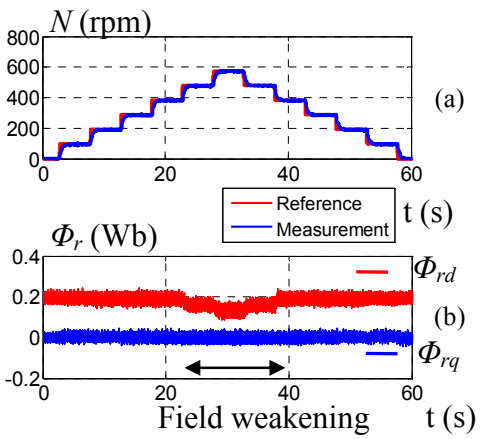

Figure App. 4 Experimental results of the rotor field oriented control with the step speed reference k1 = 1 (Experimentation-case 2)

(a) Machine speed (b) Estimated flux in the d-q axis

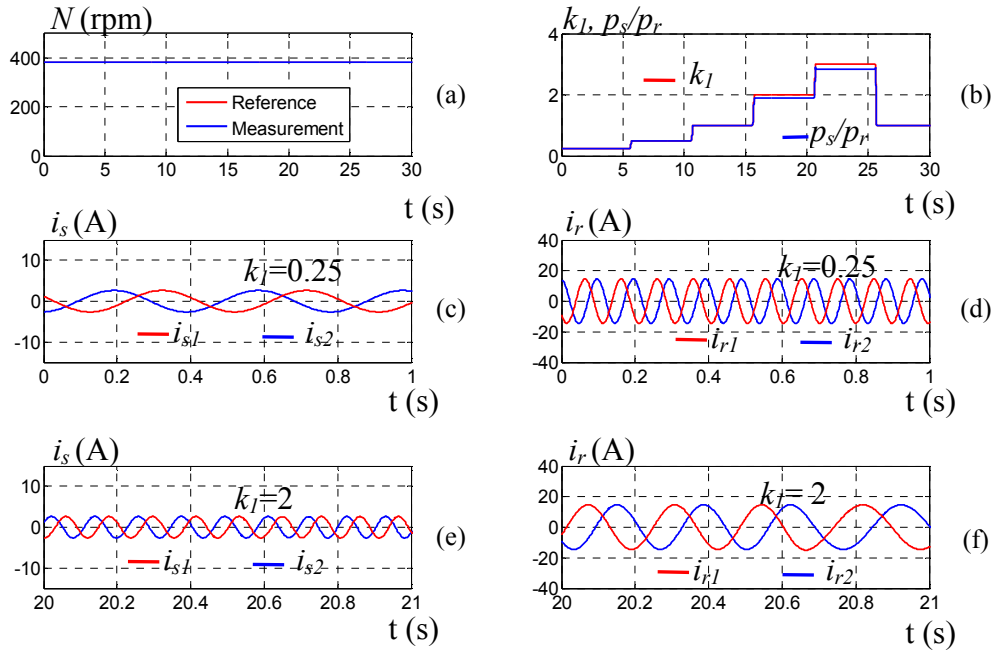

Figure App. 5 Simulation results at the constant speed with variable k1

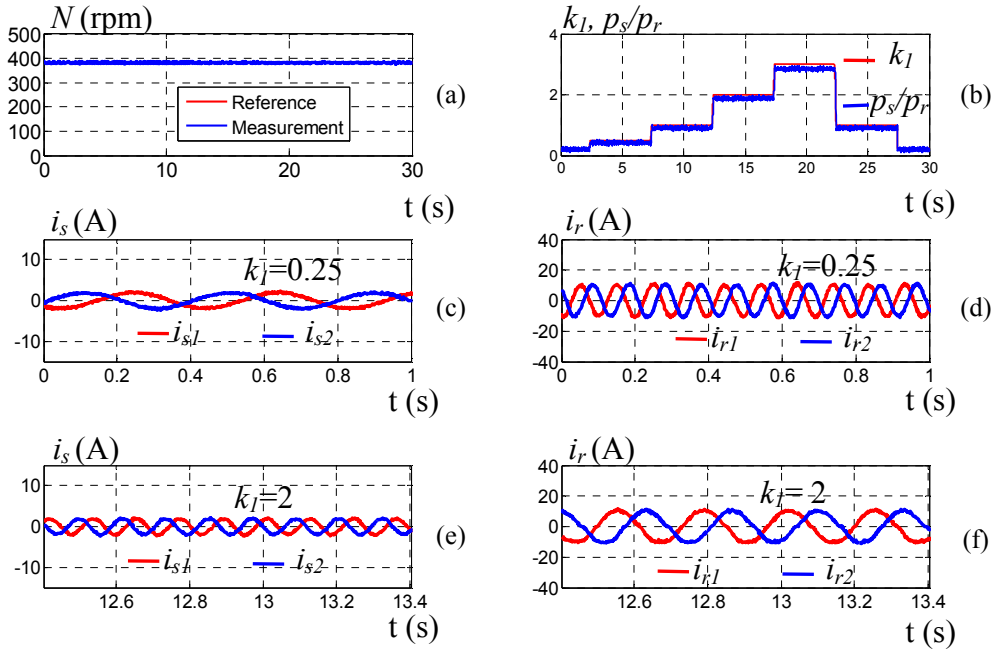

Figure App. 6 Experimental results at the constant speed with variable k1

(a) Machine speed (b) k1 and ps/pr

(a) Stator current measurement when k1=0.25 (d) Rotor current measurement when k1=0.25

(e) Stator current measurement when k1=2 (f) Rotor current measurement when k1=2

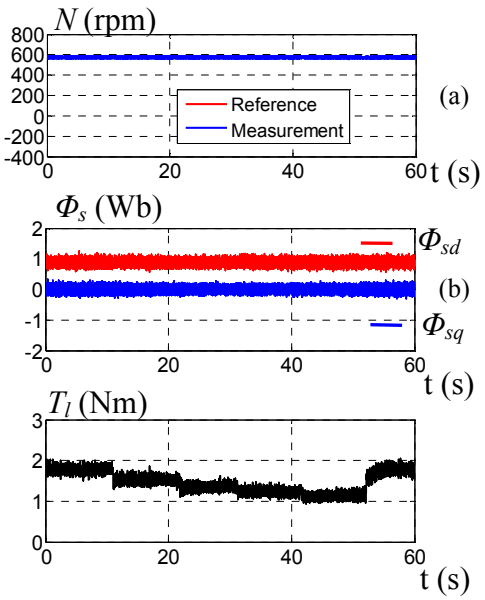

Figure App. 7 Experimental results of the stator field oriented control with constant speed and step load torque (case 1)

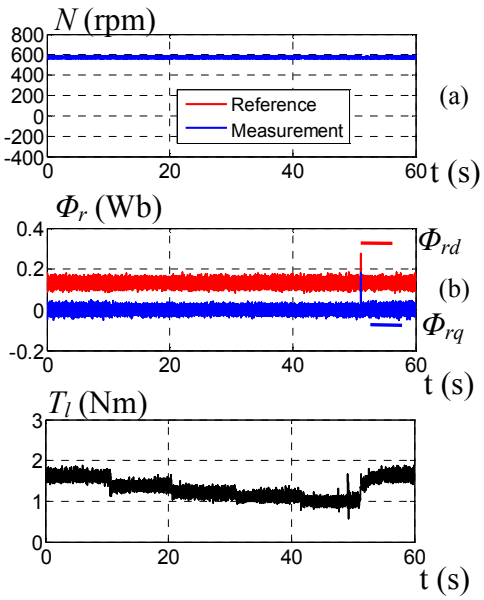

Figure App. 8 Experimental results of the rotor field oriented control with constant speed and step load torque (case 2)

(a) Machine speed (b) Estimated flux in the d-q axis (c) Load torque

4. Validation of the minimum copper loss strategy

Two tests are presented in Table App. 2 with a load torque of 1.1 Nm. In the first test shown in Table App. 2, different values of k_3 are set. After the transient state, the copper losses are estimated using the measured current. It can be noted that k_3 = -1.7 yields minimum copper losses of 17.2 W. In the second test, k_3 is calculated on line using (2.54) under the stator field orientation condition. The estimated copper losses are 17.1 W, which is close to the minimum copper losses in the first test. This means that the on-line calculation minimizes the copper losses.

Two other tests are presented in Table App. 3 with a load torque of 1.7 Nm. In the first test, k_3 = 1.7 yields minimum copper losses of 17.5 W. It is close to the results obtained using (2.55) under the rotor field orientation condition.

These experimental results show that the stator and rotor losses can be minimized using (2.54) when the stator field oriented control is used, or (2.55) when the rotor field oriented control is used.

Table App. 2. Experimental copper losses versus k3 (N=500rpm, Tl= 1.1 Nm)

k3	-0.4	-0.6	-0.8	-1	-1.2	-1.4	-1.7	-1.8
Ploss(W)	25.3	22.1	21.3	19.1	18.2	17.7	17.2	18.2
k3	On-line calculation using (2.54)							
Ploss(W)	17.1							

Table App. 3: Experimental copper losses versus of k3 (N= -500rpm, Tl= 1 Nm)

k3	0.4	0.6	0.8	1	1.2	1.4	1.7	1.8
Ploss(W)	25.3	22.5	20.7	19.5	18.5	18.0	17.5	19.2
k3	On-line calculation using (2.55)							
Ploss(W)	17.3							

Appendix 3
Calculation of i_{sd_ref} of salient pole PMSMs

In order to obtain the minimum copper losses of a salient pole PMSM, the following condition is necessary:

$$\frac{\partial {i_s}^2}{\partial i_{sq}} = \frac{2}{(L_{sd} - L_{sq})^2}\left(\frac{T_{em}}{p i_{sq}} - \Phi_f\right)\left(-\frac{T_{em}}{p i_{sq}}\right)\frac{1}{i_{sq}} + 2i_{sq} = 0 \qquad \text{(App. 10)}$$

From (2.26),

$$\left(\frac{T_{em}}{p i_{sq}} - \Phi_f\right) = i_{sd}(L_{sd} - L_{sq}) \qquad \text{(App. 11)}$$

thus

$$\frac{T_{em}}{p i_{sq}} = i_{sd}(L_{sd} - L_{sq}) + \Phi_f \qquad \text{(App. 12)}$$

From (App. 10) and (App. 12),

$$-\frac{i_{sd}^2}{i_{sq}} - \frac{\Phi_f}{(L_{sd} - L_{sq})}\frac{i_{sd}}{i_{sq}} + i_{sq} = 0 \qquad \text{(App. 13)}$$

Thus

$$i_{sq}^2 = i_{sd}^2 + \frac{\Phi_f}{(L_{sd} - L_{sq})} i_{sd} \qquad \text{(App. 14)}$$

From (2.26) and (App. 14),

$$\left(L_{sd} i_{sd} + \Phi_f\right)^2 + L_{sq}^2 i_{sq}^2 = \left(\frac{V_{s\_\max}}{\omega}\right)^2$$

$$(L_{sd}^2 + L_{sq}^2) i_{sd}^2 + \left(2L_{sd} + \frac{L_{sq}^2}{(L_{sd} - L_{sq})}\right)\Phi_f i_{sd} + \Phi_f^2 - \left(\frac{V_{s\_\max}}{\omega}\right)^2 = 0 \qquad \text{(App. 15)}$$

$$\text{If } \; a = (L_{sd}^2 + L_{sq}^2), \; b = \left(2L_{sd} + \frac{L_{sq}^2}{(L_{sd} - L_{sq})}\right)\Phi_f \text{ and } \; c = \Phi_f^2 - \left(\frac{V_{s\_\max}}{\omega}\right)^2 \qquad \text{(App. 16)}$$

The smaller negative solution for (App. 15) using $i_{sd} = \frac{-b \pm \sqrt{b^2 - 4ac}}{2a}$ is chosen such that :

$$i_{d\_ref} = f_{fieldw}(\Omega_{ref})$$

$$= \frac{-\left(2L_{sd} + \frac{L_{sq}^2}{(L_{sd} - L_{sq})}\right)\Phi_f + \sqrt{\left(2L_{sd} + \frac{L_{sq}^2}{(L_{sd} - L_{sq})}\right)^2 \Phi_f^2 + 4(L_{sd}^2 + L_{sq}^2)\left(-\Phi_f^2 + \left(\frac{V_{s\_\max}}{p\Omega_{ref}}\right)^2\right)}}{2(L_{sd}^2 + L_{sq}^2)} \qquad \text{(App. 17)}$$

Appendix 4
Other results for the salient pole SM

Simulation results -The machine speed reference is given, as shown in Figure App. 9. (a). The load torque is obtained using the induction machine, as shown in Figure App. 9 (b). The machine speed closely follows the reference (Figure App. 9. a). When the machine runs beyond its base speed (absolute value: 800 rpm), the *d*-axis flux is weakened using i_{sd} negative to make the machine operate at higher speeds, as shown in Figure App. 9 (c). The *q*-axis flux is proportional to i_{sq} which depends on the machine torque, as shown in Figure App. 9 (d). The simulation results are close to the experimental results.

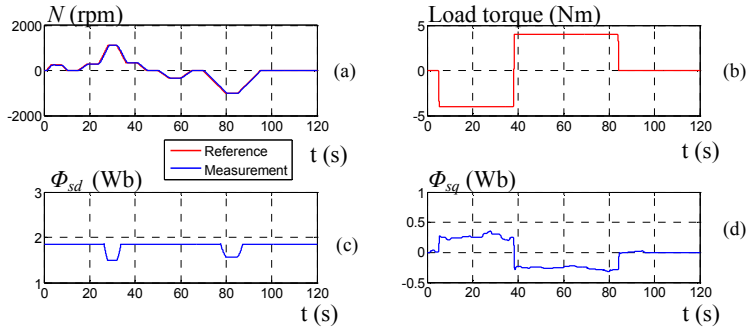

Figure App. 9 Simulation results of a salient pole PMSM
(a) Measurement and reference of the speed (b) Load torque (c) Estimated Φsd (d) Estimated Φsq

Experimental results using a trapezoidal speed reference with constant load - Figure App. 10. a shows that the salient pole SM follows the positive trapezoidal step speed reference. The load torque is given using the induction machine, as shown in Figure App. 10. b. After 16s, the load torque remains constant. When the machine speed is greater than 800 rpm, the *d*-axis flux is weakened using i_{sd} negative, as shown in Figure App. 10. c. The *q*-axis flux is positive after 16s. It is proportional to the *q*-axis current which depends on the machine torque, as shown in Figure App. 10. d. Figure App. 10. e shows the stator current between 10.2s and 10.8s. Since the switching frequency is 1.2 kHz, the stator current forms can be improved using a higher switching frequency.

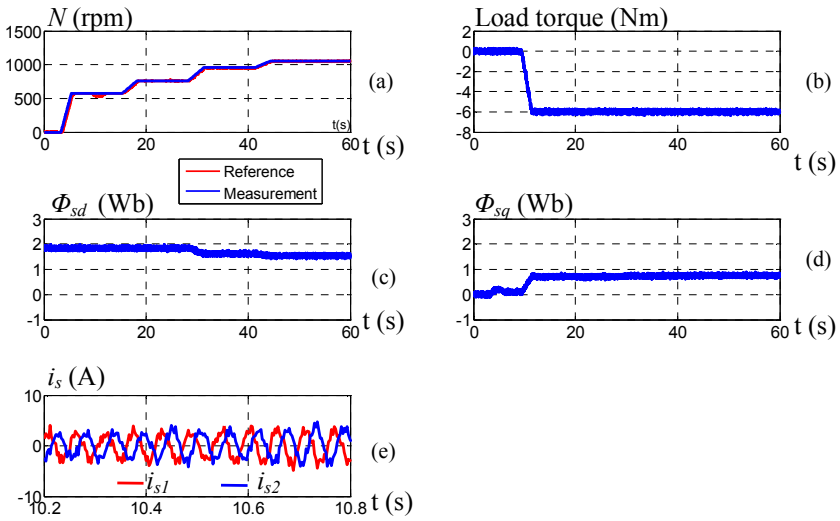

Figure App. 10 Experimental results of the trapezoidal speed with constant load
(a) Measurement and reference of the speed (b) Load torque (c) Estimated Φsd (d) Estimated Φsq (e) Stator current measurement

Experimental results using a trapezoidal speed reference with step load - Figure App. 11.a shows that the salient pole SM follows the positive trapezoidal step speed reference. The load torque is given by the induction machine, as shown in Figure App. 11.b. The *d*-axis flux is weakened when the speed is greater than its based value (800 rpm) (Figure App. 11. c). The *q*-axis flux varies according to the load torque (Figure App. 11. d). Figure App. 11. e shows the stator current between 20.4s and 21s, which can be improved using a higher switching frequency.

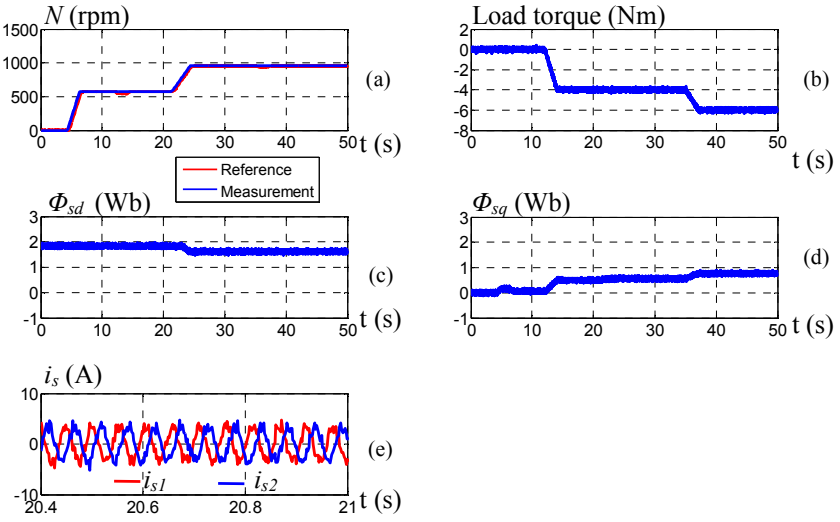

Figure App. 11 Experimental results of the trapezoidal speed with step load
(a) Measurement and reference of the speed (b) Load torque (c) Estimated Φsd (d) Estimated Φsq (e) Stator current measurement

Appendix 5
Simplest matrix equation of series-parallel HEVs using a planetary gear

The torque-speed equations of the shafts on a planetary gear in series-parallel HEVs can be written in matrix form as follows:

$$\begin{bmatrix} 1 & -1 & -1 & -1 & 0 & 0 & 0 & 0 \\ 0 & 0 & 0 & 0 & 1 & -1 & 0 & 0 \\ 0 & 0 & 0 & 0 & 0 & 0 & 1 & -1 \end{bmatrix} \begin{bmatrix} T_{EM1} \\ T_R \\ T_{res} \\ T_{br} \\ T_{ICE} \\ T_C \\ T_{EM2} \\ T_S \end{bmatrix} = \begin{bmatrix} J_{EM1}+J_{eq} & 0 & 0 \\ 0 & J_{ICE} & 0 \\ 0 & 0 & J_{EM2} \end{bmatrix} \frac{d}{dt} \begin{bmatrix} \Omega_{EM1} \\ \Omega_{ICE} \\ \Omega_{EM2} \end{bmatrix} + \begin{bmatrix} f_{EM1} & 0 & 0 \\ 0 & f_{ICE} & 0 \\ 0 & 0 & f_{EM2} \end{bmatrix} \begin{bmatrix} \Omega_{EM1} \\ \Omega_{ICE} \\ \Omega_{EM2} \end{bmatrix} \quad \text{(App. 18)}$$

This matrix equation can be transformed into a simplest matrix equation. Using $\begin{bmatrix} k_R \times \text{Row2} + \text{Row1} \\ k_S \times \text{Row2} + \text{Row3} \end{bmatrix}$, (App. 18) becomes:

$$\begin{bmatrix} 1 & -1 & -1 & -1 & k_R & -k_R & 0 & 0 \\ 0 & 0 & 0 & 0 & k_S & -k_S & 1 & -1 \end{bmatrix} \begin{bmatrix} T_{EM1} \\ T_R \\ T_{res} \\ T_{ICE} \\ T_C \\ T_{EM2} \\ T_S \end{bmatrix} = \begin{bmatrix} J_{EM1}+J_{eq} & k_R J_{ICE} & 0 \\ 0 & k_S J_{ICE} & J_{EM2} \end{bmatrix} \frac{d}{dt} \begin{bmatrix} \Omega_{EM1} \\ \Omega_{ICE} \\ \Omega_{EM2} \end{bmatrix} + \begin{bmatrix} f_{EM1} & k_R f_{ICE} & 0 \\ 0 & k_S f_{ICE} & f_{EM2} \end{bmatrix} \begin{bmatrix} \Omega_{EM1} \\ \Omega_{ICE} \\ \Omega_{EM2} \end{bmatrix} \quad \text{(App. 19)}$$

Since $T_R = -k_R T_C$ and $T_S = -k_S T_C$ (see (3.5)), (App. 19) can be written as:

$$\begin{bmatrix} 1 & 0 & -1 & -1 & k_R & 0 & 0 & 0 \\ 0 & 0 & 0 & 0 & k_S & 0 & 1 & 0 \end{bmatrix} \begin{bmatrix} T_{EM1} \\ T_R \\ T_{res} \\ T_{ICE} \\ T_C \\ T_{EM2} \\ T_S \end{bmatrix} = \begin{bmatrix} J_{EM1}+J_{eq} & k_R J_{ICE} & 0 \\ 0 & k_S J_{ICE} & J_{EM2} \end{bmatrix} \frac{d}{dt} \begin{bmatrix} \Omega_{EM1} \\ \Omega_{ICE} \\ \Omega_{EM2} \end{bmatrix} + \begin{bmatrix} f_{EM1} & k_R f_{ICE} & 0 \\ 0 & k_S f_{ICE} & f_{EM2} \end{bmatrix} \begin{bmatrix} \Omega_{EM1} \\ \Omega_{ICE} \\ \Omega_{EM2} \end{bmatrix} \quad \text{(App. 20)}$$

The variables T_R, T_C and T_S can be deleted:

$$\begin{bmatrix} \mathbf{1} & \mathbf{-1} & \mathbf{-1} & k_R & \mathbf{0} \\ \mathbf{0} & \mathbf{0} & \mathbf{0} & k_S & \mathbf{1} \end{bmatrix} \begin{bmatrix} T_{EM\,\mathbf{1}} \\ T_{res} \\ T_{br} \\ T_{ICE} \\ T_{EM\,\mathbf{2}} \end{bmatrix} = \begin{bmatrix} J_{EM\,\mathbf{1}} + J_{eq} & k_{\mathrm{R}} J_{ICE} & \mathbf{0} \\ \mathbf{0} & k_{\mathrm{S}} J_{ICE} & J_{EM\,\mathbf{2}} \end{bmatrix} \frac{d}{dt} \begin{bmatrix} \Omega_{EM\,\mathbf{1}} \\ \Omega_{ICE} \\ \Omega_{EM\,\mathbf{2}} \end{bmatrix} + \begin{bmatrix} f_{EM\,\mathbf{1}} & k_{\mathrm{R}} f_{ICE} & \mathbf{0} \\ \mathbf{0} & k_{\mathrm{S}} f_{ICE} & f_{EM\,\mathbf{2}} \end{bmatrix} \begin{bmatrix} \Omega_{EM\,\mathbf{1}} \\ \Omega_{ICE} \\ \Omega_{EM\,\mathbf{2}} \end{bmatrix} \quad \text{(App. 21)}$$

Given that $\Omega_{ICE} = k_R \Omega_{EM\mathbf{1}} + k_S \Omega_{EM\mathbf{2}}$, (App. 21) becomes:

$$\begin{bmatrix} \mathbf{1} & \mathbf{-1} & \mathbf{-1} & k_R & \mathbf{0} \\ \mathbf{0} & \mathbf{0} & \mathbf{0} & k_S & \mathbf{1} \end{bmatrix} \begin{bmatrix} T_{EM\mathbf{1}} \\ T_{res} \\ T_{br} \\ T_{ICE} \\ T_{EM\mathbf{2}} \end{bmatrix} = \begin{bmatrix} J_{EM\mathbf{1}} + J_{eq} & k_{\mathrm{R}} J_{ICE} & \mathbf{0} \\ \mathbf{0} & k_{\mathrm{S}} J_{ICE} & J_{EM\mathbf{2}} \end{bmatrix} \frac{d}{dt} \begin{bmatrix} \Omega_{EM\mathbf{1}} \\ k_R \Omega_{EM\mathbf{1}} + k_S \Omega_{EM\mathbf{2}} \\ \Omega_{EM\mathbf{2}} \end{bmatrix} + \begin{bmatrix} f_{EM\mathbf{1}} & k_{\mathrm{R}} f_{ICE} & \mathbf{0} \\ \mathbf{0} & k_{\mathrm{S}} f_{ICE} & f_{EM\mathbf{2}} \end{bmatrix} \begin{bmatrix} \Omega_{EM\mathbf{1}} \\ k_R \Omega_{EM\mathbf{1}} + k_S \Omega_{EM\mathbf{2}} \\ \Omega_{EM\mathbf{2}} \end{bmatrix} \quad \text{(App. 22)}$$

$$\begin{bmatrix} \mathbf{1} & \mathbf{-1} & \mathbf{-1} & k_R & \mathbf{0} \\ \mathbf{0} & \mathbf{0} & \mathbf{0} & k_S & \mathbf{1} \end{bmatrix} \begin{bmatrix} T_{EM\mathbf{1}} \\ T_{res} \\ T_{br} \\ T_{ICE} \\ T_{EM\mathbf{2}} \end{bmatrix} = \begin{bmatrix} J_{EM\mathbf{1}} + J_{eq} + k_{\mathrm{R}}^{\mathbf{2}} J_{ICE} & k_R k_S J_{\mathrm{ICE}} \\ k_R k_S J_{\mathrm{ICE}} & k_{\mathrm{S}}^{\mathbf{2}} J_{ICE} + J_{EM\mathbf{2}} \end{bmatrix} \frac{d}{dt} \begin{bmatrix} \Omega_{EM\mathbf{1}} \\ \Omega_{EM\mathbf{2}} \end{bmatrix} + \begin{bmatrix} f_{EM\mathbf{1}} + k_{\mathrm{R}}^{\mathbf{2}} f_{ICE} & k_R k_S f_{\mathrm{ICE}} \\ k_R k_S f_{\mathrm{ICE}} & k_{\mathrm{S}}^{\mathbf{2}} f_{ICE} + f_{EM\mathbf{2}} \end{bmatrix} \frac{d}{dt} \begin{bmatrix} \Omega_{EM\mathbf{1}} \\ \Omega_{EM\mathbf{2}} \end{bmatrix} \quad \text{(App. 23)}$$

$$\begin{bmatrix} k_R T_{ICE} + T_{EM\mathbf{1}} - T_{br} - T_{res} \\ k_S T_{ICE} + T_{EM\mathbf{2}} \end{bmatrix} = \begin{bmatrix} J_{EM\mathbf{1}} + J_{eq} + k_{\mathrm{R}}^{\mathbf{2}} J_{ICE} & k_R k_S J_{\mathrm{ICE}} \\ k_R k_S J_{\mathrm{ICE}} & k_{\mathrm{S}}^{\mathbf{2}} J_{ICE} + J_{EM\mathbf{2}} \end{bmatrix} \frac{d}{dt} \begin{bmatrix} \Omega_{EM\mathbf{1}} \\ \Omega_{EM\mathbf{2}} \end{bmatrix} + \begin{bmatrix} f_{EM\mathbf{1}} + k_{\mathrm{R}}^{\mathbf{2}} f_{ICE} & k_R k_S f_{\mathrm{ICE}} \\ k_R k_S f_{\mathrm{ICE}} & k_{\mathrm{S}}^{\mathbf{2}} f_{ICE} + f_{EM\mathbf{2}} \end{bmatrix} \frac{d}{dt} \begin{bmatrix} \Omega_{EM\mathbf{1}} \\ \Omega_{EM\mathbf{2}} \end{bmatrix} \quad \text{(App. 24)}$$

Appendix 6
Modeling of a Continuously Variable Transmission

The primary side of a Continuously Variable Transmission (CVT) is connected to the ICE and EM2 through a mechanical coupling. The secondary side of the CVT is connected to the vehicle differential (Figure App. 12).

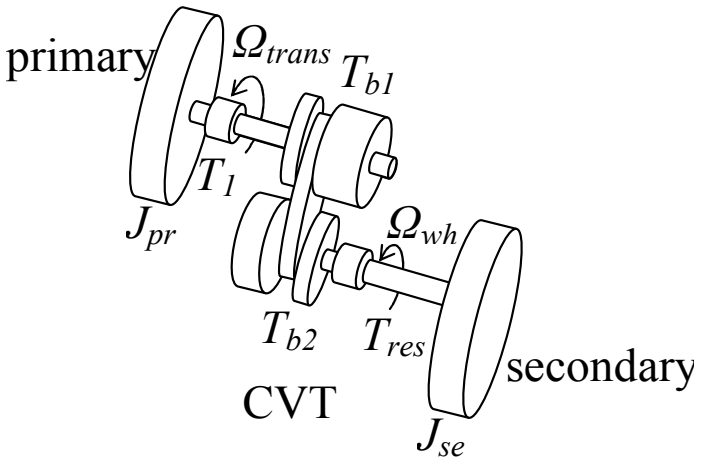

Figure App. 12 CVT [Roell M. van 2001]

The equations related to the two sides of the CVT are:

$$J_{pr}\frac{d}{dt}\Omega_{trans} = T_2 - T_{b1} \quad \text{(App. 25)}$$

$$J_{se}\frac{d}{dt}\Omega_{wh} = T_{b2} - T_{res} \quad \text{(App. 26)}$$

with J_{pr} the primary side inertia, J_{se} the secondary side inertia, Ω_{trans} the primary side speed, Ω_{wh} the secondary side speed (the wheel speed), T_2 the total torque of the ICE and EM2 acting on the primary side, T_{res} the resistance torque acting on the secondary side, and T_{b1}, T_{b2} the torques transmitted on the primary side and the secondary side.

Assuming no force is lost, the forces transmitted between the primary and secondary sides F_{b1} and F_{b2} (Figure App. 13) are equal:

$$F_{b2} = F_{b1} \quad \text{(App. 27)}$$

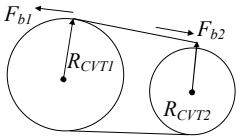

Figure App. 13 Forces in the CVT

Therefore:

$$\frac{T_{b2}}{R_{CVT2}} = \frac{T_{b1}}{R_{CVT1}} \quad \text{(App. 28)}$$

where R_{CVT1} and R_{CVT2} are the effective radii of the primary and secondary sides. The geometric ratio k_{trans_r} is:

$$k_{trans\_r} = \frac{R_{CVT2}}{R_{CVT1}} \quad \text{(App. 29)}$$

The relationship between T_{b1} and T_{b2} is:

$$T_{b2} = \frac{R_{CVT2}}{R_{CVT1}} T_{b1} = k_{trans\_r} T_{b1} \quad \text{(App. 30)}$$

If the speed ratio is defined as:

$$k_{trans} = \frac{\Omega_{trans}}{\Omega_{wh}} \quad \text{(App. 31)}$$

the output power efficiency is

$$\eta_{trans} = \frac{T_{b2}\Omega_{wh}}{T_{b1}\Omega_{trans}} = k_{trans\_r} \frac{\Omega_{wh}}{\Omega_{trans}} = \frac{k_{trans\_r}}{k_{trans}} \quad \text{(App. 32)}$$

The relationship between T_{b1} and T_{b2}(App. 30) can also be written as:

$$T_{b2} = \eta_{trans} k_{trans} T_{b1} \quad \text{(App. 33)}$$

From (App. 25) - (App. 33), the CVT dynamics equation can be written as [Foley 2001]:

$$(J_{pr} + \frac{1}{k_{trans} k_{trans\_r}} J_{se}) \frac{d}{dt} \Omega_{trans} = T_1 - \frac{1}{k_{trans\_r}} T_{res} + J_{eq} \Omega_{trans} \frac{1}{k_{trans\_r}} \frac{d}{dt} \frac{1}{k_{trans}^2} \quad \text{(App. 34)}$$

If no loss is taken into account (η_{trans}=100%), the speed ratio k_{trans} and geometric ratio k_{trans_r} are equal. It can be noted that, if the transmission is a fix reduction gear, the last term of (App. 34) is zero. Therefore (App. 34) can be also used to represent the fixed reduction gear. The CVT model can be more complex if more mechanical nonlinearities are taken into account [Setlur 2003].

Appendix 7
eV (electricity and Vehicle) experimental platform of L2EP

The eV (electricity and Vehicle) experimental platform of L2EP is composed of supercapacitors, batteries, fuel cells, DC Machines (DCMs), Synchronous Machines (SMs), Induction Machines (IMs), power electronics, an electric assist bicycle, an electric moto etc. The test setup used in this thesis is shown in Figure 4.15.

Two identical test electric machine benches are available. Each bench is composed of a salient pole SM, an IM and a DCM with a common shaft. Each electrical machine has rated power of 1.5kW.

Two 6-leg IGBT converters can be used for the control of these machines. Each converter has its own adjustable DC bus. Every leg can be used separately and independently from each other. Two modules of supercapacitors can be connected in series or in parallel. Each module is 9,67 F / 90 V. Two inductors of 200 mH and several variable resistances are also available.

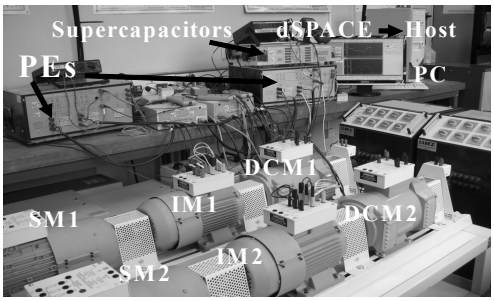

Figure App. 14 Test bench for Series HEV

A dSPACE 1103 system is used to test the control prototype. In the dSPACE system, there is a Digital Signal Processor (DSP) chip based on data acquisition and control processing hardware. The dSPACE system is also equipped with a multi-channel A/D Converter board (analog-to-digital converter) and a multi-channel D/A converter board (analog-to-digital converter).

Using a Host PC, the control prototype written in Matlab/simulink is complied automatically in C-code through the Real Time Workshop (RTW). This executable code is downloaded through the Real Time Interface (RTI) on to the DSP chip to run the real-time experiments.

A dSPACE Controldesk acts as a front end software interface between users and the dSPACE board. The dual-port memory communication capability of the dSPACE board allows the control parameters to be changed by users on-line in the ControlDesk environment in real-time. The actual experimental results are displayed on the ControlDesk windows in real-time.

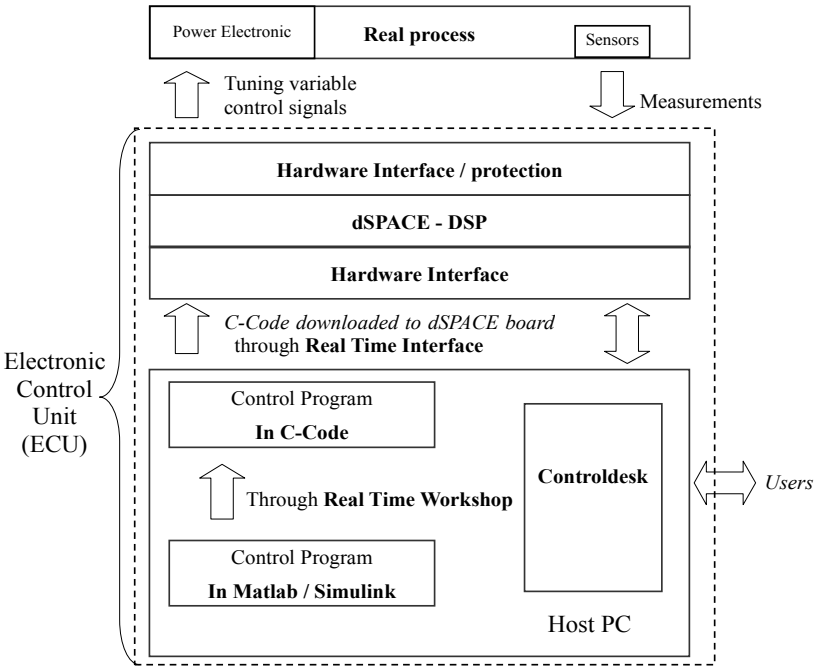

Figure App. 15 Verification in the real-time environment with real processes using a dSPACE system

References

A

1 [ADEME 2007] L'Agence de l'Environnement et de la Maîtrise de l'Energie (ADEME), "Les normes euro pour limiter les émissions de polluants des véhicules neuf" (text in French), *http://194.117.223.129/servlet/getBin*, Mais 2007.

2 [Aimani 2003] S. E. Aimani, F. Minne, B. François, B. Robyns "Modeling and simulation of doubly fed induction generators for variable speed wind turbines integrated in a distribution network", *EPE'03*, September 2003, Toulouse (France).

3 [Allegre 2009] A. L. Allègre, A. Bouscayrol, R. Trigui, "Influence of control strategies on battery/supercapacitor hybrid energy storage systems for traction applications", *IEEE-VPPC'09*, September 2009, Dearborn (USA) (common paper of L2EP and INRETS within the framework of MEGEVH).

4 [Allegre 2010] A. L. Allegre, A. Bouscayrol, J.-N. Verhille, P. Delarue, E. Chattot, S. E. Fassi, "Reduced-scale power hardware-in-the-loop simulation of an innovative subway", *IEEE trans. on Industrial Electronics*, accepted in 2009 for publication in 2010.

5 [Armstrong-Helouvry 1994] B. Armstrong-Helouvry, C. Dupont, C. Candudas de Wit "A survey of models, analysis tools and compensation methods for the control of machines with friction", *Automatica,* July 1994, vol. 30, no. 7, p. 1083-1138.

6 [Anderson 1995] C. Anderson, E. Pettit "The effects of APU characteristics on the design of hybrid control strategies for hybrid electric vehicles", *SAE 950493*, February 1995, p. 65-71.

B

7 [Balcells 2005] Josep Balcells, Alfonso Santolaria, Antonio Orlandi, David Gonzalez, Javier Gago, "EMI Reduction in Switched Power Converters Using Frequency Modulation Techniques", IEEE Trans on Electromagnetic Compatibility, August 2005, vol. 47, no. 3, p. 569-576.

8 [Barre 2006] P. J. Barre, A. Bouscayrol, P. Delarue, E. Dumetz, F. Giraud, J. P. Hautier, X. Kestelyn, B. Lemaire-Semail, E. Semail, "Inversion-based control of electromechanical systems using causal graphical descriptions", *IEEE-IECON'06*, November 2006, Paris (France).

9 [Barsali 2002] S. Barsali, M. Ceraolo, A. Possenti, "Techniques to control the electricity generation in a series hybrid electrical vehicle", *IEEE Trans. on Energy Conversion*, June 2002, vol.17, no.2. p. 260-266.

10 [Barsali 2004] S. Barsali, M. Ceraolo, A. Possenti, "A Control strategy to minimize fuel consumption of series hybrid electric vehicles", *IEEE Trans. on Energy Conversion*, March 2004, vol.19, no.1. p. 187-195.

11 [Bellis 2009] M. Bellis, "Automobile History, The History of Cars and Engines", About.com/Invertors, http://inventors.about.com/od/cstartinventions/a/Car_History.htm, June 2009.

12 [Bogosyan 2007] S. Bogosyan, M. Gokasan, D. J. Goering, "A novel model validation and estimation approach for hybrid serial electric vehicles", *IEEE Trans. on Vehicular Technology*, July 2007, vol. 56, no. 4, p. 1485-1497.

13 [Bonnet 2007] F. Bonnet, P.E. Vidal, and M. Pietrzak-David, "Dual Direct Torque Control of Doubly Fed Induction Machine", *IEEE Trans. on Industrial Electronics*, October 2007, vol. 54, no. 5. p. 2482-2490.

14 [Boulon 2008] L. Boulon, D. Hissel, A. Bouscayrol, M-C. Pera, P. Delarue, "Multi physics modeling and representation of power and energy sources for hybrid electric vehicles", *IEEE-VPPC'08*, September 2008, Harbin (China), (common paper of FEMTO-ST and L2EP within the framework of MEGEVH).

15 [Boulon 2009-a] L. Boulon, "Modélisation multiphysique des éléments de stockage et de conversion d'énergie pour les véhicules électriques hybrides. Approche systémique pour la gestion d'énergie", *Ph. D thesis* (text in French), July 2009, University of Franche Conté, Belfort (France), (within the framework of MEGEVH).

16 [Boulon 2009-b] L. Boulon, D. Hissel, M.-C. Pera, O. Pape, A. Bouscayrol, "Energy based modeling of a 6 wheel drive hybrid heavy truck", *IEEE-VPPC'09*, September 2009, Dearborn (USA), (common paper of FEMTO-ST and L2EP within the framework of MEGEVH).

17 [Bouscayrol 2003] A. Bouscayrol, "Formalismes de représentation et de commande des systèmes électromécaniques multimachines multiconvertisseurs", *HDR thesis (text in French)*, December 2003, University of Lille 1, Lille (France).

18 [Bouscayrol 2005-a] A. Bouscayrol, P. Delarue, B. Francois, J. Niiranen, "Control implementation of a five-leg AC-AC converter to supply a three-phase induction machine", *IEEE Trans. on Power Electronics*, January 2005, vol. 20, no. 1, p. 107-115.

19 [Bouscayrol 2005-b] A. Bouscayrol, P. Delarue, X. Guillaud, "Power strategies for maximum control structure of a wind energy conversion system with a synchronous machine", *Renewable Energy*, May 2005, vol.

30, no. 1, p. 2273-2288.

20 [Bouscayrol 2006-a] A. Bouscayrol, M. Pietrzak-David, P. Delarue, R. Pena-Equiluz, P. E. Vidal, X. Kestelyn, "Weighted control of traction drives with parallel-connected AC machines", *IEEE Trans. on Industrial Electronics*, December 2006, vol. 53, no. 6, p. 1799-1806, (common paper of L2EP and LEEI).

21 [Bouscayrol 2006-b] A. Bouscayrol, W. Lhomme, P. Delarue, B. Lemaire-Semail, S. Aksas, "Hardware-in-the-loop simulation of electric vehicle traction systems using Energetic Macroscopic Representation", *IEEE-IECON'06*, November 2006, Paris (France), p. 5319-5324, (common paper of L2EP and dSPACE).

22 [Bouscayrol 2008] A. Bouscayrol, "Different types of Hardware-in-the-loop simulation for electric drives", *IEEE-ISIE'08*, June 2008, Cambridge (UK).

23 [Bouscayrol 2009] A. Bouscayrol, X. Guillaud, P. Delarue, B. Lemaire-Semail, "Energetic macroscopic representation and inversion-based control illustrated on a wind energy conversion systems using hardware-in-the-loop simulation", *IEEE trans. on Industrial Electronics,* December 2009, vol. 56, no. 12, p. 4826-4935.

24 [Bouscayrol 2010] A. Bouscayrol, "Hardware-in-the-loop simulation", *Industrial Electronics Handbook,* Chapter-M35, Edition Taylor and Francis, to be published in 2010.

25 [Boussak 2005] M. Boussak, "Implementation and experimental Investigation of sensorless speed control with initial rotor position estimation for interior permanent magnet synchronous motor drive", *IEEE Trans. on Power Electronics*, November 2005, vol. 20, no. 6, p. 1413-1422.

26 [Brekken 2007] T.K.A. Brekken, N. Mohan, "Control of a doubly fed induction wind generator under unbalanced grid voltage conditions", *IEEE Trans. on Energy Conversion*, March 2007, vol. 22, no. 1, p. 129 – 135.

27 [Brinkman 2005] N. Brinkman, M. Wang, T. Weber, T. Darlington, "Well-to-wheels analysis of advanced fuel/vehicle systems — a north american study of energy use, greenhouse gas emissions, and criteria pollutant emissions", *Argone National Laboratory report*, www.transportation.anl.gov, May 2005.

28 [Bruyere 2008] A. Bruyere, E. Semail, A. Bouscayrol, F. Locment, J.-M. Dubus, J.-C.Mipo, "Modeling and control of a 7-phase claw-pole starter-alternator for a micro-hybrid automotive application", *IEEE-VPPC08*, September 2008, Harbin (China), (common paper of L2EP and Valeo).

29 [Bruyere 2009-a] A. Bruyere, "Modélisation et commandé d'un alterno-demarreur heptaphase pour application automobile micro-hybride", *Ph. D thesis (text in French),* May 2009, École Nationale Supérieure d'Arts et Métiers (ENSAM), Lille (France).

30 [Burke 2000] A. Burke, "Ultracapacitors: why, how, and where is the technology," *J. Power Sources*, November 2000, vol 91, no. 1, p. 37–50.

31 [Burke 2007] A. F. Burke, "Batteries and ultracapacitors for electric, hybrid, and fuel cell vehicles", *Proceedings of the IEEE*, April 2007, vol. 95, no. 4, p. 806 – 820.

C

32 [Camara 2008] M. B.Camara, H.Gualous, F. Gustin, A.Berthon, "Design and new control of DC/DC converters to share energy between supercapacitors and batteries in hybrid vehicles" *IEEE Trans. on Vehicular Technology*, September 2008, vol. 57, no. 5 p.2721-2735.

33 [Camara 2010] M. B. Camara, H. Gualous, F. Gustin, A. Berthon, B. Dakyo, "DC/DC converter design for supercapacitor and battery power management in hybrid vehicle applications - polynomial control strategy", *IEEE Trans. on Industrial Electronics*, February 2010, vol. 57, no. 2, p. 587-597.

34 [Caron 1995] J.P. Caron, J. P. Hautier , "Modélisation et commande de la machine asynchrone", *Technip* (*text in French)*, first edition*,* January 1995, France, ISBN10 : 2-7108-0683-5.

35 [Ceraolo 2008] M. Ceraolo, A. di Donato, G. Franceschi, "A general approach to energy optimization of hybrid electric vehicles", *IEEE Trans. On Vehicular Technology,* May 2008, vol. 57, no. 3, p. 1433-1441.

36 [Chau 2007] K. T. Chau, C. C. Chan, "Emerging energy - efficient technologies for hybrid electric vehicles", *Proceedings of the IEEE*, April 2007, vol. 95, no. 4, p. 821 – 835.

37 [Chan 2009] C. C. Chan, Y. S. Wong, A. Bouscayrol, K. Chen, "Powering sustainable mobility: roadmaps of electric, hybrid, and fuel cell vehicles", *Proceeding of IEEE*, April 2009, vol. 97, no. 4, p. 603-607.

38 [Chan 2010] C. C. Chan, A. Bouscayrol, K. Chen, "Electric, hybrid and fuel cell vehicles: architectures and modeling", *IEEE Trans. on Vehicular Technology*, accepted in 2009 for publication in 2010.

39 [Chen 2007] K. Chen, P. Delarue, A. Bouscayrol, R. Trigui, "Influence of control design on energetic performance of an electric vehicle", *IEEE-VPPC'07*, September 2007, Arlington (U.S.A.), (common

paper of L2EP and INRETS-Bron within the framework of MEGEVH).

40 [Chen 2008-a] K. Chen, A. Bouscayrol and W. Lhomme, "Energetic macroscopic representation and inversion-based control: application to an electric vehicle with an electrical differential", *Journal of Asian Electric Vehicles*, June 2008, vol. 6, no. 1, p. 1097-1102.

41 [Chen 2008-b] K. Chen, Y. Cheng, A. Bouscayrol, C. C. Chan, A. Berthon, S. Cui, "Inversion-based control of a hybrid electric vehicle using a split electric variable transmission", *Proceeding of IEEE-VPPC'08*, September 2008, Harbin (China), (common paper of MEGEVH in France and HIT in China).

42 [Chen 2009-a] K. Chen, A. Bouscayrol, A. Berthon, P. Delarue, D. Hissel, R. Trigui, "Global modeling of different vehicles: using energetic macroscopic representation to focus on system function and system energy properties", *IEEE Vehicular Technology Magazine*, June 2009, vol. 4, no. 2, p. 80-89 (common paper of L2EP, FEMTO-ST, and INRETS-Bron within the framework of MEGEVH).

43 [Chen 2009-b] K. Chen, A. Bouscayrol, P. Delarue, A. Berthon, "Simulation of a unified control scheme for different hybrid electric vehicles", *IEEE-IECON'09*, Novembre 2009, Porto (Portugal), (common paper of L2EP and FEMTO-ST within the framework of MEGEVH).

44 [Chen 2009-c] K. Chen, W. Lhomme, A. Bouscayrol, A. Berthon, "Comparison of two series-parallel hybrid electric vehicles focusing on control structures and operation modes", *IEEE-VPPC'09*, September 2009, Dearborn (USA), (common paper of L2EP and FEMTO-ST within the framework of MEGEVH).

45 [Chen 2010] K. Chen, P. Delarue, A.Bouscayrol, P.-E. Vidal, M.Pietrzak-David, "Minimum copper loss and power distribution control strategies of double-inverter-fed wound-rotor induction machines using energetic macroscopic representation", *IEEE Trans. on Energy Conversion*, accepted for publication in 2010.

46 [Cheng 2006] Y. Cheng, J. Van Mierlo, P. Bossche, P. Lataire, "Super capacitor based energy storage as peak power unit in the applications of hybrid electric vehicles", *PEMD'06*, April 2006, p.404 – 408, Dublin (Ireland).

47 [Cheng 2007] Y. Cheng, S. Cui, L. Song, C. C. Chan, "The study of the operation modes and control strategies of an advanced electromechanical converter for automobiles", *IEEE Trans. on Magnetics*, January 2007, vol. 43, no. 1, p. 430-433.

48 [Cheng 2009-a] Y. Cheng, K. Chen, C.C. Chan, A. Bouscayrol, S. Cui. "Global

modeling and control strategy simulation using electric variable transmission in hybrid electric vehicles", *IEEE Vehicular Technology Magazine*, June 2009, vol. 4, no. 2, p. 73-79 (common paper of HIT in China and L2EP in France).

49 [Cheng 2009-b] Y. Cheng, C.C. Chan, S. Cui. "Control strategies for an electric variable transmission based hybrid electric vehicle", *IEEE-VPPC'09*, September 2009, Dearborn (USA).

D

50 [Datta 2000] R. Datta, "Rotor side control of grid-connected wound rotor induction motor and its application to wind power generation", *PhD thesis*, 2000, Dept. of Electrical Engineering, Indian Institute of Science, Bangalore.

51 [Delarue 2003-a] P. Delarue, A. Bouscayrol, E. Semail, "Generic control method of multi-leg voltage-source-converters for fast practical implementation", *IEEE Trans. on Power Electronics*, March 2003, vol. 18, no. 2, p. 517-526.

52 [Delarue 2003-b] P. Delarue, A. Bouscayrol, A. Tounzi, G. lancigu, "Modelling, control and simulation of an overall wind energy conversion system", *Renewable Energy*, July 2003, vol. 28, no. 8, p. 1156-1324.

53 [Depenbrock 1988] M. Depenbrock, "Direct self-control of inverted-fed induction machines", *IEEE Trans. on Power Electronics*, October 1988, vol. 3, no. 4, p. 420-429

54 [Delprat 2004] S. Delprat, J. Lauber, T. M. Guerra, J. Rimaux, "Control of a parallel hybrid Powertrain: optimal control", *IEEE Trans. on Vehicular Technology*, May 2004, vol. 53, no. 3, p. 872-881.

55 [Dempsey 2006] M. Dempsey, "Dymola for multi-engineering modeling and simulation", *IEEE-VPPC'06*, September 2006, Windsor (UK).

56 [Drid 2007] S. Drid, M. Tadjine, M.S. Nait-Said, "Robust backstepping vector control for the doubly fed induction motor", *IET Control Theory and Application*, 2007, vol. 1, no. 4, p. 861-868.

E

57 [EC 2009] European Research Area – European Comission, " R&D involvement in the EU economic recovery plan: focus on the three public private partnerships - the energy-efficient buildings, factories of future and european green cars initiatives", *http://ec.europa.eu/research/press/2009/pdf/ppp-fact-sheet_en.pdf,* March 2009.

58 [Ehsani 1997] M. Ehsani, K. M. Rahman, H. A. Toliyat, "Propulsion system design of electric and hybrid vehicles", *IEEE Trans. on Industrial Electronics*, February 1997, vol. 44, no. 1, p. 19-27.

59 [Eshani 2005] M. Eshani, Y. Gao, S. E. Gay, A. Emadi, "Modern electric, hybrid electric and fuel cell vehicles: fundamentals, theory; and design", *CRC Press*, New York, 2005, 2nd edition, ISBN-10: 0849331544.

60 [Ehsani 2007] M. Ehsani, Y. Gao, J. M. Miller, "Hybrid electric vehicles: architecture and motor drives", *Proceedings of the IEEE*, April 2007, vol. 95, no. 4, p. 719-728.

61 [Ehsani 2010] M. Ehsani, Y. Gao, A. Emadi, "Modern electric, hybrid electric and fuel cell vehicles, fundamentals, theory, and design", *CRC Press, second edition*, ISBN-10: 1420053981.

F

62 [Filippa 2005] M. Filippa, C. Mi, J. Shen, R. Stevenson, "Modeling a hybrid electric vehicle powertain test cell using bond graph", *IEEE Trans. on Vehicular Technology*, May 2005, vol. 54, no. 3, p. 837-845.

63 [Foley 2001] D.C. Foley, N. Sadegh, E.J. Barth, G.J. Vachtsevano, "Model identification and backstepping control of a continuously variable transmission system", *American Control Conference*, June 2001, vol. 6, p. 4591-4596, Arlington (USA).

64 [Franceplan 2009] Ministère de l'écologie, de l'énergie, du développement durable et de la mer en charge des technologies vertes et des négociations sur le climat, "Lancement du plan national pour le développement des véhicules électriques et hybrides rechargeables", *(text in French)*, *http:// http://www.developpement-durable.gouv.fr/IMG/pdf/dossier_de_presse_vehicules_ecologiques_cle097ee4.pdf*, october, 2009.

G

65 [Gao 2007] D. W. Gao, C. Mi, A. Emadi, "Modeling and simulation of electric and hybrid vehicles", *Proceedings of the IEEE*, April 2007, vol. 95, no. 4, p. 729 – 745.

66 [Gawthrop 2007] P. J. Gawthrop, G. P.Bevan, "Bond-Graph modeling a tutorial introduction for control engineers", *IEEE Control System*, January 2007, vol. 27, no. 2, p. 24-45.

67 [Giraud 2004] F. Giraud, B. Semail, J. T. Audren, "Analysis and phase control of a piezoelectric traveling-wave ultrasonic motor for haptic stick application", *IEEE Trans on Industry Applications*, Novem-

ber-December 2004, vol. 40, no. 6, p. 1541 – 1549.

68 [Grossi 2009] F. Grossi, W. Lhomme, R. Zanasi, A. Bouscayrol, "Modelling and control of a vehicle with tire-road interaction using energy-based techniques", *IEEE-VPPC'09*, September 2009, Dearborn (USA).

69 [Guzzella 1999] L. Guzzella, A. Amstuz, "CAE tools for quasi-static modeling and optimization of hybrid powertrains", *IEEE trans on Vehicular Technology,* November 1999, vol. 48, no. 6, p. 1762-1769.

H

70 [Hasse 1969] K. Hasse, "On the dynamics of speed control of a static ac drive with a squirrel-cage induction machine", *PhD thesis*, 1969, Tech. Hochschule, Darmstadt.

71 [Hautier 1996] J. P. Hautier, J. Faucher, "Le graphe informationnel causal", *(text in French), Bulletin de l'Union des Physiciens*, Juin 1996, vol. 90, p. 167-189.

72 [Hautier 2004] J. P. Hautier, P. J. Barre, "The causal ordering graph – a tool for modelling and control law synthesis", *Studies in Informatics and Control Journa*l, December 2004, vol. 13, no. 4, p. 265-283.

73 [He 2006] B. He, M. Yang, "Robust LPV control of diesel auxiliary power unit for series hybrid electric vehicles", *IEEE Trans. on Power Electronics*, May 2006, vol. 21, no. 3. p. 791-798.

74 [Hellgren 2007] J. Hellgren, "Life cycle cost analysis of a car, a city bus and an intercity bus powertrain for year 2005 and 2020", *Energy Policy,* January 2007, vol. 35, no. 1, p. 39-49.

75 [Hilairet 2006] M. Hilairet, J. Mazouari, C. Marchand, "Position and speed estimations of a switched reluctance machine using current harmonic", *IEEE-IECON'06*, November 2006, Paris (FRANCE), p. 5063-5068.

76 [Hochgraf 1996] C. Hochgraf, M. Ryan, H. Wiegman "Engine control strategy for a series hybrid electric vehicle incorporating load-levling and computer controlled energy management", *SAE 960230,* 1996, p. 11-24.

77 [Hoeijmakers 2006] M. J. Hoeijmakers, J. A. Ferreira, "The electric variable transmission", *IEEE Trans. on Industry Applications,* July/August 2006, vol. 42, no. 4. p. 1092-1100.

78 [Hopfensperger 2001] B. Hopfensperger, D. J. Atkinson, "Double-fed a.c machines: classification and comparison," *EPE'01*, August 2001, Graz (Austria).

79 [Husain 2005] I. Husain, S. A. Hossain, "Modeling, simulation, and control of switched reluctance motor drives", *IEEE Trans. on Industrial Electronics*, December 2005, vol. 52, no. 6, p. 1625-1634.

I

80 [IEA 2009-a] International Energy Agency Implementing Agreement on Hybrid and Electric Vehicles, "Hybrid and electric vehicles – The electric drive established a market foothold", Feburary 2009.

81 [IEA 2009-b] International Energy Agency Implementing Agreement on Hybrid and Electric Vehicles, "outlook for hybrid and electric vehicles", http://www.ieahev.org/pdfs/ia-hev_outlook_2009.pdf, *IA-HEV Outlook*, June 2009.

82 [Ioannou 1988] P.A. Ioannou and J. Sun, "Theory and design of robust direct and indirect adaptive control schemes," *Int. J. Control,* ,1988, vol. 47, pp 775-813.

83 [Isermann 1999] R. Isermann, J. Schaffnit, S. Sinsel, "Hardware-in-the-loop simulation for the design and testing of engine-control systems", *Control Engineering Practice*, May 1999, vol. 7, no. 5, p. 643-653.

84 [Iwasaki 1994] I. Iwasaki, H. A. Simon, "Causality and model abstraction"*, Artificial Intelligence, Elsevier*, 1994, vol. 67, p. 143-194.

J

85 [Jalil 1997] N. Jalil, N. A. Kheir, M. Salman, " A rule-based energy management strategy for a series hybrid vehicle", *American Control Conference*, June 1997, Albuquerque (USA).

86 [Jeanneret 1999] B. Jeanneret, R. Trigui F. Badin, F. Harel, "New hybrid concept simulation tools, evaluation on the Toyota Prius Car", *EVS-16*, October 1999, Beijing (China).

87 [Jong-Seob 2005] Won Jong-Seob, R.Langari, "Intelligent energy management agent for a parallel hybrid vehicle-part II: torque distribution, charge sustenance strategies, and performance results", *IEEE Trans. on Vehicular Technology,* May 2005, vol. 54, no. 3, p. 935-953.

K

88 [Karnopp 1975] D. Karnopp, R. Rosenberg, "System dynamics: a unified approach", *John. Wiley & sons*, 1975.

89 [Karnopp 2006] D. Karnopp, L. Margolis, R. Rosenberg, "System dynamics – modelling and simulation of mechatronic systems", *John Wiley & sons*, 2006.

90 [Kawabata 1999] Y. Kawabata, E. Ejiogu and T. Kawabata, "Vector-Controlled Double-Inverter-Fed Wound-Rotor Induction Motor Suitable for High-Power Drives", *IEEE Trans. on Industry Applications*, September-October 1999, vol. 35, no. 5, p. 1058-1066.

91 [Kermani 2009] S. Kermani, "Gestion énergétique des véhicules hybrides. De la simulation à la commande temps réel", *Ph. D thesis (text in French)*, September 2009, University of Valenciennes, Valenciennes (France), (within the framework of MEGEVH).

92 [Kestelyn 2002] X. Kestelyn, B. Francois, J.-P. Hautier, "A torque estimator for a switched reluctance motor using an orthogonal neural network", *EERR (Electrical Engineering Research Report*), December 2002, no. 14, p. 8-14.

93 [Kessels 2007] J. Kessels, "Energy management for automotive power net", *Phd thesis*, February 2007, Eindhoven University of Technology, Eindhoven (Holland).

94 [Kessels 2008] J.T.B.A. Kessels, M.W.T. Koot, P.P.J. van den Bosch, D.B. Kok, "Online energy management for hybrid electric vehicles", *IEEE Trans. on Vehicular Technology,* November 2008, vol. 57, no. 6, p. 3428-3440.

95 [Kim 1997] J. M. Kim and S. K. Sul, "Speed control of interior permanent magnet synchronous motor drive for the flux weakening operation", *IEEE Trans. on Industry Applications*, January- February 1997, vol. 33, no. 1. p.43-48.

L

96 [Lecocq 1993] D. Lecocq, P. Lataire, W. Wymeersch, "Application of the double fed asynchronous motor (DFAM) in variable-speed drives", *Fifth European Conference on Power Electronics and Applications*, September 1993, vol. 5, p. 419 – 425, Brighton (UK).

97 [Lee 1998] H.D. Lee, S.-K. Sul, "Fuzzy-logic-based torque control strategy for parallel-type hybrid electric vehicle," *IEEE Trans. on Industrial Electronics*, August 1998, vol. 45, no. 4, p. 625–632.

98 [Leonard 1896] H.W. Leonard, "Volts versus ohms. The speed regulation of electric motors", *AIEE*, 1896, vol. 13, p. 375-384.

99 [Letrouve 2009] T. Letrouve, P. Delarue, A. Bouscayrol, "Modeling and contol of a double parallel hybrid electric vehicle using energetic macroscopic

representation", *ElectroMotion'09*, Lille, France, July 2009.

100 [Levi 2007] E. Levi, R. Bojoi, F. Profumo, H. A. Toliyat, S. Williamson, "Multiphase induction motor drives – a technology status review", *IET Electric Power Applications*, July 2007, vol. 1 no. 4, p. 489-516.

101 [Lhomme 2004] W. Lhomme, A. Bouscayrol, P. Barrade, "Simulation of series hybrid electric vehicles based on energetic macroscopic representation", *IEEE-ISIE'04*, Ajaccio (France), vol. 2, p. 1525 – 1530, (common paper of L2EP in France and EPFL in Switzerland).

102 [Lhomme 2007] W. Lhomme, "Gestion d'énergie de véhicules électriques hybrides basée sur la représentation énergétique macroscopique", *Ph. D thesis (text in French),* November 2009, University of Lille 1, Lille (France), (within the framework of MEGEVH).

103 [Lhomme 2008-a] W. Lhomme, R. Trigui, P. Delarue, B. Jeanneret, A. Bouscayrol, F. Badin, "Switched causal modeling of transmission with clutch in hybrid electric vehicles", *IEEE Tran. on Vehicular Technology*, July 2008, vol. 57, no. 4, p. 2081-2088 (common paper of L2EP and INRETS-Bron within the framework of MEGEVH).

104 [Lhomme 2008-b] W. Lhomme, M. J. Hancock, F. Assadian, D. Cieslar, "Multi-model of a hybrid electric vehicle's four-wheel drive system with automatically-engaging clutch", *IEEE-VPPC'08*, September 2008, Harbin (China).

105 [Lhomme 2009] W. Lhomme, P. Delarue, A. Bouscayrol, P. Le Moigne, P. Barrade, A. Rufer, "Comparison of control strategies for maximizing energy in a supercapacitor storage subsystem", *EPE Journal*, July 2009, vol. 19, no. 3, (common paper of L2EP in France and EPFL in Switzerland).

106 [Lhomme 2010] W. Lhomme, R. Trigui, A. Bouscayrol, P. Delarue, B. Jeanneret, F. Badin, "Inversion-based control of a vehicle with a clutch using a switched causal modelling ", *International Journal of Systems Science*, accepted for publication in 2010 (common paper of L2EP and INRETS–Bron within the framework of MEGEVH).

107 [Liu 2008] J. Liu, H. Peng, "Modeling and control of a power-split hybrid vehicle", *IEEE Trans. on Control Systems Technology*, November 2008, vol. 16, no. 6, p. 1242-1251.

108 [Locment 2006] F. Locment, "Conception et modélisation d'une machine synchrone à 7 phases à aimants permanents et flux axial: commande vectorielle en modes normal et dégradé", , *Ph. D thesis (text in French),* December 2006, École Nationale Supérieure d'Arts et Métiers (ENSAM), Lille (France).

109 [Lovelace 1998] E. C. Lovelace, T. M. Jahn, J. L. Kirtley, Jr., and J. H. Lang, "An interior PM starter/alternator for automotive application,"ICEM'98, September 1998, vol. 3, p. 1802–1808, Istanbul (Turkey).

110 [López 2008] J. López, E.Gubía, P. Sanchis, X. Roboam, L. Marroyo, "Wind turbines based on doubly fed induction generator under asymmetrical voltage dips", *IEEE Trans. on Energy Conversion*, March 2008, vol.23, no.1, p. 321 – 330.

111 [Lu 2001] Q. Lu, Y. Z. Sun, and S. W. Mei, "Nonlinear control systems and Power system dynamics", *Norwell, MA: Kluwer*, 2001.

M

112 [Maggetto 2000] G. Maggetto, J. Van Mierlo, "Electric and electric hybrid vehicle technology: a survey", *IEE Seminar, Electric, Hybrid and Fuel Cell Vehicles*, April 2000.

113 [Makhijani 2006] A. Makhijani, A. Makhijani, "Low-carbon diet without nukes in France – An energy technology and policy case study on simultaneous reduction of climate change and proliferation risks", *Institute for Energy Environmental Research*, http://www.ieer.org/reports/energy/france/lowcarbonsummfr.pdf, May 2006.

114 [Makni 2007] Z. Makni, M. Besbes, and C. Marchand, "Multiphysics design methodology ofpermanent-magnet synchronous motors", *IEEE Trans. On Vehicular Technology*, July 2007, vol. 56, no. 4, p.1524-1530.

115 [Marie-Francoise 2005] J. N. Marie-Francoise, H. Gualous, R. Outbib,A. Berthon, "42V powernet with supercapacitor and battery for automotive applications", *Journal of power sources*, 2005, vol. 143, no. 1-2, p. 275-283.

116 [Marie-Francoise 2006] J.N. Marie-Francoise, H. Gualous, A. Berthon, "Supercapacitor thermal- and electrical- behaviour modelling using ANN", *IEEE Proceedings Electronic power Applications*, March 2006, vol. 153, no. 2, p. 255-262

117 [Martin 2004] J. H. Martin, J. A. Ferreira, "The electrical variable transmission," *IEEE-IAS 39th*, HongKong (China), October 2004.

118 [MEGEVH 2007] A. Bouscayrol, S. Delprat, D. Hissel and R. Trigui, "MEGEVH project: graphical modelling for energy management of hybrid electric vehicles", *EET'07*, May-June 2007, Brussel (Belgium).

119 [McGraw 2003] McGraw Hill Higher Education, "Dictionary of electrical and

computer engineering", *The McGraw-Hill Companies,* Second edition, July 2003.

120 [Mierlo 2004] J. V. Mierlo, P. V. d. Bossche, G. Maggetto, "Models of energy sources for EV and HEV: fuel cells, batteries, ultracapacitors, flywheels and engine-generators", *Journal of Power Sources,* March 2004, vol. 128, no. 1, p. 76-89.

121 [Miller 2006] J. M. Miller, "Hybrid electric vehicle propulsion system architectures of the e-CVT type", *IEEE Trans. on Power Electronics*, May 2006, vol. 21, no. 3, p. 756-767.

122 [MMS 2000] A. Bouscayrol, B. Davat, B. de Fornel, B. François, J. P. Hautier, F.Meibody-Tabar, M. Pietrzak-David, "Multimachine multiconverter sstem: application for electromechanical drives", *European Physics Journal - Applied Physics*, May 2000, vol. 10, no. 2, p. 131-147.

123 [MMS 2003] A. Bouscayrol, B. Davat, B. de Fornel, B. François, J. P. Hautier, F. Meibody-Tabar, E. Monmasson, M. Pietrzak-David, H. Razik, E. Semail, M. F. Benkhoris, "Control structures for multi-machine multi-converter systems with upstream coupling", *Mathematics and Computers in Simulation*, November 2003, vol. 63, no. 3-5, p. 261-270.

124 [Morselli 2006] R. Morselli, R. Zanasi, "Modeling of automotive control systems using power oriented graphs", *IEEE-IECON'06*, November 2006, Paris (France).

N

125 [Nordlund 2002] E. Nordlund, C. Sadarangani, "The four quadrant energy transducer," *IEEE-IAS 37th*, October 2002, Pittsburgh (U.S.A), p. 390–391.

O

126 [Olszewsky 2006] M. Olszewsky, R. H. Staunton, C. W. Ayers, L. D. Marlino, J. N. Chiassion, T. A. Burress, "Evaluation of 2004 Toyota Prius hybrid rlectric drive system", *Report prepared by Oak Ridge National Laboratory*, Submitted to Energy Efficiency and Renewable Energy Freedom Car and vehicle Technologies, May 2006.

127 [Onoda 2004] S. Onoda, A. Emadi, "PSIM-based modeling of automotive power systems: conventional, electric, and hybrid electric vehicles" *IEEE Trans. on Vehicular Technology*, March 2004, vol. 53, no. 2, p. 390 – 400.

128 [Ortega 2010] C.Ortega, A. Arias, C. Caruana,; J. Balcells, G. Asher, "Improved waveform quality in the direct torque control of matrix converter-fed PMSM drives", *IEEE Trans on Industrial Electronics*, accepted in 2009 for publication in 2010.

P

129 [Peng 2009] L. Peng, B. Francois, Y. Li, "Improved crowbar control strategy for DFIG based wind turbines to ride-through grid faults", *IEEE-APEC '09*, March 2009, Washington (USA).

130 [Paganelli 1999] G. Paganelli, "Conception et commande d'une chaîne de traction pour véhicule hybride parallèle thermique et électrique", *Ph. D thesis (text in French)*, 1999, University of Valenciennes and of Hainaut-Cambrésis.

131 [Paynter 1961] H. Paynter, "Analysis and design of engineering systems", *MIT Press*, 1961.

132 [Pisu 2007] P. Pisu, G. Rizzoni, "A comparative study of supervisory control strategies for hybrid electric vehicles", *IEEE Trans. on Control Systems Technology,* May 2007, vol. 15, no. 3, p. 506-518.

133 [Poddar 2004] G. Poddar, V. T. Ranganathan, "Direct torque and frequency control of double-inverter-fed slip-ring induction motor drive", *IEEE Trans. on Industrial Electronics*, December 2004, vol. 51. no. 6, p. 1329-1337.

134 [Poddar 2005] G. Poddar, V. T. Ranganathan, "Sensorless double-inverter-fed wound-rotor induction-machine drive", *IEEE Trans. on Industry Electronics*, December 2005, vol. 53, no. 1, p. 86-95.

135 [PSAT] PSAT documentation [Online], available http://www.transportation.anl.gov/software/PSAT/

136 [Pusca 2004] R. Pusca, Y. Ait-Amirat, A. Berthon, J. M .Kauffmann, "Fuzzy-logic based control applied to a hybrid electric vehicle with four separate wheel drives", *IEE Proceedings Control Theory and Applications*, January 2004, vol. 151, no. 1, p 73-81.

R

137 [Rabelo 2006] B. Rabelo, W. Hofmann, L. Pinheiro, "Loss reduction methods for doubly-fed induction generator drives for wind turbines", *IEEE-SPEEDAM'06*, May 2006, Taormina (Italie).

138 [Raskin 2006] P A. Raskin, S. Shah, "The emergence of hybrid vehicles – ending oil's stranglehold on transportation and the economy",

http://www.calcars.org/alliance-bernstein-hybrids-june06.pdf, June 2006.

139 [Rizzoni 1999] G. Rizzoni, L. Guzzella, B. M. Baumann, "Unified modeling of hybrid electric vehicle drivetrains", *IEEE/ASME Trans. on Mechatronics*, September 1999, vol. 4, no. 3, p. 246-257.

140 [Roell M. van 2001] D. Roell M. van, "Transmission design of the zero inertia powertrain", *Projet report*, 2001, Eindhoven University of Technology, http:// alexandria.tue.nl/extra2/200141350.pdf.

141 [Rufer 2004] A. Rufer, P. Barrade, D. Hotellier, and S. Hauser, "Sequential supply for electrical transportation vehicles: Properties of the fast energy transfer between supercapacitive tanks," *Journal of Circuits, Systems and Computers*, August 2004, vol. 13, no. 4, p. 941–955.

S

142 [Salmasi 2007] F. R. Salmasi, "Control strategies for hybrid electric vehicles: evolution, classification, comparison and future trends", *IEEE Trans. on Vehicular Technology*, September 2007, vol. 56, no. 5, p. 2393-2404.

143 [Sasaki 1998] S. Sasaki, "Toyota's newly developed hybrid powertrain", *ISPSD'98*, June 1998, Kyoto (Japon), p. 17 – 22.

144 [Sastry 1989] S. Sastry, M. Bodson, "Adaptive control - stability, converglence, and robustness", *Prentice, Hall, New Jersey*, 1989.

145 [Scordia 2004] J. Scordia, "Approche systématique de l'optimisation du dimensionnement et de l'élaboration de lois de gestion d'énergie de véhicules hybrides", *Ph. D thesis (text in French)*, January 2004, Henri Poincaré University, Nancy (France).

146 [Semail 2003] E. Semail, A. Bouscayrol, J. P. Hautier, "Vectorial formalism for analysis and design of polyphase synchronous machines", *European Physical Journal - Applied Physics,* June 2003, vol. 22, no. 3, p. 207-220.

147 [Serrano-Iribarnegaray 2007] L. Serrano-Iribarnegaray, J. Martinez-Roman, "A unified approach to the very fast torque control methods for DC and AC machines", *IEEE Trans. on Industrial Electronics*, August 2007, vol. 54, no. 4, p. 2047-2056.

148 [Setlur 2003] P. Setlur, J.R. Wagner, D.M. Dawson, B. Samuels, "Nonlinear control of a continuously variable transmission (CVT)", *IEEE Trans. on Control Systems Technology*, January 2003, vol. 11, no. 1, p. 101-108.

149 [Schaible 1999] U. Schaible and B. Szabados, "Dynamic motor parameter iden-

tification for high speed flux weakening operation of brushless permanent magnet synchronous machines “, *IEEE Trans. on Energy Conversio*n, September 1999, vol. 14, no. 3, p.486 – 492.

150 [Schönfeld 2004] R. Schönfeld, G.-H. Geitner, “Power flow and information flow in motion control system”, *EPE-PEMC’04*, September 2004, Riga.

151 [Sciarretta 2004] A. Sciarretta, M. Back, L. Guzzella, “Optimal control of parallel hybrid electric vehicles”, *IEEE Trans. on Control Systems Technology*, May 2004, vol. 12, no. 3, p. 352-363.

152 [Scuiller 2004] F. Scuiller, E. Semail, J.F. Charpentier, S. Clénet, “Comparison of conventional and unconventional 5-phase PM motor structures for naval application systems”, *IASME Trans.* April 2004, vol. 1, no. 2, p 365-370.

153 [Sepe 2001] R. Sepe, C. Morrison, J. M. Miller, A. Gale, “High efficiency operation of a hybrid electric vehicle starter generator over road profile”, *IEEE Industry Application Conference*, September-October 2001, vol. 2, p. 921 - 925.

154 [Sozer 2007] Y. Sozer, D.A. Torrey, “Optimal turn-off angle control in the face of automatic turn-on angle control for switched-reluctance motors”, *IET Electric Power Applications,* May 2007, vol. 1, no. 3, p. 395-401.

155 [Syed 2006] F. U. Syed, M. L. Kuang, J. Czubay, H. Ying, “Derivation and experimental validation of a power-split hybrid electric vehicle model”, *IEEE Trans. on Vehicular Technology*, November 2006, vol. 55, no. 6. p. 1731-1744.

156 [Syed 2009] F. U. Syed, M. L. Kuang, M. Smith, S. Okubo, H. Ying, “Fuzzy gain-scheduling proportional–integral control for improving engine power and speed behavior in a hybrid electric vehicle”, *IEEE Trans. on Vehicular Technology,* January 2009 vol. 58, no. 1, p. 69-84.

157 [Syrota 2008] J. Syrota, P. Hirtzman, R. Beaume, J. Loyer, H. Pouliquen, D. Ravet, P. Rossinot, “Perspectives concernat le vehicule ‘grand public’ d’ici 2030”, (text in French), *Centre d’analyse strategique, Conseil general des mines,* septembre 2008.

T

158 [Takahashi 1986] I. Takahashi, T. Noguchi, “A new quick-response and high-efficiency control strategy of an induction motor”, *IEEE Trans. on Industrial Application*, September/October 1986, vol. IA-22, no. 5, p. 820-827.

159 [Tapia 2006] G. Tapia, A. Tapia, J. X. Ostolaza, "Two alternative modeling approaches for the evaluation of wind farm active and reactive power performances", *IEEE Trans. on Energy Conversion*, December 2006, vol. 21, no. 4, p. 909 – 920.

160 [Thounthong 2007] P. Thounthong, S. Rael, B. Davat, "Control strategy of fuel cell and supercapacitors association for a distributed generation system" *IEEE Trans. on Industrial Electronics*, December 2007, vol. 54, no. 6, p. 3225-3233.

161 [Tiller 2003] M. Tiller, P. Bowles, M. Dempsey, "Development of a vehicle modeling architecture in modelica", *International Modelica Conference*, Linköping (Sweden), p. 75-86, November 2003.

162 [Tnani 1995] S. Tnani, S. Diop, A. Berthon, J. M. Kauffmann, "Generalised model of double-fed induction machines", *IASTED'95*, February 1995, Innsbruck (Austria).

163 [Trigui 2004-a] R. Trigui, J. Scordia, M. Desbois Renaudin, B. Jeanneret, F. Badin, "Global forward backward approach for a systematic analysis and implementation of hybrid vehicle management laws", *EET'04*, March 2004, Estoril (Portrugal).

164 [Trigui 2004-b] R. Trigui, B. Jeanneret, F. Badin, "Modélisation systémique de véhicules hybrides en vue de la prédiction de leurs performances énergétiques et dynamiques. Construction de la bibliothèque de modèles VEHLIB", (Text in French), *Revue Recherche Transport Sécurité (RTS)*, April-June 2004, no. 83, p. 129-150.

165 [Trigui 2007] R. Trigui, B. Jeanneret, B. Malaquin, F. Badin, C. Plasse "Hardware in the loop summation of a diesel parallel mild-hybrid electric vehicle" *IEEE–VPPC'07*, Arlington (USA), September 2007.

U

166 [Uhrig 2007] R. E. Uhrig, "Using plug-in hybrid vehicles", http://www.tbp.org/pages/publications/BENTFeatures/Sp05Uhrig.pdf, June 2007.

V

167 [Vaclavek 2008] P. Vaclavek, P. Blaha, "Interior permanent magnet synchronous machine field weakening control strategy – the analytical solution", *SICE annual conference*, August 2008, p. 753-757, Tokyo (Japan).

168 [Verhille 2007-a] J. N. Verhille, "Représentation énergétique macroscopique du métro VAL 206 et structures de commande déduites par inversion", *Ph. D thesis (text in French)*, July 2007, École Nationale Supérieure d'Arts et Métiers (ENSAM), Lille (France).

169 [Verhille 2007-b] J-N Verhille, A. Bouscayrol, P-J Barre, J-P Hautier, "Validation of anti-slip control for a subway traction system using Hardware-In-the-Loop simulation ", *IEEE-VPPC'07*, October 2007, Arlington (USA).

170 [Vidal 2007] P.E. Vidal, M. Pietrzak-David, F. Bonnet, "Mixed control strategy of a doubly fed induction machine", *Electrical Engineering*, September 2007, vol. 9, no.5, p. 337-346.

171 [Vinot 2008] E. Vinot, J. Scordia, R. Trigui, B. Jeanneret, F. Badin, "Model simulation, validation and case study of the 2004 THS of Toyota Prius", *International Journal of Vehicle Systems Modelling and Testing*, 2008, vol. 3, no. 3, p. 139-166.

W

172 [Waltermann 1996] P. Waltermann, "Modelling and control of the longitudinal and lateral dynamics of a series hybrid vehicle", *Proceedings on Control Applications,* Septembre 1996, Dearborn (USA), pp.191 – 198.

173 [Willamson 2005] S. S. Willamson, A. Emadi, "Comparative assessment of hybrid electric and fuel cell vehicles based on comprehensive well-to-wheels efficiency analysis", *IEEE Trans. on Vehicular Technology*, May 2005, vol. 54, no. 3, p. 856–862.

174 [Wipke 1999] K. B. Wipke, M. R. Cuddy, S. D. Burch, "ADVISOR 2.1 a user-friendly advanced powertrain simulation using a combined backward/forward approach", *IEEE Trans. on Vehicular Technology*, November 1999, vol. 48, no. 6, p. 1751-1761.

175 [Won 2005] J. Won, R. Langari, "Intelligent energy management agent for a parallel hybrid vehicle—part II: torque distribution, charge sustenance strategies, and performance results", *IEEE Trans. on Vehicular Technology*, May 2005, vol. 54, no. 3, p. 35-953.

Y

176 [Yang 2000] I. W. Yang, Y. S. Kim, Y.-S, "Rotor speed and position sensorless control of a switched reluctance motor using the binary observer" *IEEE Proc. of Electric Power Applications*, May 2000, vol. 147, no. 3, p. 220 – 226.

177 [Yoo 2008] H. Yoo, S.-K. Sul,Y. Park, J. Jeong, "System integration and power-flow management for a series hybrid electric vehicle using supercapacitors and batteries", *IEEE Trans. on Industry Applications*, January/February 2008, vol. 44, no. 1, p. 108-114.

Z

178 [Zanasi 1996] R. Zanasi, "Power-oriented graphs for modeling electrical machines", *MELECOM'96*, Bari (Italy), May 1996, p. 1211-1214.

179 [Zheng 2007] P. Zheng, R. Liu, P. Thelin, E. Nordlund, C. Sadarangani, "Research on the parameters and performances of a 4QT prototype machine used for HEV", *IEEE Trans. on Magnetics*, January 2007, vol. 43, no. 1, p. 443-446.

180 [Zhu 2007] Z.Q. Zhu, D. Howe, "Electrical machines and drives for electric hybrid and fuel cell vehicles", *Proceedings of the IEEE*, April 2007, vol. 95, no. 4, p. 746-765.

181 [Zhou 1999] K. M. Zhou, "Essentials of robust control", *Englewood Cliffs, NJ: Prentice-Hall*, 1999.

182 [Zordan 2000] M. Zordan, P. Vas, M. Rashed, S. Bolognani and M. Zigliotto, "Field-weakening in vector controlled and DTC PMSM drives, a comparative analysis", *PEVD'00*, September 2000, London (UK).

Acronyms and abbreviations

AC	Alternating Current
ACEA	European Automobile Manufacturers Association (French: Association des Constructeurs Européens d'Automobiles)
BEV	Battery-powered Electric Vehicle
BAT	Battery
BMS	Battery Management System
CFCs	chlorofluorocarbons
CH4	methane
CNG	Compressed Natural Gas
CO	carbon monoxide
CO2	carbon dioxide
COG	Causal Ordering Graph
DC	Direct Current
DCM	Direct Current Machine
DFIM	Double Fed Induction Machine
DIF-WRIM	Double-Inverter-Fed Wound-Rotor Induction Machine
ECU	Electronic Control Unit
EM	Electric Machine
EMR	Energetic Macroscopic representation
ESS	electric Energy Storage Systems
EU	European Union

EUDC	Extra Urban Driving Cycle
FCV	Fuel-Cell Vehicle
GHG	Green House Gasses
HEV	Hybrid Electric Vehicle
HIL simulation	Hardware-In-the-Loop simulation
ICE	Internal Combustion Engine
IEA	International Energy Agency
IM	Induction Machine
LNG	Liquefied Natural Gas
MEGEVH	A national scientific network on HEV in France (French: Modélisation Energétique et Gestion d'Energie de Véhicules Hybrides / Energy Modelling and Energy Management of Hybrid Vehicles)
O3	ozone
OPEC	Organization of the Petroleum Exporting Countries
PE	Power Electronics
PFD	Power Flow Diagram
PHEV	Plug-in Hybrid Electric Vehicle
PMSM	Permanent Magnet Synchronous Machine
POG	Power Oriented Graph

PSAT	Powertrain System Analysis Toolkit
RG	Reduction Gear
NEDC	New European Driving Cycle
N2O	nitrous oxide
NOx	nitrogen oxides
NGV	Natural Gas Vehicle
SM	Synchronous Machine
SOx	sulfur oxides
SOC	State Of Charge
SRM	Switched Reluctance Machine
VEHLIB	Hybrid Electric Vehicle Library
VSI	Voltage-Source-Inverter
WRIM	Wound-Rotor Induction Machine
ZEV	Zero Emission Vehicle

List of symbols

d	*referring to d-axis components*
q	*referring to q-axis components*
s	*referring to stators*
r	*referring to rotors*
est	*referring to estimations*
mea	*referring to measurements*
ref	*referring to references*
f	*viscous friction coefficient (Nms)*
$[f]$	*viscous friction coefficient matrix (Nms)*
F_{br}	*mechanical braking force (N)*
F_{env}	*environmental resistance force (N)*
F_{tran}	*Transmission force (N)*
i_{conv}	*received electrical source (DC bus) current (A)*
i_{d_sr}	*current vector in the d-axis (A)*
i_{q_sr}	*current vector in the q-axis (A)*
i_{s_con}	*DC current of the stator converter (A)*
i_{r_con}	*DC current of the rotor converter (A)*
i_s	*stator current vector (A)*
i_{s_dq}	*d-q stator current vector (A)*
i_{sd}	*stator current in the d-axis (A)*
i_{sq}	*stator current in the q-axis (A)*
i_r	*rotor current vector (A)*
i_{r_dq}	*d-q rotor current vector (A)*
i_{rd}	*rotor current in the d-axis (A)*
i_{rq}	*rotor current in the q-axis (A)*
i_{tot}	*received ESS current (A)*
i_1	*PE1' current on the DC bus side (A)*
i_2	*PE2' current on the DC bus side (A)*
k_1, $k_2(k_{21}, k_{22})$, k_3	*strategy outputs for DIF-WRIMs*
$[K_{eq}]$	*gain matrix*

k_d	*distribution ratio for the distribution power between mechanical braking and propulsion machines*
k_T, k_R, k_S	*presenting mechanical coupling relationships between machines and the transmission for different HEVs*
k_{trans}	*transmission ratio*
e_d	*e.m.f in the d-axis (V)*
e_q	*e.m.f in the q-axis (V)*
e_{d_sr}	*equivalent e.m.f in the d-axis (V)*
e_{q_sr}	*equivalent e.m.f in the q-axis (V)*
E_{sc}	*Energy of supercapacitors (J)*
J	*total moment of inertia (kg·m2)*
$[J]$	*coefficients of the matrix of the moments of inertia (kg·m2)*
J_{eq}	*Equivalent total moment of inertia (kg·m2)*
$[L_{eq}]$	*equivalent induction matrix (H)*
L_{sd}	*cyclic stator inductance in the d axis (H)*
L_{sq}	*cyclic stator inductances in the q axis (H)*
L_s	*cyclic stator inductance (H)*
L_r	*cyclic rotor inductance (H)*
M	*vehicle mass (kg)*
M_{sr}	*stator-rotor mutual inductance (H)*
m_s	*stator converter modulation vector*
m_r	*rotor converter modulation vector*
p	*pole pair number*
P_{bat_req}	*required battery power depending on the SOC (W)*
$P_{est}(SOC)$	*available battery power based on the SOC (W)*
p_{cl}	*clutch position (%)*
P_l	*estimated system losses (W)*
p_r	*rotor power (W)*
P_{req}	*Required vehicle power (W)*
P_{req_h}	*highest required vehicle power in a strategy for a series HEV (W)*
P_{req_l}	*lowest required vehicle power in a strategy for a series HEV (W)*
p_s	*stator power (W)*
P_{trac_req}	*required traction power (W)*

R_C	*carrier radius (m)*
$[R_{eq}]$	*equivalent resistance matrix (Ω)*
R_{est}	*estimated reduction coefficient which depends on the system losses and the system limitation used in a control strategy for supercapacitor based ESS*
R_s	*stator resistance (Ω)*
R_r	*rotor resistance (Ω)*
R_R	*ring radius (m)*
R_S	*sun radius (m)*
R_{wh}	*radius of the wheels (m)*
SOC	*state of charge*
SOC_h	*highest value of supercapacitor voltage with in its range*
SOC_l	*lowest value of supercapacitor voltage with in its range*
T_{br}	*mechanical braking torque (Nm)*
T_C	*carrier torque (Nm)*
T_{cl1_M}	*clutch torque on the mechanical coupling side (Nm)*
T_{cl_max}	*maximal clutch torque (Nm)*
T_{em}	*machine torque (Nm)*
T_{EM1}	*EM1 torque (Nm)*
T_{EM2}	*EM2 torque (Nm)*
T_{ICE}	*ICE torque (Nm)*
T_l	*lord torque (Nm)*
T_{res}	*resistance torque acting on the transmission shaft (Nm)*
T_R	*ring torque (Nm)*
T_S	*sun torque (Nm)*
T_{tran}	*Transmission torque (Nm)*
$[T(\theta)_x]$	*Park transformation matrix*
$[T_i]$	*current transformation matrix which is used in Y or Δ circuits*
$[T_{vu}]$	*voltage transformation matrix which is used to convert the phase-to-phase voltages u to the phase-to-neutral voltages v in Y or Δ circuits*
u_r	*rotor phase-to-phase voltage vector (V)*
u_s	*stator phase-to-phase voltage vector (V)*
u_{SC}	*supercapacitor voltage (V)*
u_{SC_h}	*highest value of supercapacitor voltage with in its range (V)*
u_{SC_l}	*lowest value of supercapacitor voltage with in its range (V)*
v_{dc}	*DC Bus voltage (V)*

v_{d_sr}	*voltage vector in the d-axis (V)*
v_{q_sr}	*voltage vector in the q-axis (V)*
v_{s_dq}	*d-q stator voltage vector (V)*
v_{sd}	*stator voltage in the d-axis (V)*
v_{sq}	*stator voltage in the q-axis (V)*
v_{r_dq}	*d-q rotor voltage vector (V)*
v_{rd}	*rotor voltage in the d-axis (V)*
v_{rq}	*rotor voltage in the q-axis (V)*
v_{hev}	*vehicle velocity(km/h)*
τ_s	*stator electric time constant*
τ_r	*rotor electric time constant*
σ	*magnetic leakage factor between the stator and rotor windings*
$\theta_{d/s}$	*angle between the d-axis and the α_s-axis*
$\theta_{d/r}$	*angle between the d-axis and the α_r-axis*
θ	*electrical angle between the rotor and the stator*
ω	*electric pulsation (rad/s)*
$\omega_{d/s}$	*electric pulsation between the d-axis and the α_s-axis (rad/s)*
$\omega_{d/r}$	*electric pulsation between the d-axis and the α_r-axis (rad/s)*
ω_{lim}	*base speed of PMSMs (rad/s)*
Φ_f	*permanent magnet flux linkage (Wb)*
Φ_{sd}	*stator flux in the d-axis (Wb)*
Φ_{sq}	*stator flux in the q-axis (Wb)*
Φ_{rd}	*rotor flux in the d-axis (Wb)*
Φ_{rq}	*rotor flux in the q-axis (Wb)*
Ω	*machine rotation speed (rad/s)*
$\Omega_{\_ref}$	*machine rotation speed reference (rad/s)*
Ω_{cl1}	*clutch speed on the mechanical coupling side (rad/s)*
Ω_{EM1}	*EM1 speed (rad/s)*
Ω_{EM2}	*EM2 speed (rad/s)*
Ω_{ICE}	*ICE speed (rad/s)*
Ω_{tran}	*transmission speed on the mechanical coupling side (planetary gear side, for example) (rad/s)*